LOW ENERGY REACTION MECHANISM STUDIES

IN SOME LIGHT NUCLEI

By

G. P. Lawrence

A dissertation submitted to
the Australian National University
for the degree of Doctor of Philosophy

February, 1964.

PREFACE

The work described in this thesis comprises part of a program of research being carried out with the Cockroft-Walton and Tandem Van de Graaff accelerators and associated facilities, at the Research School of Physical Sciences, Australian National University.

The experiments of Chapter II, concerning neutron irradiation of solid state detectors were performed during the period Nov. 1960 - Aug. 1961, in collaboration with Dr. W. E. Deuchars (on leave from A.W.R.E., Aldermaston).

The $Al^{27}(p,\alpha)Mg^{24}$ reaction study described in Chapter III was carried out during the period Nov. 1961 - Jan. 1963., in collaboration with Dr. A. R. Quinton (on leave from Yale University), with the exception of the detailed measurements of section 3.5, which were obtained by myself subsequent to Dr. Quinton's departure.

The quantitative analysis of the $Al^{27}(p,\alpha)Mg^{24}$ data from the point of view of Statistical Model cross section fluctuations, given in Chapter VI, was initiated and carried out by myself. In this connection I am particularly grateful for illuminating conversations with Professor K. J. LeCouteur

and Dr. L. G. Lawrence (of this laboratory), Dr. N. W. Tanner (on leave from Oxford University) and Mr. J. Menadue (University of Melbourne).

The study of the reaction $C^{12}(O^{16}, \alpha)Mg^{24}$ was initiated by Dr. Quinton and myself, with a preliminary experiment performed with the experimental equipment used in the $Al^{27}(p, \alpha)Mg^{24}$ work. Subsequent to Dr. Quinton's departure, a more thorough investigation of this reaction was carried out (using equipment described in Chapter IV), at first by myself, and later in collaboration with Dr. D. E. Groce. Drs. G. G. Ohlsen and T. R. Ophel are thanked for their support during the early stages of this work.

The semi-automatic handling and analysis (Chapter V) of the $C^{12}(O^{16}, \alpha)Mg^{24}$ data were carried out with Dr. Groce, who bore the major share of the computer programming.

I should like to thank Professor Titterton for his constant encouragement, guidance, and helpful criticism.

In addition acknowledgements are due to Mr. N. F. Bowkett and his staff, for maintenance and operation of the Cockroft-Walton and Tandem Van de Graaff accelerators, and in particular for their co-operation in connection with the difficulties experienced with the O^{16} beams.

Thanks are also due to Mr. G. Clarkson, who inked the scattering chamber figures.

Lastly, I would like to express special gratitude to Miss Greta Berge-Phillips, who typed the drafts and final manuscript.

Some of the work described in this dissertation has been reported in the following publications:-

(1) Interaction of 14 Mev Neutrons with a Silicon Semiconductor Nuclear Particle Detector,
Nature, 191 (1961), 995. (with W. E. Deuchars).

(2) The Reaction $Si^{29}(n, \alpha)Mg^{26}$ at 14 Mev Neutron Energy.
Nature, 192 (1961), 1278 (with W. E. Deuchars).

(3) The Energy Levels of Mg^{24}.
Nuclear Physics, 37 (1962), 244 (with A. R. Quinton).

(4) An 8^+ State in Si^{28}.
Physics Letters, 6 (1963), 231 (with A. R. Quinton).

A publication containing the cross section data of Chapter III and the analysis of Chapter VI is presently in preparation. The results of the $C^{12}(O^{16}, \alpha)Mg^{24}$ data analysis of Chapter V will be prepared for publication when the program is completed.

No part of this dissertation has been submitted for a degree at any other University.

G. P. Lawrence

TABLE OF CONTENTS

CHAPTER 1.

INTRODUCTION

CHAPTER 1

The purpose of these introductory pages is to give a somewhat cursory indication of the material contained in the following chapters. These are, for the most part, self-contained, and it is felt that a detailed background discussion at this point would be superfluous.

Section 1. ARRANGEMENT OF MATERIAL.

The work reported in this dissertation falls into the following two distinct segments. (1) A study of charged particle reactions induced by fast neutron bombardment of Silicon semiconductor detectors; and (2) A partial investigation of the reaction mechanisms involved in the formation of the compound nuclear system Si^{28} at high excitation, and its decay by alpha-particle emission. The compound system was assembled both by proton bombardment of Al^{27}, and by O^{16} bombardment of C^{12}.

Part (1) is encompassed entirely in Chapter II, and Part (2) in the remaining chapters, whose contents are distributed as follows. Chapter III contains the experimental details concerning the measurements performed on the $Al^{27}(p,\alpha)Mg^{24}$ reaction, along with all results and a rather qualitative discussion. Chapter IV contains

experimental details pertaining to the study of the $C^{12}(O^{16}, \alpha)Mg^{24}$ reaction, and Chapter V gives the procedure used in reducing and analyzing the large body of data acquired, along with a qualitative and somewhat tentative discussion of the results so far obtained. Since experimental techniques applied in both the $Al^{27}(p, \alpha)Mg^{24}$ and $C^{12}(O^{16}, \alpha)Mg^{24}$ were similar, there is necessarily some repetition in the material of Chapters III and IV; this has been held to a minimum by cross-referencing, where possible. Chapter VI contains a quantitative analysis of the $Al^{27}(p, \alpha)Mg^{24}$ data from the point of view of recent interesting extensions to Statistical Model theory, along with a detailed introduction to these features. It might be reasonably argued that this material should have been placed immediately following Chapter III. However, it was considered more appropriate to present all data from both the $Al^{27}+p$ and $C^{12}+O^{16}$ reactions before taking up possible theoretical interpretations; moreover the statistical model extensions are also of interest in connection with the $C^{12}+O^{16}$ data, although no analysis of the type applied to the $Al^{27}+p$ data has been undertaken.

Section 2. PART (1), NEUTRON IRRADIATION OF SOLID STATE DETECTORS.

During the period in which the study of Chapter II was carried out, the Silicon solid state detector was just

coming into general use in charged particle spectroscopy as a replacement for gas ionization and proportional counters. The response to fast neutron bombardment was of instrumental interest since: (a) it was important to know the spectral background level which might be induced in detectors observing charged reaction products emitted in competition with neutrons; and (b) considerable attention was currently being focussed on the possibility of utilizing the Silicon detectors (via suitable conversion reactions) as neutron spectrometers, and it was necessary in this connection to know how much interference could be expected from direct neutron reactions with the detector material itself.

In addition to the foregoing, the work of Chapter II demonstrates a simple and straightforward method for measuring the Si^{28} and Si^{29} (n,p) and (n, α) cross sections. The particular advantages are that integrated (over angle) cross sections are obtained automatically and that due to the high intrinsic detector resolution, many states in the final nuclei can be resolved. The relatively finite size of the detectors available to us introduced difficulties connected with wall effects. The required corrections involve what are essentially line shape problems and have been considered in some detail.

In the experimental work of Chapters III and IV, Silicon solid state detectors were employed throughout; however, for the charged particle reactions observed, the secondary effects in the detectors due to competing neutrons were always negligible and were ignored.

Section 3. PART (2). REACTION MECHANISMS IN Si^{28} COMPOUND SYSTEM

3.1. The $Al^{27}(p,\alpha)Mg^{24}$ Reaction.

The Si^{28} compound system was first examined via the $Al^{27}(p,\alpha)Mg^{24}$ reaction, largely for reasons of experimental convenience. During the course of this work it became clear that the strong energy dependence of the measured differential cross sections at high compound excitations, might provide an opportunity for testing the developing theory of statistical fluctuations.

The Statistical Model of nuclear reactions had formerly considered only average nuclear properties, in analogy with thermodynamical averages; in particular, its parameters were extracted only from average, slowly varying, experimental cross sections, mainly obtained with cyclotrons and other poor resolution high energy accelerators. However, with the introduction of few-kev resolution (via Tandem van de Graaff accelerators) at the high compound excitations (15-30 Mev) where the Statistical Model description had been

most valid, it became evident that strong cross section fluctuations (width = a few kev to a few tens of kev) were a prominent reaction feature. The theoretical extensions to the Statistical Model (Chapter VI), which were put forward to treat these phenomena, showed that considerable nuclear information could, in principle, be extracted from a systematic examination of their widths, amplitudes and correlations, as a function of compound nucleus and reaction channel - that, in fact, the cross section fluctuations could be used as a powerful tool in the analysis of nuclear reaction mechanisms.

On the tentative premise, based on qualitative considerations given in Chapter III, that the $Al^{27}(p,\alpha)Mg^{24}$ results could be interpreted via a compound nucleus reaction mechanism and that the Statistical Model should therefore apply, these data were analyzed by the cross-section fluctuation expressions of Chapter VI. Although it was possible to draw some reasonably definite conclusions from the results of this analysis, it is stressed that the whole treatment should be considered chiefly as a probe into the possible limitations of the method. In particular it should be noted that very few analyses of a similar type have yet been performed, so that comparison material is almost non-existent; and in addition there is yet practically no

information on the purely operational criteria, such as how much data is required for meaningful analysis, how does the density of experimental points in a given energy range affect the results, and so on.

3.2. The $C^{12}(O^{16}, \alpha)Mg^{24}$ Reaction.

In the $C^{12}(O^{16}, \alpha)Mg^{24}$ reaction, the Si^{28} compound system formation conditions are considerably different from those for the Al^{27}+p reaction, due to the high Coulomb barrier in the C^{12}+O^{16} entrance channel and the large amounts of orbital angular momentum which can be introduced.

It was initially hoped that it would prove possible to use the C^{12}+O^{16} reaction to cover the same excitation energy range in Si^{28} as that covered in the Al^{27}+p reaction, or at least to obtain a reasonable overlap of excitation ranges, in order to make direct comparisons between cross sections and cross section energy dependence for the two methods of assembling the Si^{28} compound system. However, due to the rapidly decreasing $C^{12}(O^{16}, \alpha)Mg^{24}$ yield at Si^{28} excitations just a few Mev above the highest excitation attained in the $Al^{27}(p, \alpha)Mg^{24}$ reaction (at top of Tandem range), this was not experimentally feasible.

The $C^{12}(O^{16}, \alpha)Mg^{24}$ experimental work was approached with two reaction mechanism possibilities in mind. At

energies near the Coulomb barrier, it was thought that a "quasi-molecular" mechanism (similar to that recently observed in the $C^{12} + C^{12}$ system by the Chalk River Tandem group) might be important. At higher energies the $C^{12}(O^{16}, \alpha)Mg^{24}$ cross sections were expected to be explainable in terms of Statistical Model fluctuations, in analogy with those seen in the $Al^{27}(p, \alpha)Mg^{24}$ reaction at lower Si^{28} excitations. Since the analysis of results is at present incomplete, it has not been possible to give much more than a qualitative assessment (in Chapter V) of the degree to which the $C^{12}(O^{16}, \alpha)Mg^{24}$ data favour either of these reaction mechanisms.

CHAPTER II

NEUTRON INDUCED CHARGED PARTICLE REACTIONS IN A SILICON SEMI-CONDUCTOR DETECTOR

CHAPTER II

Section 1. INTRODUCTION.

The following work consists of a study of the interaction of 14 Mev neutrons with Silicon semiconductor detectors, embracing particularly the reactions $Si^{28}(n,\alpha)Mg^{25}$, $Si^{28}(n,p)Al^{28}$, and $Si^{29}(n,\alpha)Mg^{26}$. The experiment was undertaken during the period November, 1960 - August, 1961 in collaboration with W. M. Deuchars.*

Studies of (n,α) and (n,p) reactions reported before 1961 are principally concerned with total cross section measurements, and generally employed activation techniques (Pa53, Ke59, Ma56). In certain cases scintillating crystals served both as target and detector (Sm60, Mo59, Ga59), but individual charged particle groups are not resolved in the spectra obtained.

The recent development of Silicon semiconductor nuclear particle detectors has provided a convenient method for the study of partial cross sections for individual groups of charged particles emitted from neutron

*Selby Fellow on leave from A.W.R.E., Aldermaston.

induced reactions in the Silicon isotopes. The properties which make such devices particularly suitable for this work are the following:-

a) Target and detector are identical, so that energy loss variation due to target thickness is unimportant.

b) Low concentration of target impurities (of order one part in 10^9).

c) High intrinsic detector resolution.

d) The possibility of using the variable sensitive thickness property to partially discriminate between different species of emitted charged particles.

Section 2. NEUTRON INDUCED CHARGED PARTICLE REACTIONS IN SILICON.

Natural Silicon is composed of 92.2% Si^{28}, 4.7% Si^{29}, and 3.1% Si^{30}. The Q-values for the neutron induced charged particle emitting reactions in these isotopes are given in Table 2.1. The listed values are taken from the least squares adjustment of Wapstra, et al. (Wa60). Where table positions have been replaced by a dashed line, the corresponding reaction is not energetically possible at 14 Mev incident neutron energy.

TABLE 2.1
NEUTRON INDUCED REACTIONS IN SILICON.

Reaction Type	Si^{28}		Si^{29}		Si^{30}	
	Q(Mev)	Final Nucleus	Q(Mev)	Final Nucleus	Q(Mev)	Final Nucleus
(n,p)	-3.856	Al^{28}	-2.980	Al^{29}	-6.510	Al^{30}
(n,α)	-2.655	Mg^{25}	-0.036	Mg^{26}	-4.213	Mg^{27}
(n,d)	-9.356	Al^{27}	-10.109	Al^{28}	-11.370	Al^{29}
(n,He^3)	-12.135	Mg^{26}	- - -	Mg^{27}	- - -	Mg^{28}
(n,np)	-11.580	Al^{27}	-12.334	Al^{28}	-13.590	Al^{29}
(n,2p)	-13.416	Mg^{27}	-13.389	Mg^{28}	- - -	Mg^{29}
(n,T)	- - -	Al^{26}	-11.576	Al^{27}	- - -	Al^{28}

The implications of Table 2.1 are considered in several of the following sections. No discussion, therefore, is offered at this point.

Section 3. EXPERIMENTAL APPARATUS AND PROCEDURE.

The experimental equipment in final form is shown in Fig. 2.1, and consists of two distinct components: a target chamber for producing a high flux of 14 Mev neutrons, and a separate enclosure containing the irradiated semiconductor detector. The main features are labelled in the accompanying figure caption.

3.1. The Neutron Source.

The neutron flux was supplied by the reaction $T(d,n)He^4$. A thin T-Zr target deposited on a thick copper backing* was bombarded by a beam of 500 kev deuterons produced in the A.N.U. 1.2 Mev Cockroft - Walton accelerator. An inspection of the $T(d,n)He^4$ kinematics at this deuteron energy shows that the smallest neutron energy variation with laboratory emission angle occurs at 98° (lab.). The target-detector assembly was therefore generally placed at this angle during irradiations.

The energy of the emitted neutrons at 98°, for 500 kev deuterons is 14.03 ± 0.05 kev; most of the charged particle spectra in the present work were obtained at this energy.

*Supplied by Isotopes Division, A.E.R.E., Harwell.

Fig. 2.1 Experimental apparatus for the study of neutron-induced charged particle reactions in a Silicon semiconductor detector.

Numbered details are :

1. T-Zr target on Cu backing (neutron source)
2. Retractable plate to intercept α-source particles
3. Silicon surface barrier detector
4. ThC'-ThC" α-particle source
5. Insulating detector mounting stud
6. Brace to support He^4 monitor
7. CsI crystal
8. Photomultiplier
9. Ta collimating disc
10. Al light-reflecting layer
11. Beam collimating assembly.

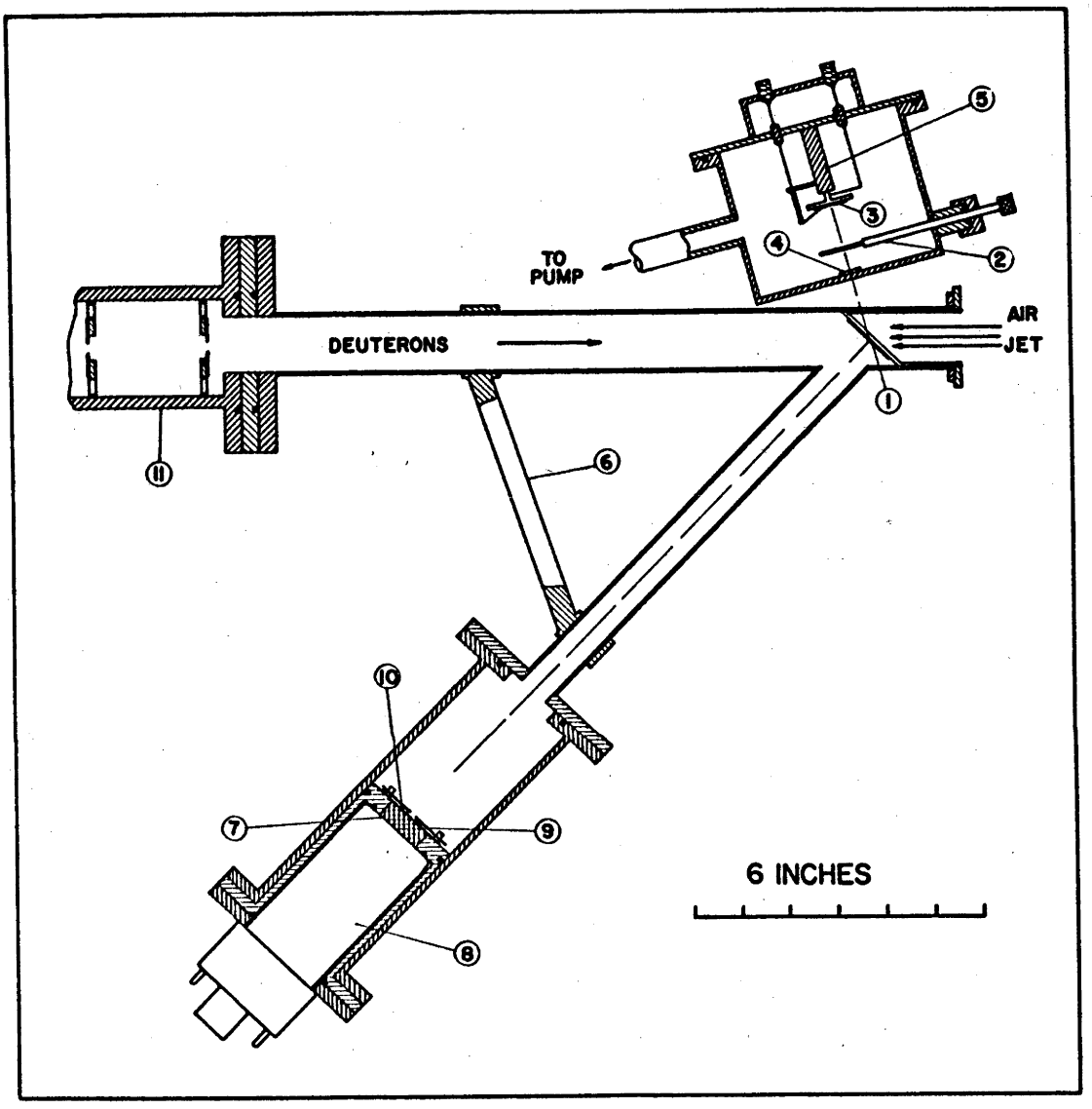
TO
PUMP
DEUTERONS
AIR
JET
1
2
3
4
5
6
7
8
9
10
11
6 INCHES

Since one of the chief experimental requirements was good energy resolution, it was essential to minimize energy degradation of the direct neutron flux due to excess mass surrounding the T-Zr target; for this purpose the target chamber was constructed from 0.015" thick telescopic tubing. The background flux of neutrons (having a wide distribution of energies) due to unfocussed beam striking accelerator surfaces, such as magnet boxes, collimators, etc. was reduced by paraffin shielding. Similar background caused by single and double scattering of the primary source neutrons, was held to a minimum by extending the accelerator beam line so that the neutron source could be placed well clear of large local mass concentrations.

The deuteron beam was collimated on to the target by two .020" thick Ta discs containing $\frac{1}{8}$" diam. holes. The collimator unit was insulated from the target chamber and from the beam tube, so that beam current could be measured at both collimator and target. This permitted best focus conditions to be precisely established. Target currents were typically 20 - 50 μA of deuterons; these were fed to a current integrator, which served only to provide a rough check on the He^4 monitor (described in Section 3.2).

The copper-backed T-Zr target was mounted at 45° to the incident beam on a retractable section of telescopic tubing. Target heating was prevented by forced air cooling of this section, as shown in Fig 2.1.

3.2. The Neutron Flux Monitor.

Neutron flux intensity was measured by monitoring the recoil alpha particle counting rate at a laboratory angle of 45°, and normalizing to the differential cross section data of Fowler and Brolley (Fo56). This is a standard technique and will not be discussed in detail. The He^4 recoils were detected by a collimated CsI crystal-photomultiplier assembly*. Photomultiplier pulses were transmitted by cathode follower to a linear amplifier whose output was recorded by a single scaler.

3.3. The Detector Chamber.

The chamber in which the semiconductor detector was mounted during neutron irradiation consisted of a thin-walled brass cylinder, containing provision for a calibrating alpha particle source (on the rear face), and a retractable Ta shutter. This was inserted between detector

* Generously supplied by R. N. Glover of this laboratory.

and source when actual neutron-induced charged particle spectra were being accumulated.

A single Silicon surface barrier detector was mounted and insulated from the chamber on a perspex rod fixed to the removable chamber lid. Unshielded leads connected to front and rear detector contacts and passed through Kovar vacuum seals to BNC sockets within a shielding cap attached to the lid, as shown. The detector mount was accurately positioned on the chamber centerline, which was in turn accurately set at 98^{o} with respect to the deuteron beam, and aimed at the T-Zr target centre.

The chamber was maintained at a pressure of 10^{-6} mm Hg and liquid air trapped by an adjustable tubing arrangement connected to a portable pumping bench. Separation of the detector chamber from the T-Zr target chamber removed the detector from the effects of scattered beam and stray ions produced in the target vicinity. A preliminary experiment, with the detector mounted inside the tritium target chamber showed that these registered a considerable background counting rate.

During part of the work, a Ta cap was placed over

the front face of the detector, in order to intercept charged particles produced by neutron induced reactions in the chamber walls.

3.4. The Electronics.

The electronics used in this work, in final form, are shown in Fig. 2.2.

Pulses could be taken from either the front or rear contacts of the detector. However, experiment showed that operation with the front surface earthed and pulses taken from the rear contact was generally more satisfactory than the reverse situation. Positive bias up to 90V was applied to the detector through a 10 MΩ current-limiting resistor and suitable filter network. Connection to the input of a charge-sensitive preamplifier* was made via a short shielded cable, to reduce input capacitance to a minimum. The preamplifier gain was approximately X 400. Output pulses were further amplified by a modified 1430A Harwell linear amplifier (containing variable differentiating and integrating time constants), and analyzed by a 400 channel R.I.D.L. pulse height analyser. A highly stable Hg-relay pulser, with output attenuator linear to 0.1%, was used in checking the resolution, linearity, and stability of the system.

*Design similar to that of Fairstein (Fa60).

Fig. 2.2 Electronics for Silicon detector and He^4 monitor

Details are supplied in the text.

ELECTRONICS BLOCK DIAGRAM

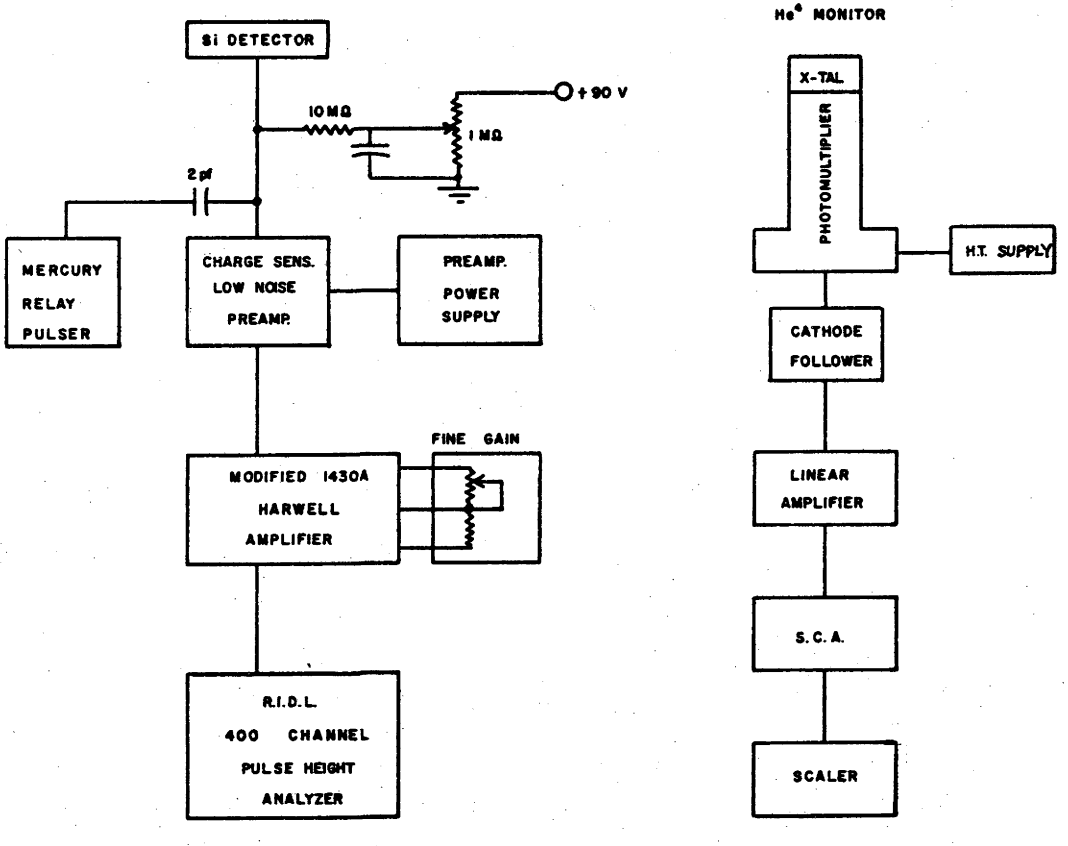

The charge sensitive preamplifier, and 400 channel analyzer were not initially available, so that during early stages of the work, equipment with considerably inferior linearity and resolution was used.

Resolution, stability, and linearity of the complete detection system is considered in Section 3.7.

3.5. The Surface Barrier Detectors.

Several different Silicon surface barrier detectors were used in this work. Two were supplied by A.W.R.E., Aldermaston, and the remainder were fabricated in this laboratory, from material of 400Ω-cm and 800Ω -cm restivity. The properties and theory of operation of diffused junction and surface barrier solid state detectors are well known, and have been adequately reviewed by a number of authors (De60a, Ma62, Br62, Gi62, Fi63). Only those points bearing directly on the present work are discussed here.

The detectors fabricated in this laboratory were manufactured by a method similar to that described by Dearnaley (De61a). This involves the careful preparation of mirror-smooth surfaces on 1 mm thick Silicon wafers, by abrasive plus acid etch treatment. Following this, the

crystals are rinsed in de-ionized water, and exposed to air at STP for several days. This permits the growth of a thin oxide surface layer, containing a high density of p-impurity sites, and the resultant formation of the required p-n junction. An Au film is vacuum deposited on the oxidized surface, and serves to define the active area of the detector.

3.6 Detector Performance.

Detectors were normally operated at 40-50 V reverse bias, which produced estimated depletion layer thicknesses of approximately 70 microns and 120 microns for the 400Ω-cm, and 800Ω -cm material respectively. The values were obtained from the relationship given by Blankenship (B160), and include a correction due to finite charge carrier collection time.

Detector performance was tested by observation of the spectrum of alpha particles emitted by a mixed ThC'-ThC" source. This source produces two strong groups of well known energy (Ev 55) at 8.78 Mev and 6.05 Mev (doublet), which provide a measure of the detector resolution and a partial check on the linearity of the entire system.

A typical source spectrum obtained with an 800Ω -cm

detector, and the electronics of Fig. 2.2 is shown in Fig. 2.3. A pulser line is included to indicate the resolution broadening due to electronics alone.

Detector lifetimes varied from a few days to several months. Causes of deterioration were thought to be connected chiefly with contamination of the surface layer by organic vapours. Similar effects have been reported by several workers (Da60a). It was occasionally possible to restore satisfactory performance by exposing the detector surface to a jet of deionized water, and permitting the oxide layer to re-form.

3.7. Detection System Resolution.

A considerable effort was expended in improving the energy resolution of the detection system. The chief sources of line broadening are:-

(a) intrinsic detector noise, generated by fluctuations in reverse junction current, and surface leakage;

(b) electronic noise, mostly contributed by the preamplifier first stage;

and

(c) amplifier gain variations.

Fig. 2.3 Spectrum of alpha-particles emitted from ThC'-ThC" source

This spectrum shows the typical resolution attained by the Si detector and electronics; an Hg-pulser line is included to indicate the resolution spread due to electronics alone.

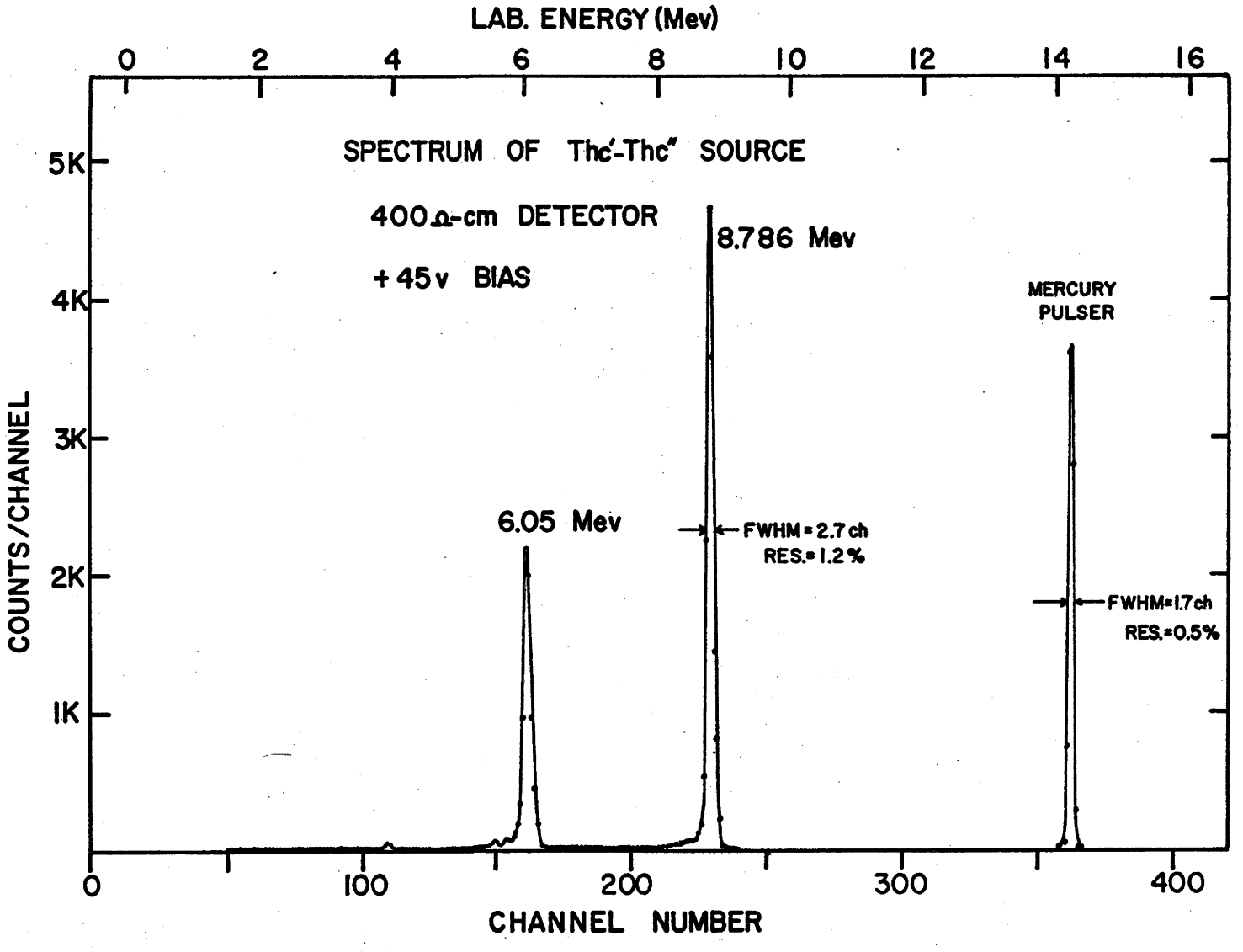
LAB. ENERGY (Mev)
0
2
4
6
8
10
12
14
16
SPECTRUM OF Thc'-Thc" SOURCE
400Ω-cm DETECTOR
+45v BIAS
8.786 Mev
MERCURY PULSER
6.05 Mev
FWHM=2.7ch
RES.=1.2%
FWHM=1.7ch
RES.=0.5%
5K
4K
3K
2K
1K
COUNTS/CHANNEL
0
100
200
300
400
CHANNEL NUMBER

Electronic noise was reduced by replacement of the original voltage sensitive preamplifier with charge sensitive circuitory feeding a standard 1430A Harwell amplifier, and finally by the Fairstein charge sensitive preamplifier mentioned in section 3.4. The input valve of this preamplifier was carefully selected for maximum S/N ratio, and the entire preamplifier cushioned to minimize the effects of microphonics.

The theory of noise and resolution, and principles of operation of charge-sensitive preamplifiers have been adequately discussed by several authors, (Ga60, Gi53, Fa60) and will not be detailed here.

Long term gain variation in the Harwell amplifiers was quite serious. This was measured by observing the peak position of amplified pulses fed from an Hg pulser, (stable to 0.1%), and analyzed in a 400 channel PHA. During an observation period of 3 hours, an overall gain shift of 3.5% was obtained. Since some of the detector irradiation periods were of 10-12 hours duration, it was necessary to compensate the gain instabiliby by including a fine gain adjustment in the 1430A amplifier . During actual runs, gain was monitored in the above fashion and adjusted at fifteen minute intervals. With this procedure,

the pulser peak could be kept to within $\pm$ 0.5 channels (in 400) of its initial position. This assured a total system gain stability of 0.15%.

Most of the detectors used in this work gave resolutions between 1.0 and 1.5% (for the ThC'-ThC" 8.78 Mev line) when connected with the final version of the electronics. It was occasionally possible to obtain $<$ 0.7% overall resolution.

Section 4. EXPERIMENTAL RESULTS.

4.1. The Charged Particle Spectra.

During neutron irradiation the detector was placed at distances from the source ranging from 3.5 - 6 cm. This furnished an acceptable compromise between the time required to accumulate statistically meaningful spectra, and neutron energy variation due to the finite solid angle subtended by the detector. Neutron flux at the detector was typically 10^8 neutrons/cm^2/sec, and incident energy variation over the detector surface was estimated to be 50 Kev.

Several spectra were obtained at 98°, using a variety of detectors, depletion layer thicknesses, and amplifier time constants. A spectrum obtained with a 800Ω -cm detector, with a depletion depth of 120 microns

(maximum attainable) is shown in Fig. 2.4. For comparison purposes a spectrum taken with the same detector set at 0^{o} to the deuteron beam is shown as an inset. This reveals the effects of the considerable energy variation with angle of neutrons emitted in the forward direction.

Since Si^{28} is 92.2% abundant in natural Silicon, it is expected that the dominant features of the spectrum of Fig. 2.4 can be attributed to neutron induced reactions in this isotope.

4.2. The $Si^{28}(n,\alpha)Mg^{25}$ Reaction.

On the assumption that the well-resolved peaks in the high energy portion of the spectrum could be attributed to the $Si^{28}(n,\alpha)Mg^{25}$ reaction, we calculated the expected energy deposited in the depletion layer by alpha particles populating the first fifteen levels of Mg^{25}, plus the energy of their respective Mg^{25} recoils. (This is just $E_n + Q$ for each group). These energies are indicated by arrows above the spectrum of Fig. 2.4, and can be seen to correspond closely with the energies of the observed groups. The level scheme for Mg^{25} was taken from the results of Hinds and Middleton (Hi60a), and the experimental energy scale was calibrated with the two strong alpha particle groups emitted by a ThC'-ThC"

Fig. 2.4 Charged particle spectra from Silicon surface barrier detector exposed to 14.03 Mev neutrons

The main spectrum was obtained with the detector at 98° to the deuteron beam, and the upper-right inset spectrum was measured with the detector at 0° to the beam. The inset energy scale is slightly expanded with respect to that of the main spectrum; for ease of comparison the $Si^{28}(n,\alpha)Mg^{24}$ g.s. peaks have been aligned, and dashed arrowsare drawn connecting corresponding $Si^{28}(n,\alpha)Mg^{24}$ groups in the two spectra. The top (lab. energy) scale is not meaningful for the 0° spectrum.

Further details are given in the text.

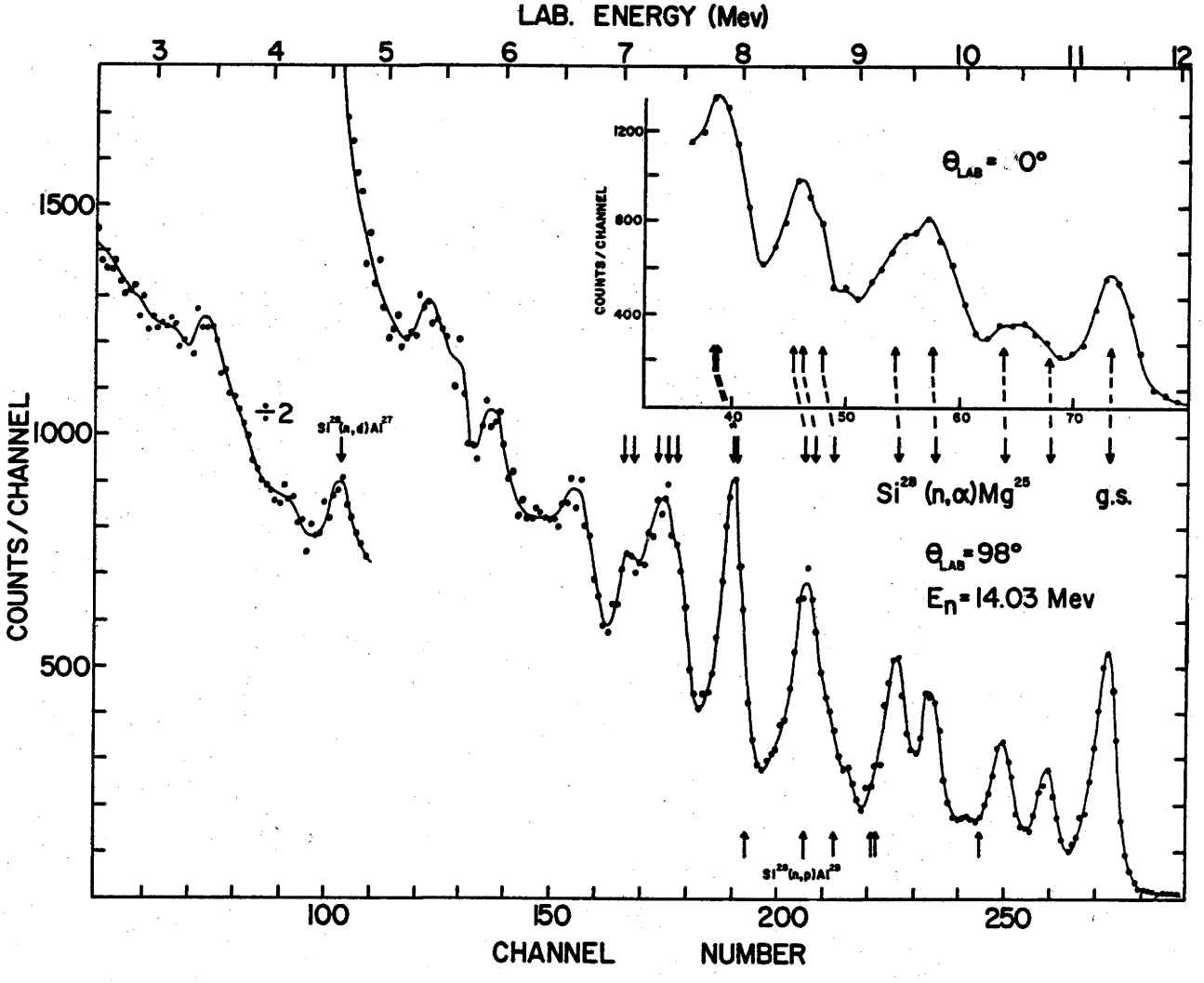
LAB. ENERGY (Mev)
3
4
5
6
7
8
9
10
11
12
1500
1000
500
COUNTS/CHANNEL
÷2
Si²⁸(n,d)Al²⁷
1200
800
400
COUNTS/CHANNEL
θLAB = 0°
40
50
60
70
Si²⁸ (n,α)Mg²⁵ g.s.
θLAB=98°
En=14.03 Mev
Si²⁸(n,p)Al²⁸
100
150
200
250
CHANNEL NUMBER

source (See section 3.6).

Since the detector sums the energies of the alpha particles and corresponding Mg^{25} recoil nuclei, the precise agreement between experimentally observed and calculated group energies indicates that the detector response to the heavily ionizing Mg^{25} nuclei is linear and identical with the response to light particles. Blanc, et al. (Bl62) have noted this point.

Cross section measurements for the reactions populating the low lying levels of Mg^{25} are discussed in Section 5.

4.3. The $Si^{28}(n,p)Al^{28}$ Reaction.

With a Q-value of -3.86 Mev, the maximum laboratory energy of emission for protons produced in the reaction $Si^{28}(n,p)Al^{28}$ by 14.03 Mev neutrons is 9.41 Mev. A comparison of the maximum detector depletion depth, and range-energy values for protons in Silicon (extrapolated from the data of Whaling (Wh58)), reveals that protons of kinetic energy greater than 3.5 Mev will not be stopped within this sensitive layer unless they are emitted in a direction near the plane of the junction. If the angular distribution of $Si^{28}(n,p)Al^{28}$ protons

populating the low lying levels of Al^{28} is nearly isotropic, a depletion depth of several hundred microns is required to observe the full energy of a large fraction. If, on the contrary, the highest energy groups have angular distributions strongly peaked at a particular emission angle, then some observational advantage is obtained by changing the orientation of the depletion layer with respect to the neutron direction.

In order to examine the $Si^{28}(n,p)Al^{28}$ more closely, the detector plane was rotated about an axis normal to a line drawn from the neutron source at 98^{o} and passing through the detector geometric centre. This varied the neutron angle of incidence at the detector, but ensured that the neutron energy spread over the detector volume remained a minimum. Spectra were obtained at several angles, but all showed no essential difference from that of Fig. 2.4.

We calculated the expected energy deposited in the detector by protons and Al^{28} recoils corresponding to the first seven levels in Al^{28}. These are shown by arrows below the spectrum of Fig. 2.4. The energy level scheme for Al^{28} was taken from the review paper of Endt

and Braams (En57). A distinct shoulder on the low energy side of the third highest alpha group is attributed to the ground state $Si^{28}(n,p)Al^{28}$ reaction, although its observed energy is slightly less than the expected value. Inspection of Fig. 2.4. reveals no evidence for proton groups corresponding to individual excited states of Al^{28}, although the large rise at lower energies is almost certainly due to the presence of low energy protons for $Si^{28}(n,p)Al^{28}$. The level density of the final nucleus, in the region corresponding to these proton energies, is too high to permit resolution of groups corresponding to individual levels. The low energy portion of the spectrum is expected to contain, in addition, a large contribution due to higher energy protons and alpha particles depositing only part of the energy in the depletion layer. This point is discussed more fully in Section 5.

4.4. The $Si^{28}(n,d)Al^{28}$ Reaction.

In Fig. 2.4 it is seen that a well defined peak is evident at an energy of 4.65 Mev. With a Q-value of -9.36 Mev, the ground state transition for $Si^{28}(n,d)Al^{27}$ corresponds to an energy release of 4.67 Mev in the detector. This is sufficiently close to the observed peak to warrant

its assignment to the (n,d) reaction. The $Si^{28}(n,d)Al^{27}$ reaction has not been previously observed.

4.5. Other Si^{28} Reactions.

An inspection of table 2.1 reveals that the Q-values for the $Si^{28}(n,He^3)$, (n,np), (n,2p) and (n,T) reactions are all highly negative (< -11.5 Mev), so that energies of corresponding emitted charged particles will be < 2.5 Mev at the given neutron energy. Possible spectrum contributions from these reactions are therefore lumped into the unresolved low energy portion, which provides no unambiguous indication of their presence.

4.6. The $Si^{29}(n,\alpha)Mg^{26}$ Reaction and Suggested Level in Mg^{26} at 1.33 Mev.

The fact that the $Si^{29}(n,\alpha)Mg^{26}$ reaction has a Q-value of -0.036 Mev means that although the isotopic abundance of Si^{29} in natural Silicon is only 4.7%, it is possible to observe this reaction in competition with the more intense Si^{28} reactions.

During the course of the present work. Dearnaley and Ferguson (De61d) reported results of observations on $Si^{29}(n,\alpha)Mg^{26}$, which furnished evidence for a previously unobserved level in Mg^{26} at an excitation of 1.33 Mev. Their experimental arrangement was similar to that

described here; incident neutron energy was 7.6 Mev.

This report prompted a re-investigation of the high energy portion of Fig. 2.4. In order to obtain statistically meaningful results it was necessary to irradiate the detector for 15-20 hour periods. Amplifier gain was stabilized as described in section 3.7. A typical spectrum is shown in Fig. 2.5. The results of Hinds and Middleton (Hi60a) for the energy level positions of Mg^{26} enable assignment of the two highest energy groups to alpha particles populating the Mg^{26} ground state and the state at 1.80 Mev excitation. The alpha particle groups corresponding to the ground state and first four excited states of Mg^{25}, populated by $Si^{28}(n,\alpha)Mg^{25}$ are also indicated. It will be seen that this spectrum provides no evidence for an alpha group corresponding to a level of Mg^{26} at 1.33 Mev excitation. This result was reported in Nature (De61c).

Previous investigations of the energy levels of Mg^{26}, notably those of Hinds and Middleton (Hi60a), using the reactions $Mg^{25}(d,p)Mg^{26}$, $Al^{27}(t,\alpha)Mg^{26}$, and $Mg^{24}(t,p)Mg^{26}$ gave no indication of a level in Mg^{26} at this excitation; nor did the experiment of Glover and Weigold

Fig. 2.5 $Si^{29}(n,\alpha)Mg^{26}$ spectrum obtained with Silicon surface barrier detector exposed to 14.03 Mev neutrons

The high energy portion of the spectrum is multiplied by 20 to reveal the significant $Si^{29}(n,\alpha)Mg^{26}$ details. Statistical counting errors are not shown, but can be inferred from the left-hand scale $\pm$ 20.

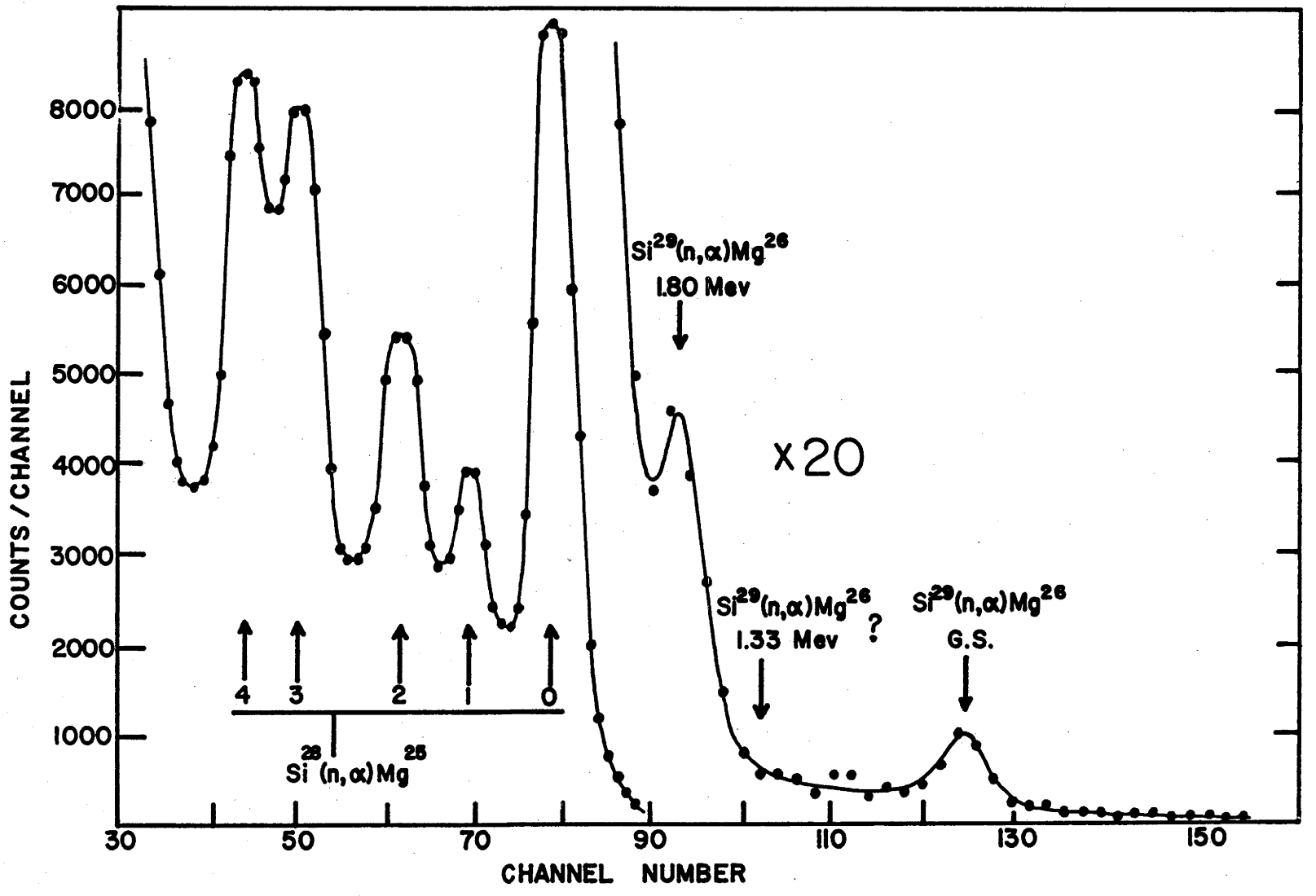
COUNTS / CHANNEL
8000
7000
6000
5000
4000
3000
2000
1000
30
50
70
90
110
130
150
CHANNEL NUMBER
Si29(n,α)Mg26
1.80 Mev
x20
Si29(n,α)Mg26
1.33 Mev
?
Si29(n,α)Mg26
G.S.
4
3
2
1
0
Si28(n,α)Mg25

(Gl61), investigating the reaction $Al^{27}(n,d)Mg^{26}$, or that of White, et al. (Wh61), examining proton inelastic scattering from Mg^{26}.

Following our experiment, Dearnley and Ferguson reinvestigated the $Si^{29}(n,\alpha)Mg^{26}$ reaction at several neutron energies, using a variety of neutron sources. This work (De62d) revealed that the alpha group in question could be attributed to the ground state $Si^{28}(n,\alpha)Mg^{25}$ reaction induced by neutrons emitted from the Titanium backing of their tritium target, via the reaction $Ti^{48}(d,n)V^{49}$. Depraz et al. (De62e), in a similar experiment at 14.0 Mev neutron energy, observed evidence for the 1.33 Mev Mg^{26} level; it seems probable that their results can be explained in the same manner as those of Dearnaley and Ferguson.

4.7. Other Si^{29} Reactions.

Since the Q-values for the reaction $Si^{29}(n,p)Al^{29}$ is -2.98 Mev, proton groups corresponding to the low lying levels of Al^{29} are obscured by the more intense $Si^{28}(n,\alpha)$ and (n,p) reactions, and are not observed. For the $Si^{29}(n,He^3)$, (n,d), (n,np), (n,2p) and (n,T) reactions, the considerations of Section 4.5 are applicable.

4.8. Si^{30} Reactions.

An inspection of Table 2.1 indicates that none of the Q-values for neutron induced charged particle reactions in Si^{30} are greater than the Q-value for the ground state Si^{28} $(n,\alpha)Mg^{25}$ reaction. The Si^{30} isotopic abundance of only 3.1% does not, therefore, permit observation of charged particles emitted by Si^{30} reactions in competition with the intense groups from Si^{28}.

Section 5. $Si^{28}(n,\alpha)Mg^{25}$ PARTIAL REACTION CROSS SECTIONS.

Partial cross sections (at 14.03 Mev neutron energy) for the reactions $Si^{28}(n,\alpha)Mg^{25}$ feeding the five lowest levels of Mg^{25}, are given in this section. Fig. 2.6, taken from the compilation of Endt and Van der Leun (En62b) shows the relevant portion of the Mg^{25} energy level scheme, and includes the low energy region of the Mg^{26} level scheme - showing the doubtful 1.33 Mev level as a dashed line.

The Si^{28} $(n,\alpha)Mg^{25}$ partial cross sections σ_j were obtained from the relation:-

$$\sigma_j = \left[\frac{\sum C_i}{(1 - \sum T_i)} \right] \Big/ N_n \text{ .S.D, where } \sum C_i \text{ is the}$$

Fig. 2.6 Low-lying energy levels of Mg^{25} and Mg^{26}.

ENERGY LEVELS OF Mg^{25}, Mg^{26}

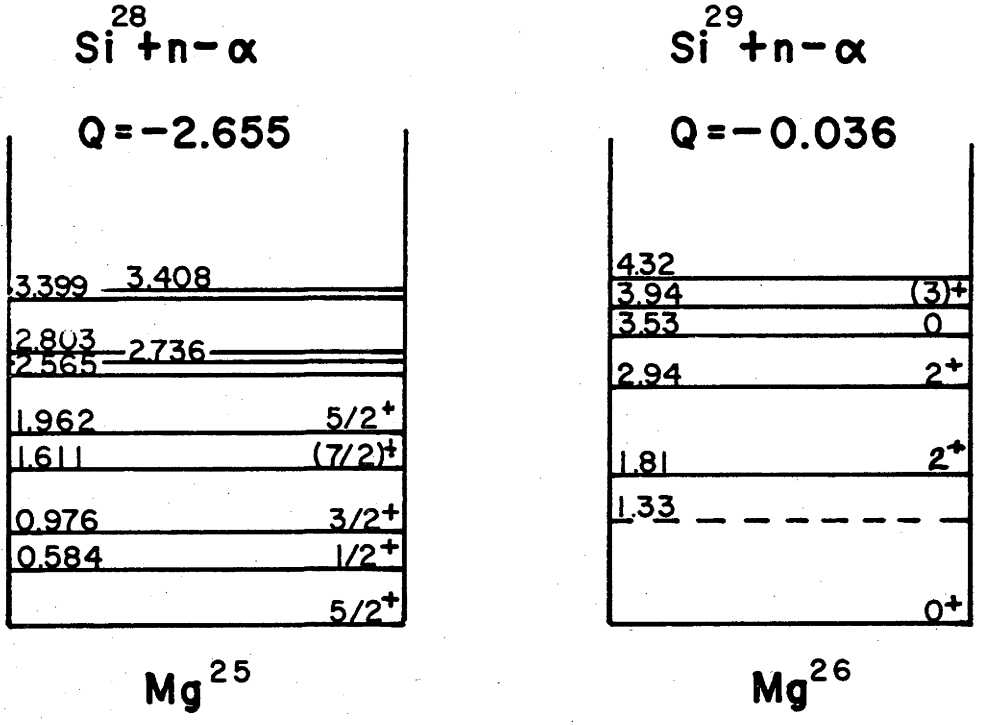

sum over all counts corresponding to each alpha peak of Fig. 2.4, S is the density of Si^{28} nuclei in natural Silicon, D, the detector depletion depth, $\sum T_i$, a correction factor described below, and N_n is the time integral of the neutron flux passing through the detector volume. N_n is just $M(\Omega_o/\Omega_m)$, where Ω_o and Ω_m are the solid angles subtended by the active detector area (assumed equal to the Au surface film area), and by the collimated CsI He^4 - recoil monitor. M is total monitor counts/per irradiation period. No correction is included for the attenuation of N_n through the detector volume, since this was estimated to be negligible.

A calculation of the ranges in Silicon (Wh58) of the highest energy alpha particles reveals that they are of the same order of magnitude as the maximum depletion layer thickness. Wall and end effects are therefore expected to be considerable - a large fraction of the emitted alpha particles depositing less than their full energy in the depletion layer. Associated with each peak of Fig. 2.4, is a tail or line shape, comprising lower energy contributions from alpha particles belonging to the same group, but which cross the depletion layer boundaries. The form of these line shapes is a function of the range-

energy relationship in Silicon and the angular distribution of the emitted alpha particles.

In order to obtain a first approximation to the required cross section corrections, it was necessary to compute line shapes for several representative cases. Calculations were performed with the aid of a simple surface barrier detector model, and a program written for an I.B.M. 1620 computer. Line shape computations of this type have not been previously reported, and are discussed in detail in Appendix A. At this point it is only relevant to indicate the results of Appendix A bearing directly on the extraction of the $Si^{28}(n,\alpha)Mg^{25}$ partial reaction cross sections. These are illustrated in Fig. 2.7.

The relative magnitude and shape of the low energy tail is shown for four cases. These are normalized to a full energy peak of constant height and FWHM. (Area = 100 arbitrary units). The lower two forms represent the theoretical line shapes associated with the most energetic $Si^{28}(n,\alpha)Mg^{25}$ alpha particles, showing the dependence on the choice of angular distribution; the upper forms give a similar comparison for line shapes associated with alpha particles feeding the 4th excited state of Mg^{25}. The symbols $\sum T_i$ indicate the fractional area of each indi-

Fig. 2.7 Line shapes for alpha particles emitted in the Reaction $Si^{28}(n,\alpha)Mg^{25}$, in a 120μ (depletion layer) Silicon detector

The 20 channel spectra, represented by thin-line histograms, have been normalized to a scale of 100. Smooth, heavy lines have been drawn through them to accentuate the significant "tail" structure. Relative channel contributions to the line shapes are normalized to a full-energy contribution of 100, which is shown as the area under a full-energy peak whose FWHM = 3%. For ease of comparison the line shapes have been shifted vertically with respect to each other by 6 units, and the entire height of the full-energy peak is shown only for the lowest line shape. Other details are given in the text.

LINE SHAPES FOR CASE
$Si^{28}(n,\alpha)Mg^{25}$
IN 120μ DETECTOR

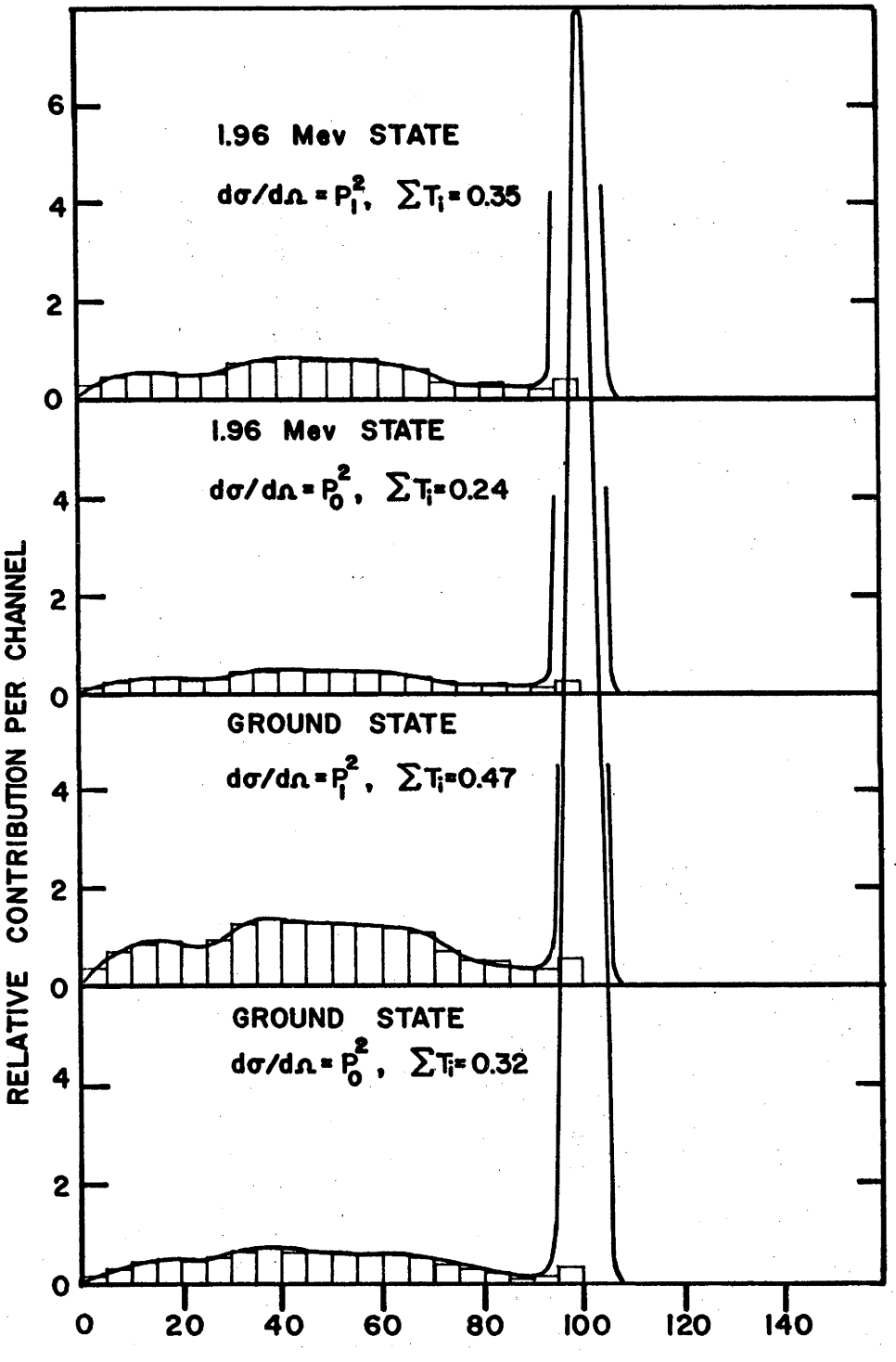

vidual alpha group lying in the low energy tail.

It can be seen that the general form of the line shapes is not very sensitive to the choice of angular distribution. However, the lack of experimental information on the real $Si^{28}(n,\alpha)Mg^{25}$ angular distribution leads to an uncertainty in the estimate of the ΣT_i factors. The two test distributions of Fig. 2.7 are extreme cases (isotropic, and strong forward and backward peaking); the actual alpha particle distributions are expected to be more intermediate. Absence of marked changes in spectra taken at various detector orientations (section 4.3) lends support to this hypothesis, and final corrections, ΣT_i, were arbitrarily chosen as the means of the quoted extremes. Correction factors applied to the three alpha groups lying between the ground state and 4th excited state group were obtained by linear interpolation.

Using line shapes corresponding to the intermediate ΣT_i we reduced the $Si^{28}(n,\alpha)Mg^{25}$ spectra with the following procedure:-

(a) The highest energy alpha peak was fitted with a Gaussian shape having the same height and FWHM. A low energy tail of appropriate shape and magnitude was extended from the peak.

(b) This entire line shape was subtracted for the original spectrum, and the number of alpha counts contributing to it approximated by $\sum C_i/(1-\sum T_i)$.

(c) The procedure was repeated for the peaks corresponding to the next four alpha groups.

Since the tail segments of higher energy peaks lying under lower energy peaks are small in comparison with the lower energy peak areas (the $\sum C_i$), the subtraction procedure is not sensitive to inaccuracies in tail shape and magnitude; uncertainties in the extracted $\sum C_i$ are of the order of 5%. The error in $\sum C_i/(1-\sum T_i)$ due to the uncertainty in the correction factor can be as large as 15%.

Before applying the above procedure to the fourth and fifth alpha groups of Fig. 2.4, it was necessary to subtract the line shape due to the ground state $Si^{28}(n,p)Al^{28}$ proton group. Colli et al. (Co61) have measured a partial angular distribution for this reaction at 14.0 Mev neutron energy, which suggests strong forward peaking. Line shape calculations using such a distribution indicate that the relative magnitude of the full energy

proton peak in Fig. 2.4 is expected to be strongly dependent on the orientation of the detector with respect to incident neutrons. Since experiment (Section 4.3) provided no evidence for this, the ground state proton line shape was computed using an isotropic angular distribution.

Since proton groups corresponding to the first and second excited states of Al^{28} were obscured by strong alpha groups, it was not possible to obtain any idea of the magnitude of the appropriate line shape subtractions, and spectrum analysis was discontinued. Six spectra similar to that of Fig. 2.4 were analyzed in the described fashion, and the extracted $Si^{28}(n,\alpha)Mg^{25}$ partial reaction cross sections are given in Table 2.2. The values quoted are simple means and the errors are R.M.S. deviations.

TABLE 2.2

PARTIAL CROSS SECTIONS FOR THE REACTION $Si^{28}(n,\alpha)Mg^{25}$.

Mg^{25} Excitation (Mev)	$\sigma(n,\alpha)$ at 14.03 Mev
0.000	1.84 ± 0.36 mb
0.582	0.75 ± 0.20 mb
0.976	0.98 ± 0.25 mb
1.612	1.19 ± 0.31 mb
1.965	1.28 ± 0.33 mb

The $Si^{28}(n,\alpha)Mg^{25}$ spectra and cross sections have been reported in Nature (De61b).

Section 6. DISCUSSION.

These results for $Si^{28}(n,\alpha)Mg^{25}$ represent the first investigation of this reaction at 14 Mev neutron energy. Several workers have since reported studies of $Si^{28}(n,\alpha)Mg^{25}$ at similar neutron energies, using similar experimental methods. With a 150 micron detector, Andersson - Lindström (An62) has obtained spectra at neutron energies of 14.1, 14.4 and 14.6 Mev. The 14.1 Mev spectrum is in good agreement with that of Fig. 2.4; cross section measurements are not given. Blanc, et al. (Bl62), using a 40μ detector and 14.6 Mev neutrons present a poorly resolved spectrum on which cross section measurements are attempted. Since wall effect correction uncertainties in such a thin detector are expected to be very large, their procedure would appear to be questionable. Dixon and Aitken (Di62), using 13.9 Mev neutrons, have obtained spectra with a triple coincidence arrangement which enables partial separation of (n,α) and (n,p) contributions. Their work is discussed in Appendix B. Didier et al. (Di63) and Facchini et al. (Fa62), using 14.0 Mev neutrons, report spectra in good agreement with that of Fig. 2.4. Dearnaley and Whitehead (De61a), Potenza et al.(Po63), and Anderson - Lindström (An63) have investigated $Si^{28}(n,\alpha)Mg^{25}$ at neutron energies in the range 3.9 Mev.

Most of the above workers have observed the alpha groups in the high energy portions of their spectra which correspond to the ground state and first excited state $Si^{28}(n,\alpha)Mg^{26}$ reactions, and also note evidence for the $Si^{28}(n,p)Al^{28}$ ground state and excited state reactions.

Several experimenters, notably Potenza (Po63), Andersson - Lindström (An63) and Colli and his collaborators (Co63, 62a:b:c) have recently measured extensive cross section excitation functions for the above reactions. Their work is more relevant to the material of Chapter VI than to that of this chapter, and is detailed there.

Section 7. APPLICATION TO NEUTRON SPECTROSCOPE.

Since neutrons are emitted in competition with almost all charged particle reactions, their background effects in Silicon semiconductor detectors must generally be taken into account in the measurement of direct charged particle spectra with these devices. This is naturally particularly true for cases in which the direct charged particle counting rate is small compared with the total neutron flux through the detector volume, or where the detector sensitive volume is large compared with its exposed surface area. The work described in this chapter is useful

in that it provides information on the form and magnitude of the neutron induced background effects.

It has been recently noted that the apparent liability of the detector neutron interaction can be turned to advantage. Marcazzan et al. (Ma62) points out that the good resolution of semiconductor detectors provides a method for measuring the energy and line width of mono-energetic neutrons, via the $Si^{28}(n,\alpha)Mg^{25}$ reaction. Birk et al. (Bi63) suggest the construction of a semi-conductor detector from separated Si^{29}, pointing out that the $Si^{29}(n,\alpha)Mg^{26}$ spectrum is more suitable for this purpose, due to the large separation between ground state and first excited state groups.

It is now well known that solid state detectors can be transformed into neutron spectrometers when used in conjunction with charged particle producing conversion reactions (such as $Li^6(n,\alpha)T$, $He^3(n,p)T$, $B^{10}(n,\alpha)Li^7$, and H(n,n)H). These techniques have been discussed by many experimenters (Ba59, Mu62, De62a, Sa62, Fe62a, De62b), and it is only relevant to note here that all have low efficiencies and suffer from competition with the Silicon background reactions.

Several workers have reported that semiconductor detectors exposed to neutron bombardment show signs of radiation damage for integrated fluxes in excess of $10^{13} n/cm^2$ (Kl61, Ba61, Bo62a). Performance deterioration takes the form of an increase in reverse current. Endres et al. (En62a) has measured the relationship between reverse current and integrated neutron flux, and points out that Silicon detectors can be usefully employed as reactor flux measuring devices.

APPENDIX A

SOLID STATE DETECTOR LINE SHAPES

This appendix presents a method for calculating line shapes for charged particle groups emitted by neutron induced reactions in a Silicon surface barrier semiconductor detector. Results are used for applying corrections to $Si^{28}(n,\alpha)Mg^{25}$ reaction cross section measurements, discussed in Chapter II, Section 5.

Charged particle reaction products released by neutron interactions in a Silicon detector are emitted in all directions. It is clear that if their ranges in Silicon are of the same magnitude, or greater than the junction thickness, a large fraction will cross the junction boundaries and deposit less than their full energy in the depletion layer. The resulting energy spectrum of a single alpha particle group consists, therefore, of a sharp peak containing full energy counts, and a lower energy tail contributed by particles depositing only part of their kinetic energy within the junction. In order to reduce the calculation of such tails to manageable dimensions, several simplifying approximations are made.

A.1. THE APPROXIMATIONS.

a.) The sensitive region of the detector is treated as a thin slab of infinite area; i.e. edge effects are neglected. Since the ratio of depletion layer depth to diameter is of order 1:100, this is a satisfactory approximation.

b.) The relative loss of the heavy reaction products (recoil nuclei) across the depletion layer boundaries is neglected, due to their extremely short range in Silicon.

c.) Depletion layer boundaries are assumed well defined. This is an excellent approximation at the surface due to the well-known lack of appreciable energy "window". It is less satisfactory for the inner boundary, since the limits of the effective charge collection region depend on local electric field strengths, and carrier mobilities, and are expected to differ considerably from point to point. The effective sensitive depth used in the calculation must therefore be treated as an average.

d.) The incident neutrons are assumed normal to the detector plane at all points in the sensitive volume. This ignores the effect of finite source-

detector solid angle.

e.) Neutron flux is assumed constant throughout the sensitive volume; i.e. no attenuation.

f.) The time and space density of reaction "events" is considered constant at all points in the detector. This is equivalent to $P(B,x_i,t) = \text{const.}$, where P is the probability of a reaction of type B occuring at point (x,y,z) and time t.

A.2. THE COMPUTER PROGRAM.

With the above simplifications, the calculation was reduced to a program executed by an I.B.M. 1620 computer. The program was coded by the present writer and is described below. A flow diagram is given in Fig. A.1.

Fig. A.2 represents an idealized surface barrier detector in cross section. Region A is just the depletion layer itself, and produces tail contributions corresponding to particles crossing either boundary. A second set of contributions is delivered by particles originating in region B and crossing into or traversing region A.

It will be seen that the axial symmetry of the

Fig. A.1 Flow diagram of computer program for calculating solid-state detector line shapes

Decisions points are represented by diamonds, and all other operations by rectangles. Arrows indicate direction of flow. Subroutine is range-energy table look-up. Indices N_x N_θ are number of spatial emission positions and angles used in the calculation; θ_M is 180°, and X_M is $D + R_o$ (see Fig. A.2.). A and B refer to different detector regions, described in Fig. A.2. E_L and E_{TOT} are energy release in junction for each event (x,θ), and total energy of particle, respectively. The weights used in the analysis phase of each energy release calculation cycle are described in the text.

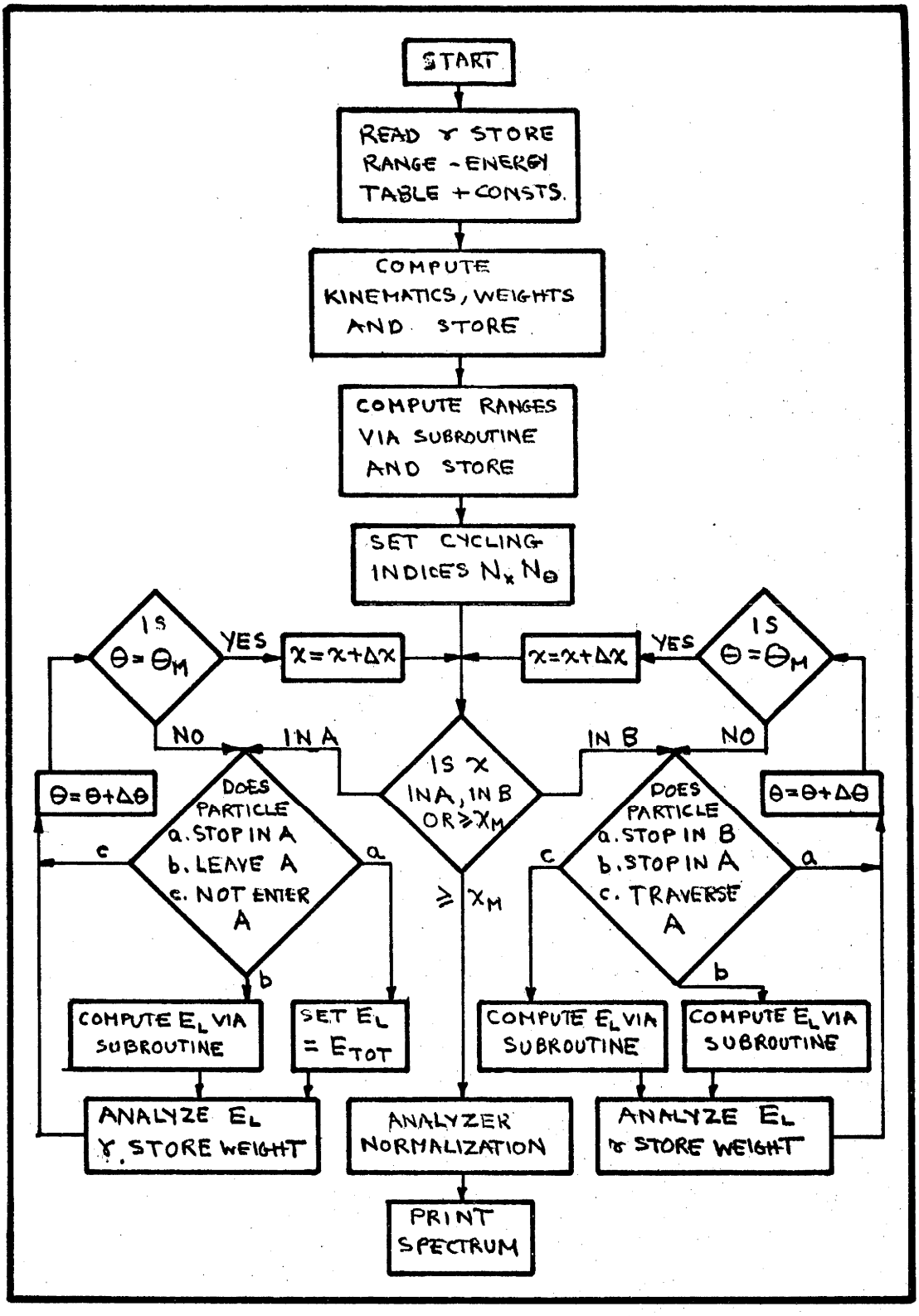
START
READ γ STORE RANGE - ENERGY TABLE + CONSTS.
COMPUTE KINEMATICS, WEIGHTS AND STORE
COMPUTE RANGES VIA SUBROUTINE AND STORE
SET CYCLING INDICES N_x N_θ
IS $\theta = \theta_M$
YES
$x = x + \Delta x$
NO
$\theta = \theta + \Delta\theta$
IS x IN A, IN B OR $\geq x_M$
IN A
IN B
$\geq x_M$
DOES PARTICLE a. STOP IN A b. LEAVE A c. NOT ENTER A
DOES PARTICLE a. STOP IN B b. STOP IN A c. TRAVERSE A
a
b
c
COMPUTE E_L VIA SUBROUTINE
SET E_L = E_{TOT}
ANALYZE E_L & STORE WEIGHT
ANALYZER NORMALIZATION
PRINT SPECTRUM

Fig. A.2 Idealized surface barrier detector in cross-section

The double line facing the incident neutrons represents the Au surface layer, which is ignored in the calculation. Region A is just the depletion layer, and B is the region outside the depletion layer from which originating particles can reach A and deposit part of their energy in the junction. X_{max} is the largest distance from the detector surface for which an event (x,θ) can contribute energy to the junction, and is the sum of depletion layer depth D, and the range R_o of a particle emitted at $\theta = 180^o$. Region boundaries are cross-hatched to emphasize their non-sharp nature; in the calculation these are treated as precise limits. Solid points near the middle of each region represent hypothetical event (x,θ) origins, and radiating arrows indicate possible emitted particle tracks. Only energy released in the solid-line track portions is recorded by the detector.

SECTION THROUGH

IDEALIZED SURFACE BARRIER DETECTOR

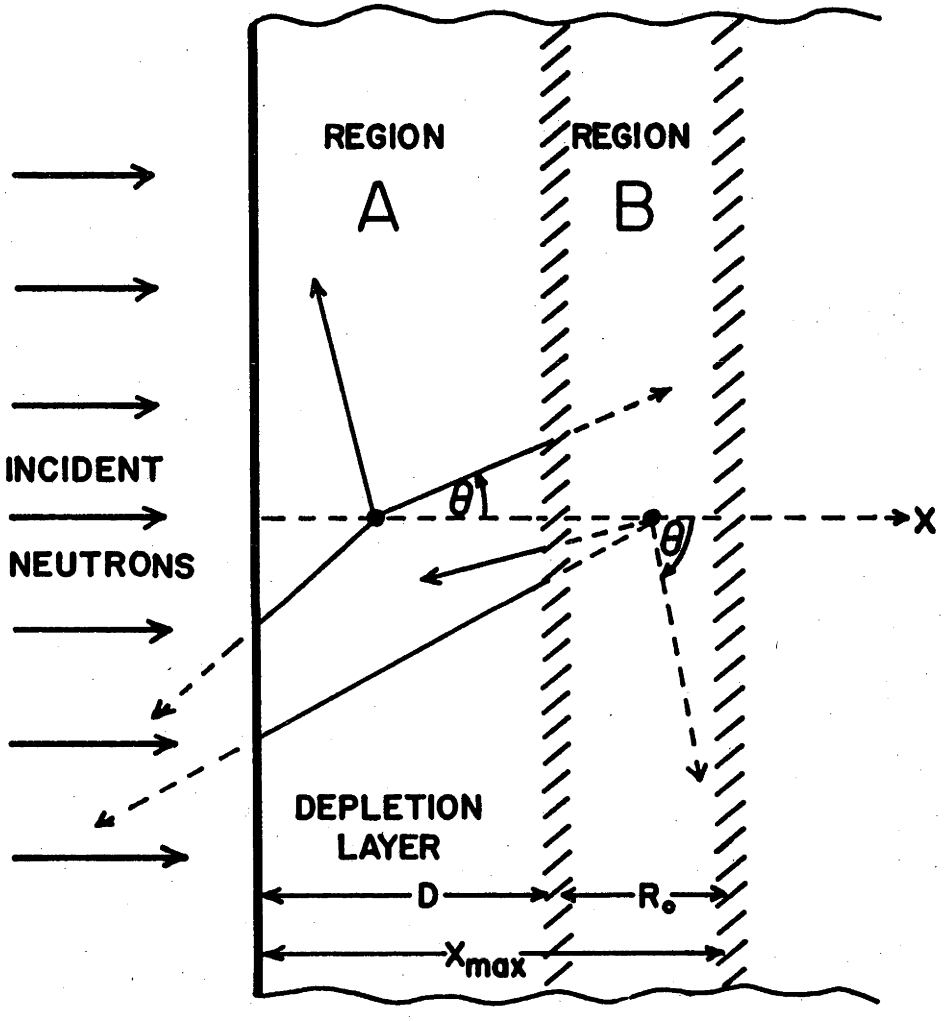

detector about the neutron flux direction, reduces the possible particle energy loss in the junction to a function of the variables x and θ cm; x is the particle point of origin, and θ cm its centre-of-mass emission angle.

The program divides the total width of regions A + B into a large number of equally spaced intervals N_x of width Δx, where Δx can be chosen arbitrarily small. Particle energy release in the junction is calculated at each x - position for a set of equally spaced emission angles (in the range 0° - 180°). These energies are sorted into a twenty-channel spectrum, each contribution supplying a weight proportional to $W(\theta) \sin \theta$ (where $W(\theta)$ is the hypothetical angular distribution chosen for the particle group). If the number of simulated particle emissions $n = N_x . N_\theta$ is made very large, the resultant constructed spectrum furnishes the magnitude and general shape of the low energy tail associated with the particle group in question. It was generally necessary to compute several thousand events per group to obtain smooth shapes.

A.3. ENERGY RELEASE IN THE DEPLETION LAYER.

The energy release for each simulated event (x, θ) was determined as follows. Range-energy data of Whaling (Wh58) for protons in aluminium (Ep = 100 kev - 12.00 Mev) were fitted by a least squares program to an expansion of the form $\log R = \sum_k a_k (\log E)^k$, where R = range, and E = initial energy. This expansion is used to generate a 120 place Al-p range-energy table*, which is transformed into a Si-p table by a small correction. A second range-energy table for alphas in Si is constructed using the well known relationship between proton and alpha particle ranges in the same material (Wh58).

The appropriate table is stored in computer memory at the start of the calculation. Energy release for each event (x, θ) (expressed as a function of ranges and energies), is obtained by operating on the stored table via a lookup-and-interpolation subroutine of the main program.

A.4. PROGRAM FLOW.

The program initially computes and stores lab. energies and emission angles for the required set of θ c.m. via a standard kinematics transformation subroutine.

*Generously supplied by G. Ohlsen of this laboratory.

The ranges for this set of lab. energies are computed via the rang-energy table and stored. Distance R_o (see Fig. A.2.) is set equal to the particle range corresponding to θ c.m. = 180^o. After setting N_x and N_θ, the program enters the main energy-loss computation cycle. A series of decisions and geometric comparisons at the beginning of each loop enable the program to select the appropriate energy-release calculation function for each event (x, θ). These are detailed in Fig. A.2. The computed energy release for each loop is analyzed as described in Section A.2. Events corresponding to a full energy release are placed in a single separate channel.

Upon completion of the set $N_x N_\theta$ the 20 channel energy spectrum is normalized to a full-energy channel contribution of 100, and printed out.

A.5. RESULTS.

Line shapes were calculated for alpha groups corresponding to the ground state and 4th excited state reactions of $Si^{28}(n,\alpha)Mg^{25}$ (14 Mev neutron energy). The depletion depth used was that of the detector described in Chapter II. Results are applied and discussed in Section 5, Chapter II, and are shown in Fig. 2.5.

Line shapes were computed for a number of other interesting cases; four are shown in Fig. A.3 The two lower shapes correspond to proton and alpha groups whose maximum range is close to 10 times the depletion depth. Both were calculated using an isotropic angular distribution. The proton line shape corresponds to that expected for the ground state $Si^{28}(n,p)Al^{28}$ group in a detector of the dimensions used in the work of Chapter II (120 microns) while the alpha line shape corresponds to that expected for the $Si^{28}(n,\alpha)Mg^{25}$ ground state group in a detector whose depletion depth is 1/10 this value.

It is seen that the low energy total in each case accounts for approximately 95% of the spectrum contributions. These fractions are indicated by the summations over the 20 channel tail spectra, $\sum T_i$. The alpha group line shape possesses a low energy structure significantly different from that of the proton group, showing a distinct splitting in the broad peak. An inspection of the alpha shapes in Fig. 2.5 reveals that this would seem to be a characteristic feature of alpha group line shapes.

The upper two shapes of Fig. A.3 indicate the

Fig. A.3 Surface barrier detector line shapes for some interesting cases.

The emitted particle group and the responsible 14.03 Mev neutron reaction are given with each line shape, along with the detector depletion layer depth D. Remarks concerning channel, and channel contribution normalization are the same as in Fig. 2.7. For the upper two cases, the calculated lineshapes have been magnified by X10 with respect to the normalizing full-energy peak, to show structural detail.

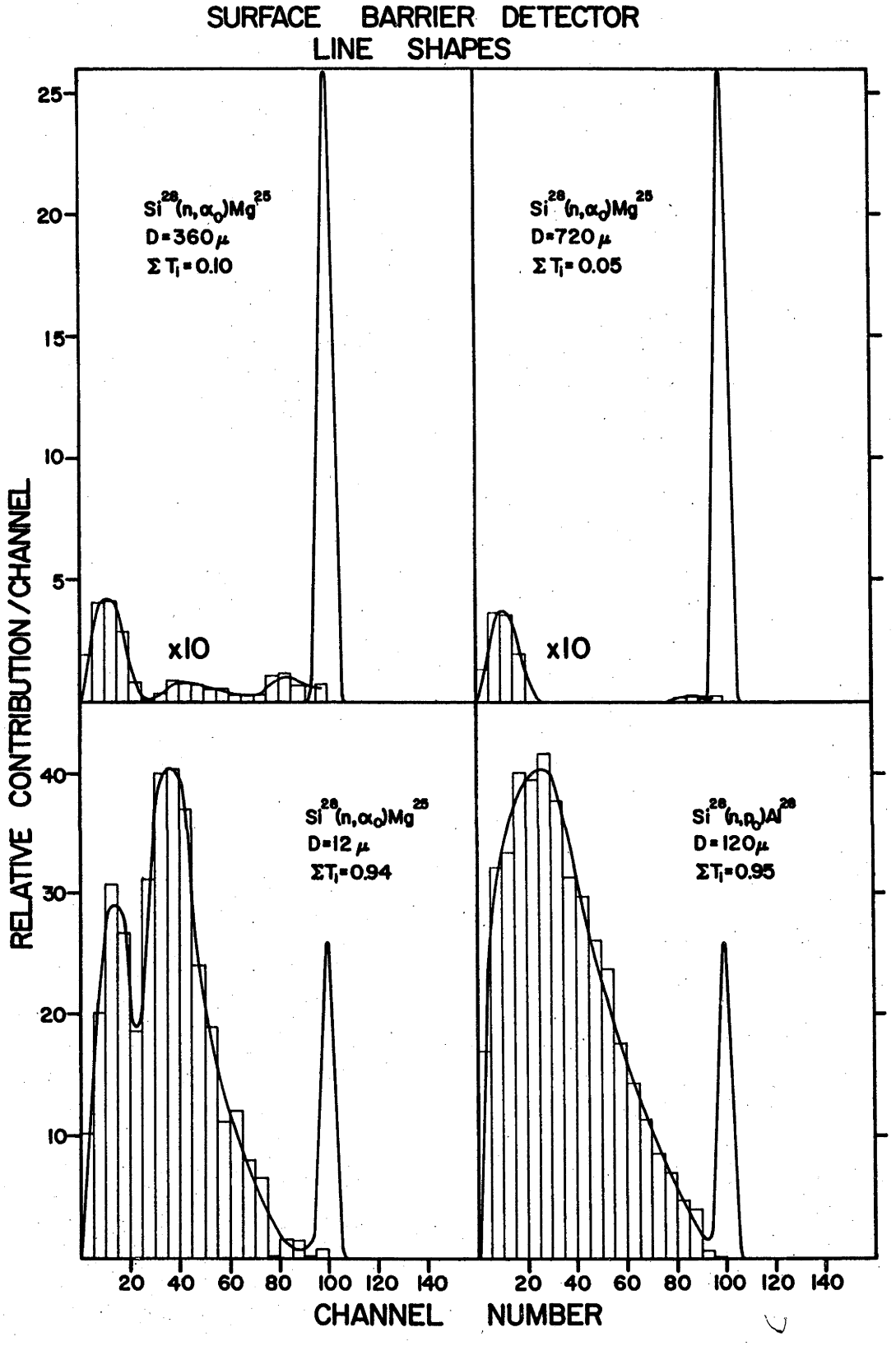
SURFACE BARRIER DETECTOR
LINE SHAPES
$Si^{28}(n,\alpha_0)Mg^{25}$
D=360 μ
ΣTi=0.10
x10
$Si^{28}(n,\alpha_0)Mg^{25}$
D=720 μ
ΣTi=0.05
x10
$Si^{28}(n,\alpha_0)Mg^{25}$
D=12 μ
ΣTi=0.94
$Si^{28}(n,p_0)Al^{28}$
D=120 μ
ΣTi=0.95
RELATIVE CONTRIBUTION/CHANNEL
CHANNEL NUMBER
5
10
15
20
25
10
20
30
40
20
40
60
80
100
120
140

results of line shape calculations for cases at the opposite extreme. These represent alpha line shapes corresponding to the $Si^{28}(n,\alpha)Mg^{25}$ ground state group, in detector depletion depths 3 and 6 times the thickness used in the experiment of Chapter II. A comparison between these shapes (magnified 10 times) and those of Fig. 2.5, reveals that the relative form varies considerably as the depletion depth is increased. The $\sum T_i$ factors show that for these cases, the low energy tails account for a small but appreciable fraction of the spectrum contribution. It would seem clear that depletion layer thicknesses of the order of 500 microns are required, in order to reduce detector wall effects to a level where they may be justifiably neglected in the extraction of $Si^{28}(n,\alpha)Mg^{25}$ reaction cross sections.

APPENDIX B

PROPOSED COINCIDENCE TECHNIQUE

Dixon and Aitken (Di62) have investigated the Si^{28} and Si^{29} neutron induced reactions using a triple coincidence technique. This is discussed briefly, along with proposed improvements. Their experimental arrangement consisted of two Silicon junction detectors set face-to-face and separated by a thin dE/dx gas filled proportional counter. Discrimination between alpha particles and protons was secured by changing the coincidence requirements on the three detectors and imposing appropriate bias conditions on the single channel analyzers receiving their amplified outputs. Protons (and deuterons) could be largely eliminated by requiring coincidences between all detectors and by setting the dE/dx output bias to reject pulses corresponding to small energy loss in the dE/dx counter. Alpha particles were eliminated and only light particles detected, by requiring anti-coincidence between the dE/dx and the coupled solid state detectors.

In addition to achieving partial separation between alpha particle and proton spectra, this procedure succeeded in significantly reducing wall and end effects. Particles not passing through all three detectors are not recorded.

This eliminates partial energy contributions from particles originating in the depletion layer and crossing the inner boundary, or crossing the surface at a shallow angle. It is still possible, of course, for energetic particles to traverse the depletion layers of both detectors without being stopped, so that wall effects are not completely suppressed.

Dixon and Aitken (Di62) show separated $Si^{28}(n,\alpha)Mg^{25}$ and $Si^{28}(n,p)Al^{28}$ spectra. Both agree closely with peak positions calculated from the Mg^{25} and Al^{28} level schemes of Endt and van der Leun (En62). Since the coincidence arrangements select particles emitted close to the direction of its axis of symmetry, it is seen that rotation of this axis with respect to the incident neutron direction should reveal any strong deviations from isotropy in the $Si^{28}(n,\alpha)$ and (n,p) angular distributions. Dixon and Aitken (Di62) have made some preliminary measurements and report evidence for such anisotropies at 13.9 Mev neutron energy.

In the following we propose a scheme which would provide a considerable improvement both on the experimental method of this chapter and the method described above.

A fully depleted thick solid state dE/dx counter is used as the target, and records the full energy of most of the neutron induced charged particles. Those which escape from either side deposit their remaining energy in proportional counters whose windows are set parallel with and as close as possible to the faces of the dE/dx counter. Energy contributions to all three detectors are summed and analyzed. In order to reject pulses corresponding to particles produced by neutron reactions in the proportional counters the dE/dx detector pulses are used to gate the delayed proportional counter pulses. It is expected that such a scheme would essentially eliminate wall effects, and enable a more precise measurement of the partial cross sections for neutron induced Silicon reactions. Angular distribution measurements could be made using the same apparatus in modified form. The dE/dx Silicon counter is used as target-detector as before, but a single proportional counter is set at a large distance D from one face. A coincidence requirement between the dE/dx and proportional counter ensures that only particles emitted in the axial direction are counted. The angular definition of this arrangement clearly depends only on the ratio of detector face (or window) dimension to the

separation D. Since the highly ionizing heavy recoil nuclei, such as Mg^{25} and Al^{28}, are stopped in the dE/dx detector, their energies are automatically added to the light particle energies. This means that spectral peak positions depend only on the various reaction Q-values, and are independent of laboratory angle, so that angular distributions taken with this arrangement are relieved from the usual kinematics problem of criss-crossing group positions.

CHAPTER III

THE REACTION $Al^{27}(p, \alpha)Mg^{24}$

CHAPTER III

Section 1. INTRODUCTION.

The following work comprises an investigation of the reaction $Al^{27}(p,\alpha)Mg^{24}$, using protons in the energy range 3.60 - 11.50 Mev. The work was performed with the A.N.U. Tandem Van de Graaff accelerator and associated experimental facilities, and was carried out for the most part in collaboration with Dr. A. R. Quinton* of this laboratory, between November, 1961 and January, 1963.

The chief motivation for this study was to obtain detailed information on the nature of the (p,α) reaction mechanism in a medium weight nucleus at high compound system excitation.

The experimental equipment, which is described in section 2, was assembled and tested mainly by the present writer. Experimental procedures and results are given in section 3 and a general discussion in section 4. Some of the results have been analyzed in terms of recent developments in the theories of the nuclear statistical model (Er 60, 62, 63; Br 63); this material is presented in Chapter VI.

*Sloane Fellow on leave from Yale University.

Section 2. THE EXPERIMENTAL APPARATUS.

The investigation of the reaction $Al^{27}(p,\alpha)Mg^{24}$ was conducted in several discrete stages, each involving somewhat different equipment and experimental method. The procedures followed in each portion are outlined below in the appropriate sections. All work, however, was carried out within a basic experimental arrangement, which is described in the present section to avoid repetition.

2.1. The Scattering Chamber.

The scattering chamber used in this study consisted of a 9" (inside diam.) Aluminium cylinder and is shown in cross section in Fig. 3.1, with details of internal and external equipment. Main points are labelled in the accompanying figure caption.

The blank bottom lid was interchangeable with one containing a thermally insulated steel spindle, capped inside the chamber by an 8" diam. Cu plate, and connecting underneath with a Cu pipe immersed in liquid air. This provided adequate vapour trapping close to targets and detectors.

The chamber interior could be observed through a

Fig. 3.1 The 9-inch scattering chamber, in vertical section

Numbered details on main diagrams are :

1. Fixed detector assembly
2. Rotating detector assembly
3. Target strip
4. Foil holder
5. Foil changing plunger
6. Lock-nuts for holding fixed detector mount
7. Geared spindle for turning (8)
8. Toothed plate holding rotating detector mount
9. Beam collimating assembly
10. Pumping holes in collimator mount
11. HVEC insulating ring
12. Permanent magnet electron suppressor
13. Ta plate
14. Remote-operated retractable quartz plate
15. Target angular position indicator
16. Teflon spacer to set target strip vertical position

Inset - Detector assembly detail

A. ORTEC surface barrier detector B. Clamping ring

C. Pumping vents D. Collimating slit plates

E. Silicon wafer

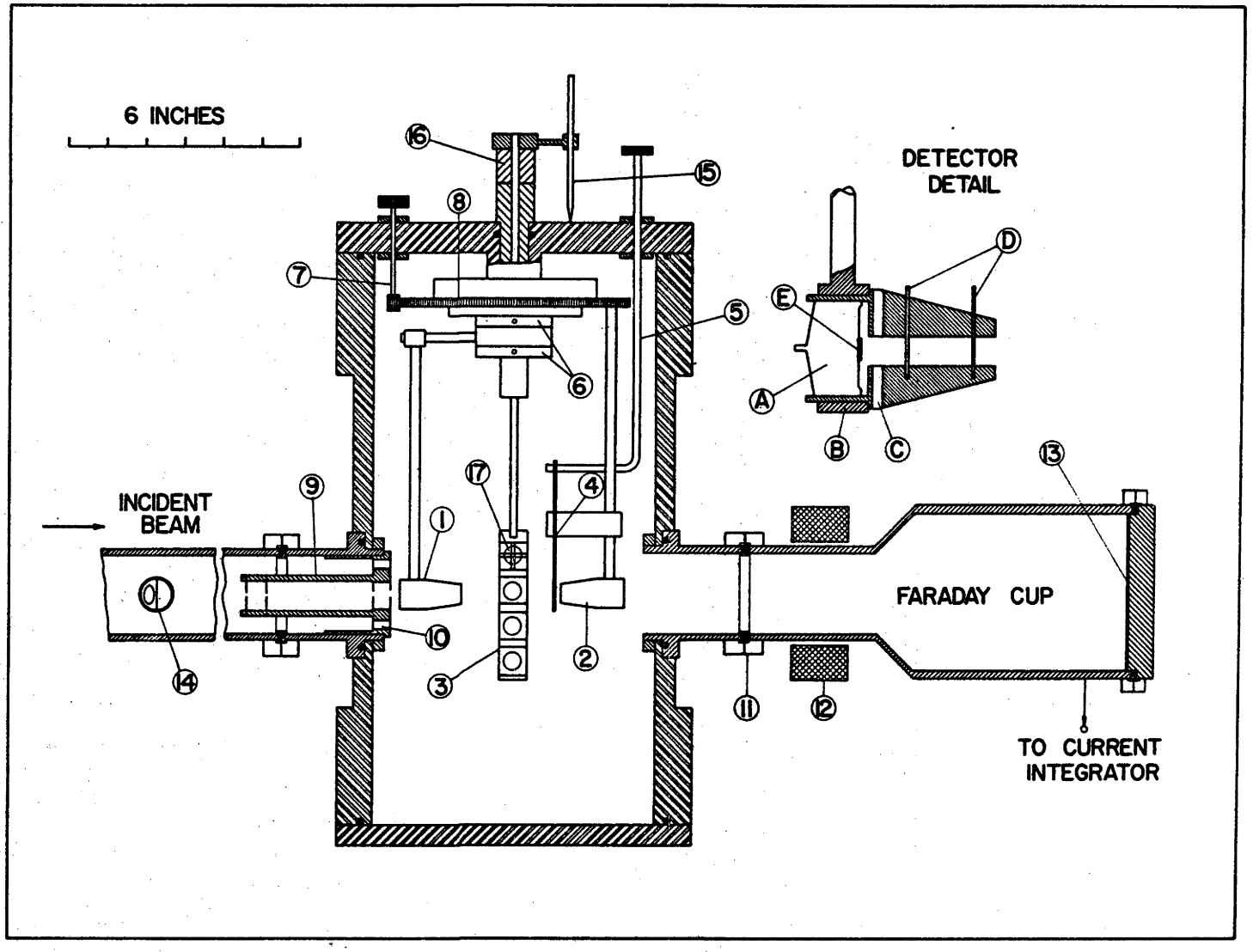
6 INCHES
DETECTOR DETAIL
INCIDENT BEAM
FARADAY CUP
TO CURRENT INTEGRATOR
1
2
3
4
5
6
7
8
9
10
11
12
13
14
A
B
C
D
E
17

2" diam. thick glass wall port (not shown) set at 45° to the beam direction and in the horizontal plane. This was normally covered by a light-tight cap when detectors were in operation.

The chamber was supported by its 2" diam. entrance and exit tubes, which were mounted in adjustable HVEC beam line clamps (not shown). It was accurately aligned on the previously established target-line geometric axis, with the use of optical targets set in the entrance and exit ports.

An internal pressure of $\sim 10^{-6}$ mm Hg was maintained by a single 6" liquid air trapped Hg diffusion pump located approximately four feet from the entrance port.

2.2. The Proton Beam, Beam Collection, Beam Collimation.

Analyzed target currents of up to 2 μA of protons, in the energy range 3.5 Mev - 11.5 Mev, were supplied by the A.N.U. Tandem Van de Graaff accelerator. For most of the work the 90° analyzing magnet slits were set to provide a beam energy resolution of 5 - 10 kev. However, in one segment (section 3.4) considerably greater precision was required. The beam position and focus could be examined via retractable quartz plates (observed by remote T.V.)

which was set upstream from the chamber entrance port and at the geometric center of the chamber. It was originally hoped that the target-line beam transport system, consisting of switching magnet tracking slits and magnetic quadruple lenses, would provide a tightly focussed and consistently well-centered beam at the target position; this would have permitted the elimination of beam collimation, and afforded relief from the usual accompanying high level of scattered beam. Experiment indicated, however, that these conditions could not be reliably guaranteed, so that use of spot-size-and-position-defining beam collimators was mandatory.

The collimating assembly could be easily removed from inside the scattering chamber and consisted of .020" Ta discs mounted on threaded brass rods at the intervals shown (see Fig. 3.1). Discs containing several hole diameters were tried; the particular arrangement used throughout the present work was two 1/16" defining holes, followed by two 1/8" anti-scatter holes. This provided a satisfactory compromise between the requirements of maximum beam transmission, minimum beam "wander" across the target face and minimum collimator edge scattering.

The beam was buried in a Faraday cup, as shown, which

was separated from the earthed scattering chamber casing by HVEC insulating rings. Current and total collected charge were measured by an Elcor A309A current integrator, which gated all pulse analyzing and recording equipment used in this work. Secondary electrons were prevented from escaping from the Faraday cup by a permanent ring magnet placed around the cup entrance. Experiment showed that the addition of an electrostatic field supplied by a 300 V dry battery produced no observable difference in measured current, so that this form of electron suppression was generally not employed.

2.3. Detector Assembly Mounts.

The detector assemblies employed in the scattering chamber consisted of surface barrier detectors inserted into brass collimating tubes, and are described in section 2.4. They were suspended on brass rods from a structure attached to the center boss of the top lid. During the early stages of the experiment, provision was made for only two assembly mounts. One was connected to the central shaft itself and could be fixed at any angle by lock nuts. The second was attached to a toothed plate bolted to a ball race rotating about the central shaft. The plate could be rotated from outside the chamber by a spindle bearing a small toothed

driving wheel. The gear ratio was chosen such that a single rotation of the driving spindle was equivalent to turning the detector mount through 22.5°. A plate fixed to the drive wheel handle was calibrated in 0.5° units and operated a revs. counter (not shown). Backlash in the gear drive was $\sim 0.1^{\circ}$, and it was considered possible to set the detector assembly relative angular position with 0.2° precision. The top lid was frequently removed to permit adjustments to detectors and other equipment; to ensure a high reset accuracy, dowel pins were used to position it on the scattering chamber rim.

2.4. Detector Assemblies.

Silicon surface barrier charged particle detectors* were used throughout the experiment and were of two types:- (a) 300Ω - cm resistivity, 25 mm^2 sensitive area, and (b) 3,000Ω-cm resistivity, 16 mm^2 sensitive area. Both types were run with the front Au plated surface earthed while positive bias was applied to, and the signal taken from, the rear contact.

The detectors were inserted into individual collimating assemblies (Detail in Fig. 3.1) which consisted of

*Supplied by Oak Ridge Technical Enterprises Corporation.

a tapered "snout" containing a $\frac{1}{4}$" diameter central hole. This restricted the solid angle observed by the detector without collimating the detector area. (See section 2.8). Two vertical slots were cut in the snouts, into which .020" thick Ta collimating slits could be inserted. Slit width ranged from 1/64" to 1/8". The forward slit was $1\frac{1}{4}$" from the detector surface and served to define the angular resolution. It was generally backed up by a wider aperture in the rear position ($\frac{1}{4}$" from detector surface), which served as an anti-scatter slit. Between this and the detector itself were a ring of vents which permitted a high pumping speed at the detector surface, to reduce the threat of vapor contamination damage.

When clamped in their assembly mounts the rotating and fixed detectors were 7.00 cm and 6.35 cm from the chamber centerline respectively and subtended, when uncollimated, an angle of $\sim 5^{o}$.

2.5. Target Strip and Foil Holder.

Targets were mounted on a steel strip containing provision for four Cu or Al frames ($\frac{3}{4}$" square). This was rigidly attached to a steel rod which passed through a teflon bushing in the center of the top lid. The target

strip could be rotated to any angle and set with an estimated accuracy of 0.5^{o} by an indicator reading on a scale inscribed on the top lid. The top target frame position was normally occupied by a quartz disc and cross wires to facilitate checks on beam focus and position. The lower target positions were set by placing teflon spacers of appropriate lengths between target strip handle and teflon bushing.

The rotatable detector mount contained a foil holder which could be manipulated from outside the scattering chamber by a grappling arrangement (see Fig. 3.1). The holder provided space for two foils, which could be placed immediately in front of the detector assembly.

2.6. Targets.

The Aluminium targets used in this experiment were of two types: (a) self-supporting Al films, and (b) Al films vacuum deposited on thin Carbon self-supporting foils. The Carbon foils were prepared by the now standard technique, involving the carbon-arc vacuum deposition of a thin carbon layer on detergent-coated glass slides - the films being later floated off in lukewarm water and picked up on suitable frames. Foils prepared in this fashion suffer from contamination due to H_2O and detergent molecules picked up during

fabrication. Proton induced reactions with the contamination elements, however, did not interfere with observation of the alpha particles from $Al^{27}(p,\alpha)Mg^{24}$, so that no attempt was made to reduce the impurity level.

Self-supporting Al foils, ranging in thickness from 10 $\mu g/cm^2$ to 70 $\mu g/cm^2$ were manufactured in a similar manner, the carbon arc being replaced by Al metal evaporated from an electrically heated Ta boat. The foils suffer from the same sources of contamination.

A second drawback to both the self-supporting and Carbon supported Al foils was a variation in effective thickness over the foil area; this was thought to be due to departures from isotropy in Al emission from the Ta boat, and to the development of wrinkles in the foils during the drying process.

All foils were mounted on Cu or Al frames containing a central hole of $\frac{1}{2}$" diameter.

2.7. Electronics.

The electronic equipment used in this work consisted mainly of two ORTEC model 101 charge-sensitive low-noise preamplifiers feeding two ORTEC model 201 linear amplifiers

(high gain stabilization). The latter contain a biassed post amplification section which permits selected portions of a given spectrum to be expanded and examined in detail. The spectral resolution broadening contributed by these systems was estimated to be ~ 20 kev. Performance characteristics of this type of equipment are well known and will not be further considered, except where directly relevant to particular points of procedure.

The detector signals were taken from the rear contacts through insulated, but not shielded, cables (to reduce stray capacitance at preamplifier input) to BNC vacuum feed-throughs (not shown in Fig. 3.1) in the top lid of the scattering chamber. Four such outputs were provided. Positive reverse bias of up to 200V was delivered to the detectors from filtered D.C. supplies built into the ORTEC amplifiers. Detectors were normally operated at biases of 20 - 40 V. Highly stable Hg-relay pulsers, (also built into the amplifier units), provided a partial check on the linearity of the systems and an energy calibration.

Both RIDL (400 channels) and RCL (512 channels) multichannel pulse-height-analyzers were used in the course of this work.

2.8. Beam Scattering and Wall Liners.

Experiment showed that the flux of protons at forward angles, arising from collimator slit edge scattering was considerably greater than the flux of target reaction products. In order to obtain spectra at forward angles reasonably free from pulse pileup effects, it was therefore essential to restrict the detector observable solid angle with the brass "snouts" (section 2.4), so that it viewed only the target strip and the section of chamber wall directly opposite. Measurements taken with the target strip retracted and detector "snout" in place revealed a smaller, but significant proton flux arriving at the detector from the opposite wall. This was attributed to second scattering in the chamber wall of protons first scattered by collimator edges, and its intensity was decreased by a factor of two when chamber walls and exit tube were lined with 1/8" polythene sheet.

Section 3. EXPERIMENTAL RESULTS.

Using section 2 as background, the separate stages of the $Al^{27}(p,\alpha)Mg^{24}$ study are described below. With the exception of section 3.1, the experimental results are presented without comment. A general discussion of all

results is given in Section 4.

3.1. Energy Levels of Mg^{24}.

During the initial investigation of the $Al^{27}(p,\alpha)Mg^{24}$ reaction it became clear that it was possible to establish the positions of a number of Mg^{24} energy levels with precision. This section describes the measurements and results.

3.1(a) Detector Resolution and Response.

Alpha particles were observed by a single 300Ω - cm detector, whose pulses were amplified by an ORTEC 101-201 system and analyzed by a 400-channel RIDL P.H.A. The detector was biassed so that its depletion layer thickness was roughly equal to the Si range of 2 Mev protons. This was determined both by the range-bias-energy relationship given by Blankenship (Bl 60), and measurement of the proton "edge" or cutoff energy in a typical calibrated spectrum. Alpha particles of energy greater than 2 Mev could thus be cleanly separated from protons. An inspection of Q-values for other possible target reactions showed that no other type of heavily ionizing particle could be present in the observed spectra.

Fig. 3.2 illustrates the detector + electronics system resolution for alpha particles from a ThC' - ThC"

Fig. 3.2 Low energy portion of a spectrum obtained from a ThC'-ThC" alpha particle source

Alpha group energies are given at the top of the figure. It is seen that the 6.067-6.086 Mev doublet is resolved.

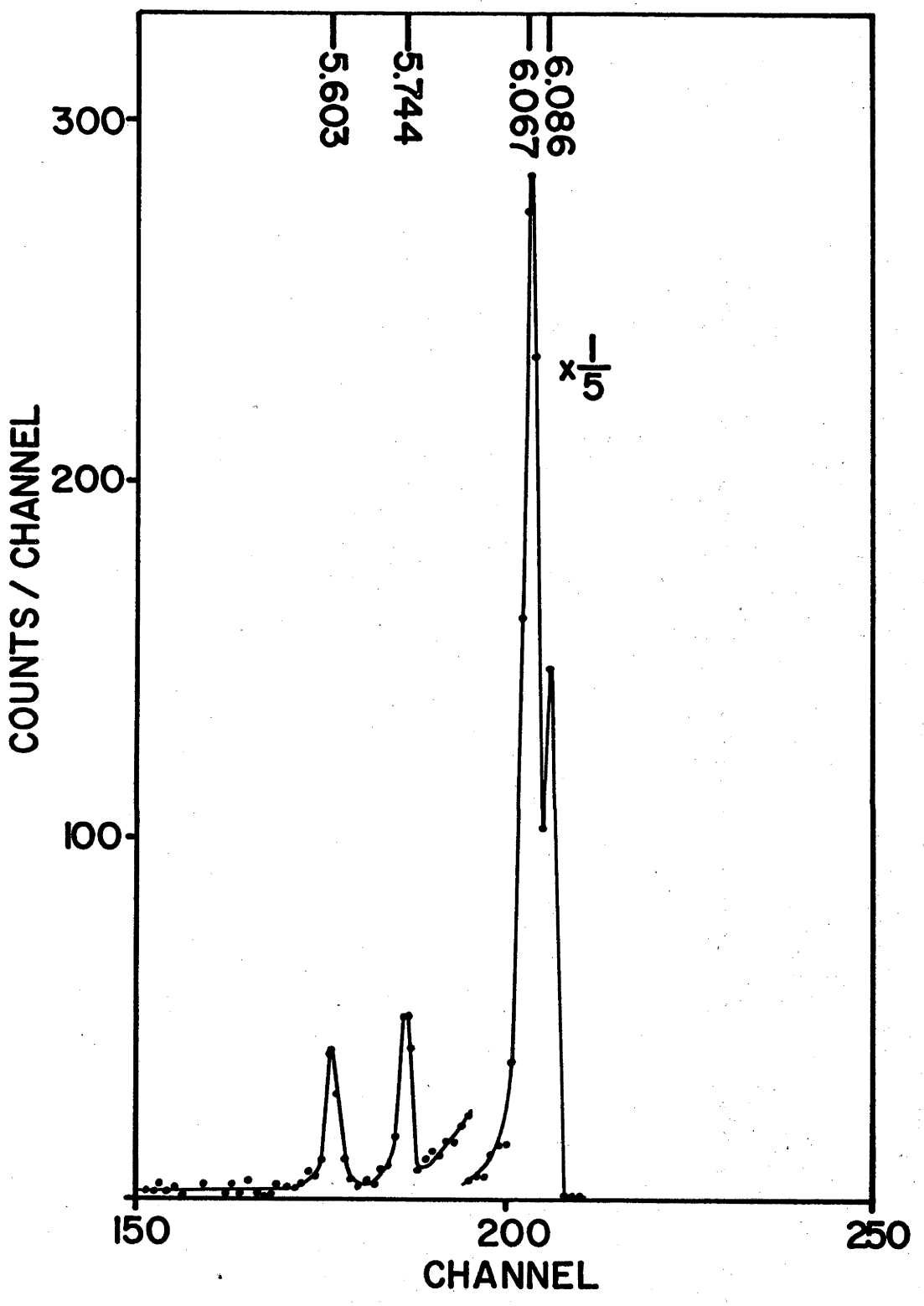
5.603
5.744
6.067
6.086
300
200
100
COUNTS / CHANNEL
x 1/5
150
200
250
CHANNEL

source. The upper part of the spectrum containing the 8.78 Mev line is not shown. For the accumulation of the spectrum the source was placed at the normal target position and the detector was uncollimated. A comparison with the absolute magnetic analysis results, reviewed by Briggs (Br 54), for this source shows that the detection system possesses a 0.5% FWHM resolution (30 kev) for 6.0 Mev alpha particles.

3.1(b) Target Thickness Measurement.

The target consisted of an Al film on a Carbon backing. The Al film thickness was determined by subtracting the Carbon foil thickness from a measurement of total target thickness. The Carbon foil thickness was fixed by measuring its energy degradation of 6 Mev. protons; this was indicated by the observed shift in energy of protons elastically scattered from the Al film when the target was rotated 180° (so that protons were required to traverse the Carbon foil before striking the Al layer). The value obtained was $40 \mu g \pm 5 \mu g$.

Total target thickness was measured by interposing the target between a ThC' - ThC" alpha source and the detector, and determining the average transmission energy loss of the 8.78 Mev. alpha group. By taking advantage of

the high resolution and stability of the detection system and using the biassed post amplifier to expand the scale, it was possible to observe shifts in the group peak energy position of as little as 1 kev. This was less than 5% of the total energy shift. The Al film thickness obtained by subtraction of the Carbon foil thickness from the above measurement was 90 μg. The overall uncertainty in this value is estimated at 10%.

3.1(c) Energy Calibration.

The beam protons incident on the target were first subjected to magnetic analysis with their energy established to 10 kev by a slit system. Their energy was calculated from the relation $E(1 + E/2Mc^2) = K/Mf^2$, where Mc^2 = 938.235 Mev. is the proton rest mass energy, f is the proton magnetic resonance frequency in megahertz and K the constant of the Tandem 90° analyzing magnet. A value of K/M of 0.019900 established from (p,n) threshold measurements was used. The beam was collimated and focussed on to the target as described (section 2.2).

To determine an energy calibration curve for the detection system advantage was taken of a previous study by Van Patter, et al. (Va 57) of the Al^{27} (p, α)Mg^{24} reaction. These magnetic analysis measurements have established both

ground state and first excited state Q-values to an accuracy of 0.5%. With this information and the well-known kinematics expressions (relating Q-values, reaction masses, and energies) the laboratory energies of the ground state and first excited state alpha groups can be precisely calculated for any choice of incident proton energy and observation angle. To generate the required energy-versus-pulse-height scale the proton energy was varied from 4.0 to 11.0 Mev in 0.5 Mev steps with the detector fixed at 90° with respect to the beam. This calibration was checked at a single energy with the ThC' - ThC" alpha particle source. The measured value agreed with the accepted value of 6.047 Mev. to within 20 kev. This error was treated as systematic and a correction to the calibration curve was applied accordingly.

3.1(d) Absolute Angle Determination and Alignment.

The method of setting the detector angle of observation (section 2.3) was such that although changes in angle were accurately known (to 0.2°), the absolute angle was not well established. To determine an absolute angular scale, pulse heights of the ground state alpha group were observed at nominally 135° to a beam of 4 Mev protons on both sides of zero angle. A further observation at 130° allowed the rate of change of pulse height with angle to be determined; these

three observations served to establish the absolute setting for zero degrees. A partial check on the correctness of this setting was made by the measurement of a Rutherford elastic scattering angular distribution of 4 Mev. protons from an Au target. The results gave close agreement with the zero angular setting obtained by the above difference method.

Considerable care was taken to ensure that the beam intercepted the target through the axis of rotation of the detector and that the beam was in the rotational plane of the detector. This was achieved by (a) an optical alignment of the detector assembly, (set at 0° and 180° consecutively), target center, and beam collimator, on the previously established beam line axis; (b) sets of cross hairs set at opposite ends of the detector assembly so that the "snout" could be aligned through the target center at any detector angle. The latter check was performed with the scattering chamber top lid demounted.

3.1(e). The $Al^{27}(p,\alpha)Mg^{24}$ Spectra.

With the accelerator energy set at 11.00 Mev., observations were made at 45°, 90° and 135°. The resulting pulse height spectra are displayed in Fig. 3.3. Separate

Fig. 3.3 $Al^{27}(p,\alpha)Mg^{24}$ spectra measured with E_p = 11.000 Mev, at laboratory angles of 45°, 90°, and 135°

Groups are labelled with the numbers of corresponding levels populated in Mg^{24}. Details are given in text.

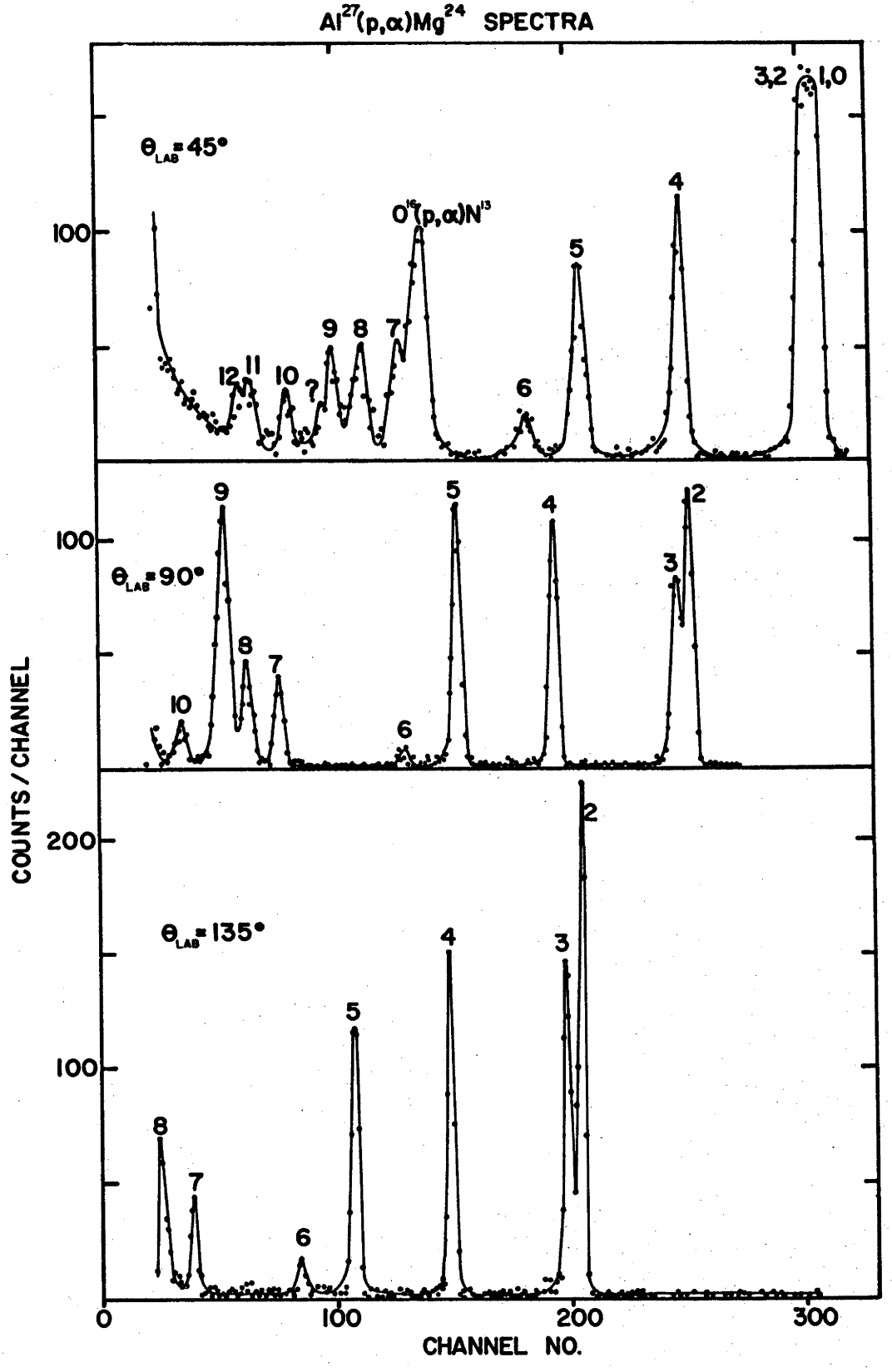
Al27(p,α)Mg24 SPECTRA
θLAB = 45°
θLAB = 90°
θLAB = 135°
O16(p,α)N13
3,2
1,0
12
11
10
?
9
8
7
6
5
4
3
2
100
200
0
100
200
300
COUNTS / CHANNEL
CHANNEL NO.

spectra were also obtained with a carbon foil of approximately the same thickness as that used for backing the Al target. To improve the reliability of the data, similar observations were made with different detectors and multi-channel analyzers.

In the 45^{o} spectrum the low energy proton cutoff is clearly visible. This set an effective lower limit to the observation of alpha particle groups. Since the detector bias was set at only 5V for this measurement, the alpha groups corresponding to the ground state and first 3 excited states of Mg^{24} are lumped together. In the 90^{o} and 135^{o} spectra all groups are well resolved but the ground state and first excited state groups are off-scale.

When analyzed to determine the Q-values of the $Al^{27}(p,\alpha)Mg^{24}$ alpha groups, it was found that the data from different angles for a particular group agreed in all cases to better than 40 kev. Since the detector bias was set for measuring alpha particle laboratory energies in the range 3 Mev. to 8 Mev., some groups did not show at all angles, and their Q-values are correspondingly less reliable. Fig. 3.4 shows the low energy level structure of Mg^{24} and gives the experimental values obtained in the present work for the levels corresponding to alpha groups

Fig. 3.4 Mg^{24} level scheme showing measured energies for levels observed in the spectra of Fig. 3.3.

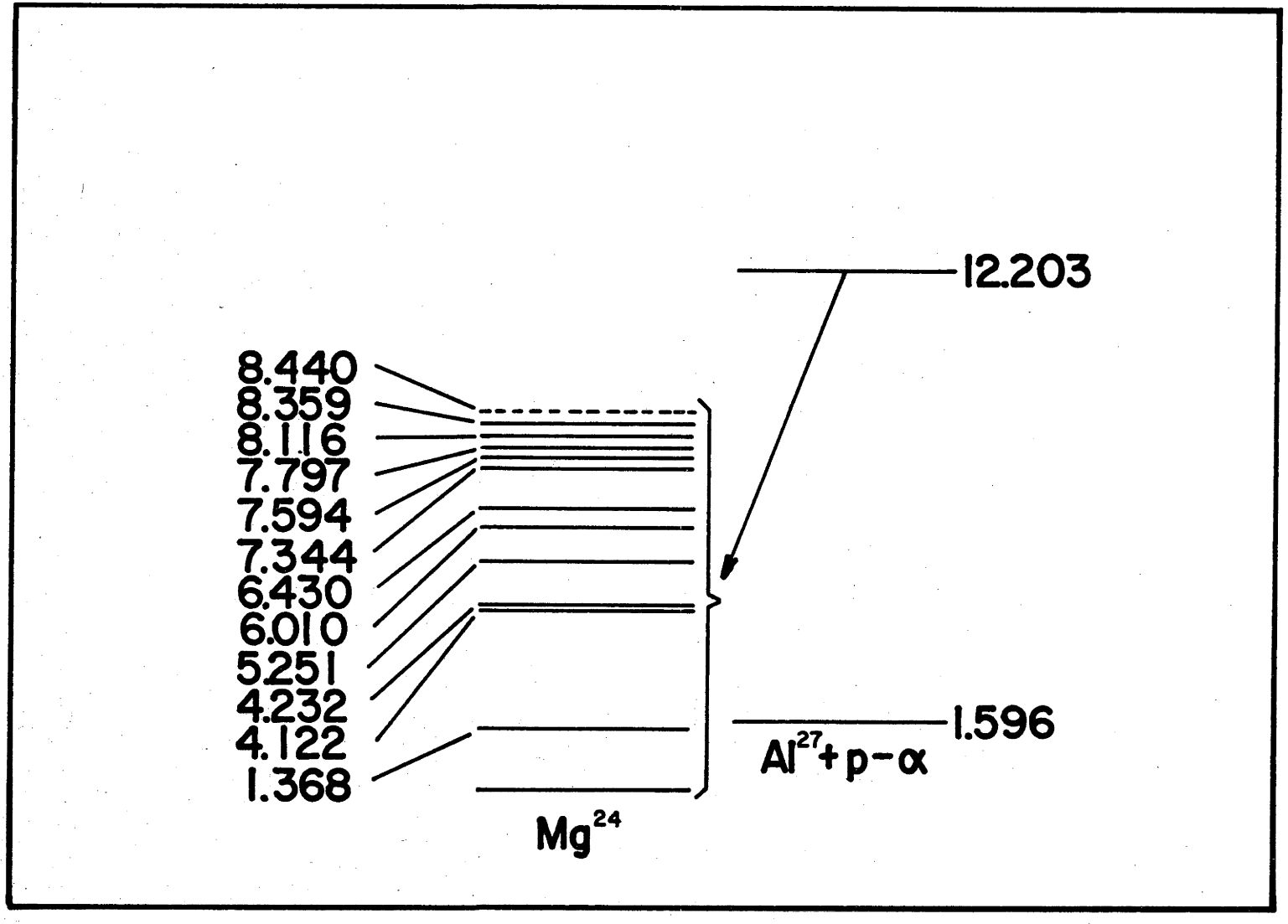
12.203
8.440
8.359
8.116
7.797
7.594
7.344
6.430
6.010
5.251
4.232
4.122
1.368
1.596
Al27+p-α
Mg24

2 to 12. Group 12 is represented as a dashed line since it was observed only at 45°. One other group (Fig. 3.3) appears only at 45° and is identified as the ground state group for the reaction $O^{16}(p,\alpha)N^{13}$ (Q = -5.218 Mev). A peak appears at the same energy when a Carbon target is bombarded with 11 Mev. protons. However, the intensity is much weaker. This presumably implies that although some oxygen contaminant is picked up in the carbon foil preparation, a far greater proportion must be attributed to the formation of the Al_2O_3 oxide on the Al film surface. It is noted that the general background level of alpha-particles from the carbon foil is very low, and coupled with the high negative Q-values for the reactions $C^{12}(p,\alpha)B^9$ and $C^{13}(p,\alpha)B^{10}$, this makes the thin Carbon foils ideal backings for this class of experiment.

An overall check on the precision and accuracy of the experimental method used here is provided by the value obtained for the group corresponding to the 2nd excited state. We measured an excitation energy of 4.122 Mev., in excellent agreement with the value given in the review by Endt & Braams (En 57). For the levels corresponding to alpha groups 2 to 10 we have assigned a probable error in the excitation energies of $\pm$ 25 kev. The sources of this error are indicated in Table 3.1.

TABLE 3.1.

Source	Probable Error (kev).
Ground State Q-value	5
Alpha Energies (location of peaks and calibration)	20
Beam Proton Energy Resolution	10
Detector Angle Uncertainty	10
Non-relativistic Kinematics	3

3.1(f). Discussion.

Using a magnetic spectrograph and the reaction $Na^{23}(He^3, d)Mg^{24}$, Hinds and Middleton (Hi60b) have recently determined the energies of the low lying levels of Mg^{24}. They observed levels at excitations of 4.122, 4.232, 5.224, 6.005, 7.350, 7.561, 7.620, 7.746, 7.808, 8.120, 8.357 and 8.439 Mev. These results are in good agreement with the values obtained in the present work. However, our level at 6.43 Mev. is not observed and they report two levels at 7.620 and 7.746 Mev., which are not seen in our spectra. The level at 6.43 Mev. was subsequently observed by Hinds

et al. (Hi 61) with the reaction $C^{12}(O^{16},\alpha)Mg^{24}$.

3.2. Coarse Excitation Function and Angular Distribution Survey.

For abbreviation, the following material employs the notation $\alpha_0, \alpha_1, \alpha_2$, etc. when referring to the ground state, 1st excited state, 2nd excited state etc. alpha particle groups from the reaction $Al^{27}(p,\alpha)Mg^{24}$ and to the corresponding reactions themselves.

The excitation functions for the groups $\alpha_0 - \alpha_6$ inclusive, were measured in 100 kev. steps over the incident proton energy (E_p hereafter) range 6.00 - 11.00 Mev. Angular distributions were obtained for most of these groups at E_p = 6.0, 7.0, 8.0, 9.0, 10.0 and 11.0 Mev.

A single 300Ω - cm detector mounted in the rotatable assembly and uncollimated was used in this work. Electronics were identical with those employed in the previous section. Since the excitation function step size was large it was convenient to minimize data collection time by using a relatively thick Al target (Carbon backed). This was $\sim$ 50 kev. thick for 8.78 Mev. alpha particles.

Typical spectra obtained at two different observation angles and proton energies are shown in Fig. 3.5. It is

Fig. 3.5 $Al^{27}(p,\alpha)Mg^{24}$ spectra obtained with C + Al target employed in measuring coarse excitation functions.

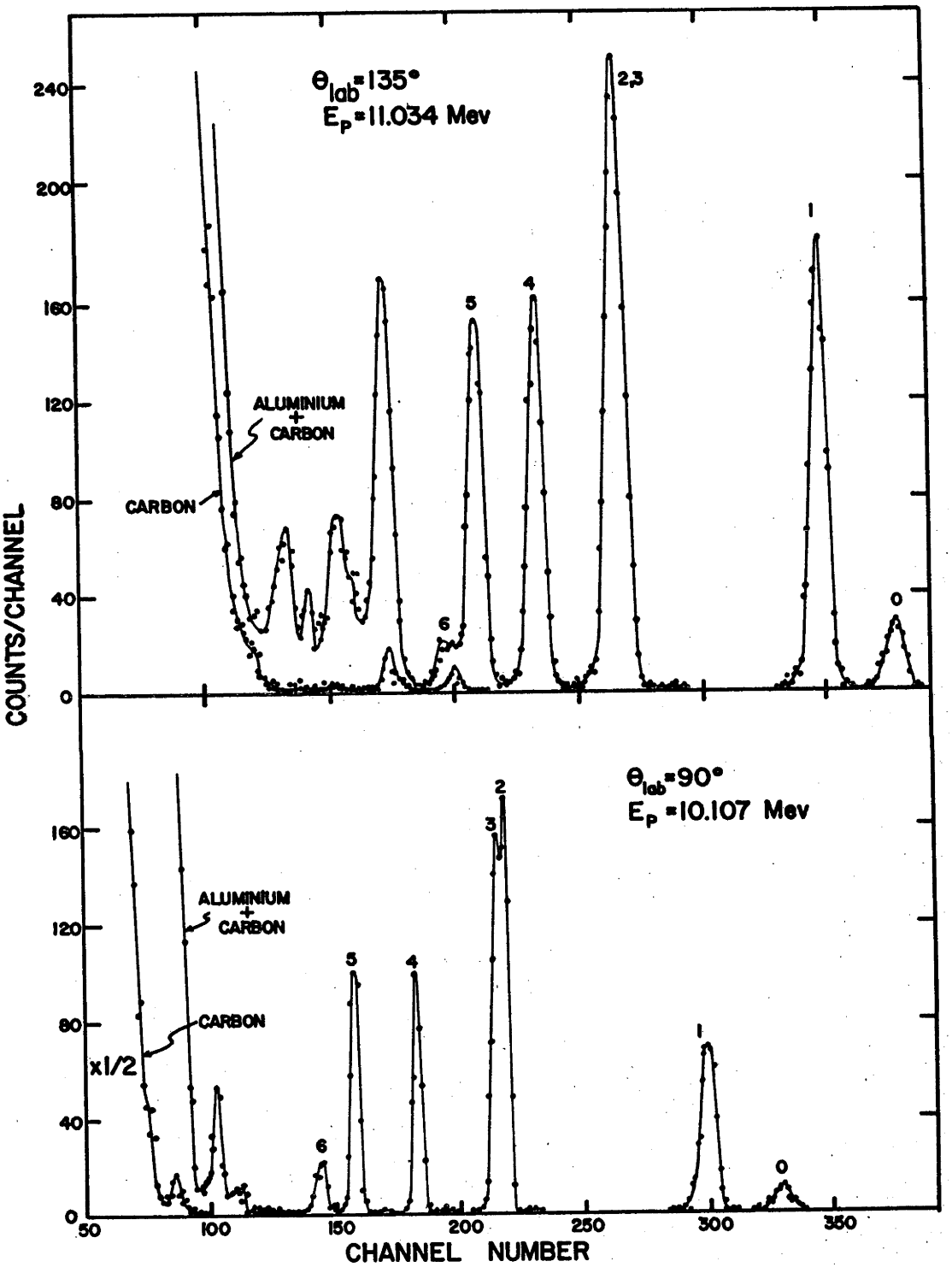
(p,α) SPECTRA FROM
THICK Al TARGET
AND CARBON FOIL
θlab=135°
Ep=11.034 Mev
θlab=90°
Ep=10.107 Mev
ALUMINIUM
+
CARBON
CARBON
x1/2
0
1
2,3
4
5
6
2
3
COUNTS/CHANNEL
CHANNEL NUMBER
0
40
80
120
160
200
240
50
100
150
200
250
300
350

seen that the finite target thickness makes groups α_2 and α_3 practically unresolvable; these were treated as a single group in the data reduction. Groups α_0, α_1, α_2, α_3, α_4, α_5 from the $Al^{27}(p,\alpha)Mg^{24}$ reaction are clearly identified in the spectra. The strong group near ch.170 in the 135° spectrum is identified as due to $O^{16}(p,\alpha)N^{13}$. Lower energy groups are almost certainly due to the $Al^{27}(p,\alpha)Mg^{24}$ reaction, but are not individually identified.

Also shown in Fig. 3.5 are spectra obtained with a Carbon foil taken from the same batch as the Al target backing. The O^{16} contamination group is weakly evident in these spectra. A weak group at higher energy in the 135° Carbon spectrum is not identified.

In reducing the data, the channels under each peak were simply summed. In general the spectrum contribution between peaks was very nearly zero and was ignored. At the most forward observation angles the high count rate, due to elastically scattered protons, produced a pulse pileup "background" under the lowest energy alpha particle groups and simple triangular subtraction corrections were made in these cases. The sharply rising proton cutoff is evident in both spectra of Fig. 3.5 and it is clear that the largest fraction of protons is contributed by the Carbon backing.

Target thickness was established by the method of section 3.1(b). No monitor was used in this work so that the relative accuracy of the yield measurements depends on the magnitude of target thickness variation within the area mapped by the beam "wander", and on the current integration precision. Experiment showed that the yield variations obtained at a fixed beam energy were of the order of 5%. Gas target measurements made by another group* using the same current integrator indicated that current collection precision was $\sim$ 1%. Hence the major source of relative yield uncertainty is thought to be due to target non-uniformity.

Spectra of the above type were obtained at 100 kev intervals over the E_p range 6.00 - 11.00 Mev., at a lab angle of 90^o. The extracted excitation functions for groups $\alpha_o - \alpha_6$ are shown in Fig. 3.6. Statistical errors for the individual points are comparable with the plotted point size, so that the curve representing the experimental yield has been merely drawn through the points. Measurements were repeated at several points, giving agreement (within statistics) with original values. The yield of groups α_2 and α_3 is presented as a single excitation function.

*Private communication by G. G. Ohlsen of this laboratory.

Fig. 3.6 $Al^{27}(p,\alpha)Mg^{24}$ $d\sigma/d\Omega(90^{\circ})$ coarse excitation functions E_p = 6.0 - 11.0 Mev.

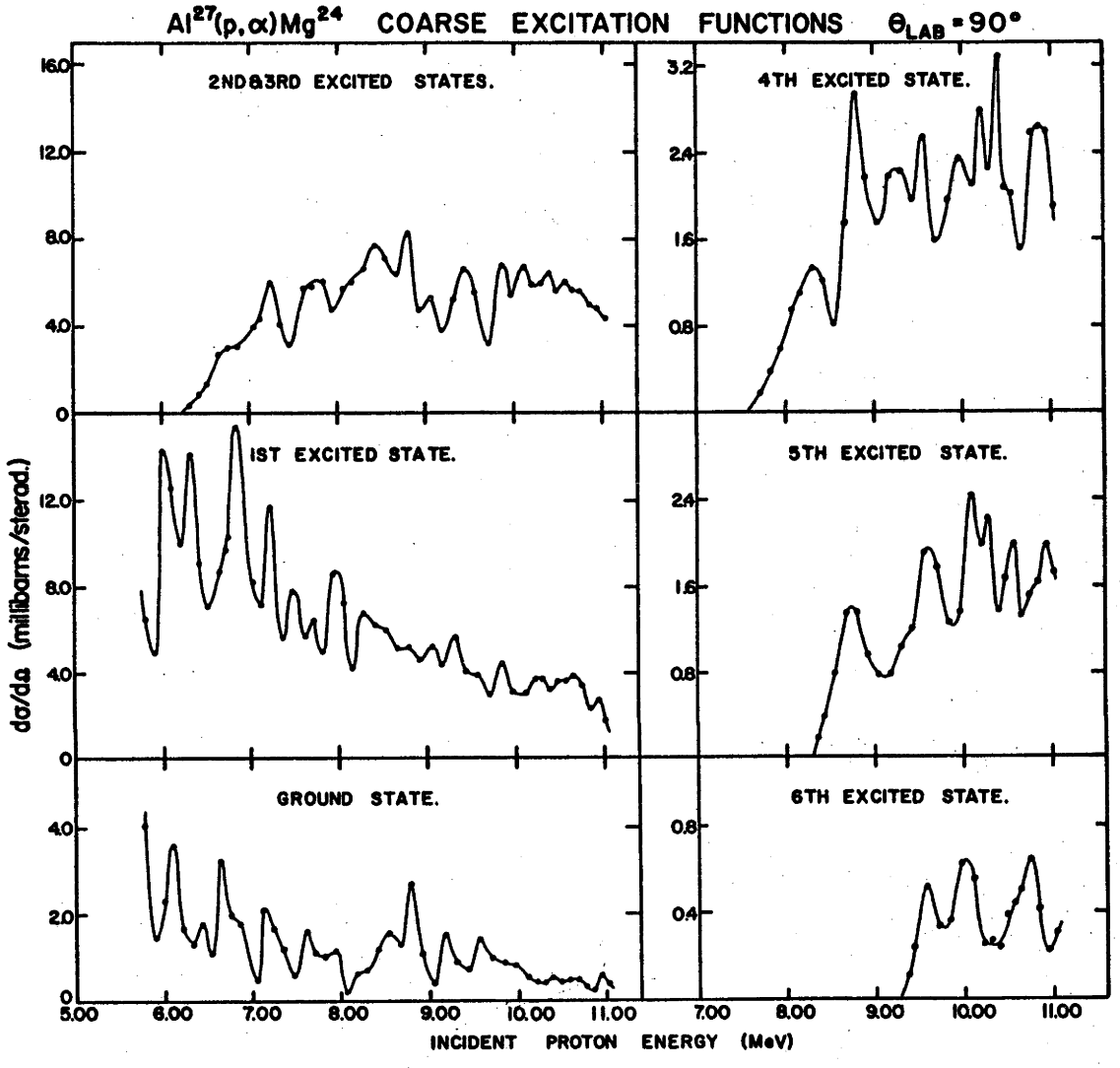
Al27(p,α)Mg24 COARSE EXCITATION FUNCTIONS θLAB = 90°
2ND & 3RD EXCITED STATES.
4TH EXCITED STATE.
1ST EXCITED STATE.
5TH EXCITED STATE.
GROUND STATE.
6TH EXCITED STATE.
dσ/dΩ (millibarns/sterad.)
INCIDENT PROTON ENERGY (MeV)

Angular distributions were measured in steps of 22.5° for groups $\alpha_0, \alpha_1, \alpha_2, \alpha_3$ and α_4 at the proton energies given above and results are indicated in Fig. 3.7. Groups α_2, α_3, and α_4 were not observable at the two lowest energies, 6.0 and 7.0 Mev., so that the corresponding angular distributions were not obtained. The absolute laboratory angle scale established in section 3.1(d) was employed in these measurements and the data have been corrected for kinematical effects. Forward angle and backward angle data were taken with the target orientation differing by 90°. With the detector at 90° data was obtained for both target orientations. The differences were generally within the 5% uncertainty discussed above.

The absolute differential cross section scales for Figs. 3.6 and 3.7 are thought to be accurate to approximately 20%, the largest part of the uncertainty being due to the target thickness measurement. The relative accuracy from point to point, of the differential cross sections is probably of the order of 5%.

3.3. Detailed Study, Excitation Function and Angular Distributions.

To examine the $Al^{27}(p,\alpha)Mg^{24}$ reaction more closely detailed differential excitation functions (25 kev steps)

Fig. 3.7 $Al^{27}(p,\alpha)Mg^{24}$ angular distribution survey, E_p = 6.0 - 11.0 Mev.

Some distributions have been multiplied by 1/2, as indicated, for convenience of representation.

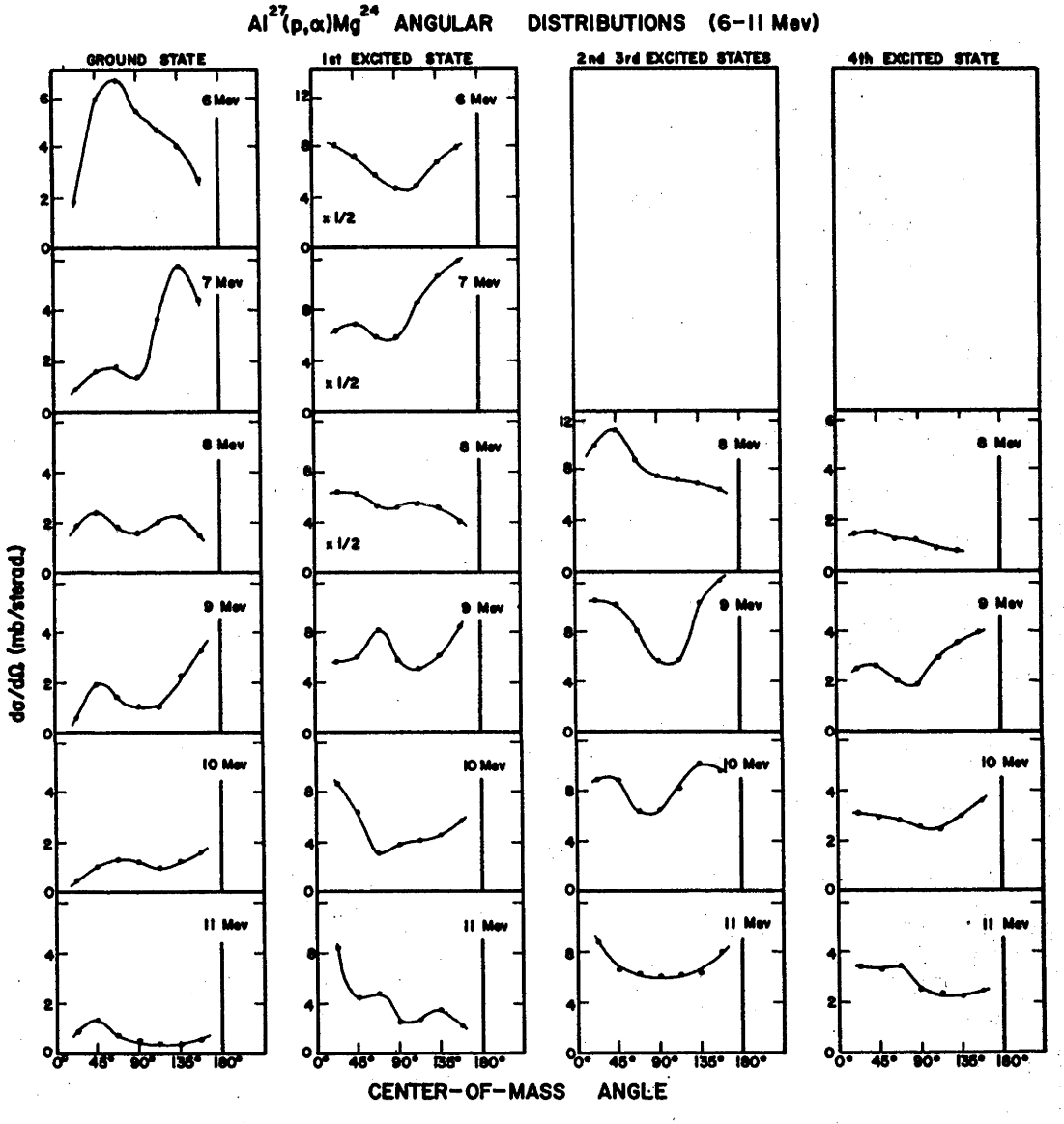
$Al^{27}(p,\alpha)Mg^{24}$ ANGULAR DISTRIBUTIONS (6-11 Mev)
GROUND STATE
1st EXCITED STATE
2nd 3rd EXCITED STATES
4th EXCITED STATE
6 Mev
7 Mev
8 Mev
9 Mev
10 Mev
11 Mev
x 1/2
dσ/dΩ (mb/sterad.)
0° 45° 90° 135° 180°
CENTER-OF-MASS ANGLE

were measured for groups $\alpha_0 - \alpha_5$ at 90° and 135°, over the range E_p = 6.0 - 10.0 Mev., and sets of angular distributions were obtained at points of particular interest.

For this work, a 300Ω- cm detector was set in the rotating mount, and a 3,000Ω- cm detector in the fixed mount. Pulses from each were fed to identical amplification systems, whose outputs were joined and analyzed by a single pulse-height-analyzer (See Fig. 3.8). The wide spacing of the Mg^{24} energy levels and the high detection system resolution made it feasible and convenient to superimpose the 90° and 135° spectra and record both simultaneously. A typical overlaid spectrum is shown in Fig. 3.8. Pulse outputs were taken from the biassed post-amplifiers, so that relative energy shifts between the 90° and 135° spectra could be compensated by adjustment of bias levels.

In order to permit resolution of alpha groups α_2 and α_3, a relatively thin self-supporting Al target was used (~20 kev for 8.78 Mev alpha particles). Arguments concerning target thickness, absolute cross section scales, and relative yield accuracy proceed as in section 3.2. Since groups α_2 and α_3 were not completely separated, it is expected that the required unfolding process leads to somewhat larger relative yield uncertainties for these groups than for others.

Fig. 3.8 Electronics block diagram showing coupled amplifiers, and typical $Al^{27}(p,\alpha)Mg^{24}$ overlaid spectra obtained with this arrangement.

The ORTEC 201 amplifiers are represented in 3 sections, to emphasize the use of the biassed post-amplication units. Spectrum peaks are labelled with corresponding alpha group number and observation angle.

ELECTRONICS BLOCK DIAGRAM.

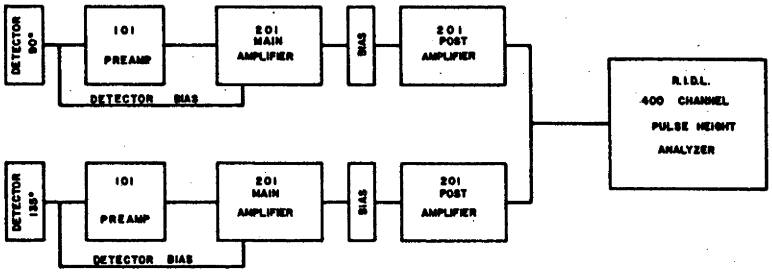

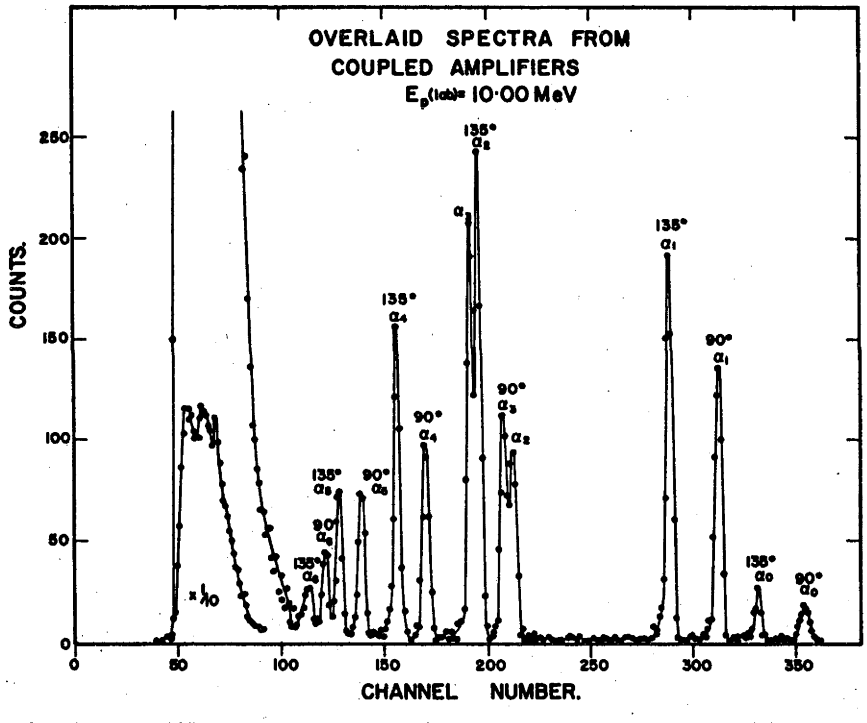

The 25 kev excitation functions for groups $\alpha_0 - \alpha_5$ are presented in Figs. 3.9, 3.10, 3.11, 3.12 and 3.13. All yields were measured with the Al target set at 135° and with uncollimated detectors. Remarks about statistical errors apply as in section 3.2.

The α_0 and α_1 excitation functions were measured over the entire range E_p = 6.0 - 10.0 Mev. The groups α_2 and α_3 were not well resolved below E_p = 7.5 Mev, so that their excitation functions were not measured below this energy. Groups α_4 and α_5 were not significantly more intense than background below 8.2 Mev and 9.2 Mev respectively.

Three sets of closely spaced (12.5 kev separation in E_p) angular distributions were measured for alpha groups α_0 and α_1 at median proton energies of 3.650 and 6.000 Mev, and for alpha groups α_0, α_1, α_2, α_3, and α_4 at a median energy of 8.725 Mev. Data were obtained at 15° intervals over the angular range 15° to 165° (except at extreme forward angles for some groups, where intense elastic proton flux produced an obscuring pulse pileup). Remarks concerning target orientation rotation apply as in section 3.2. Relative yields for each distribution were monitored by a detector fixed at 90°, and corrections were

Fig. 3.9 $Al^{27}(p,\alpha)Mg^{24}$ $d\sigma/d\Omega$ (90°, 135°) excitation functions for alpha particles populating the Mg^{24} ground state. E_p = 6.0 - 10.0 Mev.

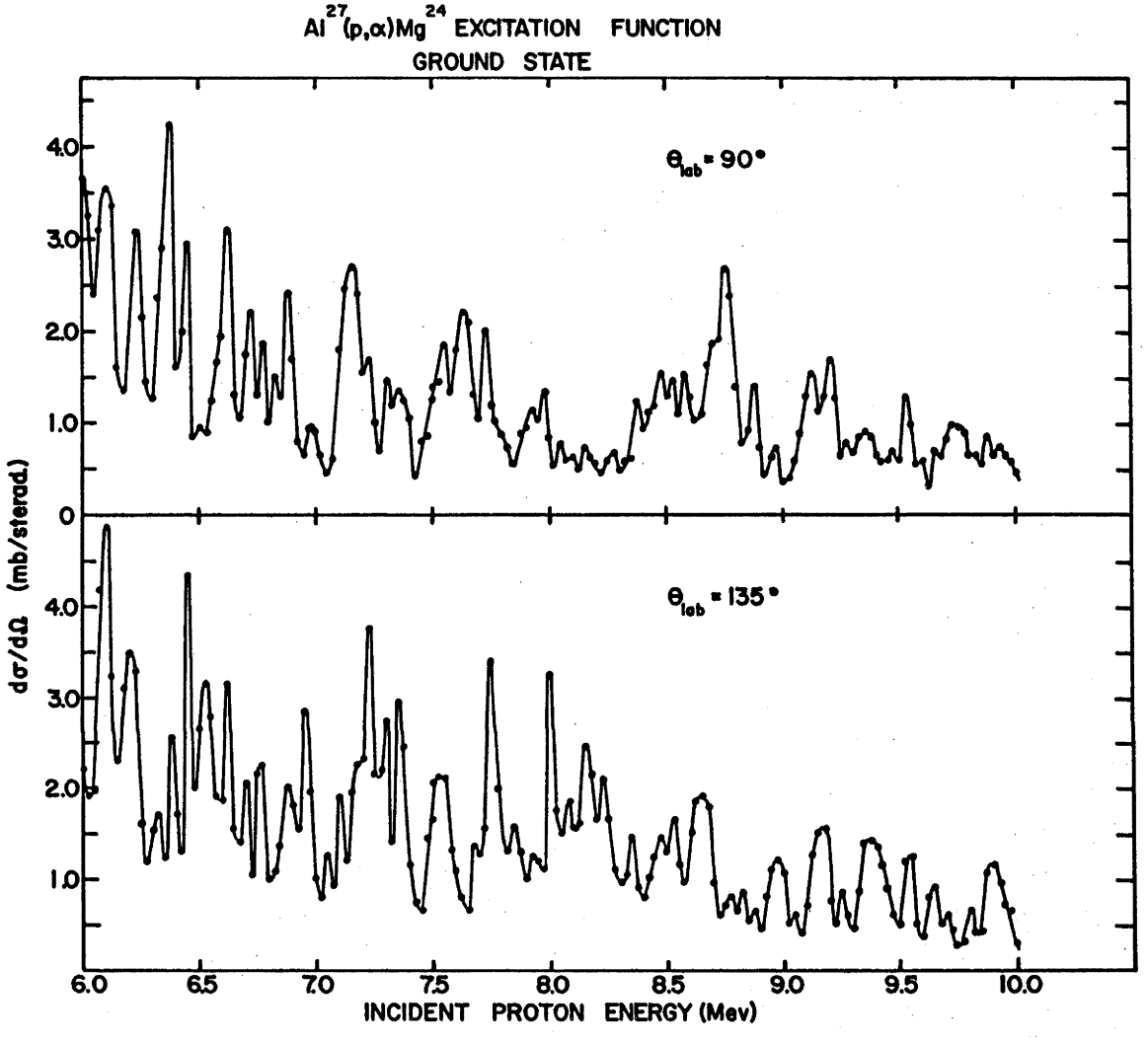
Al27(p,α)Mg24 EXCITATION FUNCTION
GROUND STATE
θlab = 90°
θlab = 135°
dσ/dΩ (mb/sterad.)
4.0
3.0
2.0
1.0
0
6.0
6.5
7.0
7.5
8.0
8.5
9.0
9.5
10.0
INCIDENT PROTON ENERGY (Mev)

3.10 $Al^{27}(p,\alpha)Mg^{24}$ $d\sigma/d\Omega$ (90°, 135°) Excitation functions for alpha particles populating the Mg^{24} first excited state. E_p = 6.0 - 10.0 Mev.

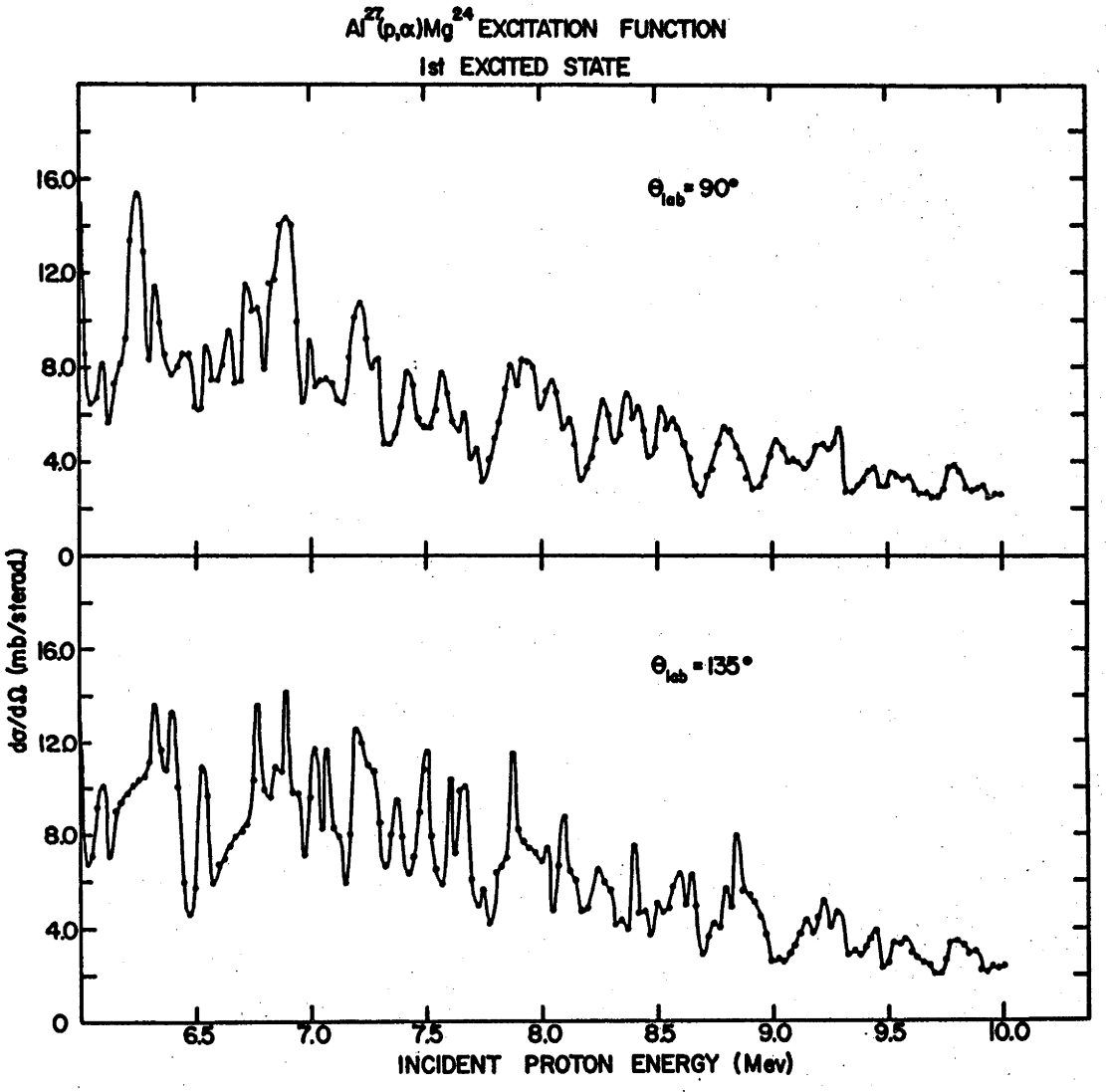
$Al^{27}(p,\alpha)Mg^{24}$ EXCITATION FUNCTION
1st EXCITED STATE
$\theta_{lab} = 90°$
$\theta_{lab} = 135°$
dσ/dΩ (mb/sterad.)
16.0
12.0
8.0
4.0
0
6.5
7.0
7.5
8.0
8.5
9.0
9.5
10.0
INCIDENT PROTON ENERGY (Mev)

Fig. 3.11 $Al^{27}(p,\alpha)Mg^{24}$ $d\sigma/d\Omega$ (90°, 135°) excitation functions for alpha particles populating the Mg^{24} second excited state. E_p = 7.5 - 10.0 Mev.

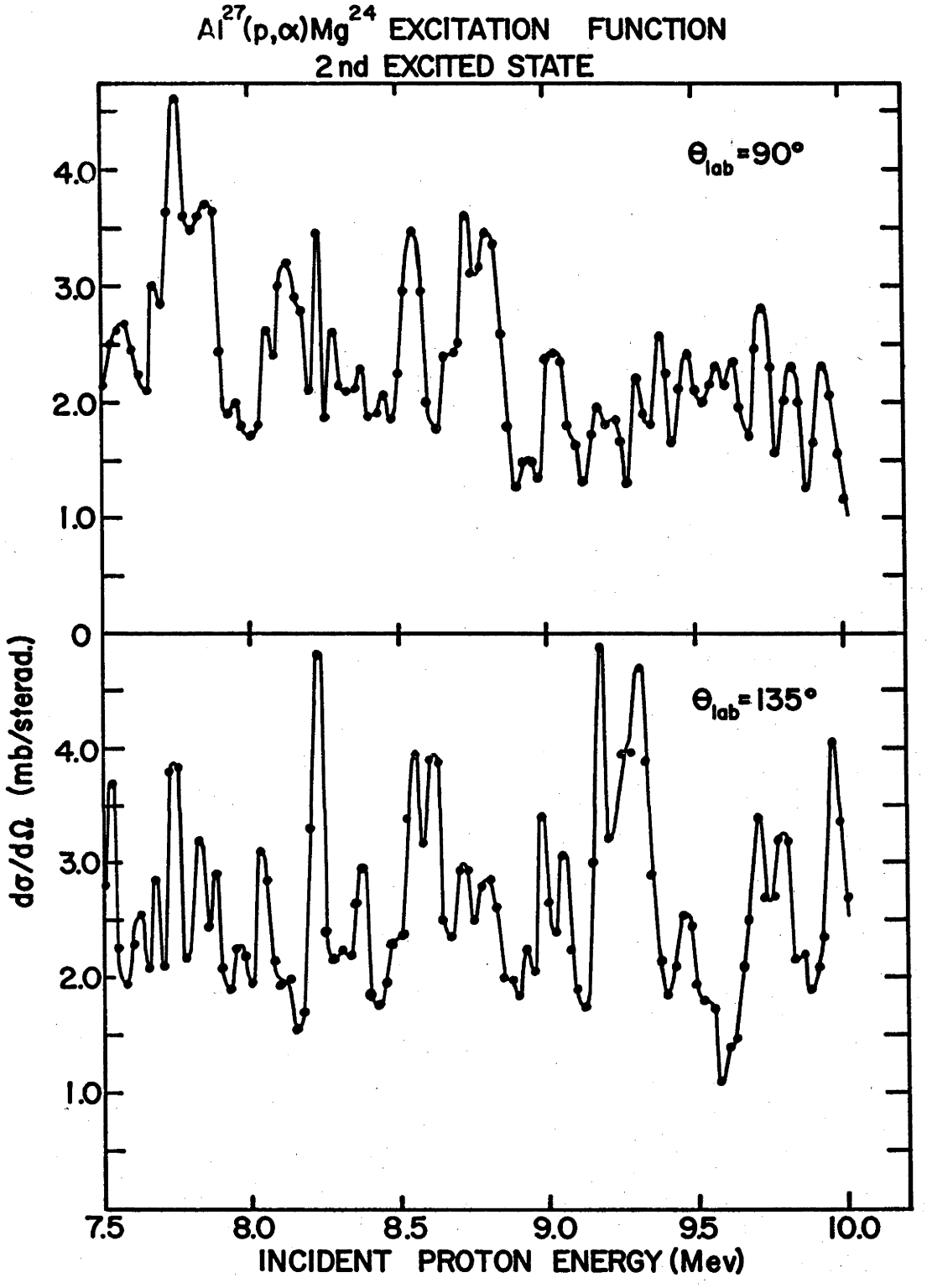
$Al^{27}(p,\alpha)Mg^{24}$ EXCITATION FUNCTION
2nd EXCITED STATE
θ_{lab}=90°
θ_{lab}=135°
dσ/dΩ (mb/sterad.)
4.0
3.0
2.0
1.0
0
7.5
8.0
8.5
9.0
9.5
10.0
INCIDENT PROTON ENERGY (Mev)

Fig. 3.12 $Al^{27}(p,\alpha)Mg^{24}$ $d\sigma/d\Omega$ (90°, 135°) excitation functions for alpha particles populating the Mg^{24} third excited state. E_p = 7.5 - 10.0 Mev.

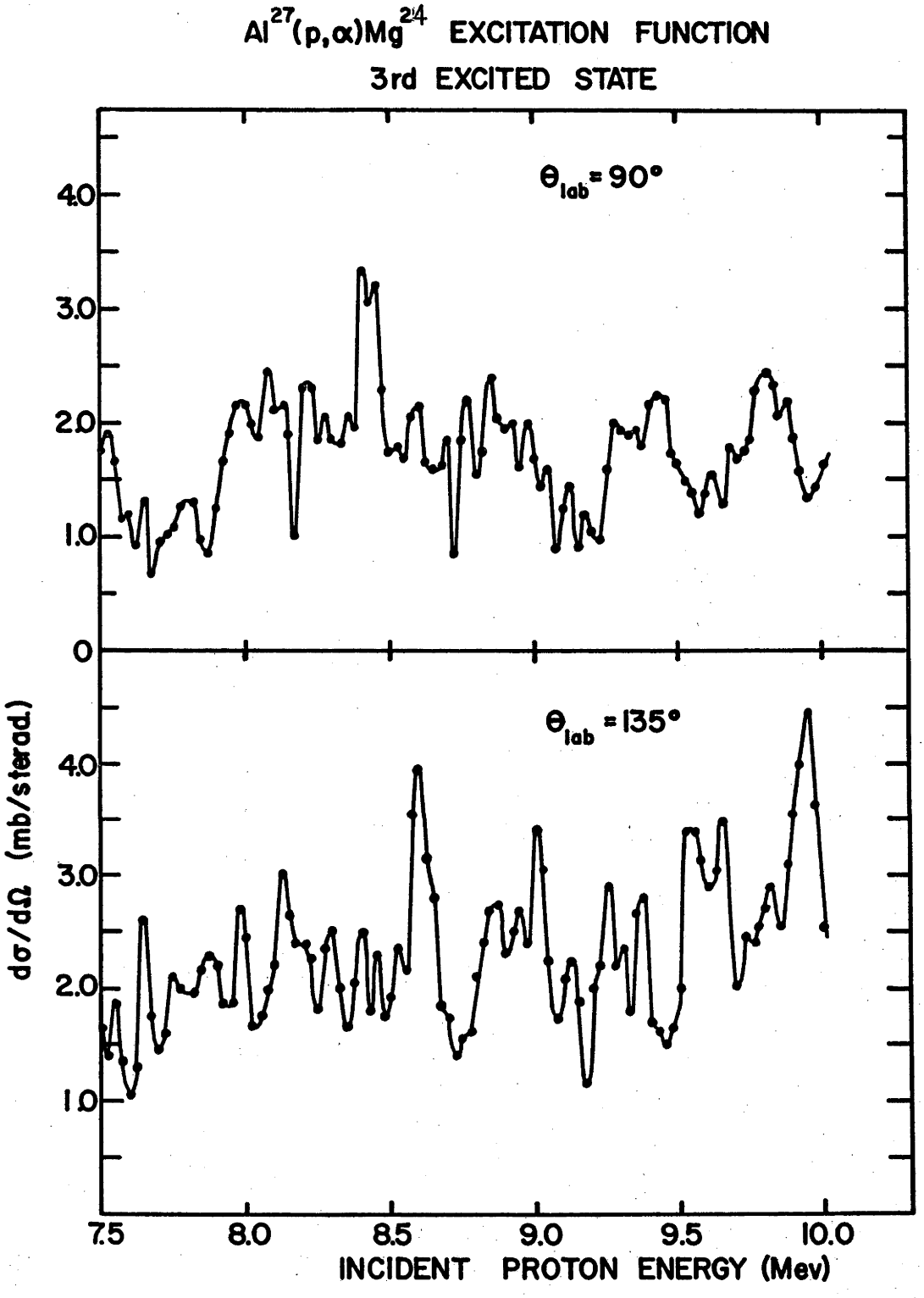
$Al^{27}(p,\alpha)Mg^{24}$ EXCITATION FUNCTION
3rd EXCITED STATE
$\theta_{lab} = 90°$
$\theta_{lab} = 135°$
4.0
3.0
2.0
1.0
0
4.0
3.0
2.0
1.0
$d\sigma/d\Omega$ (mb/sterad.)
7.5
8.0
8.5
9.0
9.5
10.0
INCIDENT PROTON ENERGY (Mev)

Fig. 3.13 $Al^{27}(p,\alpha)Mg^{24}$ $d\sigma/d\Omega$ (90°, 135°) excitation function for alpha particles populating the Mg^{24} fourth excited state (E_p = 8.2 - 10.0 Mev) and the Mg^{24} fifth excited state (Ep = 9.2 - 10.0 Mev).

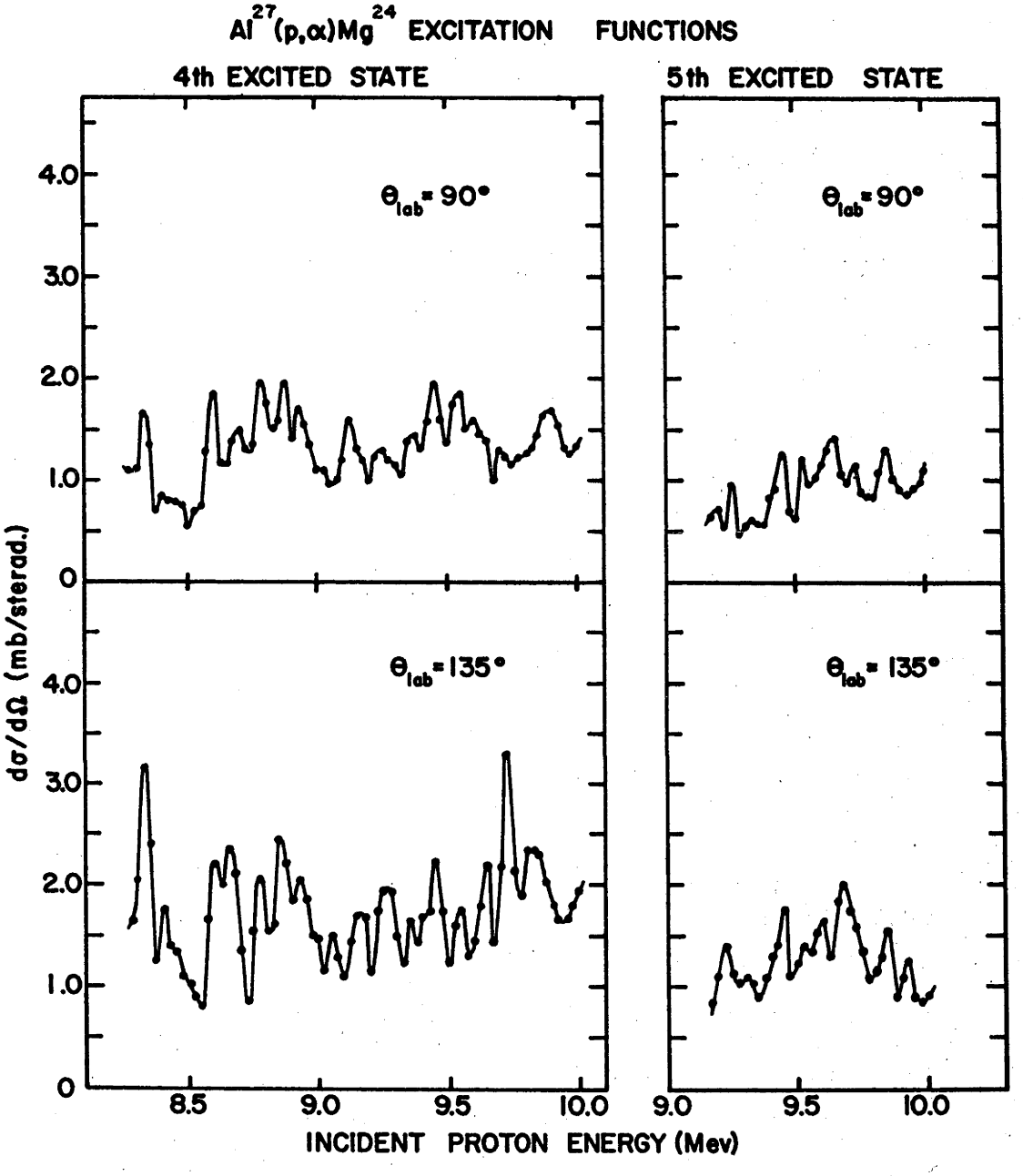
Al27(p,α)Mg24 EXCITATION FUNCTIONS
4th EXCITED STATE
5th EXCITED STATE
θlab = 90°
θlab = 90°
θlab = 135°
θlab = 135°
dσ/dΩ (mb/sterad.)
0
1.0
2.0
3.0
4.0
8.5
9.0
9.5
10.0
INCIDENT PROTON ENERGY (Mev)

applied accordingly; it is therefore believed that the relative yield uncertainty for the angular distribution data is considerably less than the 5% uncertainty in the excitation function data.

The angular distributions are given in Figs. 3.14 and 3.15. Lines have been drawn smoothly through the experimental points. The plots have been shifted relative to each other by 2.0 or 4.0 mb, as indicated, with incident proton energy increasing with curve number. Proton energies corresponding to the curve numbers are given in the appropriate figure captions.

3.4. Fine Structure Excitation Functions.

Short selected portions of the α_0 and α_1 differential excitation functions at 90° were examined with the maximum precision attainable with the Tandem van de Graaff accelerator. A very thin ($\sim$ 0.3 kev thick for 6.0 Mev protons) self-supporting Al target was used for this work. The 90° analyzing magnet object and image slits were closed down to a few thousandths-of-an-inch separation, and the field strength manually stabilized during measurements by holding the proton NMR trace-minimum at a fixed point on the display screen. It is estimated that these procedures provided a beam energy resolution of $\sim$ 1 kev.

Fig. 3.14 Angular distributions for $Al^{27}(p,\alpha)Mg^{24}$ ground state, and first excited state reactions near E_p = 3.65 Mev and 6.00 Mev.

The distributions have been shifted vertically with respect to each other by 4 mb. for clarity of presentation; the first excited state distributions are each multiplied by the factor 1/4, as indicated. The numbers labelling the distributions refer to the proton energies at which they were measured. These were as follows :

E_p (Mev) for 3.65 Mev $W(\theta)$		E_p (Mev) for 6.00 Mev $W(\theta)$	
1.	3.6250	1.	5.9750
2.	3.6375	2.	5.9875
3.	3.6500	3.	6.0000
4.	3.6625	4.	6.0125
5.	3.6750	5.	6.0250

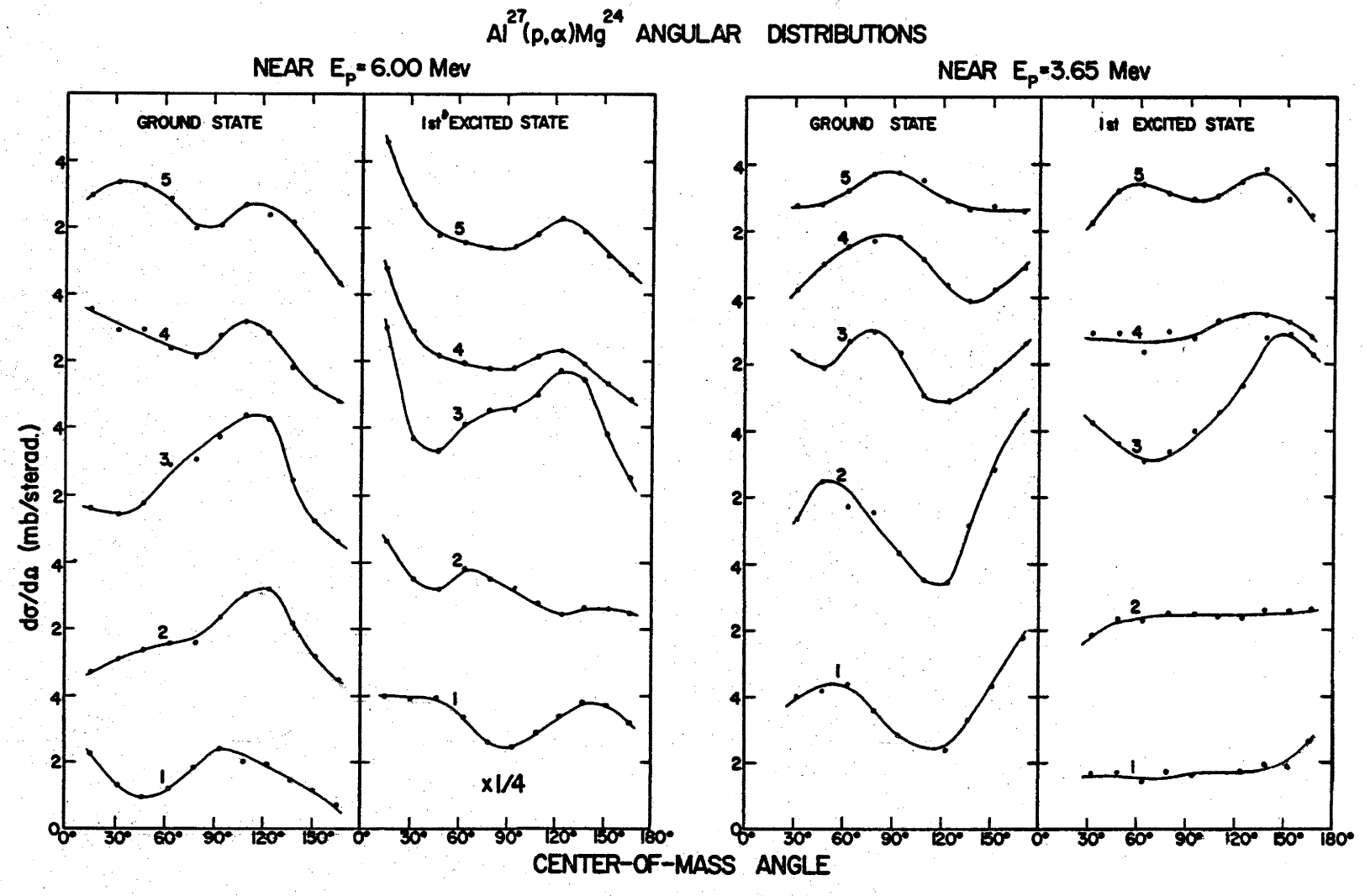
$Al^{27}(p,\alpha)Mg^{24}$ ANGULAR DISTRIBUTIONS
NEAR E_p = 6.00 Mev
NEAR E_p = 3.65 Mev
GROUND STATE
1st EXCITED STATE
GROUND STATE
1st EXCITED STATE
x1/4
dσ/dΩ (mb/sterad.)
CENTER-OF-MASS ANGLE
0° 30° 60° 90° 120° 150° 180°

Fig. 3.15 Angular distributions for $Al^{27}(p,\alpha)Mg^{24}$ ground state, first, second + third, and 4th excited state reactions near $E_p = 8.725$ Mev.

The distributions have been shifted vertically with respect to each other by 2.0 mb; first and second + third excited state distributions are multiplied by 1/2, as indicated. The numbers labelling the $W(\theta)$ refer to the proton energies at which they were measured. These were as follows :

	E_p (Mev) for 8.725 Mev	$W(\theta)$
1.	8.7000	
2.	8.7125	
3.	8.7250	
4.	8.7375	
5.	8.7500	

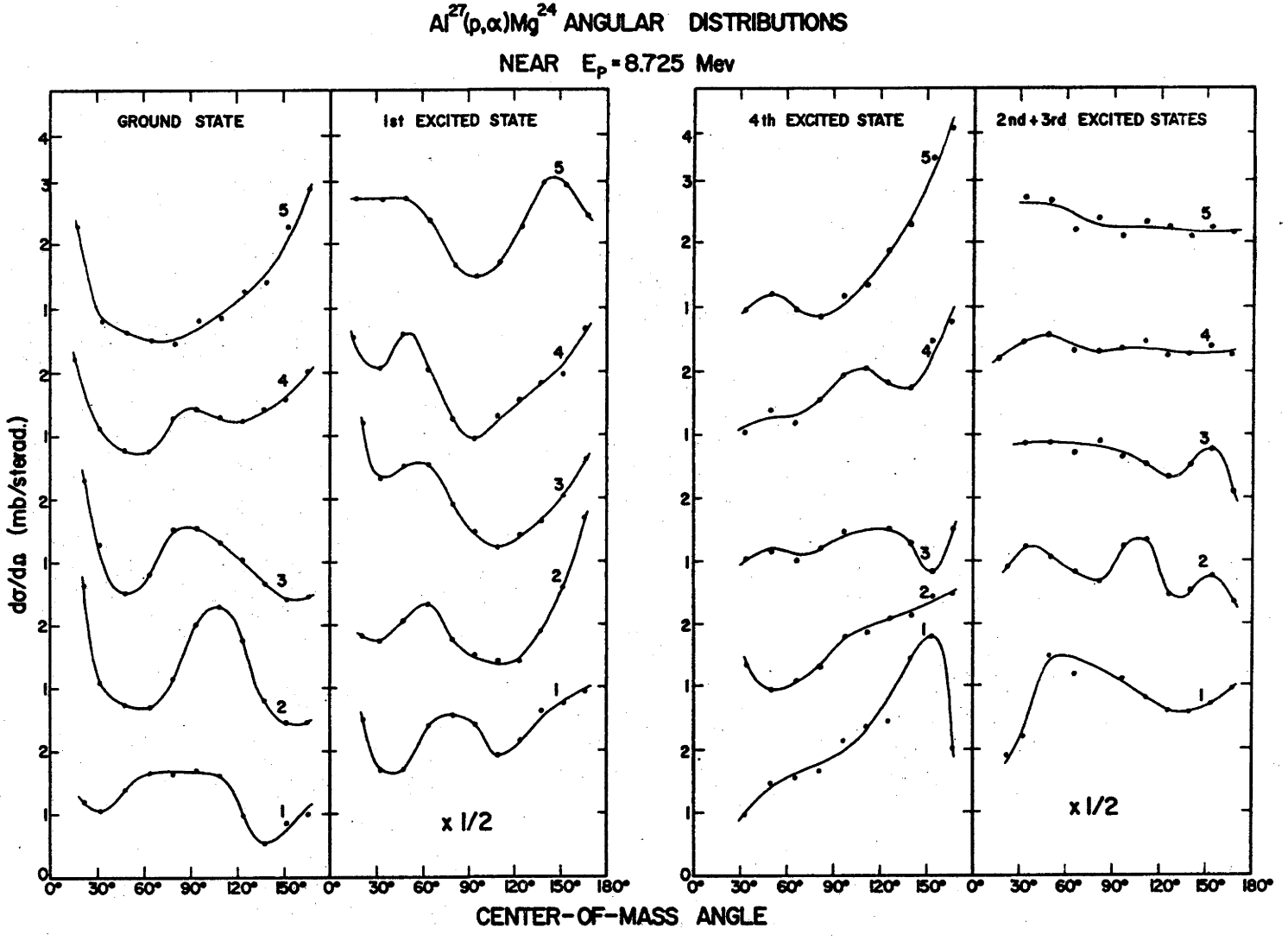
$Al^{27}(p,\alpha)Mg^{24}$ ANGULAR DISTRIBUTIONS
NEAR E_p = 8.725 Mev
GROUND STATE
1st EXCITED STATE
4th EXCITED STATE
2nd + 3rd EXCITED STATES
x 1/2
x 1/2
dσ/dΩ (mb/sterad.)
CENTER-OF-MASS ANGLE
0° 30° 60° 90° 120° 150° 180°

Two excitation function segments (of 100 kev width) near E_p = 6.00 Mev were measured in 2 kev steps. A region of similar width near E_p = 3.65 Mev was also measured. Results are indicated in Figs. 3.16 and 3.17. The smooth curves drawn through the yield points have made provision for statistical uncertainties. Several points were remeasured after re-cycling the analyzing magnet and agreed with initial values within statistical uncertainty.

3.5. Detail Study and Total Cross Sections 8.0 and 8.34 Mev.

A representative region of excitation, corresponding to the proton energy range 8.00 - 8.34 Mev, was studied in considerable detail with a view to (a) obtaining a topographical map of the $Al^{27}(p,\alpha)Mg^{24}$ reaction as a function of alpha particle group, angle and proton energy, and (b) extracting total cross section excitation functions for groups $\alpha_0 - \alpha_3$ over this range of E_p.

The data was obtained in the form of 18 angular distributions taken at proton energy intervals of 20 kev. To reduce the data taking time, an array of four detectors was used.

Three extra detector mounts and assemblies of the type described in section 2.4, were fixed to the geared

Fig. 3.16 Fine structure in $Al^{27}(p,\alpha)Mg^{24}$ $d\sigma/d\Omega$ (90°) excitation functions for ground state and first excited state reactions. E_p = 3.59 - 3.72 Mev.

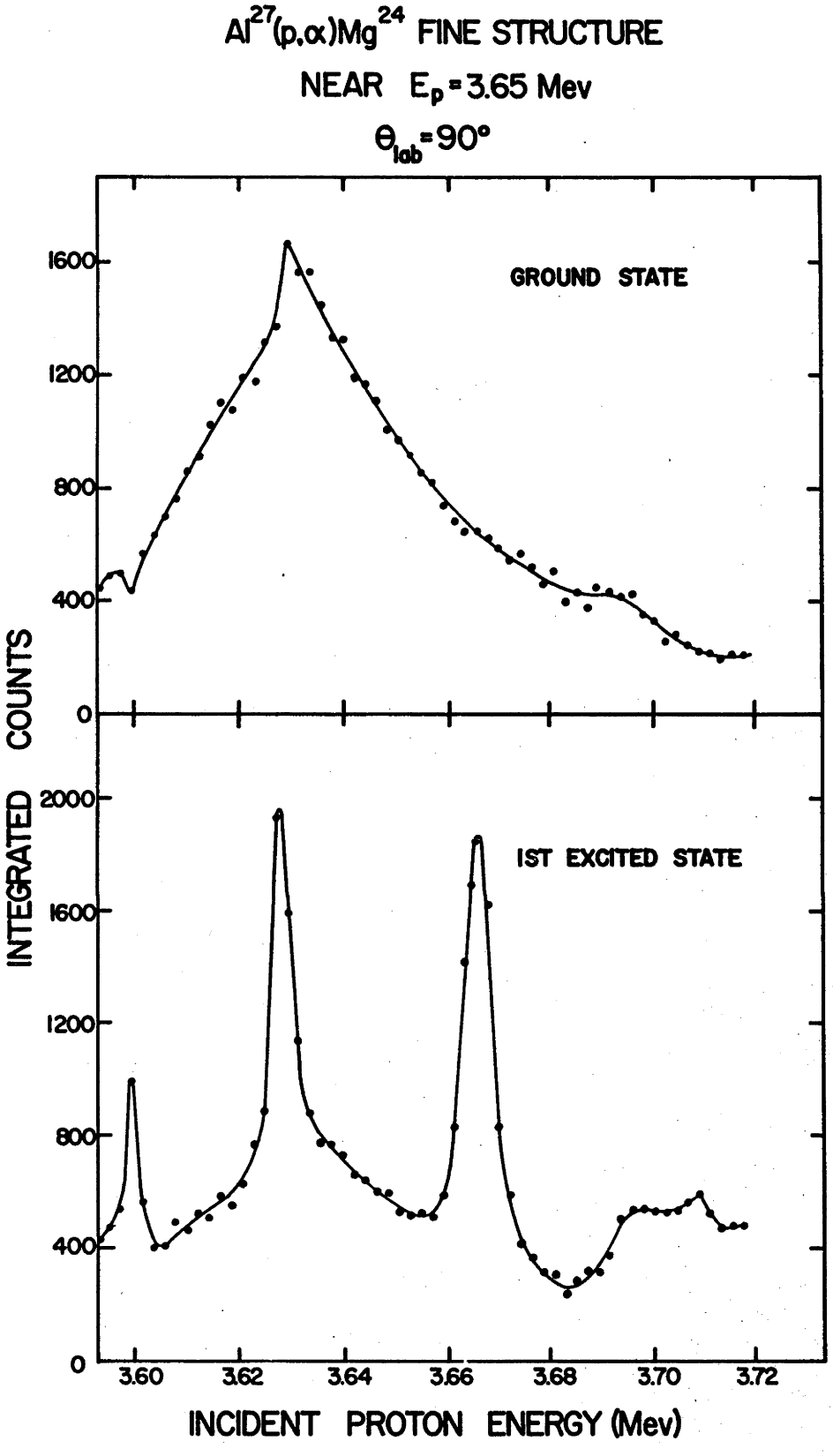
$Al^{27}(p,\alpha)Mg^{24}$ FINE STRUCTURE
NEAR $E_p = 3.65$ Mev
$\theta_{lab} = 90°$
GROUND STATE
1ST EXCITED STATE
INTEGRATED COUNTS
0
400
800
1200
1600
2000
3.60
3.62
3.64
3.66
3.68
3.70
3.72
INCIDENT PROTON ENERGY (Mev)

Fig. 3.17 Fine structure in $Al^{27}(p,\alpha)Mg^{24}$ $d\sigma/d\Omega$ (90°) excitation functions for ground state and first excited state reactions. E_p = 5.90 - 6.00 Mev and 6.10 - 6.20 Mev.

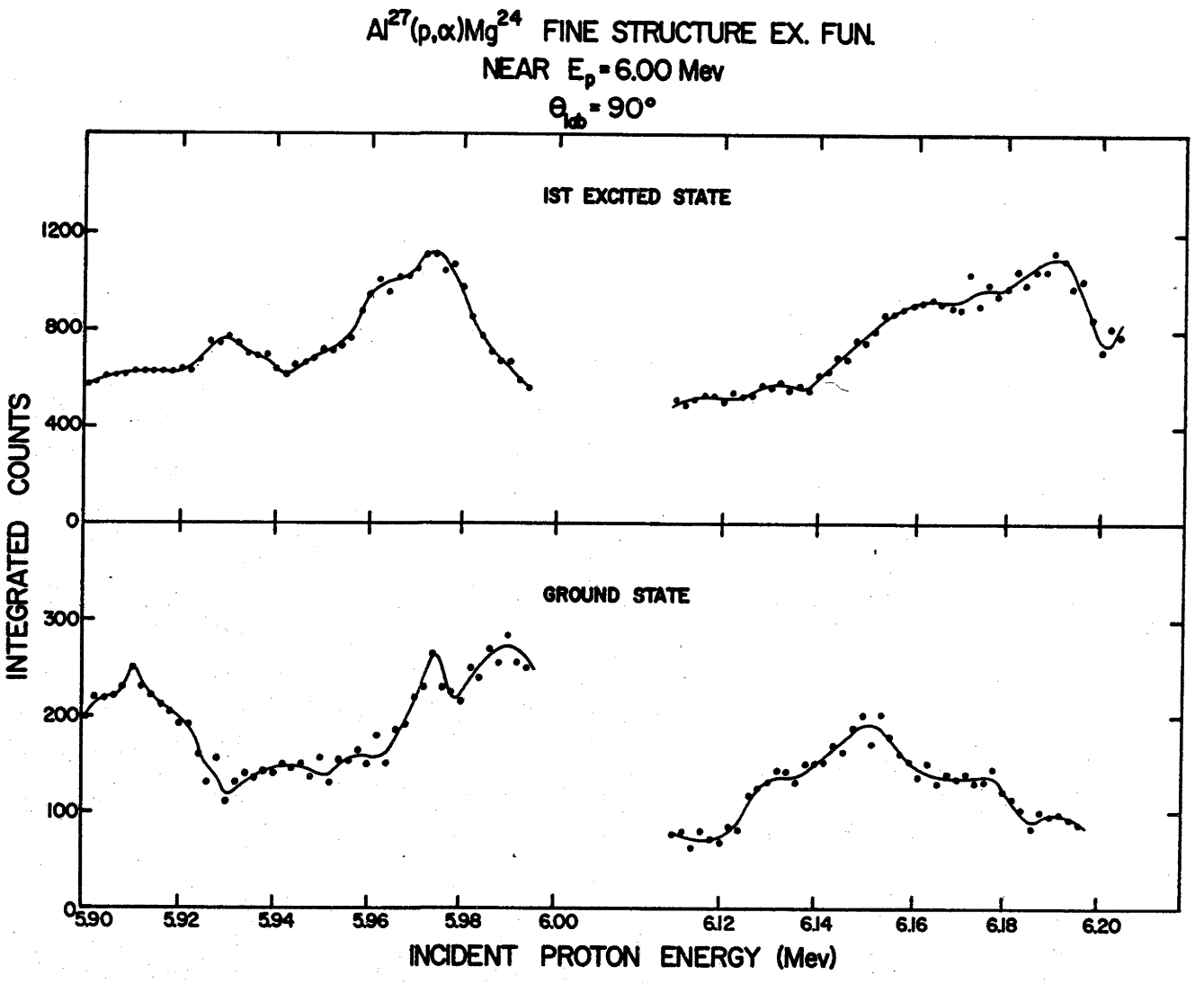
$Al^{27}(p,\alpha)Mg^{24}$ FINE STRUCTURE EX. FUN.
NEAR E_p = 6.00 Mev
θ_{lab} = 90°
IST EXCITED STATE
GROUND STATE
INTEGRATED COUNTS
0
400
800
1200
0
100
200
300
5.90
5.92
5.94
5.96
5.98
6.00
6.12
6.14
6.16
6.18
6.20
INCIDENT PROTON ENERGY (Mev)

rotating plate. A cross section through the scattering chamber, Fig. 3.18, shows the schematic arrangement. The detectors were positioned such that they swept out the angular ranges 15° - 50°, 55° - 90°, 90° - 125° and 130° - 165° simultaneously. Each segment contained 8 angular positions (5° spacing), so that in 8 settings of the rotating assembly a 32 point angular distribution was obtained (90° being observed by both detectors A and C, as a partial check on internal consistency). The detectors used in this work were two 300Ω-cm type (A and B), and two 3,000Ω-cm type (C and D). The target was the same as that used for work of section 3.3; it was oriented at 45° throughout the run. Detector solid angles were normalized to that of detector A by rotating all detectors sequentially to a fixed angle (90°) and measuring the summed yield for alpha groups $\alpha_0 - \alpha_3$, for $Al^{27}(p,\alpha)Mg^{24}$ at a fixed proton energy and constant accumulated charge.

Pulses from detectors A and B were fed to separate ORTEC 101 - 201 systems and RIDL 400 channel analyzers. (See Fig. 3.19). Detector C fed a Tennelec 101A low noise preamplifier (powered by a Franklin A-8 amplifier), and received bias from a filtered dry battery supply. Detector D received bias from a similar supply and fed an A.N.U.-made low noise preamplifier* (powered as the Tennelec preamplifier

* See Chapter II.

Fig. 3.18 Schematic arrangement of detector array in 9-inch scattering chamber.

Numbered details are :

1. Scattering chamber wall
2. Toothed plate, from which detector array is suspended
3. Typical detector assembly (identical with inset of Fig. 3.1)
4. Target strip
5. Beam collimating assembly.

Cross-hatched sections indicate the angular scan of each detector; max. and min. observation angles are also shown.

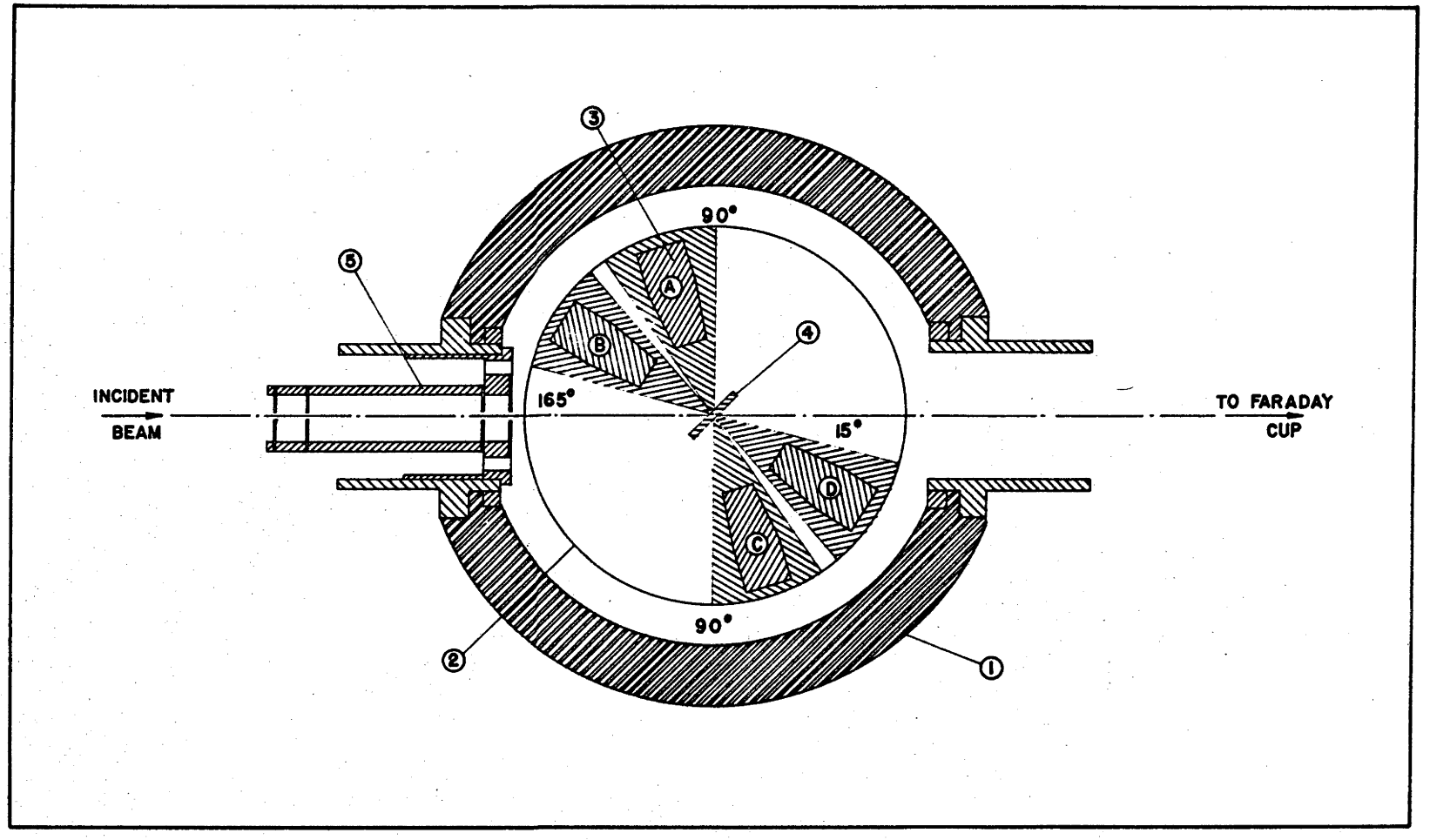
INCIDENT
BEAM
TO FARADAY
CUP
90°
90°
165°
15°
A
B
C
D
1
2
3
4
5

Fig. 3.19 Block diagram of electronics employed with detector array.

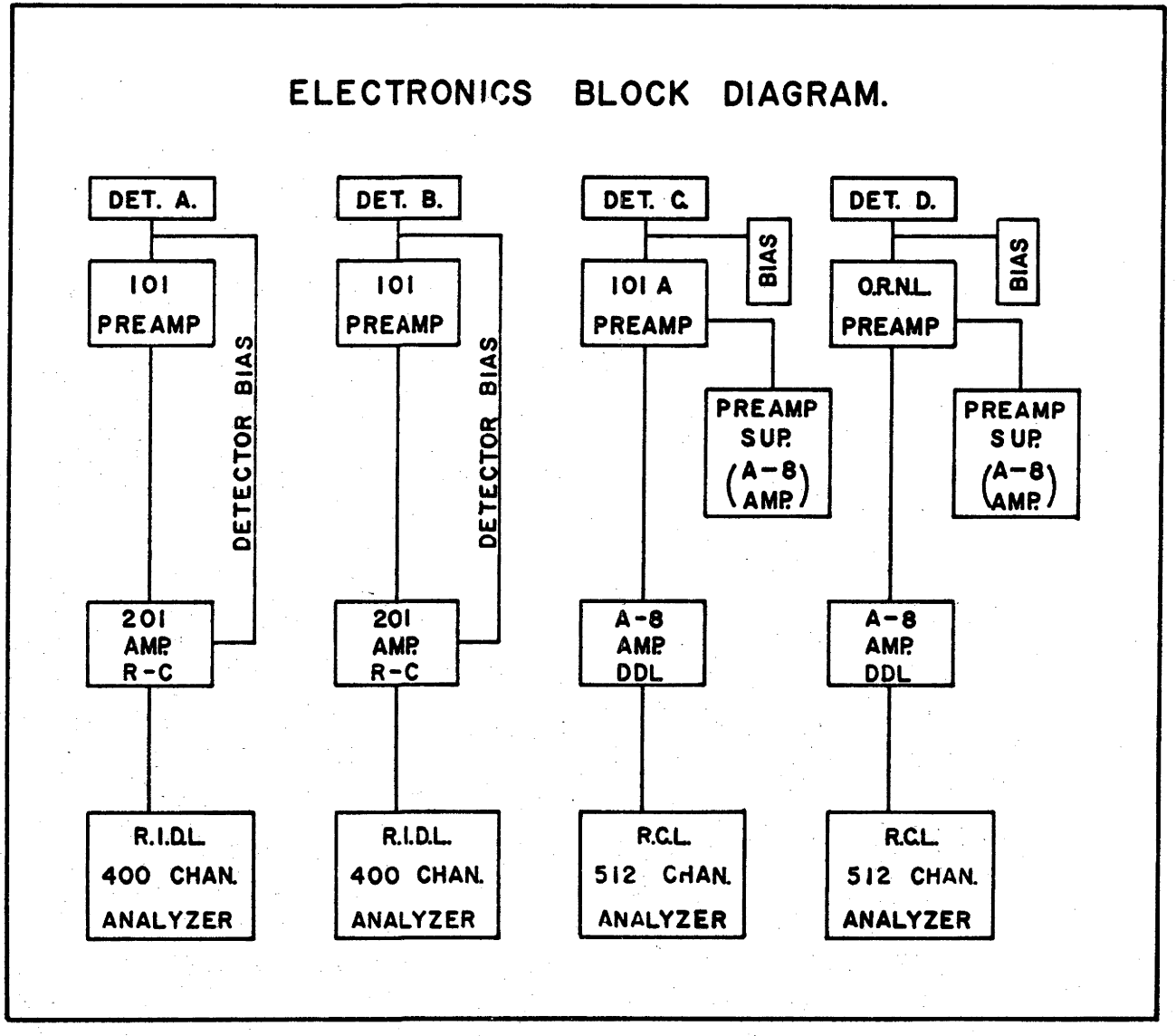
ELECTRONICS BLOCK DIAGRAM.
DET. A.
101 PREAMP
DETECTOR BIAS
201 AMP. R-C
R.I.D.L. 400 CHAN. ANALYZER
DET. B.
101 PREAMP
DETECTOR BIAS
201 AMP. R-C
R.I.D.L. 400 CHAN. ANALYZER
DET. C.
BIAS
101 A PREAMP
PREAMP SUP. (A-8 AMP.)
A-8 AMP. DDL
R.C.L. 512 CHAN. ANALYZER
DET. D.
BIAS
O.R.N.L. PREAMP
PREAMP SUP. (A-8 AMP.)
A-8 AMP. DDL
R.C.L. 512 CHAN. ANALYZER

above). C and D preamplifiers fed A - 8 double-delay-line-clipping linear amplifiers and separate RCL 512 channel analyzers. Overall energy resolution for all systems was ~1%. This proved adequate to satisfy the condition that the α_2, α_3 group doublet be well resolved.

Fig. 3.20 illustrates representative spectra obtained by each detector, taken at the mean angular setting of the detector array. It is seen that in all cases, the 4.122 Mev doublet is well resolved, and that the background between alpha groups is generally insignificant. The group α_4 is observable in each spectrum. However, at forward and backward angles it is superimposed on a sharply rising proton cutoff "background", which introduces a large uncertainty into the corresponding yield estimate. No attempt was made, therefore, to extract the yield for this group from the original data.

The arguments concerning absolute cross section scales, and relative yield accuracy proceed as in section 3.2. No monitor was used. The measured yields for alpha groups $\alpha_0 - \alpha_3$ were punched on cards and corrected by a computer program*, for detector solid angle differences, pulse-height-analyzer dead time, and laboratory-to-center-of-mass-system

*Coded for the A.N.U. 1620 computer by the present writer.

Fig. 3.20 Typical $Al^{27}(p,\alpha)Mg^{24}$ spectra obtained by each array detector at a representative array setting.

As before, peak numbers refer to alpha groups populating the corresponding Mg^{24} levels. The proton cutoff "edge" is seen at the left of all spectra.

REPRESENTATIVE SPECTRA
FROM DETECTOR ARRAY

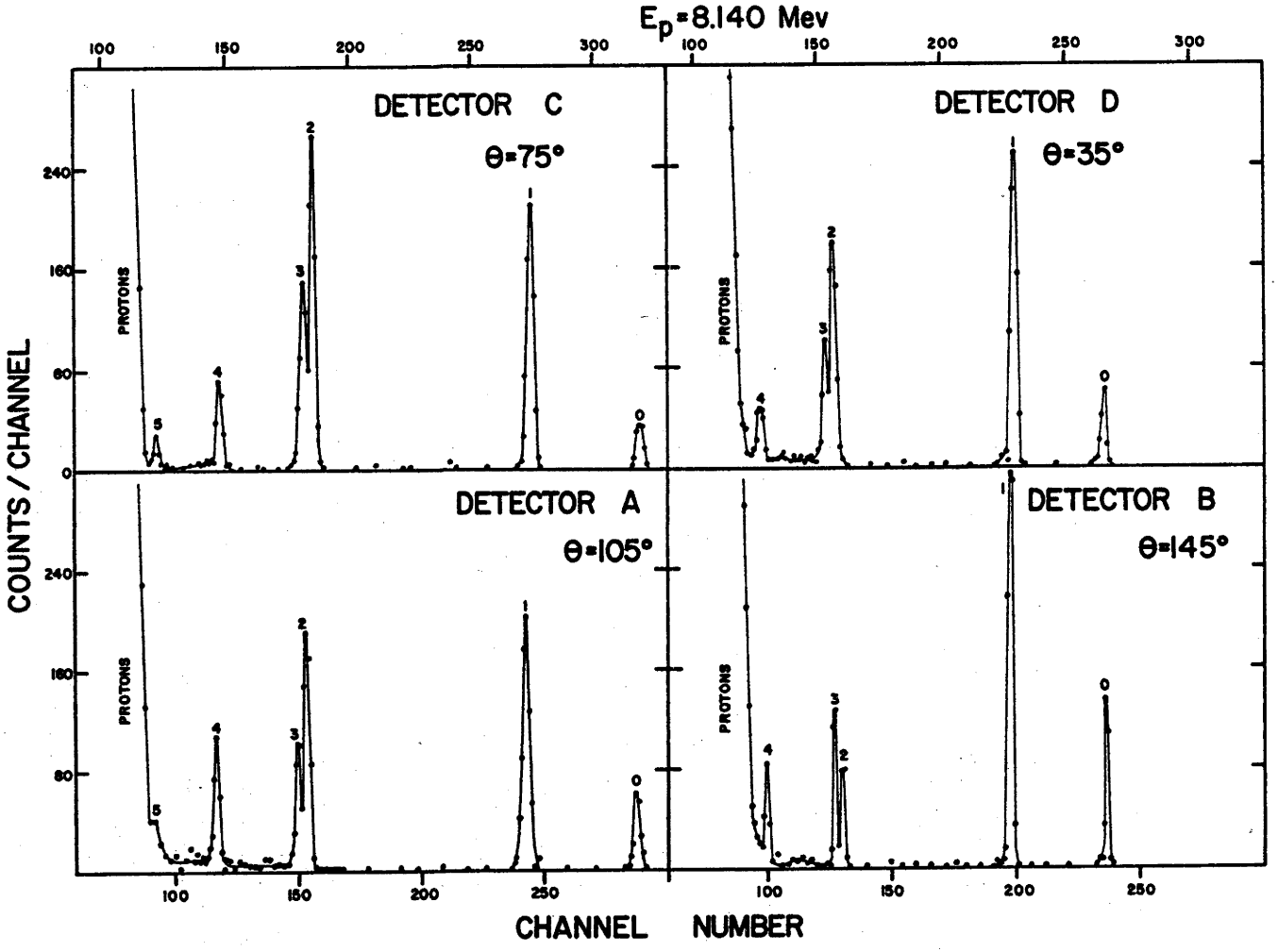

kinematics transformation. The converted and normalized yields are plotted in Figs. 3.21, 3.22, 3.23 and 3.24 as functions of proton energy and center-of-mass angle. For clarity, data points are not shown. The solid lines representing them have taken statistical uncertainties into account.

The converted sets of angular distribution for groups $\alpha_0 - \alpha_3$ were fitted by a computer program* to an expansion of the form $\sum_L A_L P_L(\cos\theta)$, via the method of Rose (Ro53). From these fits were extracted total cross section excitation functions, and excitation functions for the first four Legendre polynomical coefficients. The results are given in section 4.8.

Section 4. DISCUSSION OF RESULTS.

4.1. Literature Survey.

Several groups have studied the reaction $Al^{27}(p,\alpha)Mg^{24}$ in recent years. Much of the work has been performed with cyclotrons, using proton energy resolutions of $\sim$ 50 kev. Fischer et al. (Fi58) have measured angular distributions for groups α_0 and α_1 at 10.87 and 10.97 Mev (E_p), and excitation functions for these groups from E_p = 9.6 - 10.0 Mev. Yamashita, Ogata and their collaborators

*A.N.U. Library Program.

Fig. 3.21 Angular distributions from E_p = 8.00 to 8.34 Mev for the $Al^{27}(p,\alpha)Mg^{24}$ ground state reaction.

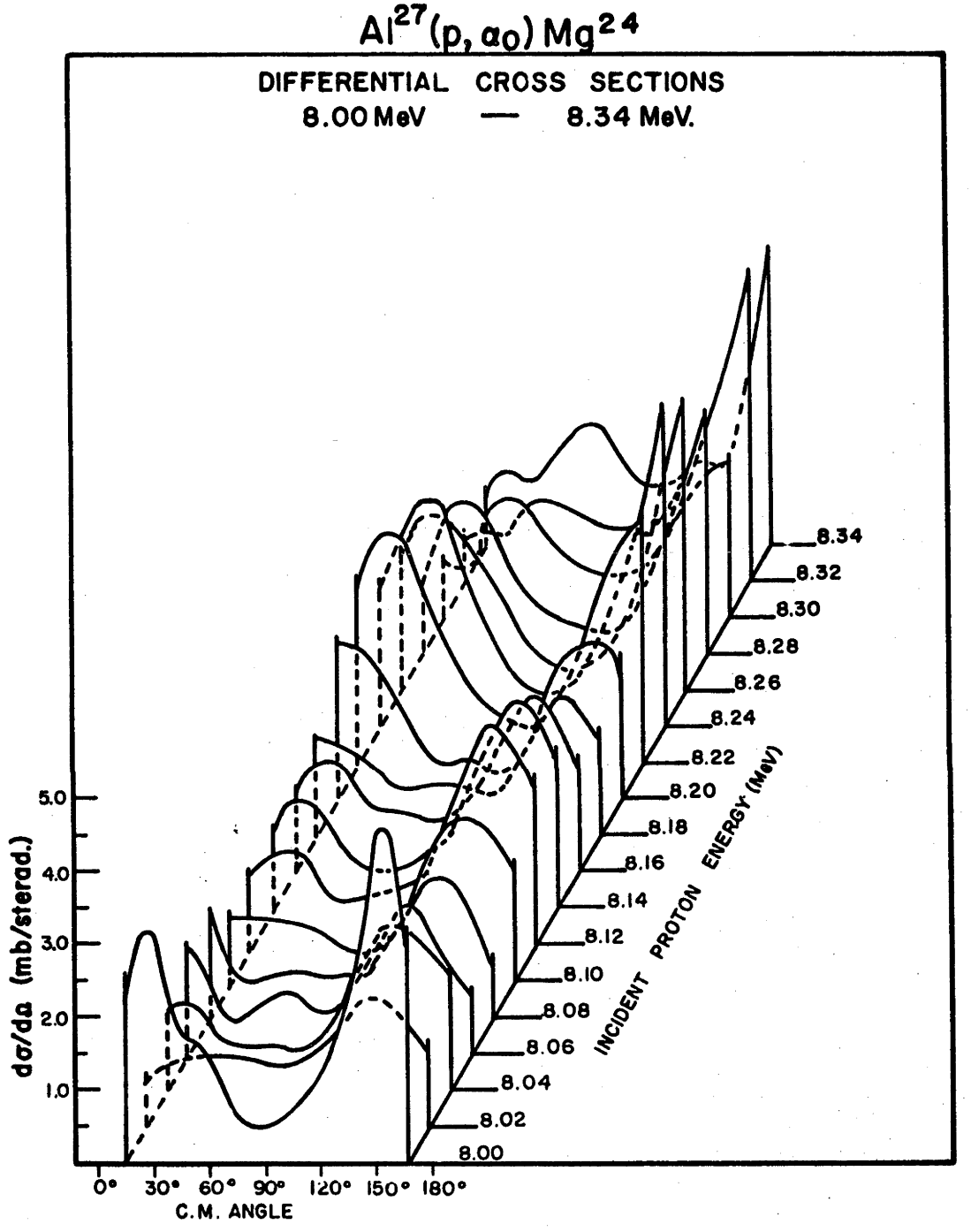
$Al^{27}(p, \alpha_0) Mg^{24}$
DIFFERENTIAL CROSS SECTIONS
8.00 MeV — 8.34 MeV.
dσ/dΩ (mb/sterad.)
5.0
4.0
3.0
2.0
1.0
0° 30° 60° 90° 120° 150° 180°
C.M. ANGLE
INCIDENT PROTON ENERGY (MeV)
8.34
8.32
8.30
8.28
8.26
8.24
8.22
8.20
8.18
8.16
8.14
8.12
8.10
8.08
8.06
8.04
8.02
8.00

Fig. 3.22 Angular distributions from E_p = 8.00 to 8.34 Mev for the $Al^{27}(p,\alpha)Mg^{24}$ first excited state reaction.

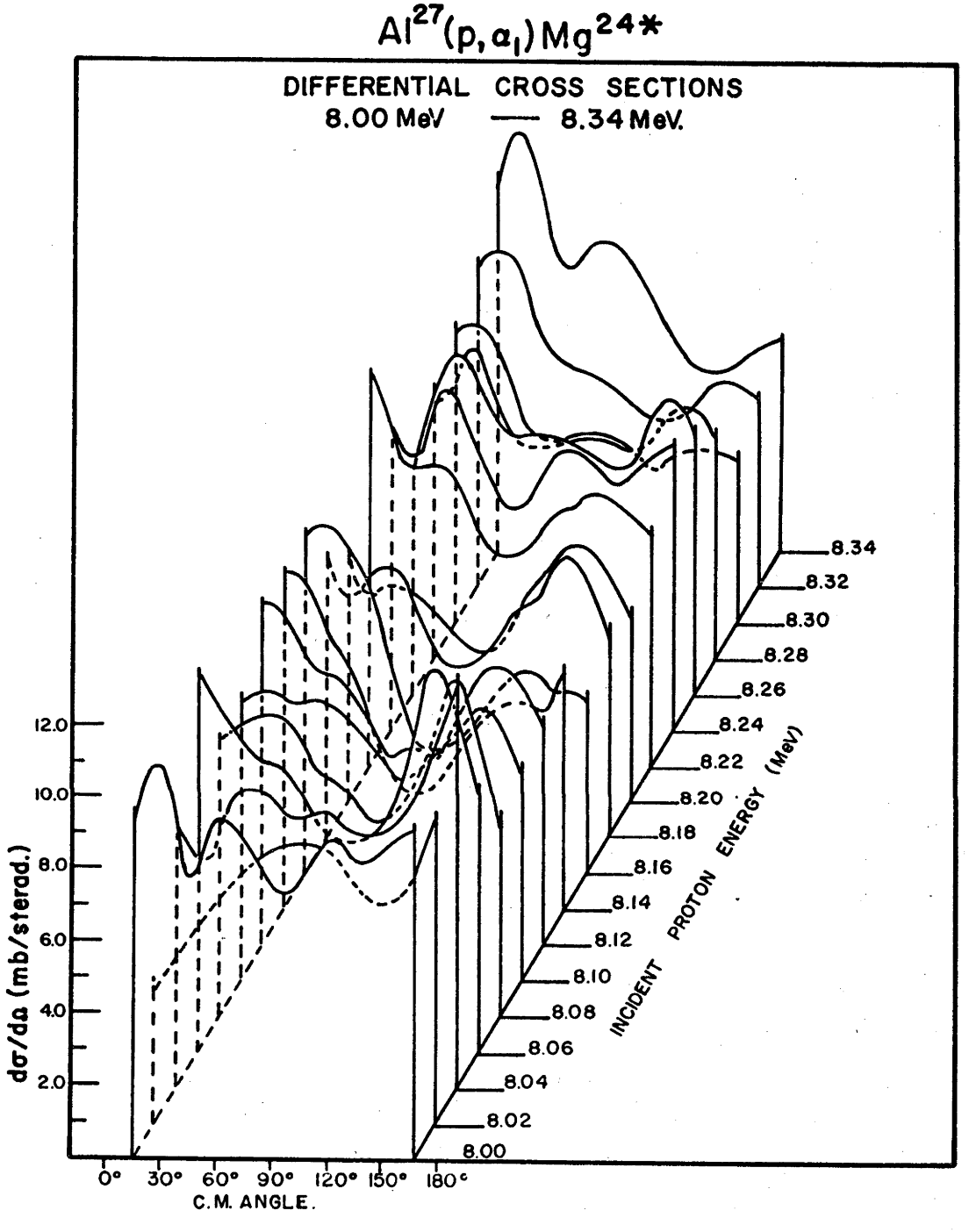
$Al^{27}(p,\alpha_1)Mg^{24*}$
DIFFERENTIAL CROSS SECTIONS
8.00 MeV — 8.34 MeV.
8.34
8.32
8.30
8.28
8.26
8.24
8.22
8.20
8.18
8.16
8.14
8.12
8.10
8.08
8.06
8.04
8.02
8.00
INCIDENT PROTON ENERGY (MeV)
12.0
10.0
8.0
6.0
4.0
2.0
dσ/dΩ (mb/sterad.)
0° 30° 60° 90° 120° 150° 180°
C.M. ANGLE.

Fig. 3.23 Angular distributions from E_p = 8.00 to 8.34 Mev for the $Al^{27}(p,\alpha)Mg^{24}$ second excited state reaction.

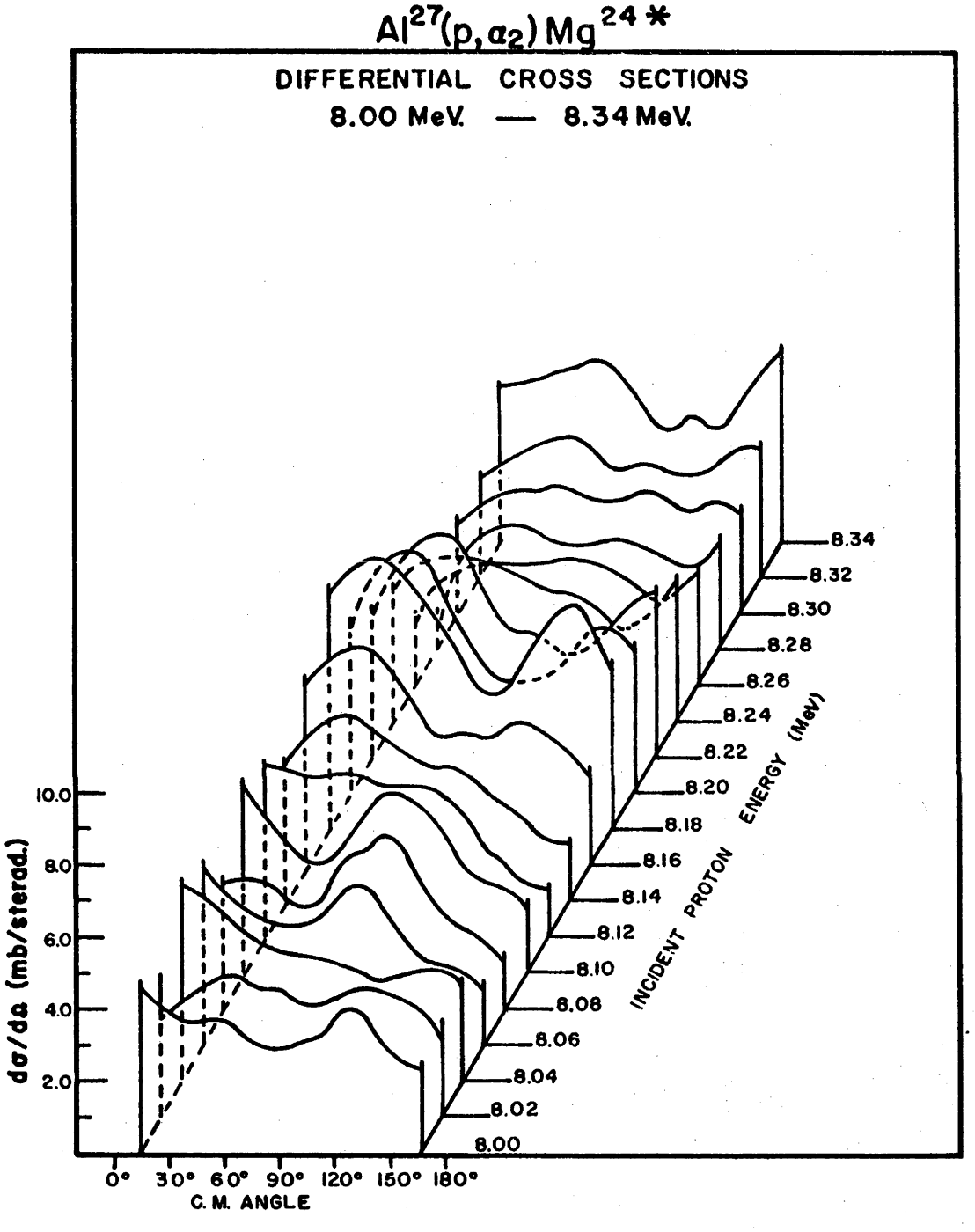
$Al^{27}(p,\alpha_2)Mg^{24*}$
DIFFERENTIAL CROSS SECTIONS
8.00 MeV. — 8.34 MeV.
dσ/dΩ (mb/sterad.)
10.0
8.0
6.0
4.0
2.0
0° 30° 60° 90° 120° 150° 180°
C. M. ANGLE
INCIDENT PROTON ENERGY (MeV)
8.34
8.32
8.30
8.28
8.26
8.24
8.22
8.20
8.18
8.16
8.14
8.12
8.10
8.08
8.06
8.04
8.02
8.00

Fig. 3.24 Angular distributions from E_p = 8.0 to 8.34 Mev for the $Al^{27}(p,\alpha)Mg^{24}$ third excited state reaction.

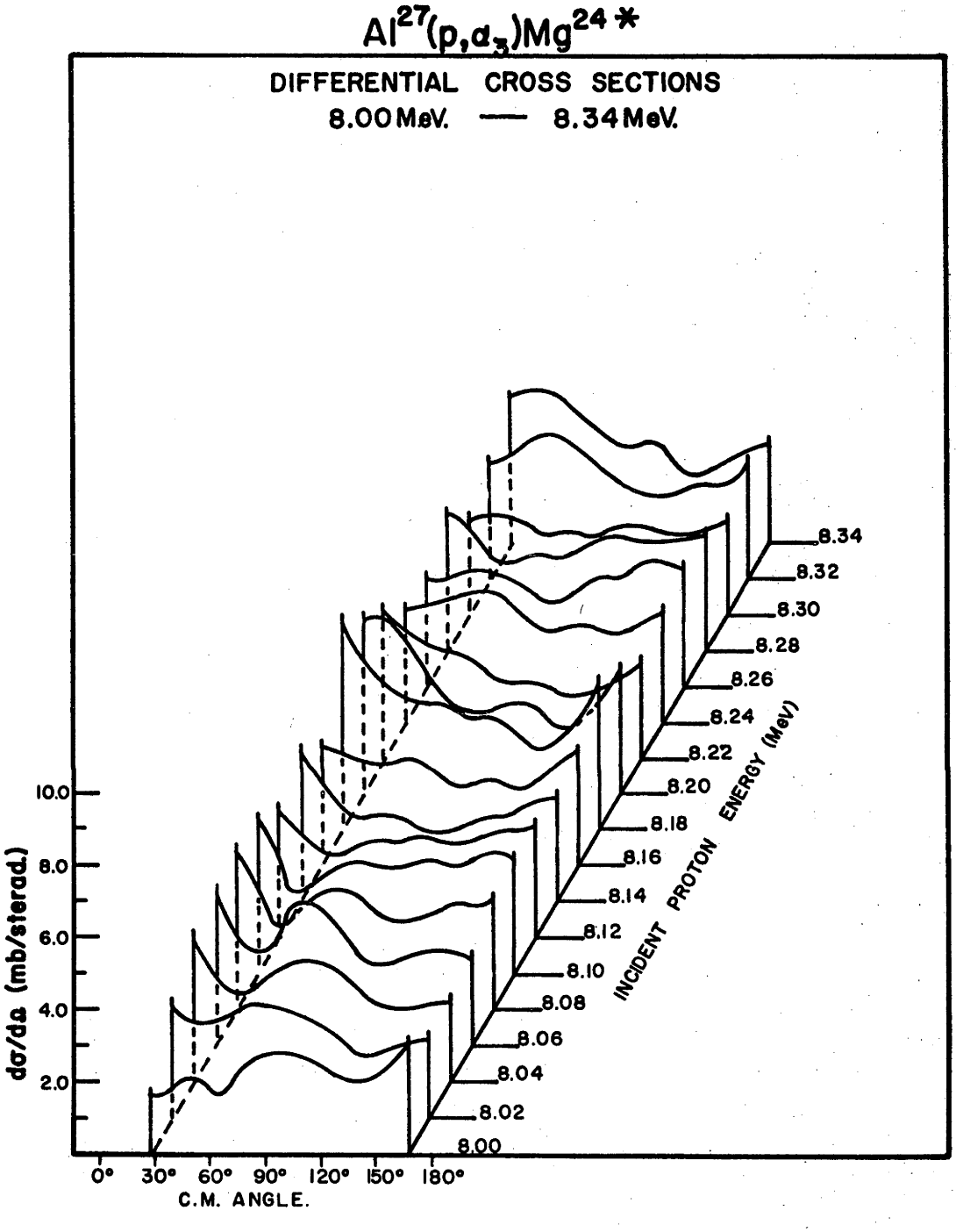
$Al^{27}(p,\alpha_3)Mg^{24}*$
DIFFERENTIAL CROSS SECTIONS
8.00 MeV. — 8.34 MeV.
dσ/dΩ (mb/sterad.)
10.0
8.0
6.0
4.0
2.0
0°
30°
60°
90°
120°
150°
180°
C.M. ANGLE.
INCIDENT PROTON ENERGY (MeV)
8.34
8.32
8.30
8.28
8.26
8.24
8.22
8.20
8.18
8.16
8.14
8.12
8.10
8.08
8.06
8.04
8.02
8.00

(Ya61, Og60) have measured angular distributions and excitation functions for α_0 and α_1 in the range E_p = 10.0 - 14.5 Mev. Both sets of excitation functions show strong energy dependence. Attempts are made by both groups to fit some of the angular distributions with simple interaction mechanisms.

Before 1962 extensive precision work had been reported only by Shoemaker et al.(Sh 51), who measured the α_0 and α_1 excitation functions at 164°, in the range E_p = 0.6 - 4.0 Mev. More recently Warsh et al. (Wa 63) have measured the 90° α_0 and α_1 differential excitation functions from E_p = 3.0 - 12.0 Mev, in 50 kev steps with Tandem energy resolution (<10 kev). They also report angular distributions taken at energies in the range 10.0 - 12.0 Mev for α_0 and α_1.

The following sections discuss the data presented in Section 3 in a general way. A quantitative analysis, based on recent developments in statistical model theory is given in Chapter VI.

4.2. Coarse Excitation Functions and Angular Distribution Survey.

The 100 kev step size excitation functions of Fig. 3.6 all show strong energy dependence. The relative

magnitude of the fluctuations or deviations from average yield appears greatest in the α_0 and α_6 excitation functions. Spins of the corresponding Mg^{24} levels are both 0. For groups α_0, α_1, and α_{2+3}, the fluctuations appear to be damped at higher energy; this is not the case for groups α_4, α_5, and α_6. The sharp increase in yields of the α_{2+3}, α_4, α_5 and α_6 groups at E_p = 6.3, 7.6, 8.3 and 9.2 Mev, respectively is presumably due to Coulomb barrier effects. Since all excitation functions show sharp changes from point-to-point, it is clear that 100 kev is too large a step size to reveal the detailed structure.

A glance at the angular distribution survey of Fig. 3.7 indicates that there is little connection between contiguous distributions for any alpha group. Some show strong forward peaking; others are backward peaked; and a number show near symmetry about 90°. Although none approach isotropy many contain large isotropic components. The main conclusion to be drawn from this survey is that the angular distribution of all alpha groups is sharply energy dependent (at least over 1 Mev intervals).

4.3. Detailed Excitation Functions at 90° and 135°.

The 25 kev step-size excitation functions of Figs. 3.9 - 3.13 all show considerably more detailed structure

than those measured in 100 kev steps. The overall agreement of the 90^{o} α_0 and α_1 data with the work of Warsh et al. (Wa 63) is good. Prominent and broad maxima correspond closely; however, since their energy increment size is twice the value used in the present work, considerably less detailed structure is shown.

The apparent energy dependence of the yields for all alpha groups is very sharp and extremely complicated consisting of a set of broad maxima upon which narrower "resonances" are superimposed. Widths of the broad maxima are of order 100 - 200 kev. There are many one-point, narrow maxima and minima, indicating the probable existence of large yield changes within energy intervals less than 25 kev. A simple count of the number of minima per Mev of excitation gives a figure of 12 ± 2 independent of energy and alpha group. This implies an average width between yield minima of 85 ± 15 kev, which must be treated as an upper limit due to the minima missed by taking too large a step size.

Comparisons between excitation functions for different groups (same angle) and between functions for different angles (same group) reveal little obvious correlation in yield variation. It is clear from Figs. 3.9 and 3.10 that

the relative amplitude of yield fluctuations from the average is considerably greater for the α_0 excitation function than for the α_1 function. However, similar comparisons for higher groups are not obvious. A quantitative examination of the above aspects is presented in Chapter VI, and further discussion is not given here.

To determine the general trend of the excitation functions, the yields were averaged over 0.5 Mev intervals. Results for all groups are indicated in Fig. 3.25. This plot reveals that the average α_0 group 90° yield is $\sim$20% - 30% less than the 135° yield between 6.0 and 8.5 Mev (E_p), and that at higher energy the two are in close agreement. Similar behaviour is noted for the α_1 group averaged yields. For groups α_2, α_3, α_4 and α_5 the averaged 90° data is generally 20% - 30% less than the averaged 135° data. The lack of comparable information at a forward angle naturally places severe restrictions on the interpretation of these results. In general however, they offer little evidence for any overall strong backward or forward peaking.

4.4. Closely-spaced Angular Distribution Sets.

The sets of closely-spaced angular distributions of Figs. 3.14 and 3.15 were measured at energies corresponding to prominent maxima in the 90° α_0 excitation function, in

Fig. 3.25 $Al^{27}(p,\alpha)Mg^{24}$ $d\sigma/d\Omega$ $(90^\circ, 135^\circ)$ excitation functions averaged over 500 kev intervals.

The average value of $d\sigma/d\Omega$ $(90^\circ, 135^\circ)$ is plotted at the midpoint of each averaging interval; straight line segments have been drawn simply as connecting links. The 90° averages are plotted as open circles, and the 135° averages as closed circles. For convenience of presentation, some of the averaged excitation functions have been multiplied by scale factors, as shown.

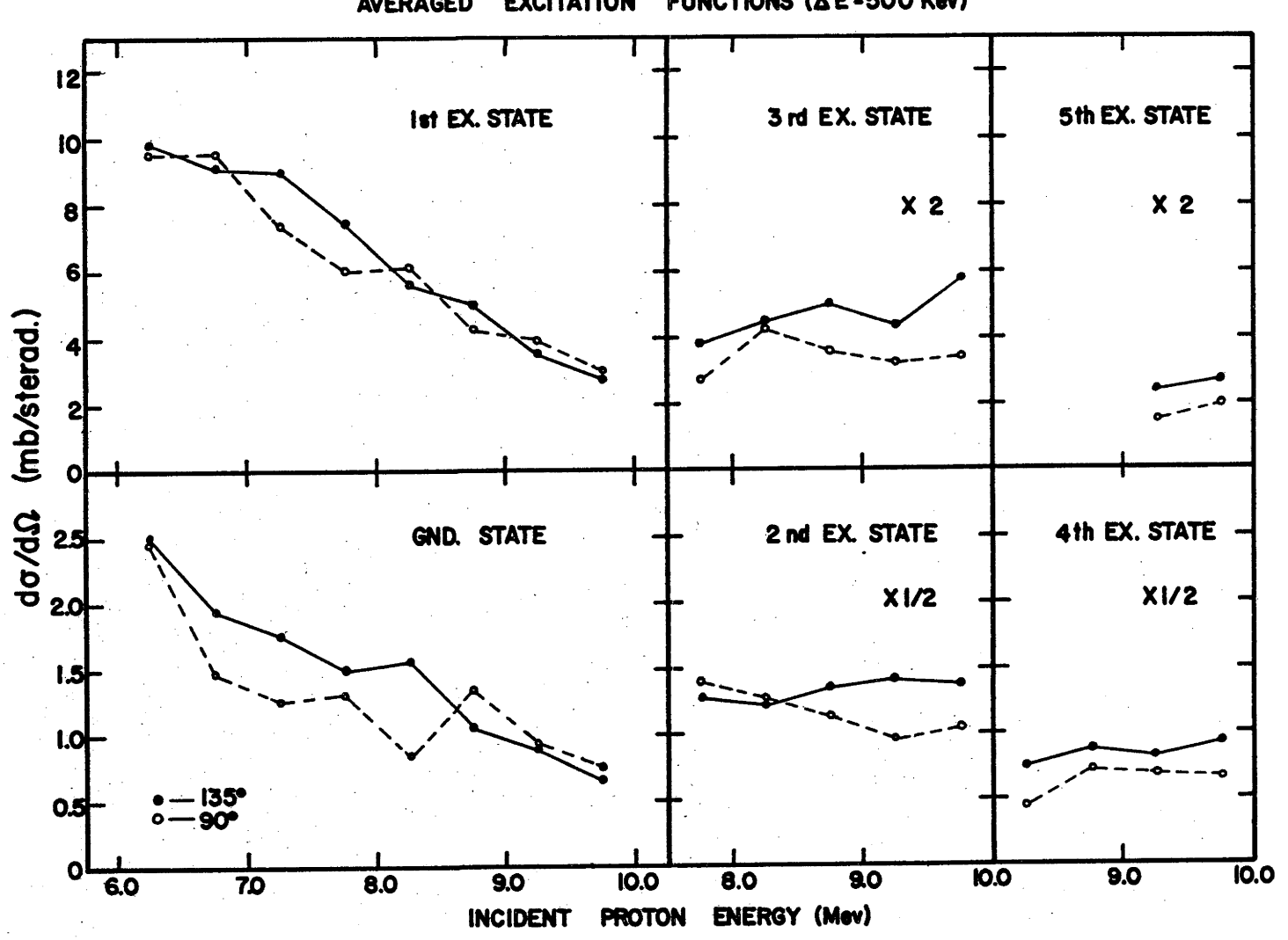
AVERAGED EXCITATION FUNCTIONS (ΔE=500 Kev)
1st EX. STATE
3rd EX. STATE
X 2
5th EX. STATE
X 2
GND. STATE
2nd EX. STATE
X1/2
4th EX. STATE
X1/2
dσ/dΩ (mb/sterad.)
135°
90°
INCIDENT PROTON ENERGY (Mev)

order to obtain information on the nature of the yield variations.

An inspection of the curves obtained near E_p = 8.725 Mev indicates considerable shape variation even between energetically contiguous angular distributions, and very marked differences between distributions separated by 40 - 50 kev in proton energy. While the relative shape is strongly energy dependent, certain features of the distributions appear to vary less rapidly. The α_0 set, for example, show persistent strong forward peaking and a maximum near 90° which moves forward as E_p is increased, while the α_1 set show persistent backward peaking and a forward-moving maximum near 60°. The α_4 set show general backward peaking.

The character of the angular distribution set taken near E_p = 6.0 Mev is similar. Relative shapes vary significantly over 12.5 kev energy intervals, but prominent features remain. The α_0 set shows a persistent peak between 95° and 120°, and a sharp fall-off at backward angles. The α_1 set displays strong forward peaking coupled with a fall-off at backward angles.

The set of angular distributions at E_p = 3.65 Mev were measured to establish a connection with the work of

Shoemaker et al. (Sh51), at similar energy, who report evidence for closely spaced single level resonances, showing interference effects in the $Al^{27}(p,\gamma)Si^{27}$ and $Al^{27}(p,\alpha)Mg^{24}$ differential excitation functions. The relative shapes of the angular distributions at E_p = 3.65 Mev appear to vary less rapidly with energy than those taken at higher proton energies. The presence of large odd order components in some of them, indicated by the strong asymmettry about 90°, lends support to the hypothesis that the reaction $Al^{27}(p,\alpha)Mg^{24}$ proceeds through a compound nucleus mechanism in this region of excitation, involving interference between neighbouring levels.

4.5. Fine Structure Excitation Function.

The 2 kev step-size excitation functions of Figs. 3.16 and 3.17 were measured to determine the minimum excitation energy increment for which strong yield variations in $Al^{27}(p,\alpha)Mg^{24}$ occur. The regions investigated (3.65 Mev and 6.00 Mev) were chosen to coincide with points of previous interest. In particular the 3.65 Mev region was known from the work of Shoemaker et al. (Sh 51) to contain narrow resonances (~5kev FWHM) and was expected to provide a check on the experimental energy precision and a measure of the significance of small yield variations at higher energy (6.00 Mev).

An examination of the 3.65 Mev data (Fig. 3.16) reveals a broad peak ($\sim$ 50 kev FWHM) in the α_0 yield and 3 narrow peaks in the α_1 yield at E_p = 3.601, 3.630 and 3.665 Mev, having FWHM widths of 5, 7 and 8 Mev respectively. This data is in good agreement with that of Shoemaker et al. (Sh51). If these peaks are assumed to correspond to single levels in the compound nucleus Si^{28}, then a crude upper limit to the average level spacing at this excitation (15.23 Mev in Si^{28}) of $\sim$30 kev can be assigned. At the much higher excitations corresponding to proton energies between 6.00 and 10.00 Mev, it is expected that the average compound nucleus level spacing is considerably reduced.

The 3.65 Mev data establishes the fact that apparent yield variations as narrow as 5 kev can be considered to be "real". The 2 kev step-size excitation functions near 6.00 Mev (Fig. 3.17) show that while major yield fluctuations are spaced at 40 - 60 kev intervals, significant variations can occur in intervals of 10-15 kev width. It is possible that small variations occur at even narrower intervals, but no evidence for this can be observed within the statistical uncertainty of the yield points.

4.6. Angular Distributions from E_p = 8.0 - 8.34 Mev.

The 8.0 - 8.34 Mev topographical "maps" of the

reactions $Al^{27}(p,\alpha)Mg^{24}$ given in Figs. 3.21 - 3.24 were measured in order to provide detailed information on the variation of angular distributions over a large range of excitation energy and on the variation with angle of the differential excitation functions over this range.

An inspection of the plots for all alpha groups indicates that, in general, neighbouring distributions (20 kev separation) show significant differences, and that distributions separated by 40 - 60 kev have little in common. This is particularly so for α_1 and α_2 plots, although less true for the α_0 plot, in which a 90° minimum characterizes several distributions near E_p = 8.24 Mev.

The relative deviation from isotropy appears considerably larger for the α_0 distributions than for the α_1, and to a lesser extent, for the α_2 and α_3 distributions. Although differential excitation functions are not explicitly plotted, it is clear from the isometric maps for all alpha groups, that their detailed shape is a strong function of angle. Quantitative analysis of the above points is given in Chapter VI.

4.7. Averaged Angular Distributions 8.00 - 8.34 Mev.

In order to determine the overall angular distribution of groups α_0 and α_3 in the energy range E_p = 8.0 - 8.34 Mev, the above sets of distributions were averaged, and the results are indicated in Fig. 3.26. The α_0 and α_1 averages both show minima at 90°, while the α_2 and α_3 averages are forward peaked. The irregularity of the latter indicates that the averageing interval may not be sufficiently wide to remove local energy dependence. This could also account for the deviation from forward-backward symmetry, which is noted in all the averaged distributions.

4.8. Partial Cross Sections.

Partial (integrated) cross sections were extracted from the above angular distribution sets and the corresponding excitation functions for groups $\alpha_0 - \alpha_3$ are given in Fig. 3.27. The plotted quantities are just $4\pi \times A_0$ (coefficient of the zeroth order Legendre Polynomial) and have been checked by simple numerical integration (via Simpson's Rule) of the distributions. It is seen that general agreement between the two procedures is good.

It is clear that the integrated cross sections for all alpha groups show strong energy dependence similar to that of the differential excitation functions. The average

Fig. 3.26 $Al^{27}(p,\alpha)Mg^{24}$ angular distributions averaged over the proton energy range 8.00 - 8.34 Mev.

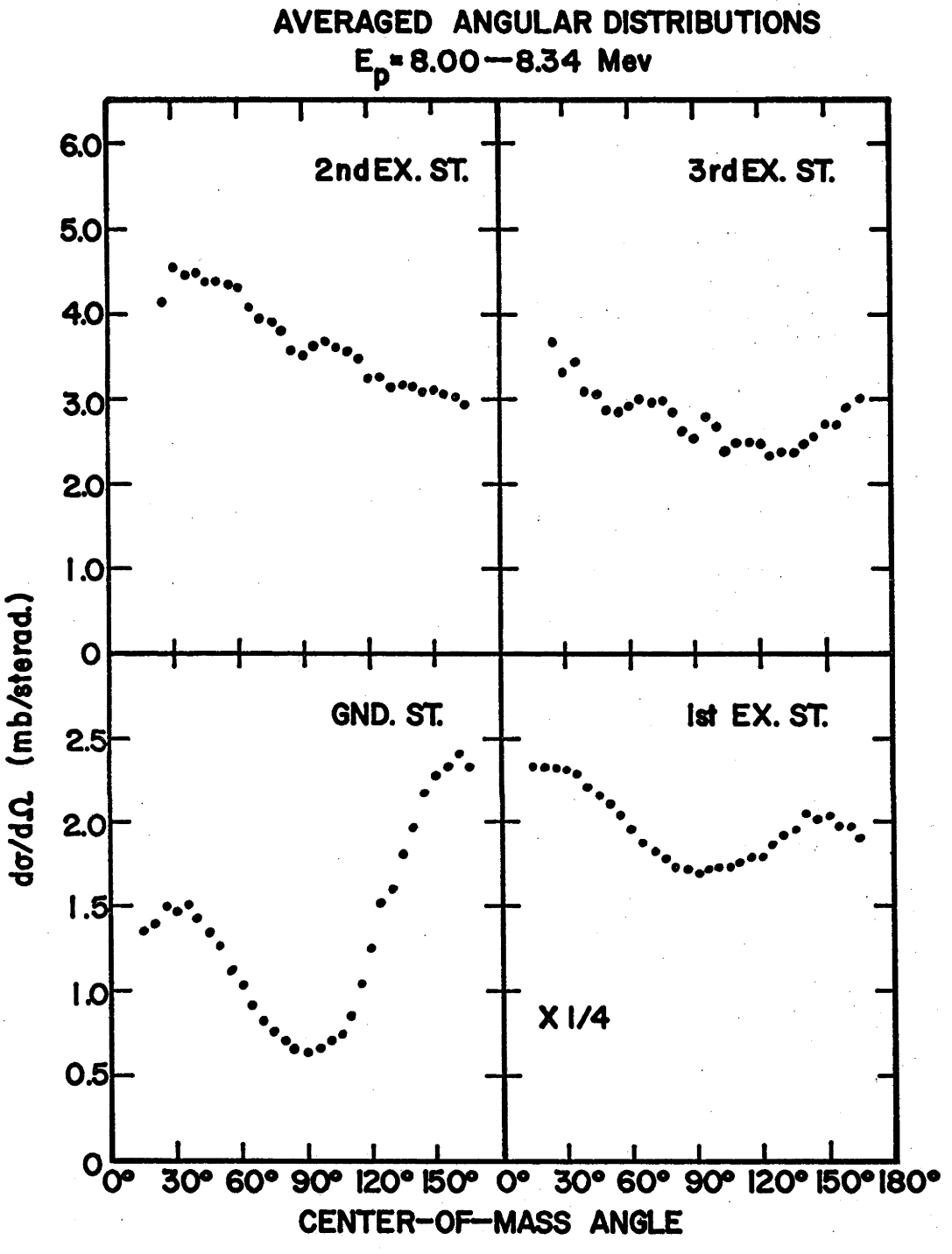
AVERAGED ANGULAR DISTRIBUTIONS
E_p = 8.00—8.34 Mev
2nd EX. ST.
3rd EX. ST.
GND. ST.
1st EX. ST.
X 1/4
dσ/dΩ (mb/sterad.)
CENTER-OF-MASS ANGLE
0
1.0
2.0
3.0
4.0
5.0
6.0
0.5
1.5
2.5
0° 30° 60° 90° 120° 150° 0° 30° 60° 90° 120° 150° 180°

Fig. 3.27 $Al^{27}(p,\alpha)Mg^{24}$ integrated cross section excitation functions, E_p = 8.00 - 8.34 Mev, for the ground state, first, second, and third excited state reactions.

Heavy circular points represent values obtained from Legendre-Polynomial expansion fits to the relevant $W(\theta)$ and crosses indicate values obtained by simple numerical integration of the $W(\theta)$.

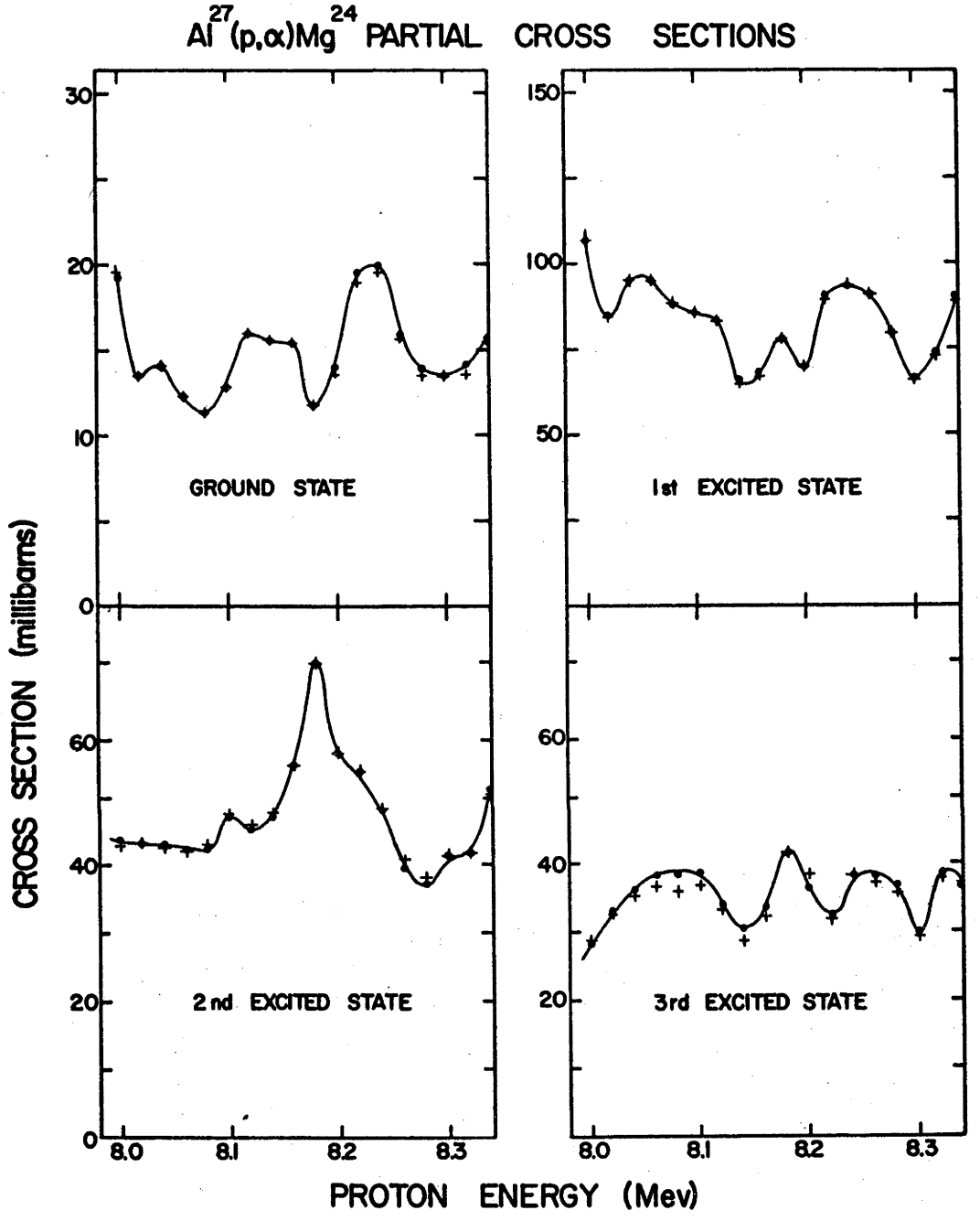
$Al^{27}(p,\alpha)Mg^{24}$ PARTIAL CROSS SECTIONS
GROUND STATE
1st EXCITED STATE
2nd EXCITED STATE
3rd EXCITED STATE
CROSS SECTION (millibams)
PROTON ENERGY (Mev)
30
20
10
0
150
100
50
60
40
20
8.0
8.1
8.2
8.3

interval between minima is 60 - 70 kev, which is slightly less than the figure obtained from the differential excitation functions. The integrated cross sections for different alpha groups appear uncorrelated in yield variation with energy, and the relative amplitudes of yield variation appear similar for all groups. These points are treated quantitatively in Chapter VI.

Excitation functions for the first five Legendre Polynomial coefficients (obtained from the least squares fit of section 3.5) for alpha groups α_0 and α_3 are plotted in Fig. 3.28. The residual and statistical errors are small for A_0, A_1 and A_2 ($< 5\%$) but for A_3 and A_4 can be as large as 30%. It is seen that all the coefficients A_i fluctuate in a manner similar to the differential excitation functions and integrated cross section excitation functions. Again, a quantitative analysis is given in Chapter VI.

4.9. Conclusions.

Within the region of excitation in Si^{28} covered in the present study (17.6 Mev to 21.6 Mev) it seems likely that the compound nucleus (if formed) can be described by the relation $\Gamma >> D$, where Γ and D are the average level width and spacing, respectively. Section 4.5 provides strong evidence for an average level spacing of less than 30 kev at 15.2 Mev excitation in Si^{28}; since the level density is a

Fig. 3.28 Excitation functions of the Legendre-Polynomial Coefficients $A_o - A_4$ obtained from least squares fits to the $Al^{27}(p,\alpha)Mg^{24}$ $W(\theta)$ of Figs. 3.21-3.24.

The coefficient excitation functions are plotted horizontally as a function of alpha group number and vertically as a function of Polynomial order. A few plots have been multiplied by scale factors, as indicated, for convenience of representation.

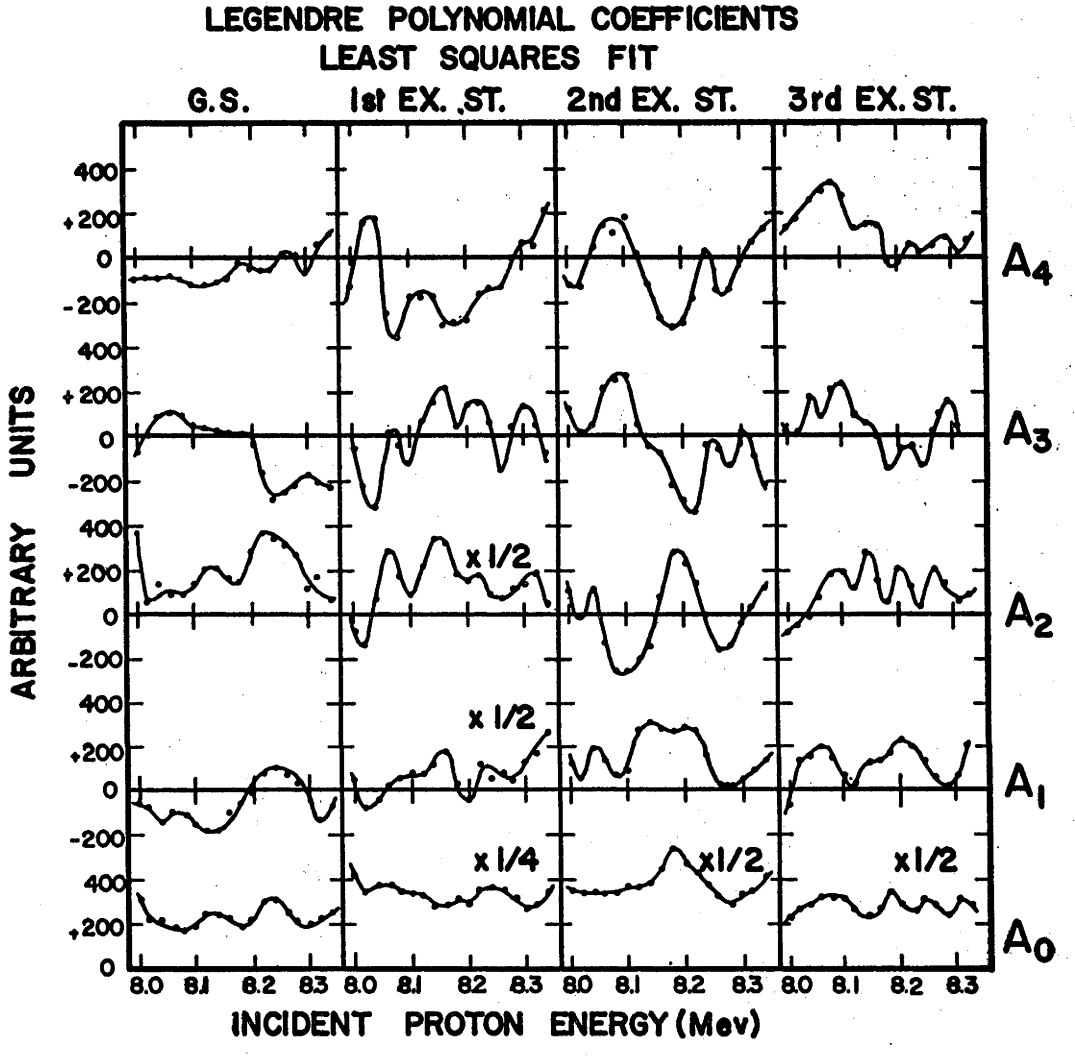
LEGENDRE POLYNOMIAL COEFFICIENTS
LEAST SQUARES FIT
G.S.
1st EX. ST.
2nd EX. ST.
3rd EX. ST.
ARBITRARY UNITS
400
+200
0
-200
A4
A3
A2
A1
A0
x 1/2
x 1/4
8.0
8.1
8.2
8.3
INCIDENT PROTON ENERGY (Mev)

rapidly increasing function of excitation, it is expected that the average level spacing at the Si^{28} energies of 17.6 to 21.6 Mev is considerably smaller - probably of order 1 kev. Excitation function yield variations reported in the previous sections show widths of 15 - 70 kev. It seems highly improbable, therefore, that the strong energy dependence can be attributed to single compound nucleus levels or even to interference between two or three levels. Rather, it would appear that many levels are excited at any given energy in Si^{28} (even for infinitely narrow experimental resolution) and contribute to the reaction yield.

As noted earlier, (section 4.1) a number of attempts have been made to analyze the $Al^{27}(p,\alpha)Mg^{24}$ reaction in terms of direct interaction mechanisms, such as triton pickup and heavy particle stripping. Reasonable fits can be obtained for isolated angular distributions, but cannot account for contiguous distributions separated by as little as 20 kev excitation energy. Moreover, direct interaction mechanisms cannot explain the very strong energy dependence exhibited in the present study by excitation functions and closely spaced angular distributions. It is suggested that forward or backward peaking of angular distributions (frequently taken as indicative of direct interaction) can be satisfactorily

accounted for by interference between several compound nucleus levels.

It is presumed that some fraction of the $Al^{27}(p,\alpha)Mg^{24}$ reaction cross section proceeds via direct or semi-direct processes. However, the results of the previous sections offer little support for supposing the fraction to be large. Direct effects would be expected to be revealed in particular by departures from backward-forward symmetry in the averaged angular distributions of section 4.7. While these certainly appear, it is difficult to see what sort of direct process could satisfactorily account for a backward peaked α_0 average distribution, and forward peaked α_1, α_2 and α_3 average distributions.

In general, it would appear that the $Al^{27}(p,\alpha)Mg^{24}$ reaction in the region E_p = 6.0 - 10.0 Mev proceeds dominantly by a compound nucleus mechanism. Chapter VI gives a quantitative analysis of the present results, which is based on this conclusion.

The results of Section 3.1 of this Chapter, on the energy level of Mg^{24}, have been published (Qu62). A paper containing the results of sections 3.2 - 3.5 is presently in preparation.

CHAPTER IV

THE REACTION $C^{12}(O^{16}, \alpha)Mg^{24}$
EXPERIMENTAL PROCEDURES

CHAPTER IV

Section 1. INTRODUCTION.

The material of this chapter consists chiefly of a description of the experimental apparatus and procedures used in a study of the reaction $C^{12}(O^{16},\alpha)Mg^{24}$, which was carried out with the A.N.U. Tandem Van de Graaff accelerator and associated facilities during the period September, 1962 - September, 1963. The experimental work was divided chronologically into three parts: (a) a brief examination of the reaction at high O^{16} bombarding energy (32 Mev), conducted as a corollary to Chalk River studies (Br60) at similar energies in the O^{16}-C^{12} system; (b) a differential-cross-section survey of the reaction from 15.0 Mev to 29.5 Mev, O^{16} energy; and (c) a detailed study of the reaction in the O^{16} energy range 15.0 - 22.5 Mev. The preliminary work (a) was performed with the equipment described in Chapter III. Since this was unsuited to heavy ion studies, the work (b) and (c) was postponed until the completion of improved equipment (4 months interim).

The basic apparatus common to (b) and (c) is described in section 2. Equipment and procedures concerning

(b) only are described in section 3, along with results. Equipment and procedure germane to (c) are discussed in section 4; the handling and analysis (semi-automated) methods applied to the very large body of data obtained in this detailed study constitute topics in their own right, and are treated in Chapter V. The high energy work (a) is considered an extension of (c), and relevant experimental details are included at the end of section 4.

Section 2. BASIC APPARATUS AND PROCEDURE.

2.1. The 20" Scattering Chamber.

A vertical section through the scattering chamber* used in the $C^{12}(O^{16}, \alpha)Mg^{24}$ reaction survey and detailed study is shown in Fig. 4.1. The chamber body was a 20" diam., Aluminium cylinder; wall thickness was $1\frac{1}{2}$". Top and bottom lids (also Aluminium) were rotatable with the chamber evacuated, low-friction bearing surfaces being provided by Teflon runners, and the drive being supplied via sprocket-and-chain from a worm-reduction gearbox (not shown). The top lid was demountable to permit easy access

*The scattering chamber was designed by Dr. G.G. Ohlsen of this laboratory, and assembled and tested by Dr. G. G. Ohlsen in collaboration with the writer and Mr. P. G. Young.

Fig. 4.1 Vertical section through 20" scattering chamber.

Numbered points are :

1. Beam collimating assembly
2. Target strip
3. Top lid detector (monitor) assembly. Vertical section.
4. Electron suppressor. Biassed permanent magnet.
5. Ta backed Faraday cup
6. Rotating seal molded O-ring, 20.5" diam.
7. Teflon bearing runners
8. Sprocket
9. Friction clamp for fixing center-boss
10. Target angular indicator
11. Centre-boss flange
12. Detector radial track
13. Typical array detector (section 4.2) in vertical section
14. Detector array mounting plate.

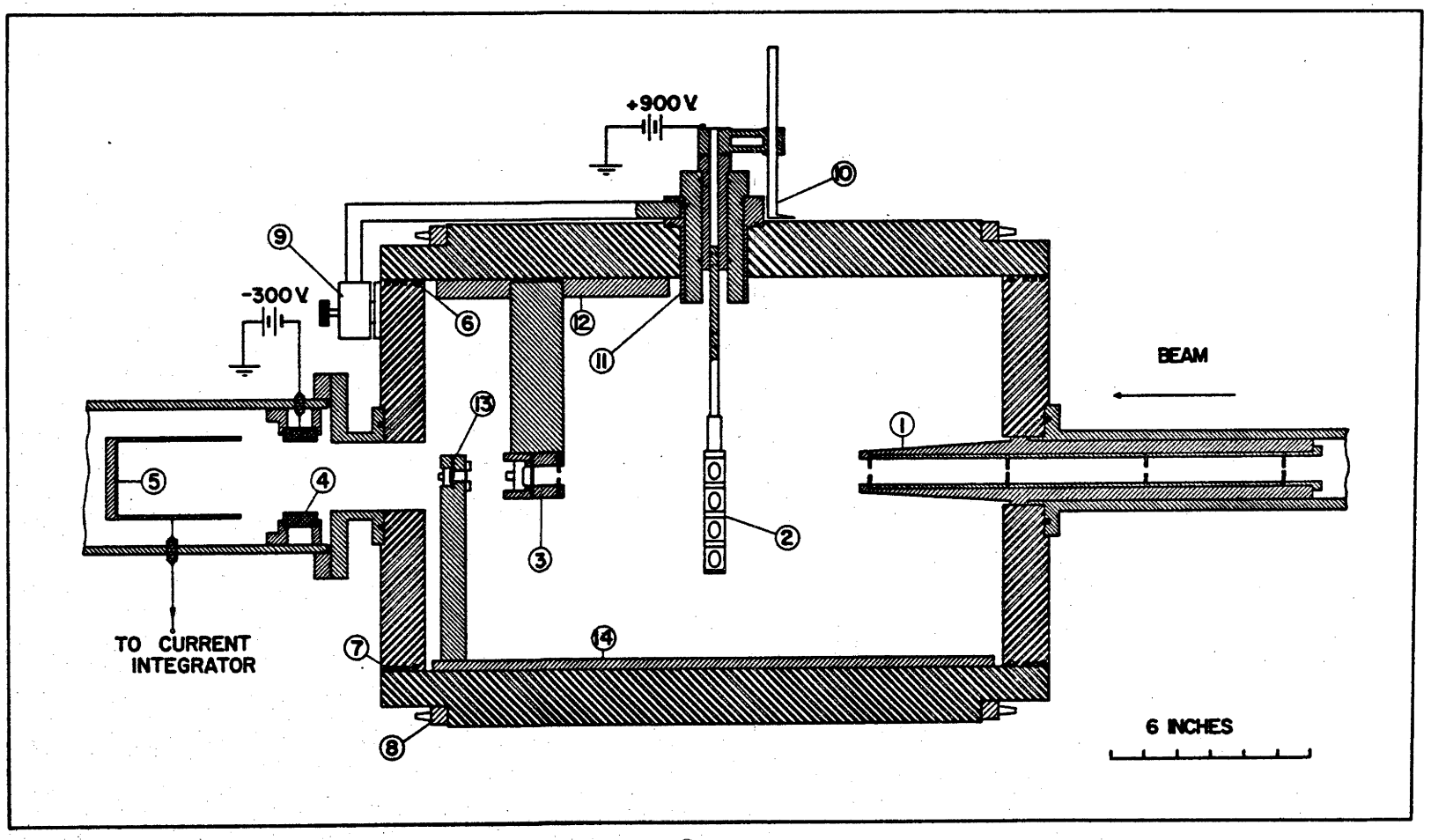
+900 V
-300 V
BEAM
TO CURRENT INTEGRATOR
6 INCHES
1
2
3
4
5
6
7
8
9
10
11
12
13
14

to the chamber interior; due to its weight (40lb) an overhead hoist and grappling cables were employed for this procedure. Lid edges were held parallel with the chamber rim by Teflon bearing blocks fixed to the outer wall (not shown); these were loosened to permit easy lid remounting. To prevent the center-boss (containing target holder and insulating sheath) from rotating with the lid, its flange was rigidly clamped to the chamber wall via a steel bar holding a friction block.

Scattering chamber support was provided by an adjustable heavy steel mounting bracket bolted to the beam-line trestle. Alignment procedures were identical with those used for the 9" chamber of Chapter III. Perspex viewing ports (covered with Al caps when detectors were in operation) were set at 30° intervals around one side of the chamber.

2.2. Target Holder.

The target holder was similar in construction to that of Chapter III, section 2.5. It was insulated from the chamber top lid by a 1" diam., Teflon sheath and held a vernier indicator reading on an angular scale inscribed on the top lid surface. The target holder could be set at

any angle, with $\pm$ 1° accuracy, and its alignment with the optical chamber-centerline was checked (using cross-hairs on the top target frame position) at several lid positions.

2.3. Targets.

Targets used in this work were thin self-supporting Carbon foils, similar to those used as backings in section 2.6, Chapter III. Target thicknesses were 10-25 μg, the measurements being made by the α-particle energy-degradation method discussed in section 3.1(b) of Chapter III. During long continuous bombardment with O^{16} beams of order 1 μA the Carbon foils were generally removed and replaced by fresh targets at 15-20 hour intervals, for the following reasons:

(a) The Carbon buildup rate due to the cracking of residual organic vapour on the target face was very rapid (as much as 4% thickness increase/hour), so that in 15-20 hours the initial target thickness could be increased by $>$ 50%, and the O^{16} beam energy-resolution appreciably broadened; since the energy spread due to the initial target thickness was of order 100 kev, further large increases were

undesirable. Although the Carbon buildup rate could have been reduced by a target shield held at liquid air temperature, this would have proved inconvenient for the target-detector geometry employed in much of the following work and it was simpler to account for Carbon buildup and differences in target thickness at change-points by the monitoring procedure described in section 4.7.

(b) After 15-20 hours of bombardment targets were always badly battered and frequently completely destroyed. This appeared to be partly a result of thermally-induced stresses (caused presumably by large O^{16} beam energy losses in the foil, coupled with poor thermal conductivity) which produced rips and tears in the vicinity of the beam impact area.

The Carbon foils behaved effectively as electron strippers when traversed by the O^{16} beam ions, and gave rise to the emission of intense fluxes of low energy electrons. This was first noted as an apparent x5 increase in the mean noise level (measured visually by cathode-ray-oscilloscope) of the observing surface-barrier detectors

when the O^{16} beam was passed through the target; the electron flux intensity appeared roughly independent of angle. It was found that a bias of +900v applied to the target strip was sufficient to provide nearly complete suppression.

The remarks on target thickness variation apply here as in Chapter III, section 2.6. The problem is more severe, in fact, due to the considerable wrinkling caused by the intense beam heating. This was of no account, in the detailed study of section 4, which relied on continuous monitoring of the effective foil thickness.

As in Chapter III, the targets contained a small but appreciable level of impurities, presumably introduced by the manufacturing procedure. The principal impurities were Hydrogen and Oxygen, but heavier elements were also present (sections 3.5 and 4.7).

2.4. The O^{16} Beams.

The $C^{12}(O^{16}, \alpha)Mg^{24}$ work was continuously hampered by difficulties encountered in accelerating the O^{16} ions. These are not detailed here. Beams of ions stripped at the Tandem terminal to both 4^+ and 5^+ charge states were used. The 4^+ beam intensity* was greater than that of the

*See bottom of following page.

5^+ within the terminal voltage range, so that 4^+ beams were preferentially employed up to an O^{16} energy of 23 Mev; the limit was imposed by severe accelerator instability due to high terminal potential (4.6 Mv) and/or excessive total (belt) charging current (350 μA). O^{16} energies higher than 23 Mev were achieved with the 5^+ beam, the effective limit being approximately 30 Mev. The maximum available analyzed beam intensity (traversing the target) varied sharply from one run to the next, and even during the course of a single continuous run. Under best machine conditions it was possible to obtain as much as 0.5 μA* of 4^+ beam and 0.2 μA of 5^+ beam, but average output was well below this level. The steady deterioration in overall accelerator performance with the O^{16} beams during the detailed measurements of section 4 forced premature curtailment of this work.

2.5. Beam Collimation.

Beam collimation at the scattering chamber entrance was provided by a demountable assembly (Fig. 4.1) containing a set of four .020" thick Ta discs. The first and third

*Beam intensity is measured in terms of "particle" current i.e. (I/N where N is the charge state, and not actual charge current).

discs (set 10" apart) contained 1/16" diam. beam defining holes, and each were backed up by discs containing 1/8" diam. anti-scatter holes. The assembly made a snug fit to the walls of the entrance tube which could be adjusted to permit precise collimator alignment, via the procedure of Chapter III. That part of the assembly extending into the scattering chamber was tapered to allow detectors to be rotated to backward angles near 180°. Experiment showed that the collimating assembly restricted beam spot size and spatial "wander" on the target face to $< 1/8"$.

2.6. Beam Collection and Integration.

Beam was collected in a Faraday cage (Fig. 4.1), around the entrance of which was set a combined electrostatic and magnetic electron suppressor consisting of a permanent (ring) magnet insulated and supported by Teflon brackets, and biased at -300 V. Current was measured and integrated by an Elcor current integrator (accurate to 1%), which was used to gate all detector output recording electronics.

2.7. Vacuum.

The scattering chamber was maintained at a pressure of 10^{-6} mm Hg by a 6" Hg-diffusion pump located 3.5' from

the entrance port. Since pumping speed through the collimating assembly was low, an additional pumping line was provided downstream from the chamber. Vacuum requirements in both scattering chamber and beam line were considerably more stringent for the O^{16} beams than for conventional beams (p, d, α, He^3) due to the much higher cross section for charge exchange between beam ions and residual gas molecules; these effects become appreciable for pressure between 10^{-5} and 10^{-4} mm Hg, and lead to errors in absolute beam current measurements.

Section 3. SURVEY OF THE REACTION $C^{12}(O^{16}, \alpha)Mg^{24}$, 15.0 - 29.5 Mev.

This section comprises a discussion of experimental procedures pertinent to and the results of a survey of the $C^{12}(O^{16}, \alpha)Mg^{24}$ reaction over the O^{16} energy range 15.0 - 29.5 Mev (lab.), in 0.5 Mev steps. The work was performed mainly as a mapping operation, preliminary to the detailed investigation described in section 4, with the object of obtaining a rough idea of the general features of the reaction and the variation of experimental conditions as a function of increasing O^{16} bombarding energy. The survey took the form of $d\sigma/d\Omega$ excitation functions, measured at 3 lab. angles (10°, 40°, 130°), for $C^{12}(O^{16}, \alpha)Mg^{24}$

reactions proceeding to several final states in Mg^{24}.

3.1. Detectors and Detector Mounts.

A single detector mount was suspended from the scattering chamber top lid (Fig.4.1) by a steel bracket which could be driven along a radial track by a worm gear operated from outside the chamber. Provision was made in the assembly, as shown, for two .020" thick steel plates containing collimating slits of various dimensions. This mount was equipped with a surface-barrier detector* of 200 mm^2 area, and 400Ω-cm resistivity.

Two other detector mounts+ (not shown in Fig.4.1) were bolted to the bottom lid. These were normally used for observation of reaction products from a gas target, but upon removal of their complicated defining-slit system were suitable for the present work. A 50 mm^2 area, 4,000Ω -cm resistivity surface-barrier detector was clamped in each of these mounts.

3.2. Detector Angular Settings.

Both top and bottom lid detector mounts were aligned along inscribed radial lines on the inner lid

*All detectors used in the $C^{12}(O^{16},\alpha)Mg^{24}$ work were supplied by Oak Ridge Technical Enterprises Corp.

+Supplied by G. G. Ohlsen of this laboratory.

surfaces. These matched precisely with inscribed lines on lid edges and outer surfaces. The absolute angular setting of the lids, and therefore the detectors, could be established to within 0.1° by perspex vernier scales reading on the lid edges, and bolted to the chamber wall at exactly 30° with respect to the optical chamber-centerline. The validity of the zero of this absolute scale was verified shortly after the scattering chamber became operational by the Rutherford scattering method of Chapter III, section 3.1(d).

During the measurement of the $d\sigma/d\Omega$ excitation functions, the 2 bottom lid detectors were set at lab. angles of 10°(A) and 40°(B), and the top lid detector (on the opposite side of the beam line) at 130°(C). All were set at radii of 8" and were uncollimated, so that detectors A, B and C subtended angles of 2.5°, 2.5° and 5° respectively. Since the $C^{12}(O^{16},\alpha)Mg^{24}$ kinematics are such that reaction products are emitted predominantly into forward angles it was considered advisable to place two detectors within the range 0° - 90°. Within this criterion, however, the choice of detector angles was arbitrary.

3.3. Detector Electronics.

Detector signals were led to BNC vacuum feed-

throughs in top and bottom lids, and electronics for each detector were as follows:

(a) Detector A: ORTEC 103-203 low-noise charge-sensitive amplification system (RC mode) feeding a 400 channel R.I.D.L. analyzer.

(b) Detector B: identical with system of detector A.

(c) Detector C: ORTEC 101-201 amplification system feeding a 512 channel R.C.L. analyzer.

Biases applied to A and B were in the range 150 - 200 v and to C were 40 - 50 v. All preamplifier-amplifier systems could be supplied with calibrating pulses as described in Chapter III, section 2.7, and all system (detector + modified electronics) resolutions, as measured with a ThC' - ThC" α-source were of order 1% or less (for 8.78 Mev line).

3.4. $C^{12}(O^{16}, \alpha)Mg^{24}$ Reaction Kinematics, and Competing Reactions.

Before discussing the procedure followed in obtaining the $C^{12}(O^{16}, \alpha)Mg^{24}$ alpha-particle spectra, it is useful to consider the reaction kinematics in the lab. system, since these differ considerably from those characteristic of reactions involving light initiating

particles and heavy targets. A 1620 computer program* was used to obtain plots of the following, at 2 Mev intervals in the O^{16} lab. energy range 15.0 - 35.0 Mev:

(a) The energy variation with angle of α-particles and recoil Mg^{24} nuclei from $C^{12}(O^{16},\alpha)Mg^{24}$ reactions populating the ground state and first 6 excited states of Mg^{24}.

(b) The energy variation with angle of O^{16} nuclei and C^{12} recoils from O^{16}-C^{16} elastic scattering.

A representative plot is given in Fig. 4.2. (for 21.0 Mev O^{16} energy), showing all relations (a) and (b) with the exception of the curves for Mg^{24} recoils corresponding to excited state reactions. It is seen that the large center-of-mass energy leads to great differences between energies of α-particles emitted in forward and backward directions (e.g. in this plot α_0 particles have 25 Mev at 0° and 6 Mev at 180°), the corollary of which is that $\partial E_{\alpha_i}/\partial\theta$ is very large over most of the angular range (between 60° and 90°, $\partial E_{\alpha_0}/\partial\theta$ = 200 kev/degree). Fig. 4.2 also indicates that the Mg^{24} recoils have energies at forward angles comparable with those of the α-particles of interest. The foregoing

Fig. 4.2 Typical laboratory kinematics for alpha particles and Mg^{24} recoils from $C^{12}(O^{16},\alpha)Mg^{24}$, and for O^{16} and C^{12} nuclei from $C^{12}(O^{16},O^{16})C^{12}$ elastic scattering.

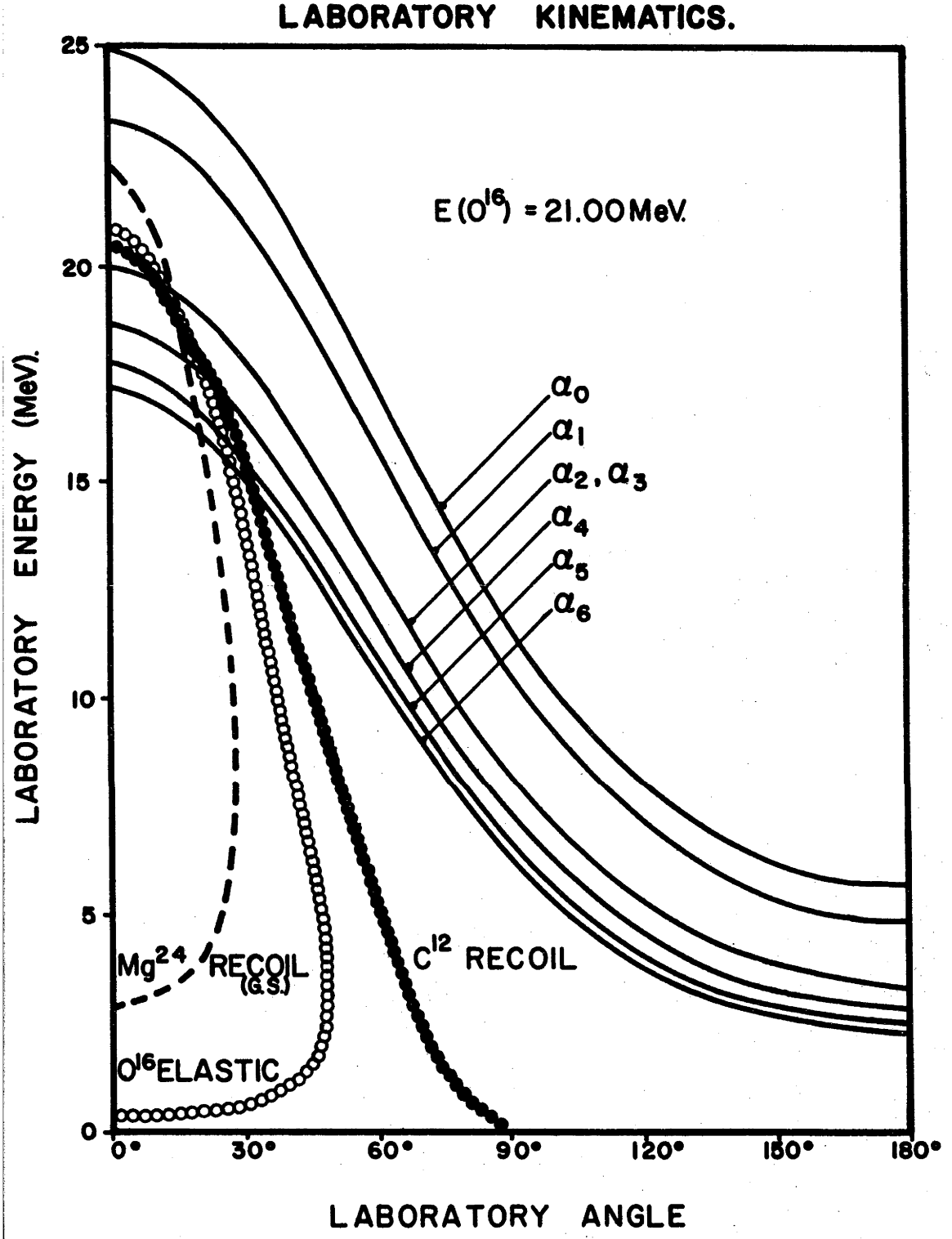
LABORATORY KINEMATICS.
E(O16) = 21.00 MeV.
α0
α1
α2, α3
α4
α5
α6
Mg24 RECOIL (G.S.)
C12 RECOIL
O16 ELASTIC
LABORATORY ENERGY (MeV.)
LABORATORY ANGLE
0
5
10
15
20
25
0°
30°
60°
90°
120°
150°
180°

conditions presented the principal experimental obstacles in the present work.

Energetically possible charged-particle emitting reactions which can be observed in competition with $C^{12}(O^{16}, \alpha)Mg^{24}$ are shown in Fig. 4.3, which represents the possible decay modes of the compound system Si^{28} in the range of excitation covered in the present experiment. It is seen that, apart from the O^{16}-C^{12} elastic scattering, the only serious competition arises from the $C^{12}(O^{16},p)Al^{27}$ reaction. The emitted protons have energies comparable with $C^{12}(O^{16}, \alpha)Mg^{24}$ α-particles but can be discriminated against in the solid state detectors by the standard depletion depth adjustment method. The lowest threshold, above that for $C^{12}(O^{16}, \alpha)Mg^{24}$, at which heavily ionizing light particles are emitted is that of $C^{12}(O^{16}, He^3)Mg^{25}$, which occurs 13 Mev higher; this places any spectral contributions due to He^3 particles well below the region containing the α-groups of interest.

3.5. Heavy Ion Stopping Foils.

Advantage was taken of the very high stopping cross section for heavy ions (relative to that of comparable energy α-particles) to reject them from the observed spectra, with the use of thin Al foils interposed between target and

Fig. 4.3 Energetically possible Si^{28} decay modes within the range of excitation energy covered in this experiment.

Numbers in the left-hand column refer to excitation in Si^{28}.

Si^{28} COMPOUND SYSTEM DECAY MODES

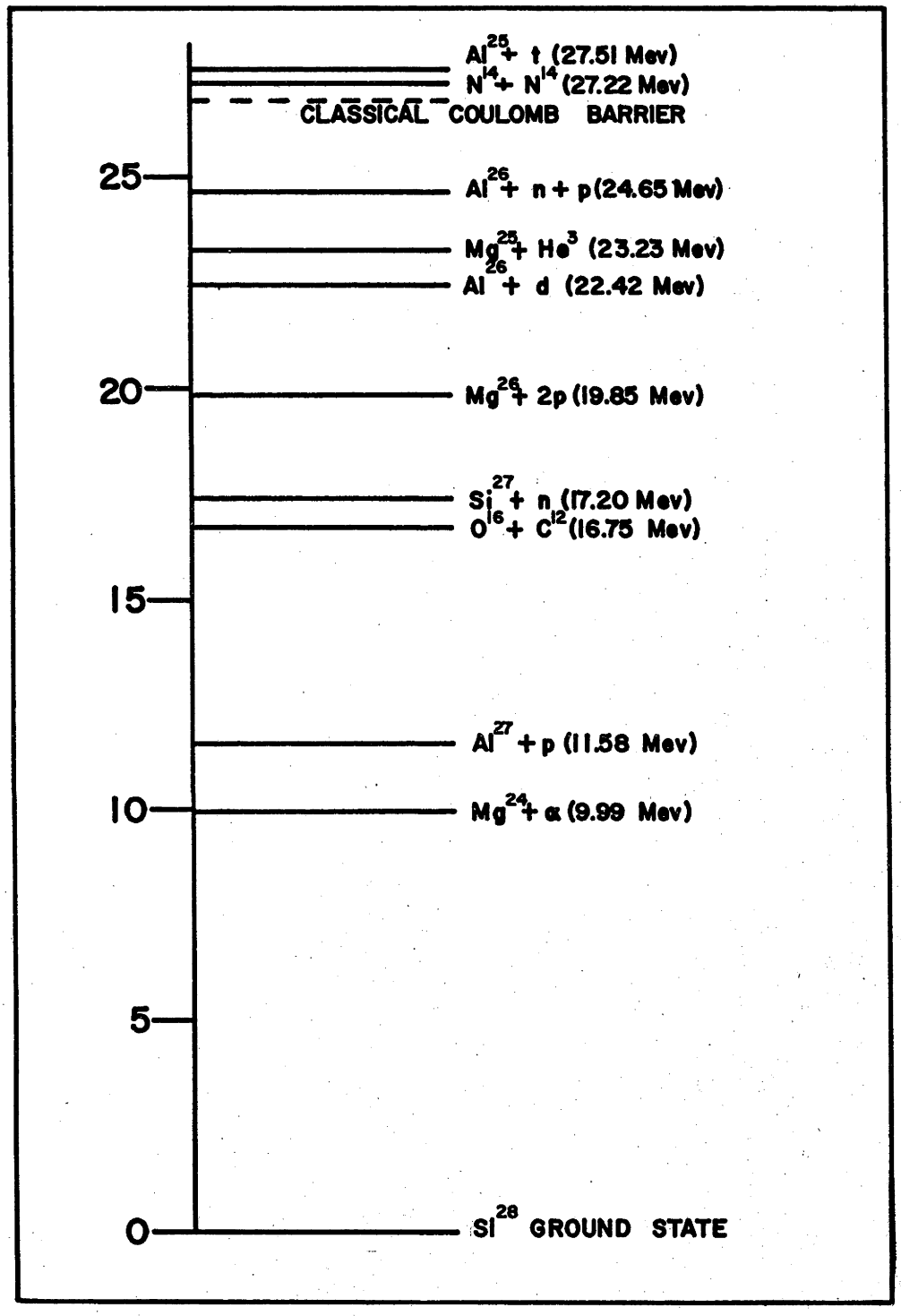

detectors. Experiment showed that it was necessary to use foils sufficiently thick to completely stop the O^{16} and C^{12} ions, since even with energies degraded to well below those of the $\alpha_0 - \alpha_6$ groups, their relatively intense flux caused a pulse-pileup great enough to obscure the weak α-groups. The required thickness of Al foil, as a function of O^{16} energy, was obtained from an inspection of plots similar to Fig.4.2 and comparison with the heavy-ion range-energy data of Roll and Steigert (Ro60). It was found convenient to employ a minimum foil thickness of .00025" Al(sufficient to stop 15 Mev C^{12}, O^{16} ions); the thickness was increased in these increments as O^{16} energy was raised. For reasons obvious from Fig. 4.2, the necessary increases were greater at the position of detector A(10°) than at that of detector B(40°); final foil thicknesses (at $E(O^{16}) = 29.5$ Mev) covering detectors A and B were .00100" and .00075" respectively.

The kinematics of Fig. 4.2 indicate that the heavy ion competition from O^{16}-C^{12} elastic scattering is nonexistent at angles backward of 90°, and it was initially expected that detector C (130°) would require no intercepting foil. However, experiment revealed the existence

of an O^{16} elastic scattering contribution, presumably from target impurities of $A > 16$, sufficiently intense to obscure the α-spectra at this angle; it was therefore necessary to employ an .00025" Al stopping foil, although the relatively slow energy gain (at 130°) of this contaminant scattering with increasing $E(O^{16})$, permitted the same foil thickness to be used for the entire O^{16} energy range.

3.6. The Alpha-Particle Spectra from $C^{12}(O^{16},\alpha)Mg^{24}$.

$C^{12}(O^{16},\alpha)Mg^{24}$ α-spectra were obtained by detectors A, B, and C at 0.5 Mev. (lab.) intervals in the $E(O^{16})$ range 15.0 - 29.5 Mev; this corresponds to ranges of 6.4 - 12.6 Mev in the c.m. system, and 23.2 - 29.4 Mev excitation in the Si^{28} compound system. The original intention was to reach an O^{16} bombarding energy of 35 Mev, but unstable accelerator behaviour made this impossible. The 0.5 Mev step size (corresponding to 214 kev in the c.m. system) was thought to be sufficiently narrow to provide a crude idea of the cross section energy dependence, while large enough to enable the available energy range to be covered in a single run.

The initial energy of 15.00 Mev was chosen to be well below the "classical" Coulomb barrier ($\sim$24 Mev in the

lab. system) in the C^{12}-O^{16} system for reasons given in Chapter V. Below 15.0 Mev the α- yield rapidly approached zero.

The 90° analyzing magnet proton-resonance frequencies corresponding to the chosen O^{16} energies were calculated from the relations given in Chapter III, section 3.1(c), using non-relativistic approximations throughout. The beam energy uncertainty due to magnet calibration error was $\pm$ 50 kev and that due to effective target thickness (target at 70°) was estimated to be $\sim$ 100 kev at midrange energy ($\sim$ 25 Mev). Integrated charge per spectrum, divided by the beam charge-state, was $\sim$ 100 μC/N, and average accumulation time/spectrum was $\sim$ 30 mins.

To reduce proton contributions to as low spectral energies as possible, the detector biases were set (at each O^{16} energy) to provide depletion layers just deep enough to stop the most energetic α- particles. At forward angles this was not strictly necessary since the energies of α_0 - α_6 groups were several Mev greater than that of the proton "edge", even at high detector bias. At the backward angle, however, it was critical since the emitted α_0 - particles had energies of only 4-6 Mev,

and after foil penetration, as much as 1 Mev less; this placed the α - groups corresponding to Mg^{24} excited states in the vicinity of the minimum proton "edge".

A spectrum observed by detector A(10^{o}) at $E(O^{16})$ = 28.5 Mev is shown in Fig. 4.4. The detector foil was .00075" thick. The six highest energy groups were identified by their energies and separations as corresponding to α - particles populating the low lying levels of Mg^{24}. The α_2, α_3 doublet is not resolved). The α - group energy resolution (FWHM) was $\sim$ 300 kev, the major part of which is due to: (a) finite observation angle, combined with large $\partial E_\alpha / \partial \theta$ (section 3.4), and (b) energy loss variation in detector covering foil. It is seen that α_5 and α_6 ($\sim$ 450 kev separation) were just resolved.

Inspection of the level scheme for Mg^{24}(En62b) revealed that the spacing rapidly becomes narrower than the

Fig. 4.4 Spectrum of alpha particles from $C^{12}(O^{16},\alpha)Mg^{24}$ measured at θ (lab.) = 10^{o} and E (O^{16}) = 28.50 Mev.

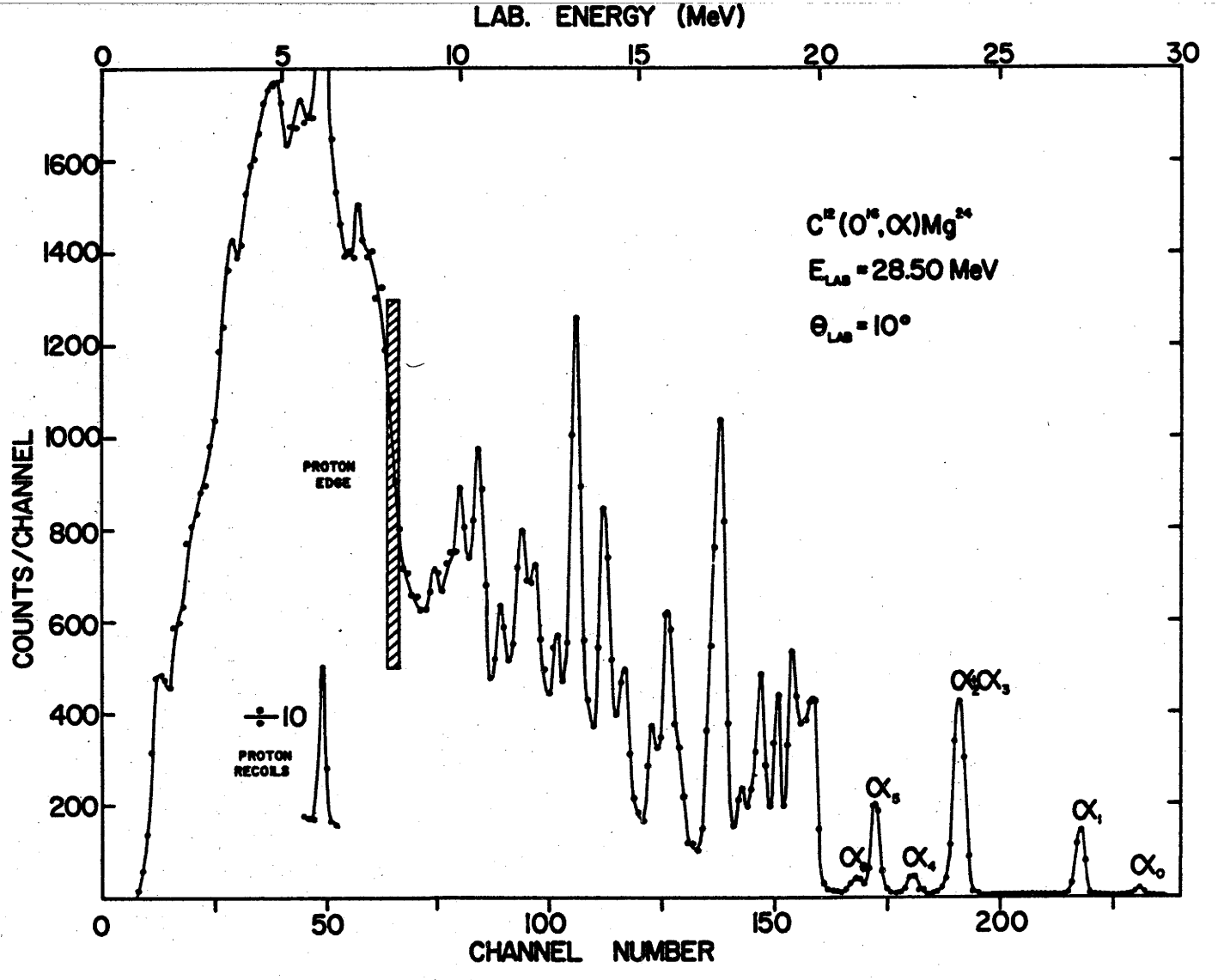
LAB. ENERGY (MeV)
0
5
10
15
20
25
30
COUNTS/CHANNEL
1600
1400
1200
1000
800
600
400
200
$C^{12}(O^{16},\alpha)Mg^{24}$
E_{LAB} = 28.50 MeV
θ_{LAB} = 10°
PROTON EDGE
÷10
PROTON RECOILS
$\alpha_2\alpha_3$
α_5
α_1
α_0
α_4
0
50
100
150
200
CHANNEL NUMBER

experimental energy resolution above the level corresponding to α_6. Therefore it was not possible to identify spectral groups below 20.5 Mev with individual levels. However, this portion of the spectrum exhibits a number of strong peaks, such as those near 17.5, 16.0, 13.8, and 13.0 Mev (lab.). Similarly strong peaks were observed at the same relative energies in spectra obtained at lower O^{16} energies, and may correspond to single levels or groups of levels in Mg^{24} which are excited with anomalously high probability. The sharp rise in yield near 8.0 Mev was attributed to the proton "edge", since an inspection of the range-bias-energy relationship of Blankenship (B160) showed that this was the maximum energy which protons could deposit in the detector. In combination with the considerations of section 3.4, this implies that the marked structure above 8 Mev is due only to α- particles from $C^{12}(O^{16},\alpha)Mg^{24}$. The Mg^{24} excitation corresponding to α- particles observed at energies just above the proton "edge" is $\sim$16 Mev.

The strong group at E = 6.5 Mev was identified as proton recoils from $H^1(O^{16}, O^{16})H^1$ elastic scattering, arising from a hydrogenous target impurity (probably H_2O).

Examples of detector B(40°) and C(130°) spectra are not shown. The 40° spectra resemble those measured at 10° with the exception that α- energies are a few Mev less, so that the lower energy portion of the α- spectrum is obscured by protons. The 130° spectra (over most of the O^{16} energy range) show only the α_0, α_1 and α_{2+3} groups; for reasons noted above, all lower energy α-groups are obscured by protons.

3.7. The $d\sigma/d\Omega(10^{\circ},40^{\circ},130^{\circ})$ Excitation Functions.

As shown in Fig. 4.4, spectrum contributions lying between α- groups were negligible, so that group yields were extracted from the spectra by direct summation of channels lying under the relevant peaks. Groups α_5 and α_6 (10° spectra) were generally not completely resolved and a simple unfolding procedure was used in their separation. Yields were normalized to constant integrated O^{16} ion flux, and a correction accounting for Carbon buildup on the target was applied as follows: (a) target thickness was measured at the beginning and end of the entire run; (b) the rate of target thickness increase was assumed proportional to the O^{16} ion flux; (c) using (a), (b) and the ratio of integrated flux per point to the total integrated flux, the average target thickness at each energy point could be estimated. It is thought that the

relative error between neighbouring yield points introduced by this procedure was $< 5\%$, but the overall uncertainty was $\sim 15\%$ (the target-thickness measurement uncertainty).

The survey $d\sigma/d\Omega(10^\circ, 40^\circ, 130^\circ)$ excitation functions are shown in Figs. 4.5 and 4.6. Fig. 4.5 gives $d\sigma/d\Omega(10^\circ)$ for groups $\alpha_0 - \alpha_6$(α_2, α_3 summed), while Fig. 4.6 gives $d\sigma/d\Omega(40^\circ)$* and $d\sigma/d\Omega(130^\circ)$ for groups $\alpha_0 - \alpha_3$. The absolute cross section scales contain an uncertainty due to: (a) detector solid angle measurement error ($\sim 5\%$); (b) target thickness measurement error ($\sim 15\%$); and (c) beam integration inaccuracy. The last is thought to be larger for the O^{16} beams than for light-particle beams due to charge exchange between beam ions and residual tube gas, and electron stripping by the target (sections 2.7 and 2.3). Target-in target-out current difference measurements were taken, and the 23.0 Mev $C^{12}(O^{16}, \alpha)Mg^{24}$ yield was obtained consecutively with both 4^+ and 5^+ beams; neither measurement offered significant evidence for charge-exchange-induced beam integration errors $> 2\%$.

*Although groups $\alpha_4 - \alpha_6$ were observable in the 40° spectra their relatively poor separation made yield extraction uncertainties very large.

Fig. 4.5 $C^{12}(O^{16},\alpha)Mg^{24}$ $d\sigma/d\Omega$ (10^{o}) excitation functions from $E(O^{16}$, lab.) = 15.0 to 29.5 Mev, for the ground state and first, second + third, fourth, fifth and sixth excited state reactions.

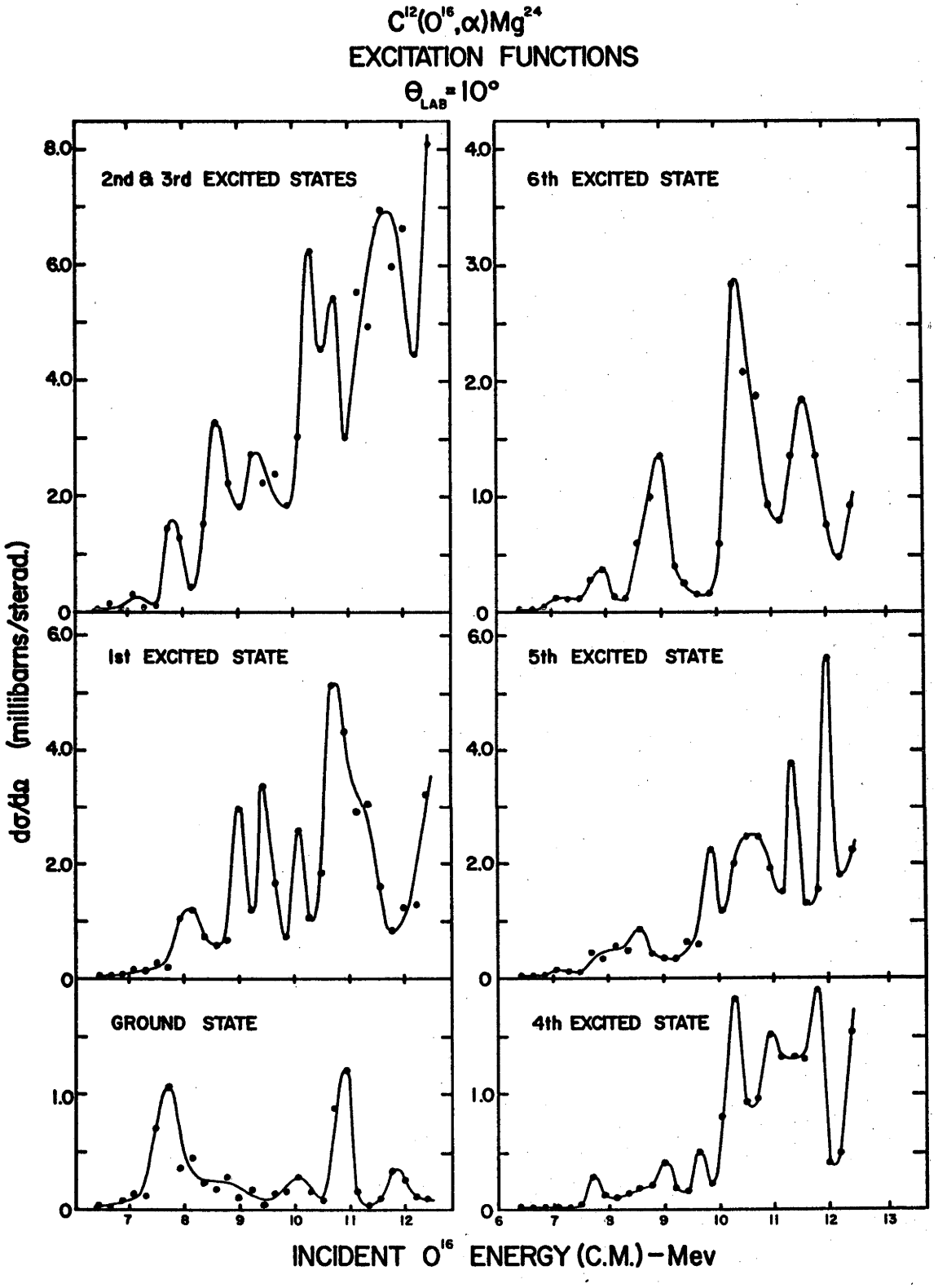
$C^{12}(O^{16},\alpha)Mg^{24}$
EXCITATION FUNCTIONS
$\theta_{LAB} = 10°$
2nd & 3rd EXCITED STATES
6th EXCITED STATE
1st EXCITED STATE
5th EXCITED STATE
GROUND STATE
4th EXCITED STATE
dσ/dΩ (millibarns/sterad.)
INCIDENT O^{16} ENERGY (C.M.) – Mev

Fig. 4.6 $C^{12}(O^{16},\alpha)Mg^{24}$ $d\sigma/d\Omega$ (40°, 130°) excitation functions from $E(O^{16}$, lab.) = 15.0 to 29.5 Mev, for the ground state, and first and second + third excited state reactions.

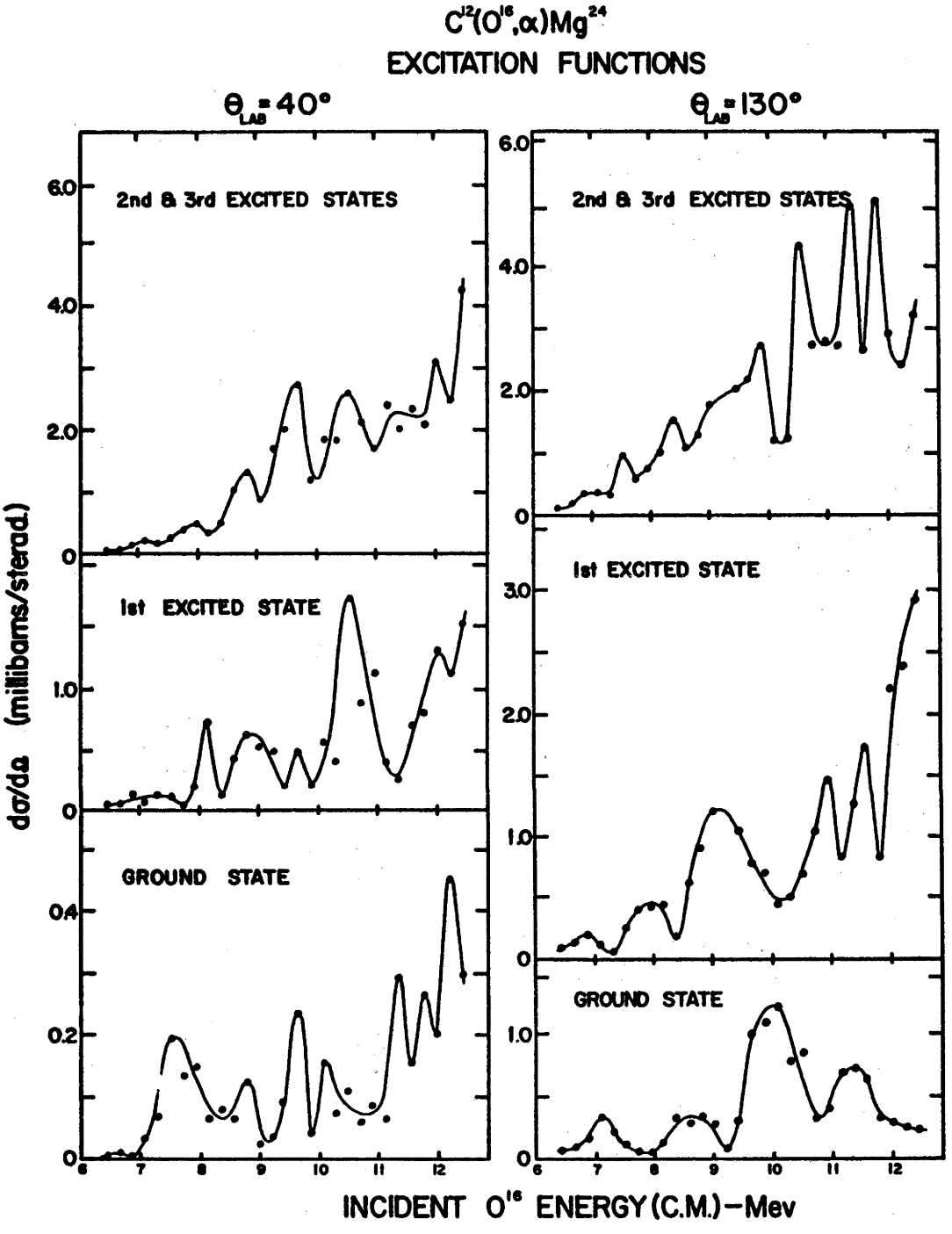
$C^{12}(O^{16},\alpha)Mg^{24}$
EXCITATION FUNCTIONS
$\theta_{LAB}=40°$
$\theta_{LAB}=130°$
2nd & 3rd EXCITED STATES
1st EXCITED STATE
GROUND STATE
2nd & 3rd EXCITED STATES
1st EXCITED STATE
GROUND STATE
dσ/dΩ (millibams/sterad.)
INCIDENT O^{16} ENERGY (C.M.) – Mev

Statistical counting errors for the weaker groups (α_0, and α_6) were $> 10\%$ but were less serious for other α - groups. No error bars have been inserted in Figs. 4.5 and 4.6, but the smooth connecting lines have been drawn with statistical uncertainties taken into account.

3.8. Discussion of Excitation Function Survey.

Features common to nearly all the $d\sigma/d\Omega$ excitation functions of Figs. 4.5, 4.6 are:-

(a) The average yield increases sharply above 6.5 Mev (O^{16} c.m. energy); this is attributed to Coulomb barrier penetration effects, the "classical" E_B for C^{12}-O^{16} being 10.3 Mev.

(b) Differential yields for all α_i show strong energy dependence in the form of peaks of irregular width and spacing. Minimum widths (FWHM) are of order 200 kev.

(c) Little qualitative correlation exists between $d\sigma/d\Omega$ for different α_i at the same observation angle or between $d\sigma/d\Omega$ at different observation angles for the same α - group.

(d) Many peaks are "single-point" maxima, implying that the precise $d\sigma/d\Omega$ energy dependence is probably considerably stronger than indicated by the large energy increments of the survey.

It is noted that the $C^{12}(O^{16},\alpha)Mg^{24}$ $d\sigma/d\Omega(\theta,\alpha_i)$ excitation function characteristics are similar to those of the $Al^{27}(p,\alpha)Mg^{24}$ reaction (Chapter III), where excitations of several Mev less in Si^{28} are involved. The mean cross-section fluctuation amplitudes, relative to the average cross-section values, are $\geq$ those evident in the $Al^{27}(p,\alpha)Mg^{24}$ data; since at the higher Si^{28} excitations involved, the relation $\Gamma >> D$ is expected to be an even better approximation than for the $Al^{27}(p,\alpha)Mg^{24}$ work, it might at first be expected that the $C^{12}(O^{16},\alpha)Mg^{24}$ $d\sigma/d\Omega$ (θ,α_i) cross section fluctuations could be explained in terms of recent extensions to Statistical Model theory (Chapter VI). This point is elaborated in Chapter V, section 5.

Section 4. DETAILED STUDY OF $C^{12}(O^{16},\alpha)Mg^{24}$ REACTION 15.0 - 22.5 Mev.

The apparent compound-system interference effects (lack of correlation between measurements at different angles) evident in the above $d\sigma/d\Omega$ survey suggested that

the $C^{12}(O^{16}, \alpha)Mg^{24}$ reaction could be more profitably studied via integrated σ excitation functions. In this connection, the results of Almqvist et al. (Al63b) for $C^{12}(C^{12}, \alpha)Ne^{20}$ - showing similar strong interference characteristics in the $d\sigma/d\Omega(\theta, \alpha_i)$ excitation functions, but prominent and correlated (between α- groups) resonances in corresponding $\sigma(\alpha_i)$ excitation functions - were particularly encouraging. The $C^{12}(C^{12}, \alpha)Ne^{20}$ resonances were attributed to "quasi-molecular" states of the C^{12}-C^{12} system (Al63b); since the O^{16}-C^{12} compound system excitation energies and bombarding energies (below Coulomb barrier) accessible in the present experiment were similar to those at which the C^{12}-C^{12} system was studied, it was anticipated that a detailed integrated cross section study of the $C^{12}(O^{16}, \alpha)Mg^{24}$ reaction might reveal evidence for the existence of such states in the corresponding O^{16}-C^{12} system. These points are elaborated in Chapter V, section 5.

4.1. Program Outline.

The initial program for the detailed study was to measure complete $C^{12}(O^{16}, \alpha)Mg^{24}$ angular distributions at O^{16} energy (lab.) intervals of 250 kev (107 kev in c.m. system) over the range 15.0 - 30.0 Mev, for groups α_0 - α_6;

the step size was 1/2 that used in the survey of section 3, and was expected (from section 3 results) to be sufficiently small to reveal most significant cross section detail, while large enough to permit the measurements to be completed within a reasonable time (several days). Unfortunately, the accelerator performance with O^{16} beams deteriorated sharply while the program was being carried out, and it proved impossible to proceed beyond $E(O^{16}) = 22.5$ Mev. The performance decline was associated with excessive total charging currents at midrange (3 Mv) terminal potentials and it is expected that the installation (presently in progress) of inclined-field acceleration tubes may restore satisfactory performance and open the possibility of extending the measurements to higher energies.

The experimental arrangements and procedures used in the detailed study of $C^{12}(O^{16}, \alpha)Mg^{24}$ are described in the following sections. Data handling and analysis procedures and results are given in Chapter V.

4.2. The Detector Array.

An array of 4 detectors was employed in measuring the angular distributions. The geometry, shown in Fig.4.7,

Fig. 4.7 Horizontal section through 20" scattering chamber, showing detector array geometry. Inset shows detector detail (horizontal section).

Numbered points are :

1. Array detectors - shown at edges of respective angular sectors
2. Ortec detector
3. Aluminium foil
4. Collimating slit
5. Detector array mounting plate
6. Beam collimating assembly

Monitor detector detail.

7. 1/16" horizontal slit
8. 1/32" vertical slit
9. 200 mm^2 Ortec detector
10. Faraday cup

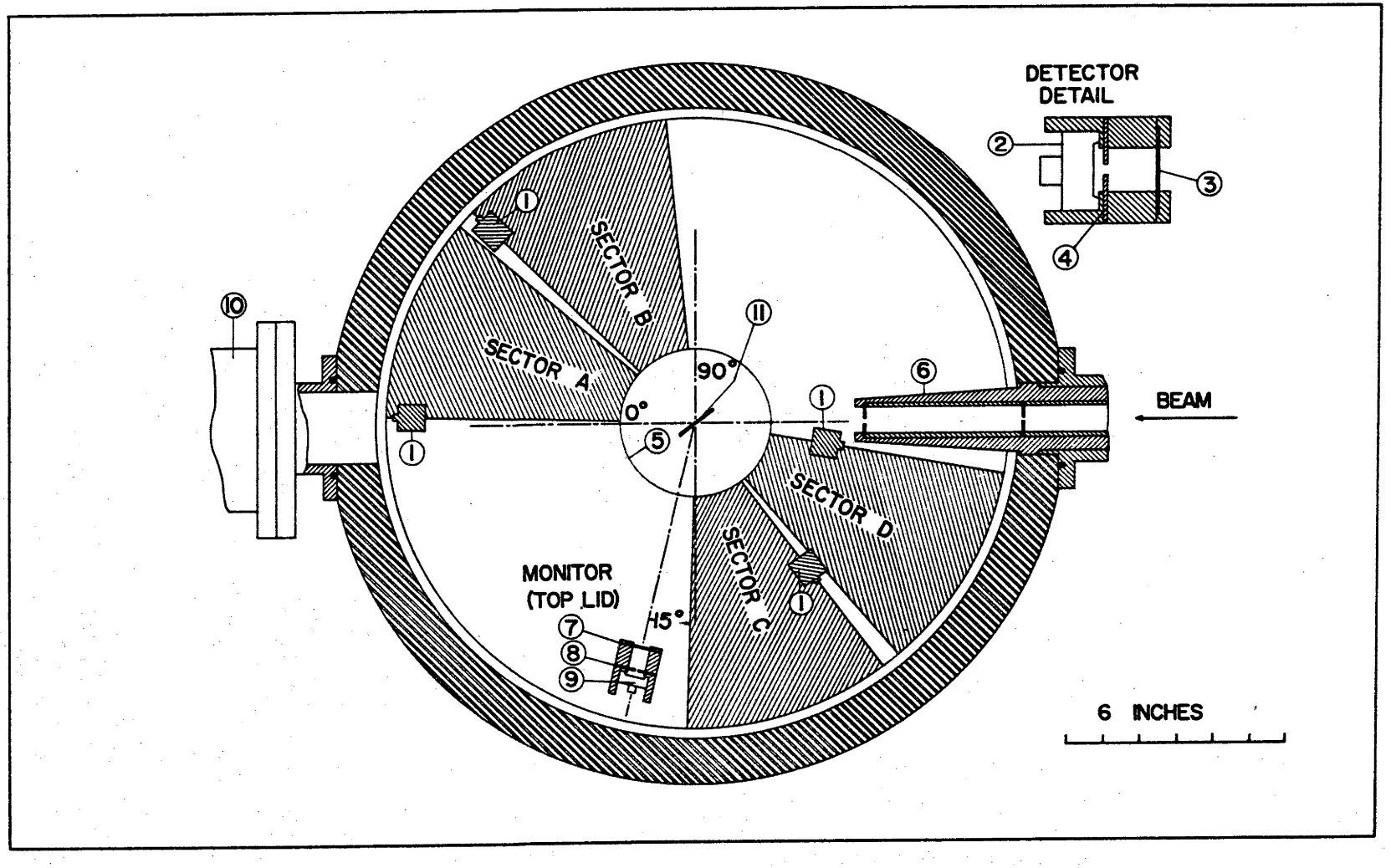
DETECTOR
DETAIL
2
3
4
1
SECTOR B
SECTOR A
10
11
90°
0°
6
BEAM
5
1
SECTOR D
SECTOR C
MONITOR
(TOP LID)
45°
7
8
9
1
6 INCHES

which represents a horizontal section through the 20" scattering chamber. All detector mounts were identical and contained provision for collimating slits and stopping foils. A representative mount is shown in vertical section in Fig. 4.1, and details in horizontal section in the inset of Fig. 4.7. The mounts were rigidly fixed to an Aluminium plate (Fig. 4.1) which was bolted concentrically to the bottom lid, as shown. Relative angular positions of the detectors were chosen so that the total angular range 2° - 170° could be scanned without sector overlap. Detectors A and B covered the ranges 2° - 41° and 45° - 84°, respectively, and C and D covered the ranges 88° - 127° and 131° - 170° respectively, but in the opposite semi-circle; thus, during angular distribution measurements A and B moved backward, while C and D moved forward, permitting the target to be held at a fixed angle (40°) for the entire experiment. The number of detector-plate settings was 9, giving a 36 point angular distribution; such a high point density was mandatory, due to the expectation that $C^{12}(O^{16},\alpha)Mg^{24}$ α- particles might be emitted with angular momenta as large as 8-10$\hbar$* (at least at higher O^{16} energies), leading to rather complicated angular distributions.

*Based on the results of Kuehner et al.(Ku63), for the $C^{12}(C^{12},\alpha)Ne^{20}$ reaction.

4.3. Detectors.

Different detector sets were employed for separate sections of the O^{16} energy range. From $E(O^{16})$ = 15.00 - 17.25 Mev, detectors A, B, C, D were 50-500, 150-500 and 200-100 respectively (where numbers indicate area and max. depletion depth in that order) and from $E(O^{16})$ = 17.25 - 22.50 Mev, detectors A,B,C,D were 50-500 , 50-500, 50-300, and 200-100. Deep depletion layer detectors were placed in the forward angle mounts, in order to stop the high energy α - particles ($\sim$ 30 Mev) emitted at forward angles.

4.4. Detector Solid-Angles and Angular Resolutions.

Detector mount radial positions (R) could be adjusted in increments of 0.5", and vertical collimating slits of width (W) ranging from 3/16" - 1/16" could be inserted directly in front of the detector faces (Fig. 4.7). The parameters R and W for each detector were chosen to compromise between the angular definition requirements of the corresponding sector and the necessity for providing the largest possible detector solid angle.

A glance at the lab. kinematics of Fig. 4.2 reveals that sectors B and C covered the angular range in which

$\partial E_\alpha / \partial \theta$ was greatest; detectors B and C accordingly required the smallest W/R ratio. The general limits on W/R $\cong \Delta\theta$ were set by the relation:

$$\Delta E(\alpha_5, \alpha_6) > \left[\left(\frac{\partial E(\alpha_5, \alpha_6)}{\partial \theta} \Delta\theta \right)^2 + \sum_i (\delta E_i)^2 \right]^{\frac{1}{2}} \qquad (4.1)$$

where $\Delta E(\alpha_5, \alpha_6)$ was the lab. energy separation (f(θ)) between spectral groups α_5, α_6 (the closest of the observed α- groups with the exception of the unresolvable α_2, α_3 doublet), and the quantities inside the right-hand square bracket are: (a) resolution broadening due to kinematics (i.e. finite W/R) alone, and (b) resolution broadening due to all other factors, such as foil, target, and detector + electronics. The δE_i factors were generally fixed parameters; in particular the resolution broadening due to detector foils was fixed (at a given O^{16} energy) by the foil thickness required to eliminate heavy ions - itself a fixed function of the heavy ion kinematics. Therefore, the required energy resolution could generally be obtained only by holding W/R to values corresponding to a kinematical resolution broadening of < 150 kev. For sector B, where α - energy variation with angle was most severe, W and R were typically 0.125" and 8.5" respectively, giving an angular resolution (lab.) of $\pm 0.5^\circ$.

4.4(a) Solid-Angle Ratios.

The ratios of solid angles subtended by detectors B, C, D with respect to that of detector A were measured as follows. A planar ThC'-ThC" α- particle source was fixed at the target position, and set to face each collimated detector in turn. Spectra were accumulated for a fixed time and the integrated counts (corrected to account for the finite source half-life) were taken as a measure of the relative solid angle subtended by each detector. Foils were removed for this procedure. Direct geometrical measurements were also made, and agreement between the two methods was within the 3% statistical counting uncertainty. Collimating slit widths, detector mount radii, and the detectors themselves were changed several times as O^{16} energy was increased, as a result of changing kinematics (section 3.4), and solid angle ratios were measured for each configuration.

4.5. Detector Foils.

Thin Al foils were clamped over the detector entrance ports as shown in Fig. 4.7. Foil thickness employed (at a given O^{16} energy) by each detector was the minimum (in the terms of section 3.5) which could be used to stop

the most energetic heavy ions emitted at any angle of the corresponding sector.

4.6. Detector Array Electronics (Routing).

Electronics for the detector array were straightforward and are schematically indicated in Fig. 4.8. Detectors A and B fed ORTEC 103-203 amplifying systems operating in the DDL mode, while detectors C and D fed ORTEC 101 preamps. (modified to by-pass the differentiating-integrating circuits) and Franklin A-8 (DDL) amplifiers. System C and D preamp-power and detector bias were supplied from ORTEC 201 main amplifiers. All system resolutions were $\sim$1.0 - 1.5% for the 8.78 Mev line of a ThC'-ThC" α - source. Outputs of A, B and C, D respectively were coupled with a simple diode arrangement (Fig. 4.8 inset). Systems A, B outputs were taken from the biased post amplifiers to allow flexibility in selecting the portions of the corresponding spectra to be analyzed; this was unnecessary for the C, D (backward angle) systems since the corresponding spectra covered a narrower lab. energy range. Output pairs A, B and C, D were fed to the A.D.C. units of R.I.D.L. 400 channel pulse-height-analyzers, as shown, and pulses from each pair component were routed into separate blocks of 200 channels by the following method:-

Fig. 4.8 Block diagram for electronics employed with detector array and monitor detector.

ELECTRONICS BLOCK DIAGRAM.

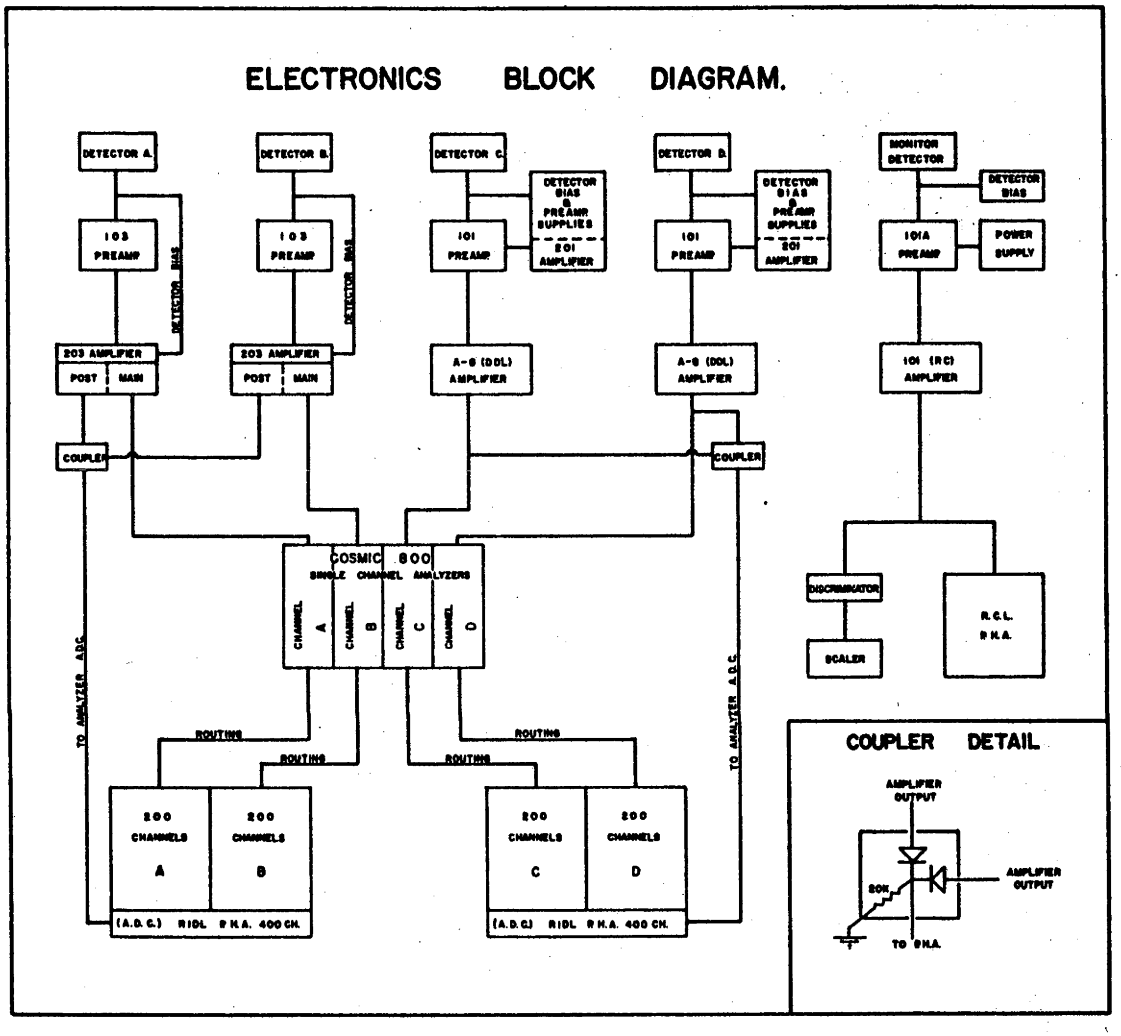

Pulses from each of the A,B,C,D amplifiers were fed to the inputs of 4 identical single channel analyzers*, which supplied uniform square-topped +10V pulses of 3.5 μsec duration and 1 μsec delay to the R.I.D.L. routing networks; these pulses exactly suited the R.I.D.L. requirements for switching the corresponding pulses arriving at the A.D.C. into the appropriate analyzer segments. Single-channel-analyzer discriminator levels were set to minimum (3.5V) and windows to maximum; amplifier pulses lower than 3.5V produced, of course, no corresponding routing pulses. This led to "cross-talk" between analyzer segments in the low energy portions of the spectra. The upper level of this meaningless region was held to $<$ 1.5 Mev in all A, B, C, D spectra by using high amplifier gains coupled with maximum analyzer A.D.C. input attenuation factors. The correct operation of the routing system for pulses corresponding to higher energy portions of the spectrum was checked periodically with the Hg-relay pulsers supplied with the ORTEC amplifiers.

4.7. The Reaction Monitor.

The product of the effective number of Carbon target atoms within the beam dimensions, and the beam intensity, and therefore the absolute yield of the $C^{12}(O^{16}, \alpha)Mg^{24}$

*Sections of a Cosmic 800 Coincidence Unit.

reaction, was monitored by measuring the O^{16}-C^{12} elastic scattering, via observation of the C^{12} recoil nuclei at 75^{o} (lab. angle). These correspond to O^{16} nuclei elastically scattered at a c.m. angle of 30^{o}, and the data of Bromley et al. (Br60) indicate that the $C^{12}(O^{16},O^{16})C^{12}$ elastic scattering at this angle is pure Coulomb for the O^{16} energies covered in this experiment. The C^{12} recoils were observed in preference to the corresponding O^{16} elastically scattered nuclei, due to the complicated heavy ion spectrum at the equivalent forward lab. angle. An inspection of the kinematics (Fig. 4.2) reveals that in this angular region O^{16} nuclei and C^{12} recoils have similar energies; experiment showed that it was difficult to resolve the O^{16} and C^{12} heavy ion spectral groups sufficiently well to allow unambiguous counting (with a simple discriminator and scaler) of only the O^{16} nuclei. A summation of both groups would have proved valueless, since the high energy C^{12} recoils correspond to O^{16} nuclei elastically scattered at backward angles (in c.m. system), where strong departures from pure Coulomb scattering are expected.

The C^{12} recoil monitor was a 200 mm^2-400Ω-cm surface barrier detector, mounted in the top lid assembly (Figs.4.1

and 4.7 show details), and collimated by crossed 1/32" and 1/16" slits to reduce the count rate to an acceptable level. The detector mount was set at its maximum radial extension (8").

The monitor detector electronics are shown in Fig. 4.8. Amplified pulses were fed to a discriminator and recording scaler and the spectrum was periodically examined by a 512 channel R.C.L. analyzer. A typical spectrum (at $E(O^{16})$ = 18.00 Mev) is shown in Fig. 4.9. The discriminator setting is indicated by a pulser line at the equivalent energy.

The appreciable low-energy tail and considerable asymmettry in the C^{12} recoil peak are thought to be due to energy straggling of the relatively low energy ($\sim$1-2 Mev) ions in the Carbon target. The strong group near channel 50 is attributed to $H^1(O^{16},O^{16})H^1$ elastic scattering proton recoils arising from target impurity (H_2O), and the sharp rise near channel 30 to detection system noise. Uncertainties in the integrated monitor recording are due to:-

(a) the finite discriminator setting, which ignores the lowest fraction of the energy-degraded spectrum tail; this fraction is estimated to contain $<$ 5% of

Fig. 4.9 Typical C^{12} recoil spectrum from $C^{12}(O^{16},O^{16})C^{12}$ elastic scattering measured at 75^{o} (lab.) by monitor detector.

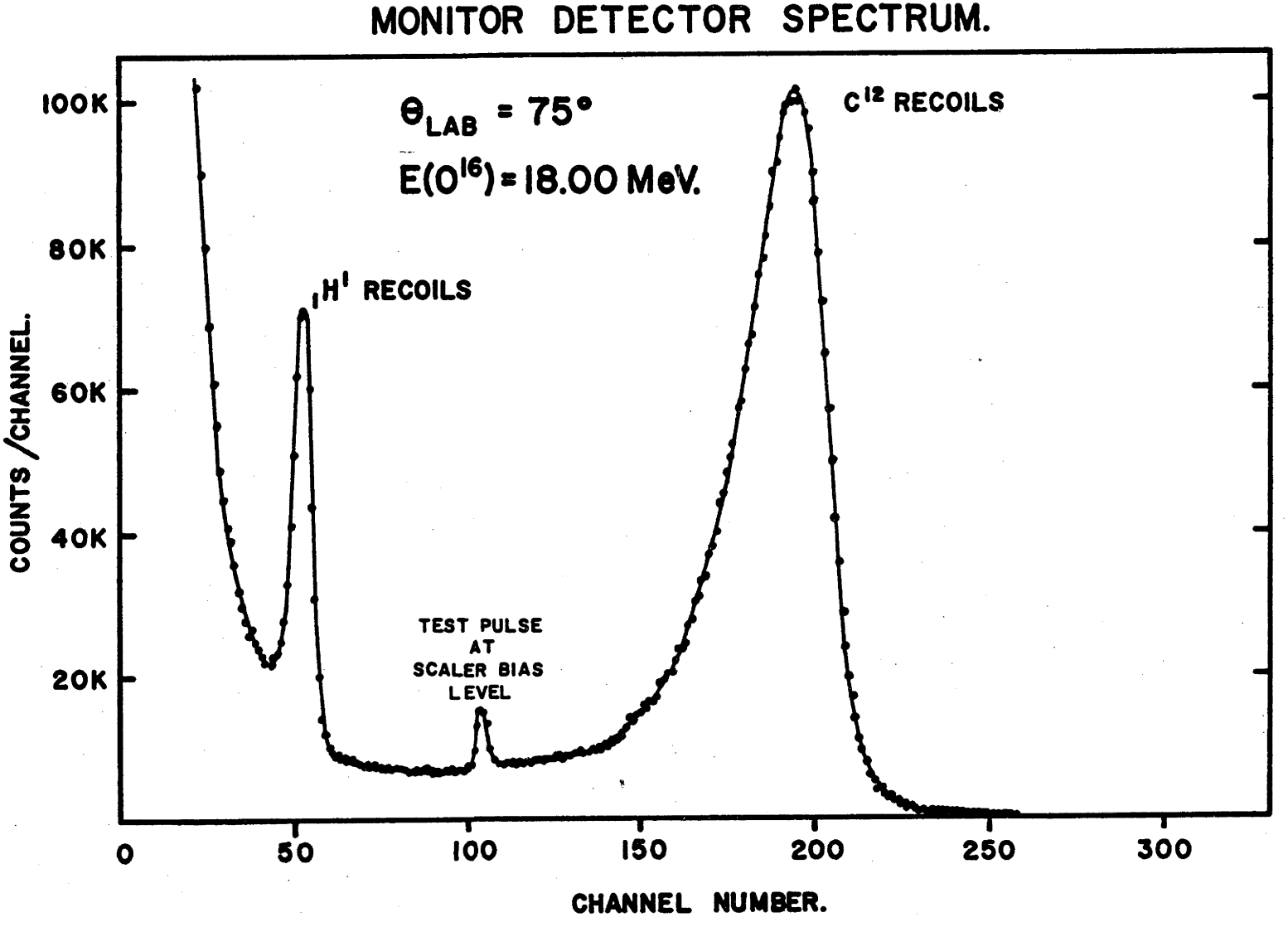
MONITOR DETECTOR SPECTRUM.
θ_{LAB} = 75°
E(O^{16}) = 18.00 MeV.
C^{12} RECOILS
$_1H^1$ RECOILS
TEST PULSE AT SCALER BIAS LEVEL
100K
80K
60K
40K
20K
COUNTS /CHANNEL.
0
50
100
150
200
250
300
CHANNEL NUMBER.

the integrated C^{12} spectrum, and decreases slowly as O^{16} energy is raised.

(b) spectrum contributions arising from O^{16}-O^{16} elastic scattering, as a result of oxygen contamination in the target. The laboratory kinematics of O^{16}-O^{16} scattering are almost identical with those of the C^{12} recoils at the monitor observation angle, so that it was not possible to directly determine the magnitude of the contamination contribution. If it is assumed that the major portion of O^{16} in the target is due to trapped H_2O molecules, then the proton recoil group in the spectrum of Fig. 4.9 provides a crude estimate of its magnitude, indicating that it probably causes an error in the integrated monitor yield of 2-3%.

Since errors (a) and (b) are both slowly varying with O^{16} energy, and are in opposing directions, a partial cancellation is expected. Statistical counting uncertainties in monitor yield are a factor of 10 lower in magnitude than uncertainties (a) and (b), due to the large number ($\sim 10^6$) of C^{12} counts recorded per measurement.

As targets were frequently changed, and Carbon buildup on target proceeded at high rates (section 2.3), it was necessary to place complete reliance on the C^{12} recoil monitor as a direct measure, independent of target and beam conditions, of the absolute $C^{12}(O^{16}, \alpha)Mg^{24}$ reaction yield. The beam-current integration served only as a rough check on the monitor detector system, and was mainly employed to regulate the time for each measurement. Monitor corrections to measured $C^{12}(O^{16}, \alpha)Mg^{24}$ yields are discussed in Chapter V, section 2.3.

4.8. Spectra from Detector Array.

Typical spectra obtained from each detector of the array are shown in Fig. 4.10, for midrange angular setting and $E(O^{16})$ near the median of the covered region. The $C^{12}(O^{16}, \alpha)Mg^{24}$ α - groups resolved in each spectrum are labelled with their respective group numbers. It is seen that while groups α_0 - α_6 are clearly observable in the forward angle detectors (A, B), progressively fewer are observable in the backward angle detectors (C, D); in C, α_5 and α_6 are obscured by protons and in D only α_0 and α_1 are clear of the proton "edge". (The reasons for deterioration of spectra at backward angles are those of sections 3.5, 3.6). It was initially anticipated that the

Fig. 4.10 Typical $C^{12}(O^{16},\alpha)Mg^{24}$ spectra obtained from each array detector at a representative array scattering, for an O^{16} energy of 19.50 Mev (lab.)

Peak numbers refer to alpha groups populating corresponding levels in Mg^{24}.

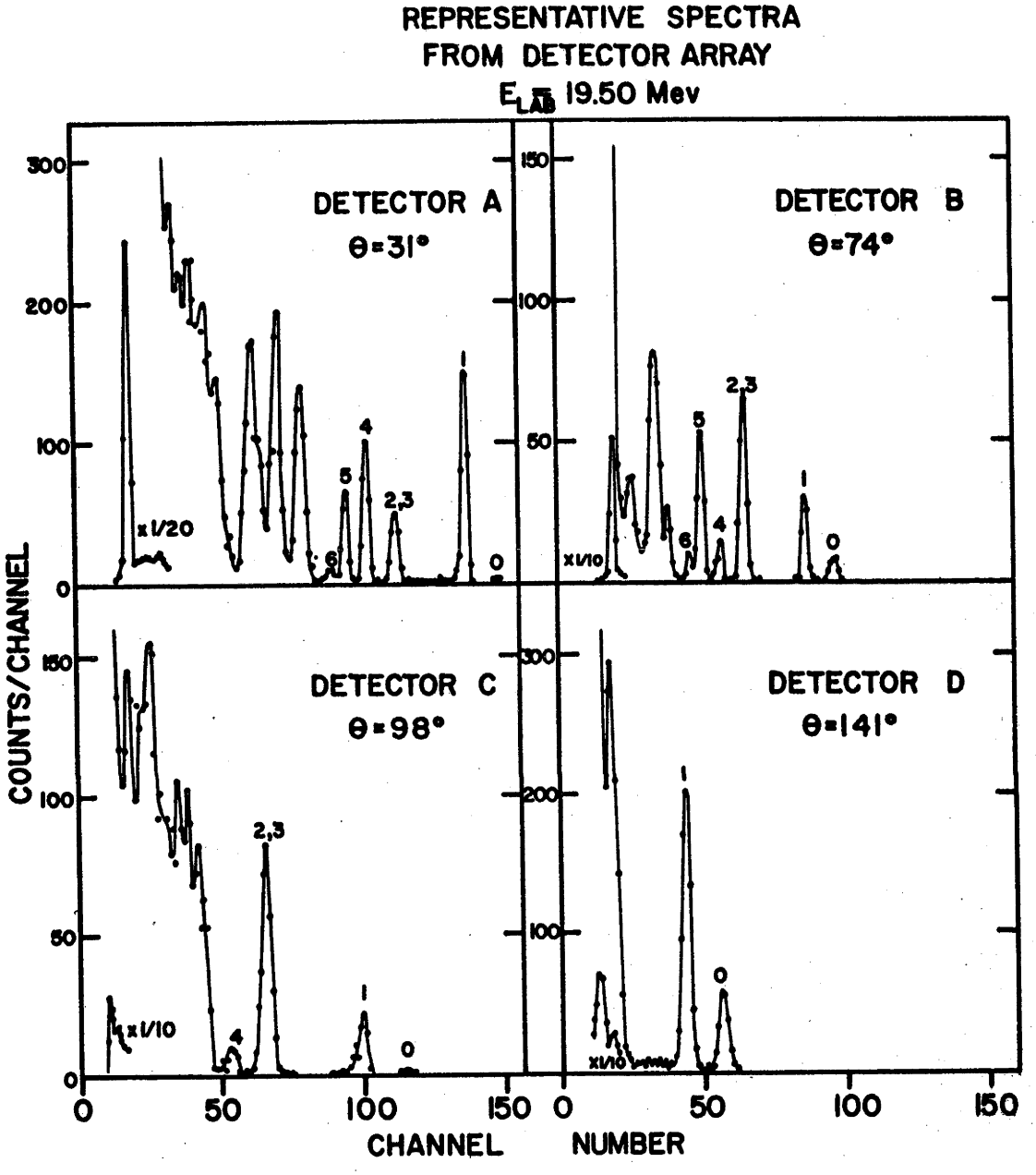
REPRESENTATIVE SPECTRA
FROM DETECTOR ARRAY
E_{LAB} 19.50 Mev
DETECTOR A
θ=31°
DETECTOR B
θ=74°
DETECTOR C
θ=98°
DETECTOR D
θ=141°
x1/20
x1/10
x1/10
x1/10
0
1
2,3
4
5
6
COUNTS/CHANNEL
CHANNEL NUMBER
0
50
100
150
200
300

lower energy spectral groups might be observed at backward angles by suitable juggling of foils and detector biases; however experiments showed that this procedure offered only a slight extension of the maximum angular range for observation of each α - group. Groups α_0 and α_1 could be clearly observed at all angles, and the doublet α_2, α_3 up to 130° - 140°, while groups $\alpha_4, \alpha_5, \alpha_6$ had progressivley smaller "cutoff" angles. However, considerable care was taken (section 4.4) at all O^{16} energies to ensure that all observable α- groups should be well-resolved at all angles, in the expectation that even partial angular distributions for groups $\alpha_2 - \alpha_6$ would provide useful information on the nature of the $C^{12}(O^{16}, \alpha)Mg^{24}$ reaction mechanism.

The spectra from the detector array were recorded simultaneously in the two R.I.D.L. analyzers (section 4.5) and printed out on paper tape. Tapes were inspected at frequent intervals to prevent printout errors. The amount of data obtained in even the abbreviated energy range $E(O^{16})$ = 15.0 - 22.5 Mev was very considerable, the total number of yield points being:

$$T = \sum_{i}^{N(\alpha)} \sum_{j}^{N(E)} N(\theta)_{ij} \approx 5{,}000 \qquad (4.2)$$

where N(E) is the number of O^{16} bombarding energies contained in the covered range, $N(\alpha)$ is the number of α - groups, and $N(\theta)_{ij}$ is the number of angles at which each α_i - group appeared in the spectrum taken at energy E_j. Such a large quantity of data required semi-automatic handling and processing and the relevant operations are described in Chapter V, along with preliminary analysis and results.

4.9. 32 Mev Angular Distribution.

In a preliminary experiment (section 1) performed prior to the assembly of the 20" scattering chamber, the $C^{12}(O^{16},\alpha)Mg^{24}$ reaction was examined at $E(O^{16}) = 32.0$ Mev. The details of this work have been included in this section, since it provides information on the reaction mechanism at higher bombarding energies than were later attainable. Experimental procedures are given here and results in section 4.7, Chapter V.

The basic apparatus was the 9" scattering chamber and associated equipment, described in Chapter III. ORTEC 300Ω - cm resistivity surface barrier detectors were inserted in the rotating and fixed mounts. An O^{16} beam of 0.1μA(5^+ charge state) was used, and the Carbon target was $\sim$ 10μg thick. A single partial angular distribution of α - particles from $C^{12}(O^{16},\alpha)Mg^{24}$ was measured at

$E(O^{16})$ = 32.0 Mev (13.70 Mev in c.m. system) in 5° steps; monitoring was provided by the fixed detector observing the O^{16}-C^{12} elastic scattering at an angle of 30° (lab.) The bombarding energy was chosen to correspond with a resonance observed by Bromley et al.(Br60) in the 30° elastic scattering $d\sigma/d\Omega$. The $C^{12}(O^{16},\alpha)Mg^{24}$ yields for α_0, α_1 were extracted from the spectra obtained at each angle, and corrected by the monitor readings, for target thickness increase due to Carbon buildup.

CHAPTER V

THE REACTION $C^{12}(O^{16}, \alpha)Mg^{24}$. DATA ANALYSIS AND RESULTS

CHAPTER V

Section 1. INTRODUCTION.

The material of this chapter comprises a description of the procedures used for handling and analysis of the $C^{12}(O^{16},\alpha)Mg^{24}$ data of section 4, Chapter IV, along with a brief discussion of results. Part of the analysis (section 4.7) is presently in progress and it is stressed that the results given in section 4 and the discussion connected with them (section 5) must be considered rather preliminary.

Section 2. DATA HANDLING PROCEDURE.

2.1. Reduction of Analyzer Tapes.

The extraction of α-group yields from the R.I.D.L. analyzer printouts of the $C^{12}(O^{16},\alpha)Mg^{24}$ spectra was manual, and rather tedious. The following procedures were employed:-

(a) The yields for as many α-groups as were well resolved were extracted from each tape printout.

(b) For group pairs only partially resolved (α_5, α_6 frequently fell in this category), simple unfolding criteria based on estimates of the average α-group FWHM, were applied.

(c) Yields were generally simple sums over the channels under corresponding peaks, with the average FWHM used to estimate the summation limits. (For the weakest groups, α_0, α_6, the selection of reasonable summation limits was critical, since small spurious "background" contributions were scattered between spectral peaks).

(d) In some backward-angle spectra, the observable groups rested on a slowly rising background, and simple triangular subtractions were made.

(e) Relative spacings of apparent groups were checked to ensure correct correspondence with expected positions; this was necessary to avoid confusing weak "real" groups with small spurious contributions.

In future extensions of the $C^{12}(O^{16},\alpha)Mg^{24}$ measurements to higher O^{16} energies, analyzer outputs will be on punched tape* (in addition to printout), and an attempt will be made to extract group yields automatically, via a simple spectrum reduction program. This is expected to alleviate a large part of the laborious manual analysis.

* Tape punch outputs are presently being installed.

2.2. Raw Data Format.

The extracted group yields (for each O^{16} energy) were recorded as a matrix of numbers whose rows corresponded to lab. angles and columns to α-group numbers. This was actually a composite of 4 sub-matrices, each containing the output of a single sector of the detector array. Since tapes were reduced sequentially, yields in sub-matrices A, B were recorded (for convenience) with angles increasing from top to bottom, and the opposite way in submatrices C, D. Also recorded with each matrix $E(O^{16})$ were: (a) the 9 monitor readings corresponding to each detector array setting; and (b) the detector solid angle ratios in use at that energy.

2.3. Data Conversion Computer Program.

The elements of the raw yield matrices (i.e. the angular distributions for each α_i) were corrected, normalized, set in sequential angular order, and transformed to the c.m. system by a program* written for the A.N.U. 1620 computer; the operations of this program and the output obtained from it are described here.

*Coded by the writer in collaboration with D. E. Groce of this laboratory.

The program input for each O^{16} energy, punched onto cards, took the following form:-

(a) The 36 x 6 matrix of raw yield elements (36 lab. angles and 6 α-groups), one card per element. For matrix positions where yields were not obtained, elements were assigned a 0 (dummy) value. The matrix was read into computer memory by rows.

(b) The detector solid angle ratios (single card), and the 9 monitor readings (one per card) for the relevant raw yield matrix.

(c) The lab. energy of the raw yield matrix.

As the yield matrix elements Y_{ij} were read into computer memory, corresponding standard deviations ($\sqrt{\text{element}}$) were calculated and stored as a separate matrix (S.D.), having the same dimensions as Y. All following operations performed on Y were simultaneously performed on (S.D), so that the statistical uncertainties in the converted Y_{ij} were always proportional to that existing initially in the raw Y_{ij}. The converted $(S.D.)_{ij}$ were later used as statistical weights in the Legendre-Polynomial analysis of the converted Y_{ij}, discussed in section 4.1. Program flow from this point

was as follows:-

(a) Elements of each submatrix were divided by the appropriate detector solid-angle ratio to normalize all submatrices to submatrix A. (Actually to submatrix A of the initial (15.00 Mev)O^{16} energy).

(b) The ith row of each submatrix was divided by the monitor reading corresponding to each detector array setting, θ_i, and multiplied by a constant equal to the monitor reading for the setting of 15.00 Mev, i = 1.

(c) All Y_{ij} were multiplied by a Rutherford scattering scale factor equal to $[E(O^{16})/15.00\ \text{Mev.}]^2$. In combination with (b), this operation normalized the Y_{ij} to a constant (target-thickness) x (O^{16} integrated-flux) x (detector-solid-angle) product (i.e. that existing for the initial measurement of the 15.00 Mev angular distribution); this was based on the assumption (section 4.6, Chapter IV) that, within the small uncertainties discussed in that section, the monitor reading at $E(O^{16})$ could be expressed as:

$$M = k \cdot d\sigma_R/d\Omega(E_{lab}, 30^\circ)\left[T \cdot F \cdot \Omega_M\right] \qquad (5.1)$$

where $d\sigma_R/d\Omega(E_{lab}, 30^\circ)$ is the O^{16}-C^{12} Rutherford scattering differential-cross-section ($\sim 1/E^2(O^{16})$) at $E(O^{16})$ and 30°(c.m.), T, F, Ω_M are the target thickness integrated flux and monitor solid-angle respectively, and k is a kinematical constant introduced as a result of measuring the O^{16}-C^{12} scattering via the C^{12} recoils.

(d) The rows of submatrices C, D were inverted, so that the entire matrix Y_{ij} was arranged with its rows in correct angular sequence.

The program now entered a kinematics subroutine which (a) computed c.m. energies for each α-group; (b) computed c.m. angles for each Y_{ij}; and (c) transformed each Y_{ij} from the lab. system to the c.m. system, via the usual multiplication by appropriate Jacobians (computed for each Y_{ij}); in this operation all 0 Y_{ij} were ignored.

The program then printed out the completely transformed and normalized Y matrix in the form shown in Fig. 5.1, where each element position contains a corrected Y_{ij} paired with its c.m. angle. Zeros correspond to missing input Y_{ij}. Similar printouts were obtained from all O^{16} bombarding energies in the range 15.0-22.50 Mev. At

Fig. 5.1 Typical printout of converted yield matrix (for O^{16} energy of 19.50 Mev).

The top row, labelled "energies", gives O^{16} lab. energy and c.m. energies of alpha groups $\alpha_o - \alpha_6$. Columns of the "output matrices" are (from left) the detector array laboratory angles, followed in alternation by c.m. angles and corresponding converted yield elements, for groups $\alpha_o - \alpha_6$.

ENERGIES 19.50 12.96 11.79 9.38 8.49 7.82 7.44

OUTPUT MATRICES

2.	2.	258.9	2.	649.4	2.	0.0	2.	0.0	2.	0.0	2.	0.0
6.	8.	167.1	8.	512.8	8.	773.5	8.	26.5	8.	207.9	8.	82.8
11.	14.	67.1	15.	317.0	15.	534.8	15.	68.2	15.	163.9	16.	41.7
16.	21.	15.2	21.	263.3	22.	326.3	22.	98.5	23.	136.8	23.	26.9
21.	28.	8.5	28.	345.1	29.	190.1	29.	204.4	30.	150.5	30.	30.3
26.	34.	3.8	35.	461.0	36.	153.5	36.	276.4	37.	145.2	37.	20.8
31.	41.	7.3	41.	378.9	43.	152.5	43.	265.0	44.	158.3	44.	36.5
36.	47.	28.7	48.	176.3	50.	172.2	50.	281.0	51.	145.6	51.	41.0
41.	54.	42.8	54.	88.5	56.	147.5	57.	248.3	58.	111.1	58.	52.9
45.	59.	49.1	60.	100.3	61.	163.3	62.	290.7	63.	129.6	64.	189.0
49.	64.	60.0	65.	131.8	67.	130.8	68.	265.1	68.	179.4	69.	62.4
54.	70.	34.4	71.	135.8	73.	98.2	74.	272.8	75.	190.3	75.	79.3
59.	76.	45.6	77.	120.3	79.	111.8	80.	153.3	81.	249.3	82.	56.4
64.	82.	66.5	83.	110.9	85.	192.9	86.	98.7	87.	247.1	88.	75.8
69.	88.	53.0	89.	96.3	91.	287.8	92.	70.9	93.	255.6	94.	93.1
74.	93.	57.7	94.	172.6	97.	352.3	98.	71.0	99.	263.0	100.	36.3
79.	99.	75.5	100.	243.8	102.	517.6	104.	73.3	105.	207.3	105.	41.0
84.	104.	47.1	105.	259.8	108.	569.5	109.	81.4	110.	67.3	111.	55.5
88.	108.	26.3	109.	163.7	112.	445.6	113.	93.0	114.	106.8	115.	56.3
93.	113.	6.5	114.	150.1	117.	432.7	118.	72.6	119.	0.0	120.	0.0
98.	118.	8.4	119.	120.4	122.	496.6	123.	68.1	124.	0.0	125.	0.0
103.	122.	19.9	123.	78.0	126.	416.7	127.	0.0	129.	0.0	129.	0.0
108.	127.	38.3	128.	59.4	131.	449.3	132.	0.0	133.	0.0	134.	0.0
113.	131.	58.2	132.	51.1	135.	474.4	136.	0.0	137.	0.0	138.	0.0
118.	136.	93.7	136.	51.9	139.	579.2	140.	0.0	141.	0.0	142.	0.0
123.	140.	88.3	140.	85.3	143.	0.0	144.	0.0	145.	0.0	145.	0.0
127.	143.	88.1	144.	172.2	146.	0.0	147.	0.0	148.	0.0	148.	0.0
131.	146.	117.1	147.	260.2	149.	824.7	150.	0.0	150.	0.0	151.	0.0
136.	150.	124.4	150.	358.2	152.	725.2	153.	0.0	154.	0.0	154.	0.0
141.	153.	143.6	154.	474.4	156.	0.0	156.	0.0	157.	0.0	157.	0.0
146.	157.	189.1	157.	543.8	159.	0.0	160.	0.0	160.	0.0	160.	0.0
151.	160.	260.4	161.	547.4	162.	0.0	163.	0.0	163.	0.0	163.	0.0
156.	164.	364.3	164.	511.8	165.	0.0	166.	0.0	166.	0.0	166.	0.0
161.	167.	447.9	167.	531.0	168.	0.0	169.	0.0	169.	0.0	169.	0.0
166.	170.	611.9	171.	464.4	171.	0.0	172.	0.0	172.	0.0	172.	0.0
170.	173.	646.2	173.	445.1	174.	0.0	174.	0.0	174.	0.0	174.	0.0

completion of printout, the same output was punched onto cards in the following sequence: Y_{ij} paired with corresponding $(S.D.)_{ij}$ were punched by columns, (one element-pair per card), in alternation with columns of corresponding c.m. angles (also 1/card), so that the output card deck took the form of a sequential set of α_i angular distributions, with yields (Y_{ij}) preceding c.m. angles. Yield zeros and corresponding angles were not punched. A final card contained the number of yield points/each α_i angular distribution. The above output was in the form required for input to the Legendre-Polynomial angular distribution fitting program discussed in section 4.1.

Section 3. THE ANGULAR DISTRIBUTIONS.

The angular distributions, $W(\theta)$, transformed by the above program have been plotted for all α_i at each $E(O^{16})$ between 15.00 and 22.25 Mev. Representative α_0 and α_1 distributions at 2 different $E(O^{16})$ are shown in Fig. 5.2. Error bars are indicated for all points where the statistical uncertainties are greater than the dimensions of the points themselves, and the curves have been smoothly drawn through the corrected experimental points in the usual fashion.

Fig. 5.2 Representative $C^{12}(O^{16},\alpha)Mg^{24}$ angular distributions for the ground state and first excited state reactions, at several O^{16} lab. energies, showing typical statistical counting uncertainties.

TYPICAL $C^{12}(O^{16},\alpha_0)Mg^{24}$ AND $C^{12}(O^{16},\alpha_1)Mg^{24*}$
DIFFERENTIAL CROSS SECTIONS.

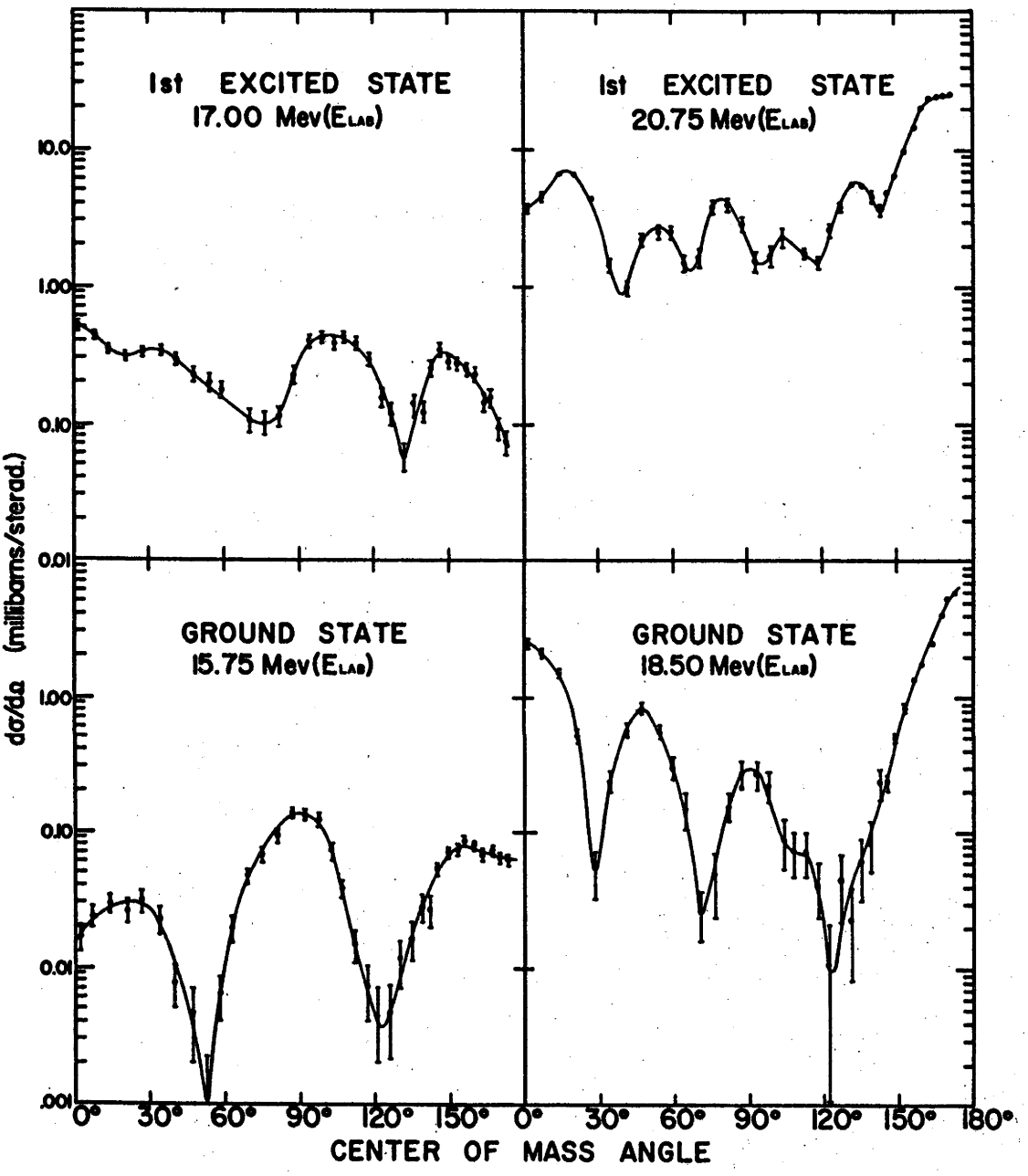

It is noted that average statistical errors are larger at midrange angles than for backward and forward angles; this is simply a reflection of the detector array geometry (section 4.2, Chapter IV) which required narrower detector angular definition (and therefore smaller solid angles and count rates) for the midrange angular sectors B, C than for the backward-forward sectors A, D. The severe kinematical effects also appear in the considerable expansion of forward angles and compression of backward angles in the Fig. 5.2. $W(\theta)$.

The absolute cross section scales are based on a constant factor multiplying the α-yield measured (in detector A) at the initial angular setting of the $E(O^{16}) = 15.00$ Mev distribution. The constant is computed from the theoretical O^{16}-C^{12} Rutherford scattering $d\sigma/d\Omega$ at the monitor detector angle, and the solid angles subtended by the monitor, and α-detector A; it contains an uncertainty, arising both from errors in the solid angle measurements and the statistical counting error in the normalizing yield, which is estimated to be $< 10\%$.

Fig. 5.2. indicates that the variation with angle of the $W(\theta)$ is very strong, and that, particularly at

higher O^{16} bombarding energies, the use of a large number of points (36) to accurately display the detailed $W(\theta)$ features is well justified.

3.1. Angular Distributions for α_0 and α_1 Groups.

The complete sets of α_0 and α_1 $W(\theta)$ measured in the O^{16} energy range covered are given in Figs. 5.3 and 5.4 respectively. These are displayed in vertical columns, (rather than isometric plots) because of their complex structure; adjoining $W(\theta)$ are displaced by scale factors of ten (log.). The lab. energies inserted at the left of the columns indicate the logarithmic baselines (each having a value of $1\mu b$) from which the correspondingly labelled $W(\theta)$ are to be measured. All distributions in the right-hand columns are multiplied by a 1/10 scale factor. For simplicity, all $W(\theta)$ are shown without experimental points; the curves were drawn to account for statistical uncertainties in a fashion similar to those of Fig. 5.2.

The following qualitative features are evident in the plots of Figs. 5.3 and 5.4:-

(a) Variation in amplitude with angle is much stronger in general for the α_0 $W(\theta)$ than for the α_1 $W(\theta)$.

Fig. 5.3 $C^{12}(O^{16},\alpha)Mg^{24}$ angular distributions from $E(O^{16})$ = 15.00 Mev to 22.25 Mev, for the ground state reaction.

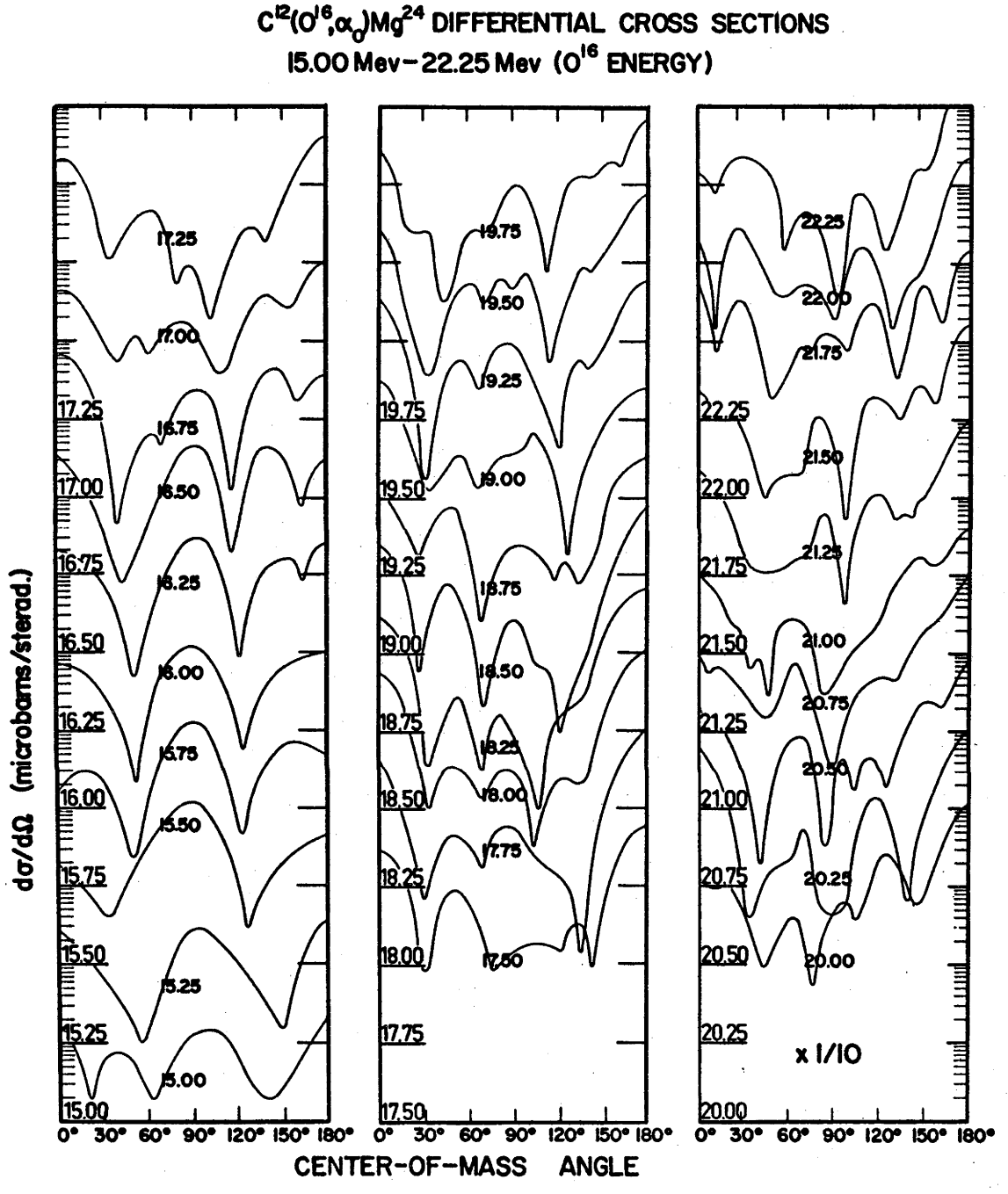
C12(O16,α0)Mg24 DIFFERENTIAL CROSS SECTIONS
15.00 Mev – 22.25 Mev (O16 ENERGY)
dσ/dΩ (microbarns/sterad.)
17.25
17.00
16.75
16.50
16.25
16.00
15.75
15.50
15.25
15.00
19.75
19.50
19.25
19.00
18.75
18.50
18.25
18.00
17.75
17.50
22.25
22.00
21.75
21.50
21.25
21.00
20.75
20.50
20.25
20.00
x 1/10
0° 30° 60° 90° 120° 150° 180°
CENTER-OF-MASS ANGLE

Fig. 5.4 $C^{12}(O^{16},\alpha)Mg^{24}$ angular distributions from $E(O^{16})$ = 15.00 Mev to 22.25 Mev for the first excited state reaction.

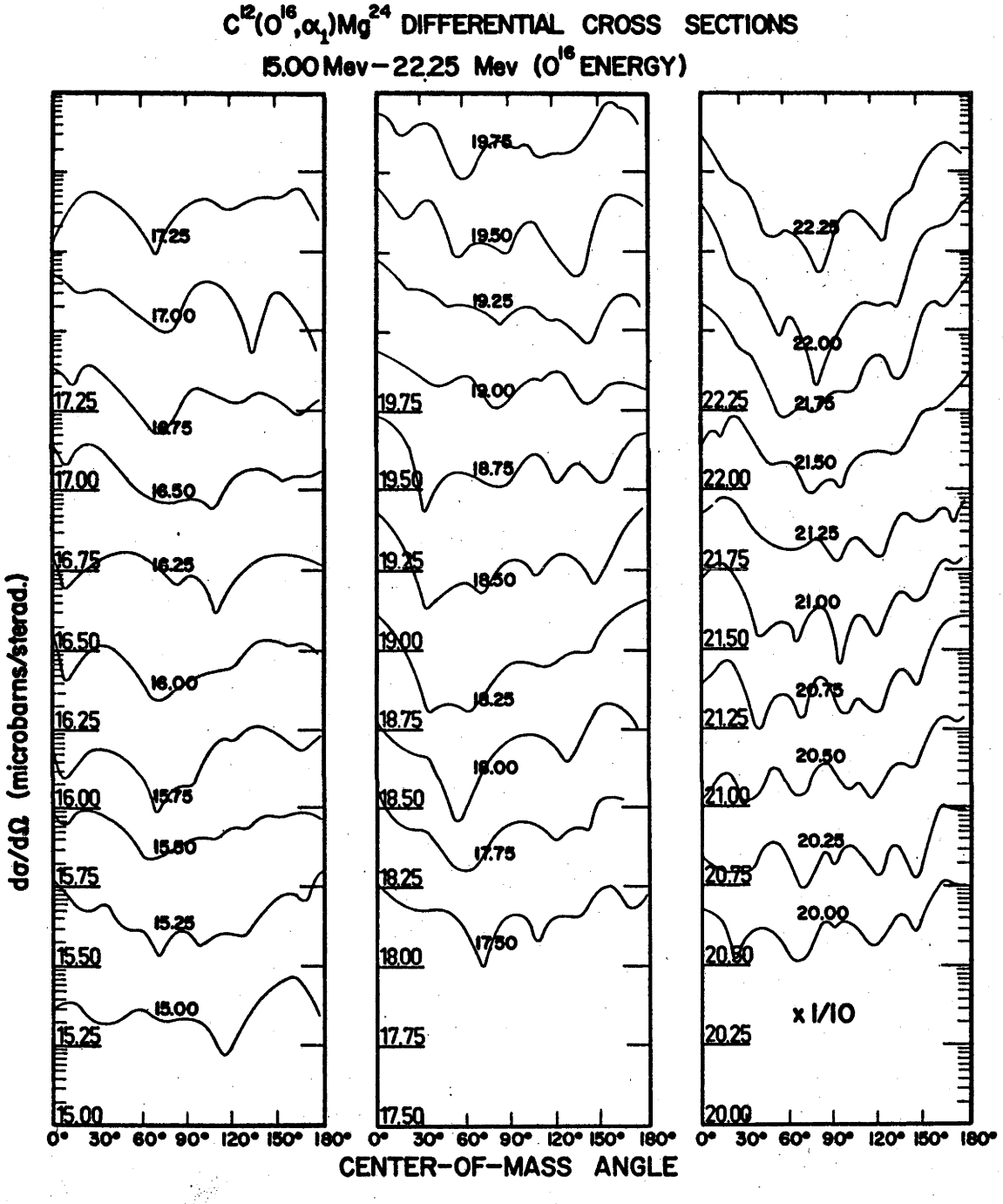
$C^{12}(O^{16},\alpha_1)Mg^{24}$ DIFFERENTIAL CROSS SECTIONS
15.00 Mev – 22.25 Mev (O^{16} ENERGY)
dσ/dΩ (microbarns/sterad.)
0° 30° 60° 90° 120° 150° 180°
CENTER-OF-MASS ANGLE
17.25
17.00
16.75
16.50
16.25
16.00
15.75
15.50
15.25
15.00
19.75
19.50
19.25
19.00
18.75
18.50
18.25
18.00
17.75
17.50
22.25
22.00
21.75
21.50
21.25
21.00
20.75
20.50
20.25
20.00
x 1/10

(b) Although the detailed shape of the $W(\theta)$ may change markedly in the minimum $E(O^{16})$ interval (250 kev), prominent features dominate over intervals as large as 1 Mev. This is not much less true for higher energies (near 20 Mev) than for lower (near 15 Mev.). This relatively weak overall-shape energy dependence is particularly noticeable in the α_0 $W(\theta)$ between $E(O^{16})$ = 15.25 and 16.25 Mev.

(c) The shape details of the $W(\theta)$ become rapidly more complex with increasing $E(O^{16})$; e.g. in the α_0 set, the 16.00 Mev $W(\theta)$ has only 2 distinct minima, whereas those at 18.00 Mev and 21.75 Mev possess 4 and 6 respectively. The trend towards increasing numbers of minima with rising $E(O^{16})$ is less obvious in the α_1 distribution set.

(d) The minima in the α_0 $W(\theta)$ set are very marked, going in several distributions to values near zero. In particular, it is noted that the 2, 4 and 6 minima appearing in the 16.00, 18.00 and 21.75 Mev distributions occur at angles corresponding closely to zeros of the P_2, P_4 and P_6 Legendre Polynomials respectively; this suggests that the relevant $W(\theta)$ contain strong contributions from such terms.

(e) There appears to be little correspondence at any O^{16} energy between shapes of $W(\theta)$ for the two α-groups, α_0, α_1.

3.2. Partial Angular Distributions for Higher α-groups.

$W(\theta)$ plots similar to the above for the higher groups $\alpha_{2+3}, \alpha_4, \alpha_5, \alpha_6$ cover angular ranges which decrease in magnitude with increasing group number, but increase gradually with rising O^{16} energy. Experimental reasons for this behaviour are given in sections 3.4 and 3.5, Chapter IV. These sets of partial $W(\theta)$ are not presented here, but their general features can be described as follows:-

(a) All sets show characteristics similar to those of the α_0, α_1 sets; i.e. relatively weak shape energy dependence (in .5 - 1.0 Mev intervals), coupled with rising complexity as $E(O^{16})$ is increased.

(b) The summed α_2, α_3 $W(\theta)$ are particularly complicated, as expected, since they include contributions for 2 α-groups.

(c) The α_4 $W(\theta)$ all show a sharp decrease at extreme forward angles, in accord with theory. (section 4.4).

(d) The α_5 $W(\theta)$ characteristics are qualitatively most similar to those of the α_1 set.

(e) The α_6 W(θ) are particularly interesting in that they reveal striking features similar to those of the α_0 set. Although the detailed shapes of the α_6 W(θ) are considerably different from the α_0 shapes (at any $E(O^{16})$), marked minima appear at positions of the P_2, P_4, and P_6 Legendre-Polynomial zeros in α_6 W(θ) corresponding to the same O^{16} energies (16.00, 18.00 and 21.75 Mev) at which the α_0 W(θ) show this character.

Section 4. EXTRACTION OF INTEGRATED-CROSS-SECTION EXCITATION FUNCTIONS.

Integrated-cross-section ($\sigma(\alpha_i)$ excitation functions were extracted from the α_1 W(θ) sets. For groups $\alpha_0 - \alpha_4$, this was accomplished by fitting the distributions with a Legendre-Polynomial (P_L) expansion, $W(\theta) = \sum_L A_L P_L(\cos\theta)$, and for groups α_5, α_6 by simple numerical integration of the W(θ). The latter procedure was also employed to check the results of the former for groups $\alpha_0 - \alpha_4$.

4.1 Least-Squares Legendre-Polynomial Fitting Program.

A modified version of an existing A.N.U. 1620 computer program was used to fit the W(θ) with P_L expansions,

via the least-squares method of Rose (Ro53). The existing program provided fits with P_L terms up to P_{12}. For reasons noted in section 4.2, Chapter IV, it was expected that α-particles from $C^{12}(O^{16},\alpha)Mg^{24}$, within the $E(O^{16})$ range covered in the present experiment, could be emitted with angular momenta as high as 8-10ħ. Since the maximum Legendre-Polynomial order appearing in an angular distribution of particles having angular momentum L is P_{2L}(Bl52), it appeared necessary to expand* the computer program to provide least-squares fits with terms up to P_{20}.

The program input was angular distribution data in the form described in section 2.3. This was visually edited with the aid of the plotted $W(\theta)$ sets, and a few questionable items of data were rejected. Data were considered questionable only if they both (a) fell well outside the smooth curve described by contiguous points, and (b) had been extracted from spectra obtained when the correct operation of the pulse-routing system (section 4.5, Chapter IV) was in doubt.

Program printout was in the form of the least-square fit (compared with input $W(\theta)$), followed by the P_L

*Program was expanded by D. E. Groce and B. A. Robson, of this laboratory.

coefficients (A_L) determined by the fit, and residual and statistical errors for these (showing goodness of fit) in the sense defined by Rose (Ro53).

To determine the highest order P_L required for a good fit to the experimental $W(\theta)$, sample distributions for each α-group (taken from different portions of the O^{16} energy range) were test-fitted with cyclicly increasing maximum P_L number. Criteria for "goodness of fit" were (a) that the A_L residual errors should not be $>$ twice the statistical errors, and that both should be $< 5\%$ of $|A_L|$ values; and (b) that the A_o coefficient should be changed only by very small amounts by further increases in maximum P_L number.

4.2. The α_o and α_1 Integrated σ from P_L Fits.

Integrated σ (σ is just $4\pi A_o$) excitation functions for groups α_o and α_1, extracted by the method of 4.1 are presented in Figs. 5.5 and 5.6. The highest order P_L required for "best fit" at higher O^{16} energies was P_{16}, although at progressively lower energies P_{10} and finally P_8 were sufficient.

The absolute cross-section scales are based on the scales of the Fig. 5.2, 5.3, 5.4 $W(\theta)$ sets. Error bars

Fig. 5.5 $C^{12}(O^{16},\alpha)Mg^{24}$ integrated σ excitation function from $E_{c.m.}(O^{16})$ = 6.4 Mev to 9.6 Mev, for the ground state reaction. Values of σ are obtained from P_L fits.

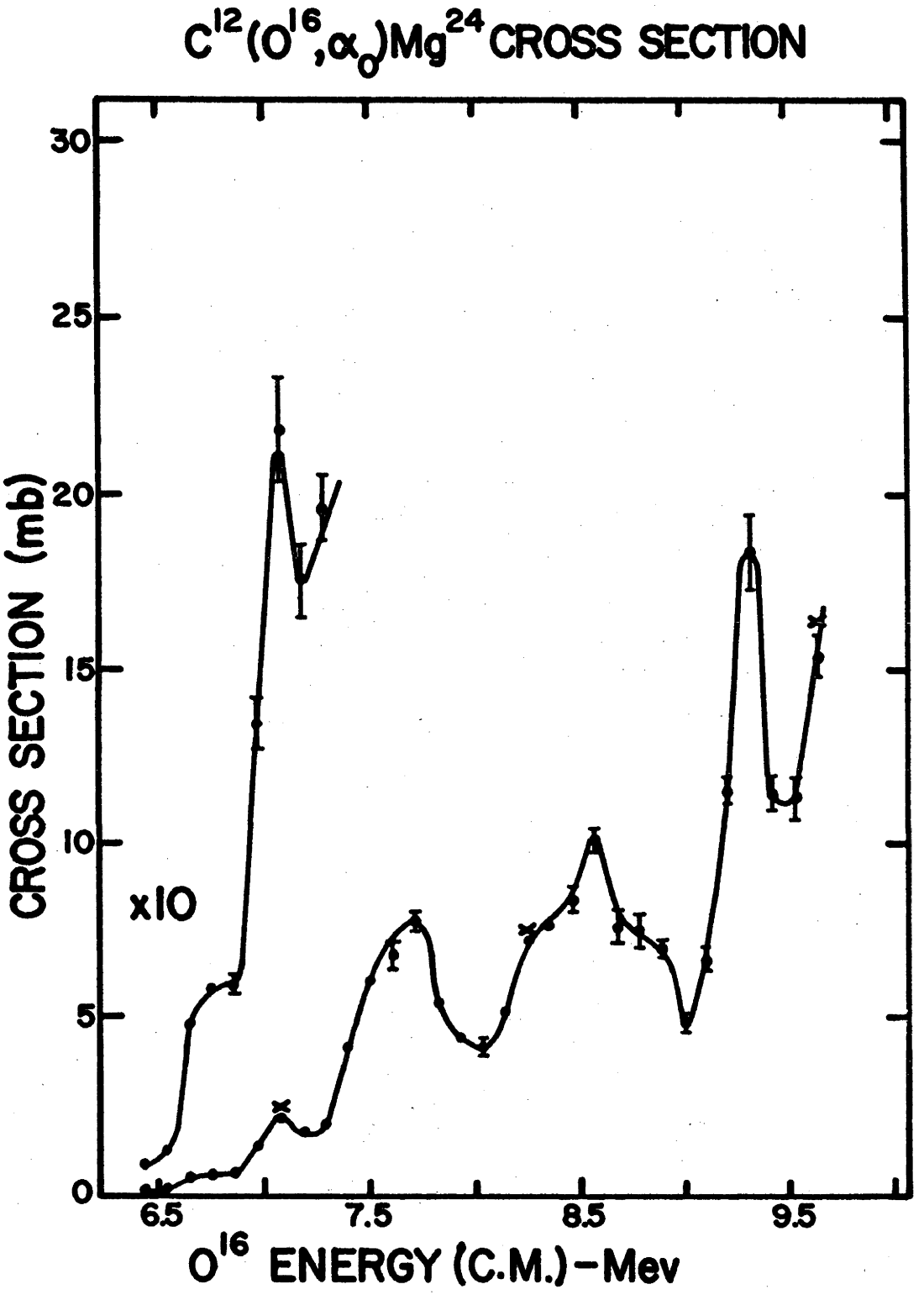
$C^{12}(O^{16},\alpha_0)Mg^{24}$ CROSS SECTION
CROSS SECTION (mb)
30
25
20
15
10
5
0
x10
6.5
7.5
8.5
9.5
O^{16} ENERGY (C.M.) – Mev

Fig. 5.6 $C^{12}(O^{16},\alpha)Mg^{24}$ integrated σ excitation function from $E_{c.m.}$ (O^{16}) = 6.4 Mev to 9.6 Mev, for the first excited state reaction. Values of σ are obtained from P_L fits.

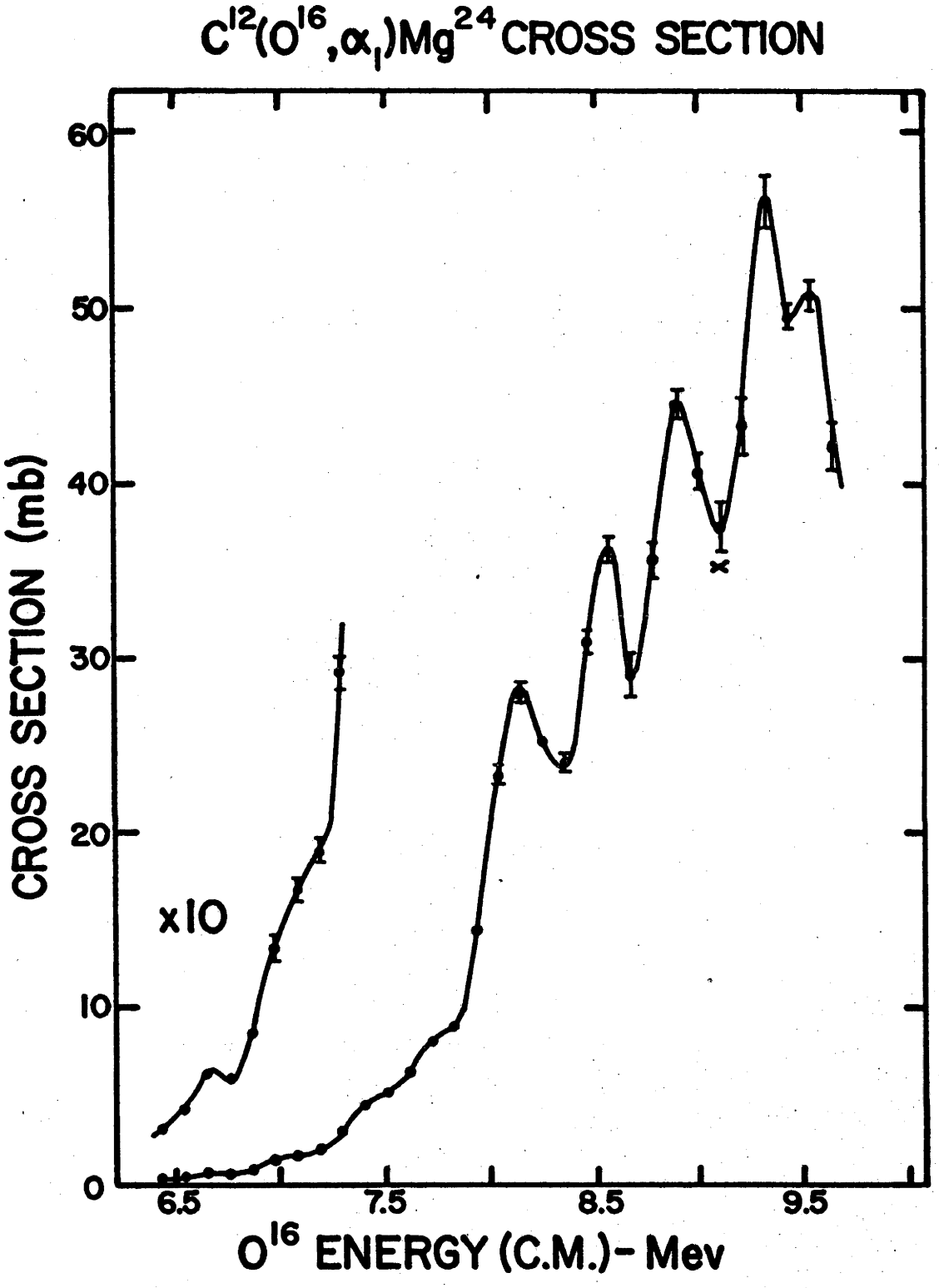
$C^{12}(O^{16},\alpha_1)Mg^{24}$ CROSS SECTION
CROSS SECTION (mb)
0
10
20
30
40
50
60
x10
6.5
7.5
8.5
9.5
O^{16} ENERGY (C.M.)- Mev

shown are residual fitting errors, which were always larger than the statistical errors. Crosses indicate values of σ obtained via the simple integration procedure of section 4.5, where they fall outside the residual errors of the σ values obtained from the P_L fits. The connecting curves have been drawn to account only for the latter. It is seen that both α_0, and α_1 excitation functions show several distinct peaks; some widths (FWHM) are as low as 200 kev (c.m.) and spacing between peaks is of order 500 kev (c.m.). Both α_0 and α_1 average σ show a marked increase over the observed energy range, which is attributed to Coulomb barrier penetration effects.

4.3. The α_{2+3} Integrated σ Excitation Function from P_L Fits.

The α_{2+3} $W(\theta)$ generally extended only to backward c.m. angles of 140° - 150°. This, however, provided a sufficient range to permit reasonable P_L fits to be carried out with a reduced maximum Polynomial order (P_8-P_{10} for higher energy distributions and P_6 at lowest energies). The extracted σ (α_{2+3}) excitation function is shown in Fig.5.7. It is seen that the residual fitting errors are considerably larger than those of the α_0, α_1, fits, reflecting the uncertainties introduced by the lack of experimental

Fig. 5.7 $C^{12}(O^{16},\alpha)Mg^{24}$ integrated σ excitation function from $E_{c.m.}$ (O^{16}) = 6.4 Mev to 9.6 Mev, for the second + third excited state reactions. Values of σ are obtained from P_L fits.

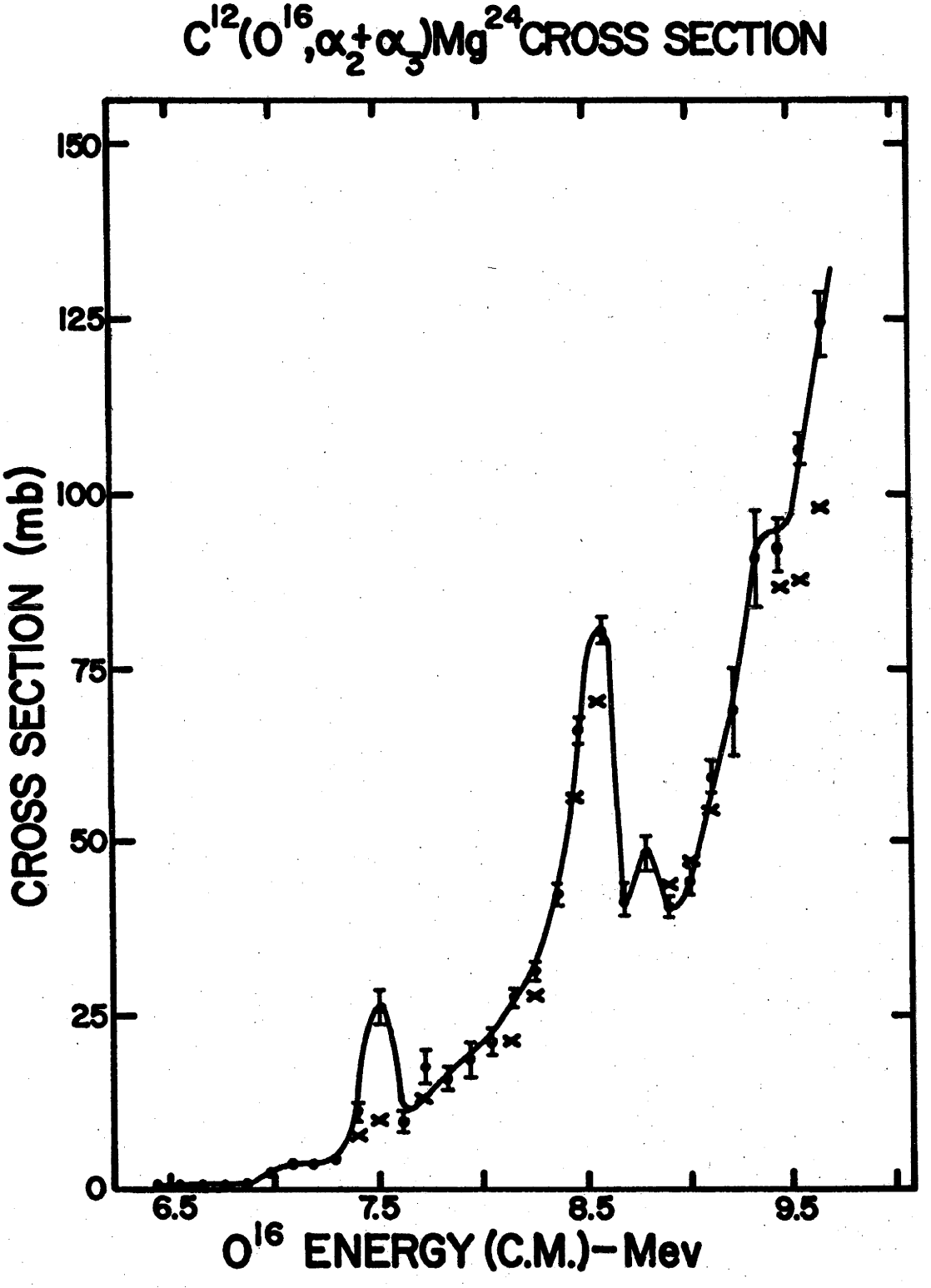
$C^{12}(O^{16},\alpha_2+\alpha_3)Mg^{24}$ CROSS SECTION
CROSS SECTION (mb)
150
125
100
75
50
25
0
6.5
7.5
8.5
9.5
O^{16} ENERGY (C.M.)– Mev

information at backward angles; in addition, the agreement with σ values obtained by numerical integration is not as good as for α_0, α_1 fits, as indicated by the larger number of crosses. The $\sigma(\alpha_{2+3})$ curve shows general characteristics similar to those of the $\sigma(\alpha_0)$ and $\sigma(\alpha_1)$ excitation functions.

4.4. The α_4 Integrated σ Excitation Functions from P_L Fits.

The angular range (c.m.) for which α_4 $W(\theta)$ data was available was even less than that for the α_{2+3} group. However, advantage was taken of a selection rule applying to the $C^{12}(O^{16}, \alpha_4)Mg^{24}$ reaction, to provide extra angular information. Litherland (Li61) has noted that reactions involving particles with all spins 0, and proceeding to "unnatural parity" states (1^+, 2^-, 3^+ etc.) in the final nucleus have the interesting property: $d\sigma/d\Omega(0^\circ, 180^\circ)=0$; this is a consequence of conservation of parity and angular momentum and is independent of the reaction mechanism or the nature of the compound system. Since the 4th excited state of Mg^{24} has spin-parity 3^+, and all reaction particles have spin 0, the $C^{12}(O^{16}, \alpha_4)Mg^{24}$ reaction satisfies these criteria, and the $d\sigma/d\Omega(\alpha_4)$ is expected to go to zero at 0° and 180°. Although experimental observations at exactly 0° were not performed, the rapid decrease in the

α_4 W(θ) at extreme forward angles, for all O^{16} energies (no exceptions), indicated that the selection rule held at 0^o; on this evidence it was also assumed valid at 180^o. Hence, 0^o and 180^o values of 0 were introduced into the α_4 W(θ) as additional points and heavily weighted in comparison with the existing experimental points.

Using this device it was possible to obtain reasonable P_L fits to the α_4 W(θ) with the same maximum Polynomial order as used for the α_{2+3} fits (P_6-P_{10}). The extracted $\sigma(\alpha_4)$ excitation function is given in Fig. 5.8., where the remarks of section 4.3 apply to residual error bars and numerical integration crosses. General characteristics of the $\sigma(\alpha_4)$ excitation function are similar to those for the lower α-groups.

4.5. The α_5 and α_6 Integrated σ Excitation Functions Numerical Integration.

The maximum c.m. angular range for which α_5 and α_6 data were available was generally 100^o-110^o, and reasonable fits to the W(θ) with P_L expansions could not be obtained. However, it appeared(from the consistency between P_L-extracted $\sigma(\alpha_{o,1,2+3,4})$ values and $\sigma(\alpha_{o,1,2+3,4})$ values obtained from direct integrations) that a good approximation to the $\sigma(\alpha_5, \alpha_6)$ values could

Fig. 5.8 $C^{12}(O^{16},\alpha)Mg^{24}$ integrated σ excitation function from $E_{c.m.}$ (O^{16}) = 6.4 Mev to 9.6 Mev, for the fourth excited state reaction. Values of σ are obtained from P_L fits.

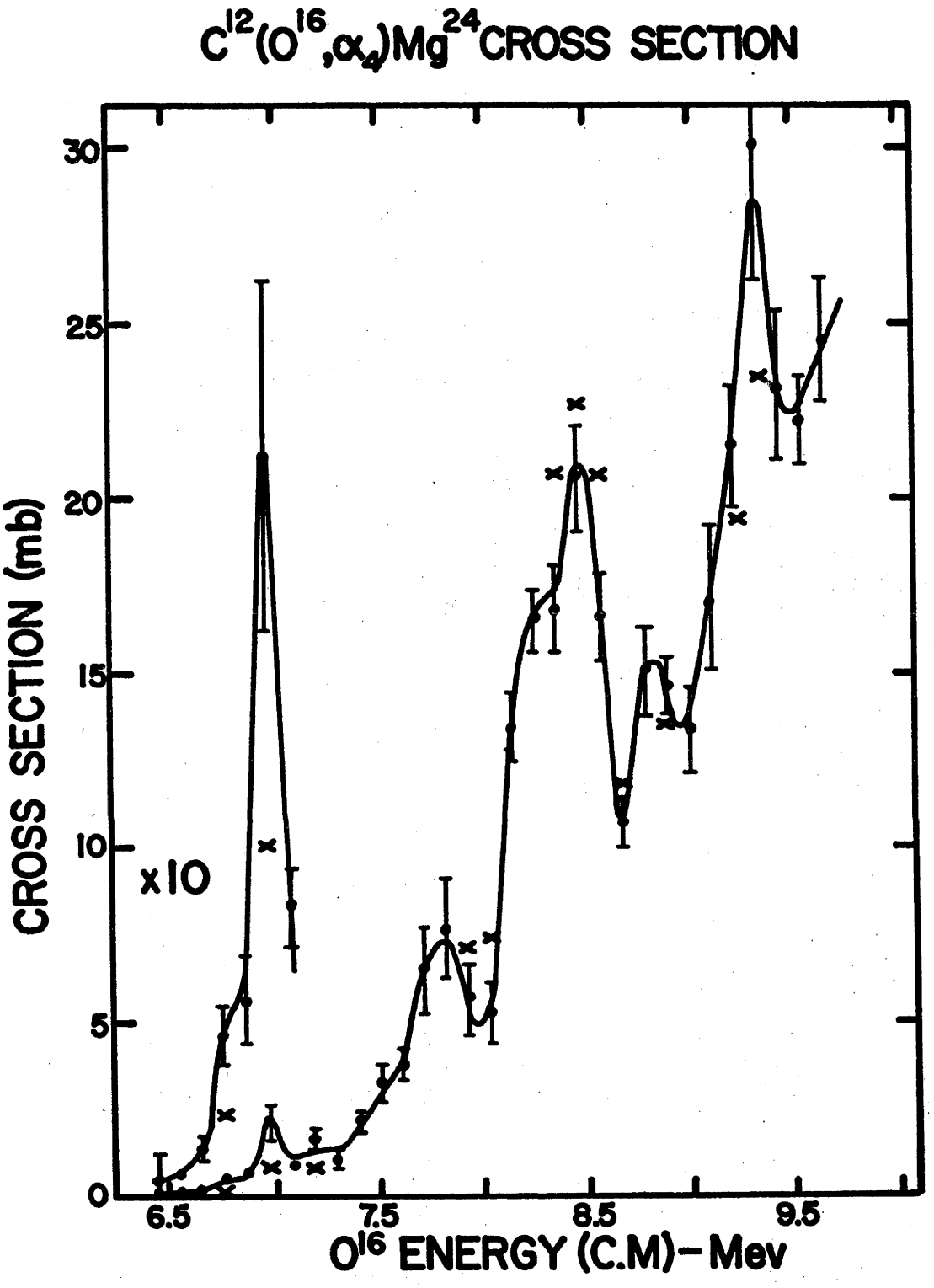
C12(O16,α4)Mg24 CROSS SECTION
CROSS SECTION (mb)
30
25
20
15
10
5
0
x10
6.5
7.5
8.5
9.5
O16 ENERGY (C.M)–Mev

be obtained via simple numerical integration of the α_5, α_6 $W(\theta)$.

The numerical integrations were carried out for all α_i $W(\theta)$ by a 1620 computer program* whose basis was the Trapezoidal Rule. For the α_0, α_1, groups the 0° and 180° $W(\theta)$ end points were estimated by visual extrapolation, and for the α_4 group were fixed by theory. For the α_{2+3}, α_5 and α_6 groups the no-data backward-angle region of the $W(\theta)$ was assigned a value, by the program, corresponding to the average amplitude in the forward-angle region. The σ excitation functions for groups $\alpha_0 - \alpha_6$, obtained by numerical integration, are shown in Fig. 5.9.

Of particular interest are the $\sigma(\alpha_5, \alpha_6)$, since the curves for the lower α-groups are essentially the same (except as noted in the appropriate section) as those of Figs. 5.5-5.8. Although the uncertainties in relative values of the $\sigma(\alpha_5, \alpha_6)$ are estimated to be large (probably $\sim 30\%$), the major amplitude changes in the $\sigma(\alpha_5, \alpha_6)$ excitation functions are nevertheless thought to be meaningful. Fig. 5.9 indicates that the α_5, α_6 curves show general characteristics similar to those of the curves for lower α-groups.

*Written by D. E. Groce.

Fig. 5.9 $C^{12}(O^{16},\alpha)Mg^{24}$ integrated σ excitation functions from $E_{c.m.}$ (O^{16}) = 6.4 Mev to 9.6 Mev, for the ground state, and first, second + third, fourth, fifth, and sixth excited state reactions. Values of σ are obtained by numerical integration.

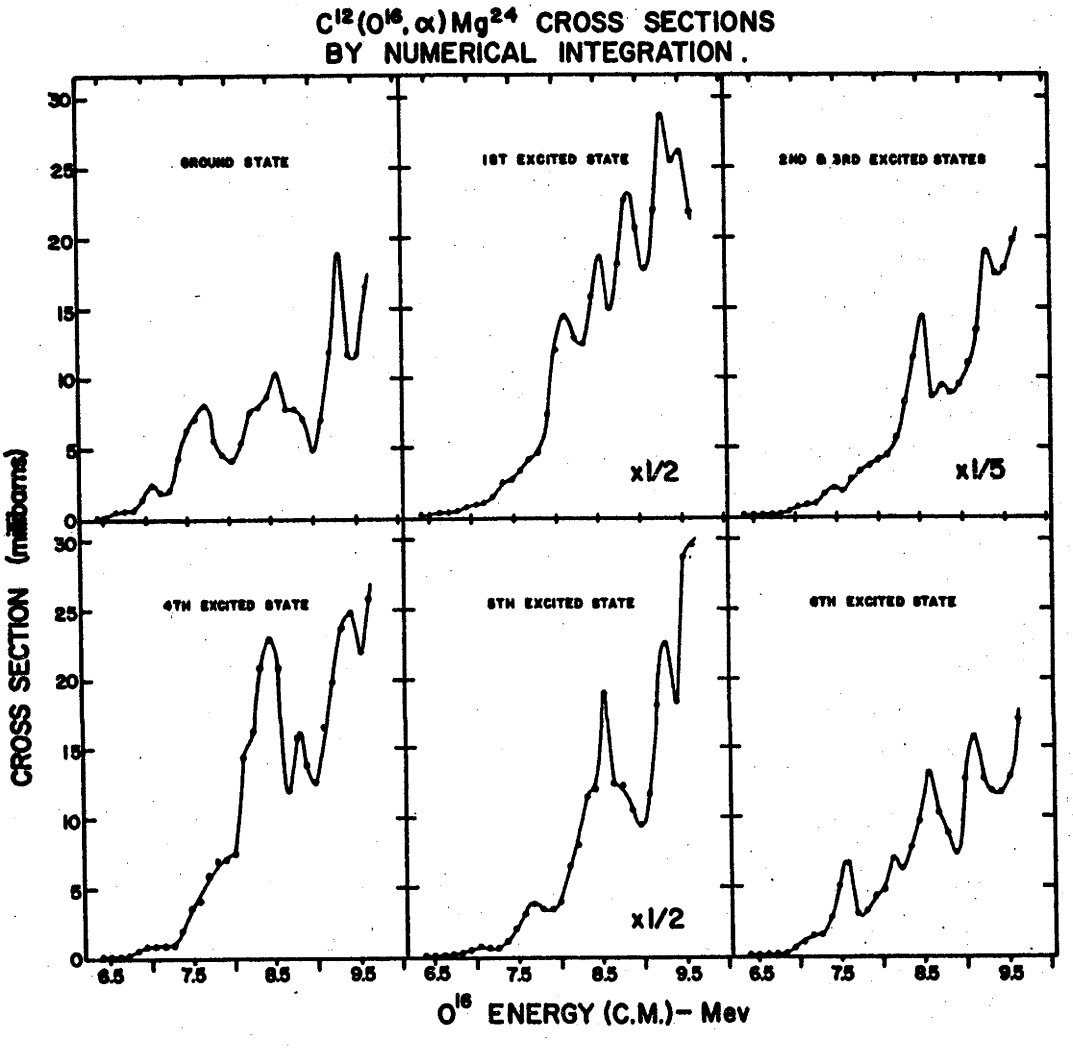
$C^{12}(O^{16},\alpha)Mg^{24}$ CROSS SECTIONS
BY NUMERICAL INTEGRATION.
GROUND STATE
1ST EXCITED STATE
2ND & 3RD EXCITED STATES
4TH EXCITED STATE
5TH EXCITED STATE
6TH EXCITED STATE
x1/2
x1/5
x1/2
CROSS SECTION (millibarns)
O^{16} ENERGY (C.M.)- Mev
0
5
10
15
20
25
30
6.5
7.5
8.5
9.5

4.6. Correlations Between Integrated $\sigma'(\alpha_i)$ Excitation Functions.

In order to determine the extent of correlation between the integrated σ' excitation functions for different α-groups, the c.m. energies of all cross section peaks have been listed in Table 5.1. For the $\sigma'(\alpha_i)$ obtained from both P_L fits and numerical integration, those energies for which prominences do not appear in both curves are labelled with an asterisk.

The approximate energies of very marked "shoulders" in the $\sigma'(\alpha_i)$ curves are also listed, and labelled with crosses to distinguish them from clear-cut-peaks.

TABLE 5.1.

$\sigma(\alpha_0)$	$\sigma(\alpha_1)$	$\sigma(\alpha_{2+3})$	$\sigma(\alpha_4)$	$\sigma(\alpha_5)$	$\sigma(\alpha_6)$
6.7+	6.7	6.7	6.7		
7.1	7.1+	7.1+	7.0*	7.1	7.1+
		7.5*			7.5
7.7	7.7+	7.7*	7.8	7.7	
	8.1				
8.3+			8.3+		8.2
8.6	8.6	8.6	8.5	8.6	8.5
8.8+	8.8	8.8	8.8	8.8+	
9.3	9.3	9.3+	9.3	9.3	9.2
	9.6				

The uncertainty in Table 5.1 energies is ± 0.1 Mev, due mainly to the relatively low density of curve points. Entries have been made in such a way that "resonance" postions in each $\sigma(\alpha_i)$ column are horizontally aligned if their energies are the same within this uncertainty.

An inspection of Table 5.1 reveals the following:-

(a) Nearly all $\sigma(\alpha_i)$ excitation functions show resonance-like behaviour at c.m. energies (within ± .1 Mev) of

7.1, 7.7, 8.6, 8.8 and 9.3 Mev.

(b) At several of the remaining energies (6.7, 7.5, 8.3 Mev), resonance-like behaviour occurs in a smaller but still significant number of the $\sigma(\alpha_i)$ curves.

(c). Only for two instances (8.1 and 9.6 Mev), both in the $\sigma(\alpha_1)$ excitation function, are there no corresponding peaks in other $\sigma(\alpha_i)$ curves.

4.7. Analysis of α_0 Integrated σ Excitation Function.

It has been noted, in connection with a study of $C^{12}(C^{12},\alpha)Ne^{20}$ (Ku63b) that alpha-particles emitted from reactions involving only spinless particles and zero entrance and exit channel spins have a particularly simple angular distribution, which can be written as:

$$W(\theta) = \left|\sum_L (2L+1)^{\frac{1}{2}}(A_L+iB_L)P_L(\cos\theta)\right|^2 \qquad (5.2)$$

where the angular momenta L carried by the alpha particles are just the spins J of the contributing states of the intermediate compound system. If the reaction proceeds through only a single isolated compound system level (in the Breit-Wigner sense), this expression reduces to:-

$$W(\theta)_J = \left| (2J+1)^{\frac{1}{2}}(A_J+iB_J)P_J(\cos\theta) \right|^2 \qquad (5.3)$$

which directly connects the level spin J with the form of the angular distribution.

The ground state and 6th excited state of Mg^{24} have spin-parity 0^+(En62b), so that alpha particles from both the corresponding reactions $C^{12}(O^{16}, \alpha_0, \alpha_6)Mg^{24}$ must have angular distributions which can be represented by the general form (5.2).

An inspection of the α_0 $W(\theta)$, $E(O^{16})$=15.0-22.5 Mev. (lab.), of Fig. 5.3 and the α_6 distribution set (not shown) revealed that the possibility of obtaining good fits with the reduced expression (5.3) was negligible, the implication being that the $C^{12}(O^{16},\alpha)Mg^{24}$ reaction (in the given O^{16} energy range) does not in fact proceed through isolated single compound system levels. However, it seemed clear that direct information on the relative amplitudes with which compound states of different spins J are excited in the $C^{12}(O^{16},\alpha)Mg^{24}$ reaction (as function of $E(O^{16})$ could be obtained by fitting the α_0 $W(\theta)$ with the general expression (5.2.). Such work is presently being carried out, using an iteration computer program*, similar to that

*Basic program was supplied by D. H. Hebbard and considerably expanded by D. E. Groce.

employed by Kuehner et al. (Ku63b) in fitting $C^{12}(C^{12}, \alpha_0)Ne^{20}$ $W(\theta)$ with the expression (5.2). This work is not complete and no results are given here.

Although, in principle, the α_6 distributions could be treated in the same fashion and should yield similarly useful information, it is thought that their incomplete angular range will not permit meaningful unambiguous fits with (5.2) to be obtained.

The behaviour (as a function of energy) of the relative amplitude (A_J+iB_J) extracted from the (5.2) fits to the α_0 $W(\theta)$, is expected to partially indicate the nature of the $\sigma(\alpha_i)$ excitation function "resonance" structure, and in particular my show whether these peaks are produced by a compound-system reaction mechanism characterized (at each peak) by dominant spins J.

It is appropriate to note here that, as recorded earlier, several of the α_0 and α_6 $W(\theta)$ show structure strongly indicative of dominant Legendre-Polynomial (A_L+iB_L) amplitudes. These distributions occur, significantly, at c.m. energies of 6.7, 7.7, and 9.3 Mev, which correspond to peak positions in most of the $\sigma(\alpha_i)$ excitation functions (Table 5.1); the important Polynomial terms at these energies

appear to be P_2, P_4 and P_6 respectively, leading to the tentative suggestion that the $C^{12}(O^{16},\alpha)Mg^{24}$ reaction mechanism is dominated at the corresponding Si^{28} excitations by compound-system resonances characterized by spins J = 2, 4 and 6 respectively. At some of the remaining Table 5.1 energies, the α_0 and α_6 angular distributions show behaviour reminiscent of strong P_5 and P_3 contributions, suggesting the possibility that other $\sigma(\alpha_i)$ peaks might be due to compound-system resonances of odd spins J=3,5. However, the qualitative angular distribution evidence for these is much weaker than that for the even spins. In the absence of quantitative confirmation via the (5.2) fitting program, the foregoing remarks must in any case be treated as little more than speculation.

As additional information bearing on the $C^{12}(O^{16},\alpha_0)Mg^{24}$ reaction mechanism, the results of the $E(O^{16})$ = 32.00 Mev (lab.) preliminary experiment described in section 4.8, Chapter IV are introduced at this point*. The α_0 angular distribution at backward angles is shown in Fig. 5.10, along with an attempted fit of the simplified form (5.3), $W(\theta)\ P_8^2(\cos\theta)$; the theoretical curve is

*These have been published in Physics Letters (Qu63).

Fig. 5.10 $C^{12}(O^{16},\alpha)Mg^{24}$ partial angular distributions for the ground state reaction at E_{lab} (O^{16}) = 32.0 Mev, and attempted fit with a theoretical distribution of the form $(P_8(\cos\theta))^2$.

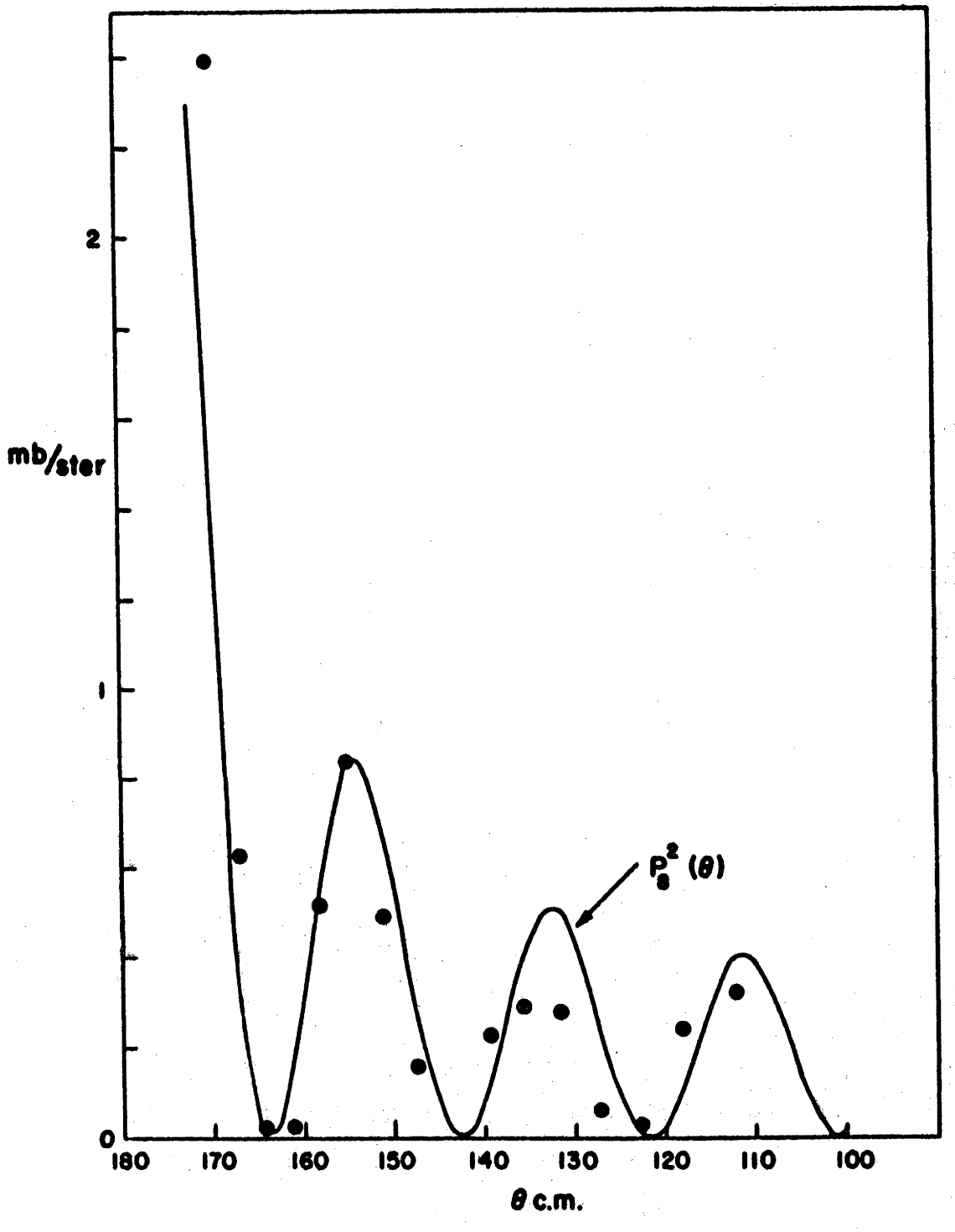
mb/ster
2
1
0
180
170
160
150
140
130
120
110
100
θ c.m.
$P_8^2(\theta)$

normalized to the experimental angular distribution at 155° (c.m.). The fit is not very satisfactory at angles near 135°, and the missing forward-angle data introduce a large uncertainty. However, in the sense outlined above, these 32.00 Mev (13.70 Mev in c.m. system) results do indicate the probable dominance of the P_8 relative amplitude (A_8+iB_8) in the more general fit (5.2), and suggest that a Si^{28} compound-system state (or states) of J = 8 is strongly excited in the $C^{12}(O^{16},\alpha_0)Mg^{24}$ reaction at this energy.

Section 5. DISCUSSION OF PRESENT RESULTS.

5.1. Previous Work on the $C^{12}(O^{16},\alpha)Mg^{24}$ Reaction.

The $C^{12}(O^{16},\alpha)Mg^{24}$ reaction has been previously investigated with Tandem Van de Graaff energies and precision by (a) Hinds, Middleton, and Litherland (Hi61), who measured a single angular distribution at 24 Mev O^{16} bombarding energy (using a multigap magnetic spectrograph); (b) Evans et al.(Ev63) who measured the 0° and 12° $d\sigma/d\Omega$ excitation functions between $E(O^{16})$ = 16.0 and 19.0 Mev for the α-groups feeding the g.s. and 1st 4 excited states in Mg^{24}, and verified the application of the selection rule discussed in section 4.4 to the (3^+) 4th excited state reaction; (c) Halbert et al.(Ha63), who have measured the

α_0, α_1, α_{2+3}, and α_4 $d\sigma/d\Omega$ excitation functions at 30°, 149° (lab.) over the O^{16} energy ranges 16.8 - 21.6 Mev and 30.0. - 32.8 Mev. (100 kev steps in lab. system).

The last experiment (c) is of particular interest since the lower energy range coincides almost exactly with that of the main body of the present work, and the higher interval includes the energy (32.0 Mev lab.) at which the preliminary angular distribution data (section 4.8, Chapter IV) were obtained. The $d\sigma/d\Omega$ of Halbert et al. (Ha63) show strong energy dependence similar to that of those presented in section 3.6, Chapter IV. Their energy step size of 100 kev (lab.), however, was much smaller than that employed in our $d\sigma/d\Omega$ reaction survey (500 kev) and even that used in the detailed angular distribution study (250 kev); a considerable amount of the $d\sigma/d\Omega$ structure observed in their work possesses width of $\sim$100 kev, which suggests that the point density in the $\sigma(\alpha_i)$ excitation functions of Figs. 5.5 - 5.9 may not have been adequate to reveal all details of the cross-section energy dependence.

5.2. Statistical Cross Section Fluctuations Interpretation.

Halbert et. al.(Ha63) have analyzed the marked energy dependence of their $d\sigma/d\Omega(30^\circ, 149^\circ)$ in terms of

the recently developed Statistical Fluctuation Theory (Er60, 62, 63), assuming that $\Gamma >> D$ in the compound system Si^{28} at the high excitations involved (24-31 Mev), and that the Statistical Model therefore applies. (See Chapter VI for elaboration of these and following points). They have performed autocorrelation and cross-correlation calculations on all $d\sigma/d\Omega(30^\circ,149^\circ)$ for all α-groups, and find (a) an average compound system "width" Γ of 116 kev; (b) no apparent correlations between $d\sigma/d\Omega(30^\circ,149^\circ)$ for different α_i (some exceptions in lower energy range). These results are questionable on the grounds that (a) the average $d\sigma/d\Omega(30^\circ,149^\circ,\alpha_i)$ amplitudes are not at all independent of energy within the intervals over which the correlation functions are taken (this is a fundamental requirement for application of Fluctuation Theory); in fact they are very sharply rising, since the Coulomb barrier falls within this energy region; and (b) the detailed work of Chapter VI on $Al^{27}(p,\alpha)Mg^{24}$ cross-section fluctuations indicates that, due to the possible breakdown of one of the main Fluctuation Theory (Er63) assumptions (that Γ is independent of compound-system spin, J), correlation analyses of differential-cross-section excitation functions may not be very meaningful (i.e. may be strongly dependent on the angles at which the $d\sigma/d\Omega(\theta)$

are measured).

The integrated $\sigma(\alpha_i)$ excitation functions obtained in the present work have not been subjected to statistical fluctuation correlation-function analysis, for the operational reason (a) given above. In any case, it is thought that Table 5.1 provides sufficiently strong evidence for large correlations between the $\sigma(\alpha_i)$ excitation functions to enable the statistical-fluctuation interpretation of their resonant behaviour to be rejected - one of the important predictions of the Statistical Fluctuation model being that there should be essentially no correlation between amplitude-fluctuations in cross sections corresponding to different states in the final nucleus.

Moreover, the $C^{12}(O^{16},\alpha)Mg^{24}$ $W(\theta)$ (Figs. 5.3, 5.4) are relatively slowly varying with energy, showing only gradual changes over 300-400 kev (c.m.) intervals; this behaviour is not consistent with that predicted by statistical fluctuation theory, which expects strong $W(\theta)$ energy dependence within energy intervals $\lesssim$ the widths of cross-section peaks (in this case $\sim$ 200 kev, c.m.).

A statistical fluctuation interpretation of the

$C^{12}(O^{16},\alpha)Mg^{24}$ cross sections is not, of course, ruled out at higher O^{16} energies than those covered in the present work.

5.2. Quasi-molecular Resonance Interpretation.

The lack of clear statistical behaviour for the $C^{12}(O^{16},\alpha)Mg^{24}$ reaction at Si^{28} excitations where $\Gamma >> D$ is expected to be a good approximation, indicates that the reaction may proceed via a mechanism in which a "classical" compound nucleus is not actually formed; i.e. since the relative K.E. of target and incident nuclei is below the Coulomb barrier for the system, and large orbital angular momenta (up to $8\hbar$) can be involved, the two nuclei may be prevented by the net repulsion from dissolving into a compound system.

This leads directly to the suggestion that the resonant behaviour observed in the $\sigma(\alpha_i)$ excitation functions may be similar to the"quasi-molecular" resonances of 100-200 kev width reported by Almqvist et al. (A163) in the $C^{12}(C^{12},\alpha)Ne^{20}$ $\sigma(\alpha_i)$ at c.m. energies in the $C^{12}+C^{12}$ system near 6.0 Mev (Mg^{24} compound-system excitations of 20 Mev). Such states in the $C^{12}+C^{12}$ system were initially revealed in the total reaction cross section, the elastic

scattering, and in the total n, p, α and γ yields (Br60, Al60), and are characterized by very large C^{12} emission reduced widths (more than 10 times that for α-emission, and 100 times the average nucleon width). In the "molecular" states, the target and incident nuclei are thought to be connected by surface interactions, while Coulomb repulsion, the angular momentum barrier, and re-arrangement energy inhibit immediate collapse into a compound nucleus of small radius. Theoretical explanations have been given by a number of authors (Vo60, Da60, Wi61, Al60), but these are not discussed here. Similar phenomena have not been observed at Coulomb barrier energies in the nearby $O^{16}+O^{16}$ system in either the elastic scattering or total (n,p,α,γ) yields. In the $C^{12}+O^{16}$ system, which is of primary interest in the present work, no resonant behaviour has been observed in the elastic scattering near barrier energies (Br60), but strong resonant behaviour appears at higher energies (12-15 Mev c.m.). However, this is thought to be different from the lower-energy quasi-molecular resonances, (Ku63a) and explainable in terms of statistical fluctuations due to overlapping compound nucleus state.

If the $C^{12}(O^{16},\alpha)Mg^{24}$ $\sigma(\alpha_i)$ excitation function resonances observed in the present work are in fact due to

a quasi-molecular reaction mechanism, precise compound-system spins should be associated with them (as demonstrated for the $C^{12}(C^{12},\alpha)Ne^{20}$ $\sigma(\alpha_i)$ resonances by Almqvist et al. (A163)). Whether or not this is the case is expected to be revealed by the behaviour (in the neighbourhood of the $\sigma(\alpha_o)$ peaks) of the (A_L+iB_L) parameters extracted from the (5.2) fits to the α_o (Fig. 5.3) angular distributions. Until these have been completed, no further conclusions can be drawn.

CHAPTER VI

STATISTICAL FLUCTUATIONS IN $Al^{27}(p,\alpha)Mg^{24}$ CROSS SECTIONS.

CHAPTER VI

Section 1. INTRODUCTION.

With the advent in recent years of variable high energy and high resolution charged particle beams, provided by Tandem Van de Graaf accelerators, it has become possible to examine in detail the excitation energy range 15 - 30 Mev in light and medium weight nuclei. Much of the data obtained in this region show the following characteristics, independent of bombarding particle, target nucleus, and reaction type:

(a) Differential and integrated cross sections reveal strong energy dependence. Excitation functions take the form of series of pronounced maxima having irregular width and spacing. Average widths and spacings are of order 10 - 100 kev. The fluctuations are of the same order of magnitude as the average cross sections, which are slowly varying functions of energy.

(b) Angular distributions show very strong energy dependence, and contain large fractions of odd order Legendre Polynomial terms. Isolated angular distributions can be fitted with combinations of

simple direct interaction mechanisms, but parameters extracted are unable to provide fits for neighbouring distributions differing in energy by as little as 20 kev.

1.1. Experimental Evidence for Cross Section Fluctuations.

The $Al^{27}(p,\alpha)Mg^{24}$ data whose broad features are discussed in Chapter III, shows the behaviour noted above. Similar results have been reported by many workers in recent years, and a partial list is given here. Only the excitation function data are recorded.

Warsh, et al. (Wa63) have measured the $Al^{27}(p,\alpha)Mg^{24}$ α_0 and α_1 $d\sigma/d\Omega(90^0)$ excitation functions at E_p=3-12 Mev in 50 kev steps, Allardyce et al.(Al63a) have measured $d\sigma/d\Omega$(several angles) for the same reactions in the range E_p= 9-12 Mev, and Ogata et al.(Og60) have obtained similar data at proton energies of 10-14 Mev. The first two experiments were performed with Tandems (few kev resolution), but the third was performed with a variable energy cyclotron (25 kev resolution).

Jenkin et al.(Je63) have measured the $F^{19}(p,n)Ne^{19}$ total in the range E_p= 4.9-11.0 Mev, and Warsh et al.(Wa63) have obtained $d\sigma/d\Omega(70^0,165^0)$ for $F^{19}(p,\alpha_0)O^{16}$ in the range E_p= 3-12 Mev. Lawrence and Hay(La63) report $Mg^{26}(P,\alpha)Na^{23}$ α_0 and α_1 $d\sigma/d\Omega(90^0;135^0)$ excitation

functions in the range E_p= 6 - 9 Mev. A heavy ion experiment showing cross section fluctuations is reported by Halbert et al.(Ha63) who have measured $C^{12}(O^{16},\alpha)Mg^{24}$ $\alpha_0, \alpha_1, \alpha_2, \alpha_3, \alpha_4$ $d\sigma/d\Omega(3^o,149^o)$ excitation functions in the $E(O^{16})$ ranges 16.8 - 21.6 Mev and 30.0 - 32.8 Mev; because entrance and exit channel spins are 0 for $C^{12}(O^{16},\alpha)Mg^{24}$ and all reaction particles have 0 spin, this work is of particular interest (see Chapter V).

Owing to the simple experimental conditions obtaining (described in Chapter II), extensive data have been obtained for neutron-induced charged particle reactions in the Silicon isotopes. Colli et al. (Co63, Co62a:b:c) report integrated σ excitation functions for $Si^{28}(n,\alpha)Mg^{25}$ $(\alpha_o - \alpha_6)$ in the neutron energy range 12.5 - 18.5 Mev. Potenza (Po63) has measured σ for $Si^{28}(n,\alpha)Mg^{25}$ (α_o, α_1) between E_n = 3.5 and 5.5 Mev, and Andersson-Lindström reports similar data between E_n= 6.00 and 9.00 Mev. The $Si^{29}(n,\alpha)Mg^{26}$ (α_o, α_1) integrated cross sections have been measured by Potenza (Po63) for E_n= 3.5 - 5.5 Mev. Similar work on $Si^{28}(n,p)Al^{28}$, feeding the lowest states of Al^{28}, has been reported by Potenza (Po63) and Andersson-Lindström (An63) in the ranges E_n= 3.5 - 5.5 Mev and E_n = 6.0 - 9.0 Mev, respectively. Tsukada (Ts63) has measured

the total Si^{28} neutron cross section in the range E_n= 3.0 - 5.0 Mev. Neutron energy resolutions for the above work were typically 20 kev, and all total and partial cross sections for the listed reactions show strong fluctuating energy dependence.

The only cross section fluctuation data reported for nuclei heavier than the mass range 20 - 30 is that of Lee and Schiffer (Le63) who have measured $Ni^{58}(p,p)Ni^{58}$, and $Ni^{60}(p,p)Ni^{60}$ $d\sigma/d\Omega(90^{o})$ excitation functions in the range E_p= 7.0 - 12.0 Mev.

The above survey serves only to indicate the great variety of reactions which exhibit strongly fluctuating cross section energy dependence; the single common feature is that all compound system excitations lie in the range E = 15 - 30 Mev. Since experimental resolution sufficiently narrow to reveal the detailed nature of the fluctuations has only recently become available at the corresponding bombarding energies, it is only now becoming clear that such phenomena are the rule, rather than the exception, at high compound excitations.

1.2 Direct and Compound System Reaction Mechanisms.

Questions which immediately arise are:- (a) What reaction mechanisms are responsible for the cross section

fluctuations; and (b) What nuclear information can be obtained from data of this type.

The general situation is extremely complex, since the following competing processes contribute to the cross sections: (a) Simple direct interaction (D.I.), singly or in combination; (b) Compound nucleus reactions; (c) Interference between compound nucleus and direct reactions; and (d) Semi-compound processes, in which only a few nucleons of the target nucleus are excited. The nuclear reaction time scale extends from 10^{-22} sec (simple direct interaction) to 10^{-15} sec ("classical" compound nucleus formation), and in principle it should be possible to distinguish reaction type via the time involved. However, direct measurements of such small time magnitudes are not yet feasible, and indirect methods must be applied (Bo62a).

It is evident that existing experimental information on the precise reaction conditions leading to long lived compound nucleus formation (in the 15 - 30 Mev excitation region) is rather meager (Bo62a), and somewhat ambiguous. There have been few serious attempts to distinguish reaction mechanisms in this region, and it would appear that a great deal of experimental and theoretical work will be required before the situation becomes much clearer.

It seems obvious, however, that the strongly fluctuating cross sections, and rapidly varying angular distributions cannot be explained in terms of pure D.I. mechanisms (either singly or in combination), as these predict only a weak energy dependence. In the following sections, D.I. effects are largely ignored. This is admittedly an arbitrary procedure, the main supporting argument being that the data accumulated so far tend to indicate (Bo62a) that the probability, in most reactions, for formation of some sort of intermediate compound system is very large (80-95%). Although it was formerly thought that this was more true for medium weight and heavy nuclei than for nuclei in the A = 20 - 30 range, the recent experiment of Glover and Weigold (G161), which finds 85-90% compound nucleus formation probability for $Al^{27}(p,n)Mg^{27}$, indicates the applicability of the argument in the mass range considered here. If, in a given reaction, a large D.I. contribution exists, it would be expected to be revealed in cross sections and angular distributions averaged over energy intervals large with respect to the fluctuation width. The data analyzed in this chapter are the $Al^{27}(p,\alpha)Mg^{24}$ excitation functions presented in Chapter III, and appropriate cross section averages and angular distribution averages provide little substantial support for the existence of a large D.I. contribution.

Section 2. THEORY OF FLUCTUATIONS.

This section presents a brief summary of the main points and predictions of theories developed in recent years to treat the cross section fluctuations. The two general approaches are based on: (a) The "classical" Statistical Model - separation of the reaction into independent formation and decay modes, and a long lived compound system. This has been developed chiefly by Ericson (Er60,62,63) and extended by Brink and Stephen (Br63); (b) the assumption that only a few of the target nucleons participate in the reaction (i.e. only a partial equilibrium occurs). This hypothesis has been developed by Izumo (Iz61,62).

2.1. Statistical Theory (Ericson)*

Ericson's central thesis is that the cross section energy dependence arises from the fluctuations associated with the average quantities of the Statistical Model. At high excitations, many reaction channels are open, (so that the average width of compound nuclear states is large) and level density is high. This produces a situation in which levels are expected to be strongly overlapping and $\Gamma >> D$ (where Γ is average level width, and D the average spacing). The width Γ is just the energy uncertainty in the compound

*Notation used here follows that of Ericson.

nucleus and contains a large number of compound states $|i\rangle$. A reaction at excitation energy E proceeds simultaneously through all states $|i\rangle$ within Γ (centered on E). Due to the many final states, the width Γ (effectively the compound nucleus width) is expected to be slowly varying with energy, and can be considered as a "coherence energy" within which compound state $|i\rangle$ matrix elements must be treated as coherent. Using the compound assumption, which permits the separation of the scattering matrix S into parts leading into and out of the compound states $|i\rangle$, the cross section for a reaction proceeding from state α to state α', can be written as:

$$\sigma_{\alpha\alpha'} \sim \left| \sum_i \langle \alpha' | S_{\alpha'} | i \rangle \, f(E,E_i) \langle i | S_\alpha | \alpha \rangle \right|^2 \qquad (6.1)$$

The bracketed quantities are the matrix elements connecting initial, compound, and final states, and $f(E,E_i)$ is the probability (a Lorentzian function of E, E_i, and Γ) of the reaction proceeding through compound state $|i\rangle$. $f(E,E_i)$ is large within Γ, and small outside, so that only states $|i\rangle$ within an energy Γ of E will participate effectively in the sum.

2.1(a) Random Phase Assumption.

The assumption now introduced is that since the number of intermediate states $|i\rangle$ is very large, the relative phases with which they are excited can be treated as random.

This leads directly to a Gaussian distribution for the matrix elements and the well known Porter-Thomas distribution for the transition probabilities:

$$P(y_i) = \frac{1}{(2\pi\bar{y})^{\frac{1}{2}}} \cdot \frac{e^{-y_i/2\bar{y}}}{(y_i)^{\frac{1}{2}}} \qquad (6.2)$$

This is similar to the expression for the Random Walk problem and is strongly fluctuating. It successfully predicts the width distribution of levels observed in the region of neutron capture energies, indicating that the random phase assumption seems justified at these excitations. However, this is several Mev below the region of $\Gamma >> D$, with which we are concerned; little supporting evidence exists for the validity of the assumption in the 15 - 30 Mev excitation range.

Since the sum of matrix elements of random phase is also a random number, the sum over contributing states $|i\rangle$ in (6.1) is a Gaussian distribution, and the cross section $\sigma_{\alpha\alpha'}$ is expected to fluctuate with a Porter-Thomas distribution. However, strong fluctuations in $\sigma_{\alpha\alpha'}$ to individual final states are expected only for energy differences $> \Gamma$. If the beam resolution is infinitely narrow, and the energy is changed by $\delta E < \Gamma$, then the matrix element sum in (6.1) will be essentially unchanged as

the $|i\rangle$ are nearly identical. Consequently $\sigma_{\alpha\alpha'}$ changes little for $\delta E < \Gamma$. Ericson(Er60) notes that this leads to the possibility of experimental measurement of Γ from the $\sigma_{\alpha\alpha'}$ excitation functions, and a method of determining the compound nucleus lifetime (which is just $\tau = \hbar/\Gamma$).

2.1(b). <u>The R.M.S. Fluctuation Amplitude</u>.

The two important quantities measurable from cross section excitation functions showing fluctuations are: (a) the R.M.S. fluctuation amplitude ($\bar{f}$); and (b) the average fluctuation width (Γ). Expressions for the former are given here, and for the latter in section (2.1(c)).

For a Porter-Thomas cross section distribution, and for $\Gamma >> D$, Ericson obtains (Er60):

$$\bar{f} = \frac{\langle(\sigma - \langle\sigma\rangle)^2\rangle}{\langle\sigma\rangle^2} \sim 1/nN \qquad (6.3)$$

where n is the number of final states included in the cross section, and N is the number of "coherence widths" Γ within ΔE, the averageing interval. In the region of $\Gamma << D$, (i.e. single, separate levels), N is just the number of states $|i\rangle$ in the compound nucleus within ΔE; some recent experiments have erroneously interpreted N in this manner for the $\Gamma >> D$ region. It is noted that (6.3) implies that

the total reaction cross section (where n is large) will have only small fluctuations.

If angular distributions for the reaction $\alpha\alpha'$, are written as (B152):

$$d\sigma_{\alpha\alpha'}/d\Omega \sim \sum_L B_L(\alpha' s' ; \alpha s) P_L(\cos\theta) \qquad (6.4)$$

where s, s' are channel spins), Ericson (Er60) shows that the even B_L fluctuate as much as the integrated $\sigma_{\alpha\alpha'}$. The same is true in absolute terms for the odd B_L, but their mean value is zero. In general, therefore, in spite of the many intermediate levels $|i\rangle$ included in Γ, it is predicted that the $d\sigma_{\alpha\alpha'}/d\Omega(\theta)$ will show no symmetry about 90°. The asymmettry is expected to disappear, however, upon averageing the $d\sigma_{\alpha\alpha'}/d\Omega(\theta)$ over $\Delta E >> \Gamma$.

2.1(c). Cross-section Correlation Functions.

This section sketches the development of theoretical expressions connecting Γ and the D.I. and compound nucleus cross section contributions which can be used for the quantitative analysis of the cross section fluctuations.

In first approximation angular momentum effects are ignored (i.e. spinless particles, and s-wave interactions only). The reaction cross section is then:

$$\sigma_{\alpha\alpha'}(E) = \pi\lambda_\alpha^2 \left| S_{\alpha\alpha'}(E) \right|^2$$

where $S_{\alpha\alpha'}(E) = S^{(p)}_{\alpha\alpha'} - i\sum_i \frac{a_i}{E - E_i}$ (Fe62b) (6.5)

$S_{\alpha\alpha'}$ is the total scattering amplitude for the reaction $\alpha\alpha'$, which is divisible into a slowly varying part ($S^{(p)}_{\alpha\alpha'}$) associated with D.I., and a part associated with the formation of compound states $|i\rangle$ (complex energy E_i), which varies rapidly with energy. The a_i are just $(\gamma_{\alpha i})(\gamma_{i\alpha})$, the width amplitudes leading into and out of the intermediate states $|i\rangle$ (Fe62b), and can be expressed as $a_i = \langle a \rangle + \delta a_i$. This is the sum of the average resonance amplitude, and the fluctuating part which varies from resonance to resonance. Also:

$$\left\langle S_{\alpha\alpha'}(E) \right\rangle = S^{(p)}_{\alpha\alpha'} - i\sum_i \frac{a_i}{E - E_i} = S^{(p)}_{\alpha\alpha'} + \frac{\pi}{D}\langle a \rangle \quad (6.6)$$

where D is the average level spacing (Bo39), so that altogether:-

$$S_{\alpha\alpha'}(E) = \left\langle S_{\alpha\alpha'}(E) \right\rangle - i\sum_i \frac{\delta a_i}{E - E_i} \quad (6.7)$$

$$\text{or } S_{\alpha\alpha'}(E) = \left\langle S_{\alpha\alpha'}(E) \right\rangle + S^{(fl)}_{\alpha\alpha'}(E) \quad (6.8)$$

where $S^{(fl)}_{\alpha\alpha'}(E)$ is the fluctuating part of the scattering

amplitude (i.e. the fluctuating compound contributions to the scattering matrix are identified with the fluctuations in the resonant amplitudes. This holds only for $\Gamma >> D$, and is more general definition of D.I. and compound nuclear processes than that customarily used in D.W.B.A. theories).

Using (6.8), Ericson finds that the averaged cross sections decompose into incoherent contributions from the D.I. and compound (fluctuating) nuclear amplitudes so that:

$$\langle \sigma_{\alpha\alpha'}(E) \rangle = \sigma_{\alpha\alpha'}^{(D.I.)} + \sigma_{\alpha\alpha'}^{(fl)} \qquad (6.9)$$

Introduction of the random phase approximation leads to:

$$\sigma_{\alpha\alpha'}^{(fl)} = \pi \lambda_\alpha^2 \frac{2\pi}{D} \frac{\langle |\delta a_i|^2 \rangle}{\Gamma} \qquad (6.10)$$

Autocorrelation Function (no angular momentum).

The above expressions are connected to the experimentally measured cross sections via the self-or-auto-correlation function, defined as:

$$F(E) = \langle (\sigma(E+\epsilon) - \langle\sigma\rangle)(\sigma(E) - \langle\sigma\rangle) \rangle \qquad (6.11)$$

By carrying out the prescribed averages, using (6.7),(6.11), and the continuum assumption for the real parts of the

resonance energies E_i, one obtains explicitly:

$$F(\epsilon) = \frac{\sigma^{(fl)}}{1 + (\epsilon/\Gamma)^2}\left[2\sigma^{(D.I.)} + \sigma^{(fl)}\right]^{*} \qquad (6.12)$$

Near $\epsilon = 0$, this expression has a Lorentzian shape, and should provide a quantitative measure of Γ, and thus of the compound system lifetime. For physical reasons discussed in section (2.1(a)), one expects: $\lim_{E\to\infty} F(E) = 0$

If $\sigma^{(D.I)}$ is $<<\sigma^{(fl)}$, then at $\epsilon = 0$, one obtains the relation:

$$F(o) = \langle(\sigma(E) - \langle\sigma\rangle)^2\rangle = \left[\sigma^{(fl)}\right]^2 \qquad (6.13)$$

which is just the R.M.S. value of the cross section fluctuations, and is identical with the expression (6.3) except for a factor $\langle\sigma\rangle^2$. Thus, a measurement of F(o) provides an experimental check on the validity of (6.3).

Cross-correlation Function.

A correlation comparison between cross sections for different final states should (Er62) provide a rigorous test of the Statistical Model explanation of cross section fluctuations. The appropriate function (symmetrized) for measuring the correlation between cross sections to final states i and j is given as:

*Subscripts $\alpha\alpha'$ have been dropped.

$$F^{ij}(\epsilon) = \tfrac{1}{2}\left\langle (\sigma_i(E+\epsilon) - \langle\sigma_i\rangle)(\sigma_j(E) - \langle\sigma_j\rangle)\right\rangle + \tfrac{1}{2}\left\langle (\sigma_i(E) - \langle\sigma_i\rangle)(\sigma_j(E+\epsilon) - \langle\sigma_j\rangle)\right\rangle \quad (6.14)\ (\text{Ha63})$$

If the Model assumptions are correct (random-phase assumption in particular), then peaks and valleys in the two cross sections should coincide only accidentally (Er62), and one expects $F^{ij}(\epsilon) = 0$, independent of ϵ, and i, j. This follows specifically from the fact that a change of reaction exit channel changes all the factors a_i(6.5); and if these possess a random distribution, no two sets will be correlated.

Autocorrelation Functions with Angular Momentum Included.

A generalization of the above theory to include angular momentum effects leads to rather more complicated relations. Via extensive algebraic manipulation, Ericson (Er63) obtains an expression for the fluctuation cross section contribution associated with each B_L coefficient (Equ. 6.4), which is similar to equation (6.10):

$$C^J_{\alpha sL;\,\alpha' s' L'} = \frac{2\pi}{D_J}\,\frac{\left\langle \left| a^J_{\alpha sL;\,\alpha' s' L'} \right|^2 \right\rangle}{\Gamma_J} \quad (6.15)$$

The average spacing D and width Γ, are replaced by D_J and Γ_J, the average spacing and width for compound states of angular momentum J. The autocorrelation function for the differential cross section at an angle θ, can then be written as:

$$F(\epsilon)=\left\langle\left(\frac{d\sigma}{d\Omega}(E+\epsilon)-\left\langle\frac{d\sigma}{d\Omega}\right\rangle\right)\left(\frac{d\sigma}{d\Omega}(E)-\left\langle\frac{d\sigma}{d\Omega}\right\rangle\right)\right\rangle \qquad (6.16)$$

$$=\frac{\lambda_\alpha^4}{(2i+1)^2(2I+1)^2}\sum_{L_1L_2}F_{L_1L_2}(\alpha,\alpha',\epsilon)P_{L_1}(\cos\theta)P_{L_2}(\cos\theta)$$

where $F_{L_1L_2}(\alpha,\alpha',\epsilon)$ is the autocorrelation function for a symmetric combination of the coefficients B_{L_1}, B_{L_2}, and is an exceedingly lengthy expression containing products of $\bar{Z}$ (Bl52) coefficients and Lorentzian factors of the type $(\Gamma_J^2/\epsilon^2+\Gamma_J^2)$. For cross sections integrated over θ simplifications occur, and the autocorrelation function becomes:

$$F(\epsilon)=\left\langle\left(\sigma_{\alpha\alpha'}(E+\epsilon)-\langle\sigma_{\alpha\alpha'}\rangle\right)\left(\sigma_{\alpha\alpha'}(E)-\langle\sigma_{\alpha\alpha'}\rangle\right)\right\rangle \qquad (6.17)$$

$$=\left[\frac{\pi\lambda_\alpha^2}{(2i+1)(2I+1)}\right]^2\sum_J(2J+1)^2\frac{\Gamma_J^2}{\epsilon^2+\Gamma_J^2}\sigma_J^{(fl)}(D.I.)^{(fl)}\left(2\sigma_J+\sigma_J\right)$$

Contributions due to each J value add incoherently. If Γ_J

is assumed constant (independent of J), then the Lorentzian factor can be taken outside the summation and a meaningful "coherence width" may be extracted from experimental cross sections. A similar reduction occurs in equation 6.16 for the $d\sigma/d\Omega(\theta)$ autocorrelation function, if this assumption is made.

The main condition imposed on the application of the correlation functions given here is that the averages prescribed should be insensitive to the choice of ΔE, the averageing interval. The well known existence of optical model "giant" resonances indicate that cross section averages show strong energy dependence over intervals of a few Mev. Since the fluctuation widths Γ are expected to vary from 50 kev (A=30) to a few ev (A=200), this should leave a large range of acceptable values for $\Delta E(Er63)$. However, in addition to the single nucleon optical model resonances, there may also exist resonant structure of a few hundred kev width, involving excitation of a small number of the target nucleons, which would impose severe restrictions on the averageing procedure. Little information is at present available on such secondary optical resonances; they are treated theoretically by Izumo (Iz61) (see section 2.2).

Normalized Correlation Functions.

In general it is more useful to measure correlation functions for "normalized" fluctuation cross sections (i.e. in which the amplitude fluctuations are divided by their mean values), so that in following sections $F(\epsilon)$ is replaced by $R(\epsilon) = F(\epsilon)/\langle\sigma\rangle^2$ and $F^{ij}(\epsilon)$ by $R^{ij}(\epsilon) = F^{ij}(\epsilon)/\langle\sigma_i\rangle\langle\sigma_j\rangle$. In particular, comparisons between R(o) for cross sections with different mean values, and between R(o) and $R^{ij}(o)$ become independent of absolute values. Ericson shows that (Er63) R(o) and $R^{ij}(o)$ are always < 1, and also that: (a) R(o) for $d\sigma/d\Omega$ excitation functions at backward and forward angles is expected to be considerably larger than R(o) for the integrated cross section; (b) largest fluctuations, i.e. largest R(o), for integrated cross sections will occur for small channel spins; and (c) for Γ independent of J, the behaviour of all the autocorrelation function ratios $R(\epsilon)$($d\sigma/d\Omega$, $\sigma_{\alpha\alpha'}$, $B_{L\alpha\alpha'}$, and total σ) near $\epsilon = 0$, is given by the simple Lorentzian $\Gamma^2/(\epsilon^2+\Gamma^2)$, so that the Γ measurement should be independent of the type of excitation function used.

2.2. Izumo's Model.

To describe the cross section fluctuations Izumo (Iz61,62) has proposed a model possessing the following characteristics:

(a) The reaction proceeds by a mechanism involving emission of the products before statistical equilibrium is achieved (i.e. in a time $<$ relaxation time (Er60)); this is referred to as a partial equilibrium process.

(b) The incident nucleon excites compound states in a few nucleon cluster; the predicted level spacing for such states is $\sim$ 800 kev for A=30, and the number of participating nucleons is expected to be $\sim$ 6.

(c) The model predicts weak energy dependence of angular distributions within energy ranges $\Delta E < \Gamma_G$, where Γ_G is the width of the few nucleon states ($\Gamma_G \sim D_G$).

(d) Strong correlations between cross sections to different final states are expected.

Although, as noted previously, it is likely that such a reaction mechanism can account for a fraction of the cross section amplitude, little supporting experimental data is available. In the following analysis of the

$Al^{27}(p,\alpha)Mg^{24}$ data of Chapter III, Izumo's model is not applied. This seems qualitatively well justified in that the angular distributions (contrary to Izumo's prediction) show marked variation within 20 kev intervals, and that cross sections to be different final states appear uncorrelated.

Section 3. CORRELATION FUNCTION ANALYSIS OF $Al^{27}(p,\alpha)Mg^{24}$ DATA

3.1. Basis for Analysis.

The conditions for application of Ericson's statistical model approach to cross section fluctuation data are mainly: (a) that the reaction proceeds dominantly via a compound nucleus mechanism; (b) that the excitation energy of the compound system is high enough for $\Gamma >> D$ to be a good approximation; and (c) channel spins are low. Evidence in support of condition (a) for the $Al^{27}(p,\alpha)Mg^{24}$ reaction has been given in section (1.2) of this chapter and in Chapter III. In general the results of similar (p,α) experiments (Br63a) indicate that the D.I. contribution is usually small in comparison with compound nucleus formation. The arguments used in Chapter III indicate that condition (b) is expected to be satisfied in the Si^{28} excitation region treated. Lawrence and Hay (La63),

investigating the reaction $Mg^{26}(p,\alpha)Na^{23}$ at slightly lower compound system excitation, argue that the rough agreement between some of the fluctuation maxima in the α_0 and α_1 cross sections, and the existence of large amounts of odd Legendre-Polynomial terms in the $d\sigma/d\Omega(\theta)$ for these groups, suggests a situation involving interference between only a small number of compound nucleus levels (i.e. Γ not $\gg$ D in this region). However, the $d\sigma/d\Omega(\theta)$ phenomena are in agreement with Ericson's predictions for $\Gamma \gg$ D, and rough agreement between a few cross section maxima cannot be claimed as significant positive correlation. Condition (c) is not very well satisfied by $Al^{27}(p,\alpha)Mg^{24}$, inasmuch as channel spins as high as 3 are involved. This does not obviate the analysis, but does place restrictions on the interpretation of results.

3.2. Computation of Correlation Functions.

With the aid of the A.N.U. 1620 computer, a correlation function analysis was performed on the $Al^{27}(p,\alpha)Mg^{24}$ data of Chapter III. Relevant procedures and results for each type of calculation are given in the following sections. The data handling method was similar for all computations and is described here*.

*All programs were coded by the writer.

Input data (punched cards) for the correlation function programs were in the following forms:-

(a) $d\sigma/d\Omega(90^{\circ}, 135^{\circ})$ excitation functions (6-10 Mev); one set of cards/α-group/angle; 25 kev energy interval between points.

(b) A_L coefficient excitation functions (from Legendre-Polynomial fit to 8.0 - 8.34 Mev data); one set of cards/α-group/A_L; 20 kev energy interval between points.

(c) Angular distribution excitation functions (8.0 - 8.34 Mev data); one set of cards/α-group/excitation energy; $\Delta\theta = 5^{\circ}$, and 20 kev energy interval between points.

These data sets were stored in computer memory as 2 or 3 dimensional matrices, where indices represented α-group number, angle, and energy. Arithmetic operations required by the autocorrelation and crosscorrelation functions (6.12, 6.14) were simple, involving sequences of sums over, multiplication of, and averageing of data items. The heart of the calculation lay in the data indexing arrangement which enabled the repetitive operations to be performed on successive appropriate set of data items, via simple manipulation of the indices. Energy variables E and ϵ were cycled in units equal to the smallest step involved (i.e. 20 or 25 kev). The averaging region, ΔE,

comprised either the full energy range (per α-group) for which data were available, or large fractions of the full range (for reasons given below).

3.3. The Differential Cross Section Excitation Functions 6 - 10 Mev.

3.3(a) Correlation-Function Dependence on ΔE.

Since the $d\sigma/d\Omega(90^\circ, 135^\circ)$ data covered an excitation range of several Mev, including many cross section maxima and minima, it was expected to provide an adequate test of the applicability of the correlation functions. In order to examine the dependence of the autocorrelation on the width of the averageing region ΔE, $R(\epsilon)$ for $d\sigma/d\Omega(135^\circ, \alpha_1)$ was measured over $\Delta E = Kx$(160, 80 and 40 points), where K = 25 kev. The same initial energy was used in each calculation. Results are indicated in Fig. 6.1. The 160 point $R(\epsilon)$ falls sharply from 0.220 - 0.140 in the range ΔE = 0 - 50 kev, and thereafter decreases very slowly. Behaviour of the 80 point and 40 point $R(\epsilon)$ is considerably different, both showing a rapid falloff to 0 (within E = 0 - 50 kev) from an R(o) value of $\cong$ 0.075, followed by small-amplitude oscillations about 0 for larger ϵ.

Fig. 6.1 Typical autocorrelation and cross-correlation functions, computed from $Al^{27}(p,\alpha)Mg^{24}$ ground state and first excited state $d\sigma/d\Omega$ (135°) excitation functions.

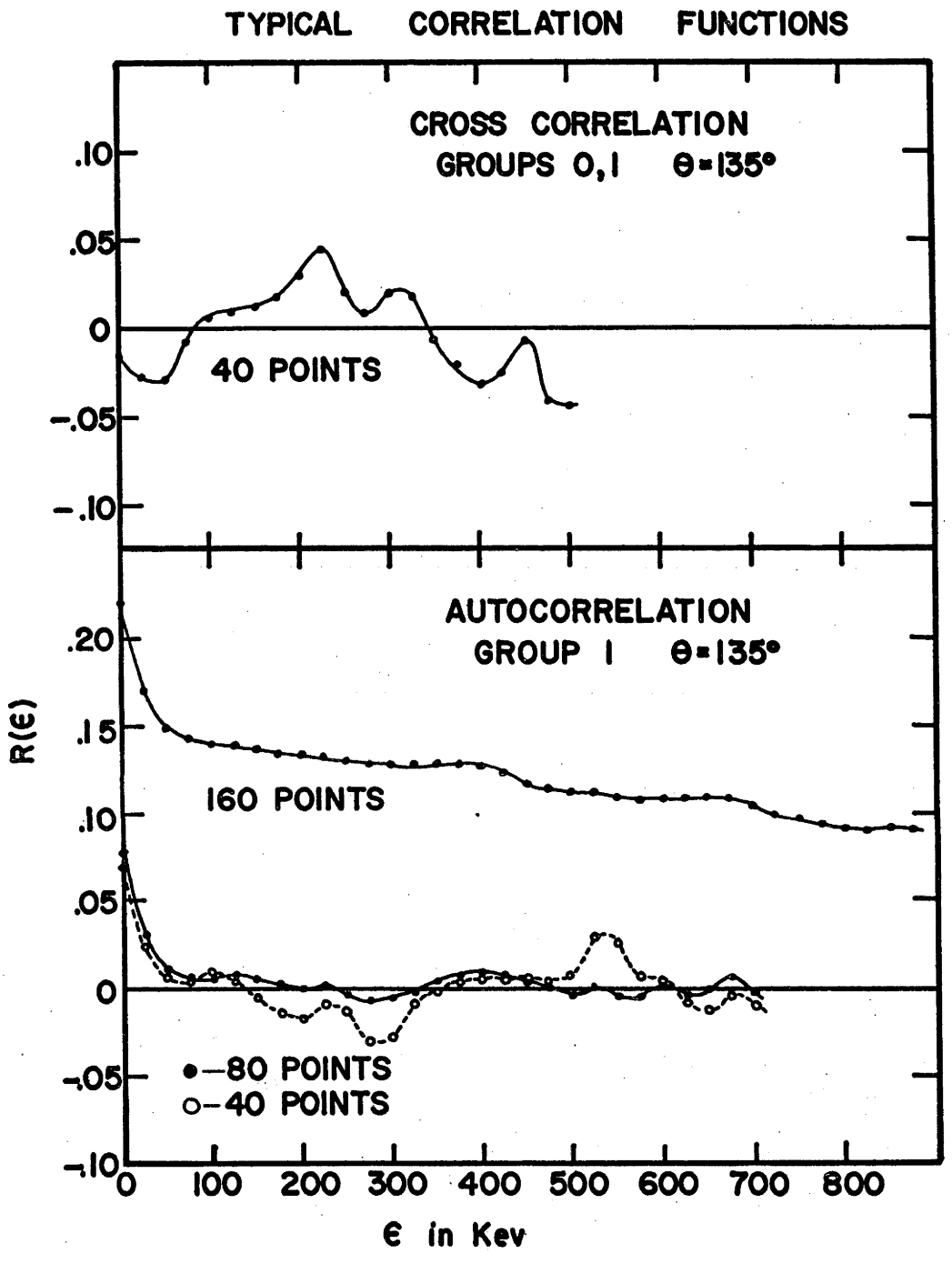
TYPICAL CORRELATION FUNCTIONS
CROSS CORRELATION
GROUPS 0,1 θ=135°
40 POINTS
AUTOCORRELATION
GROUP 1 θ=135°
160 POINTS
●—80 POINTS
○—40 POINTS
R(ϵ)
ϵ in Kev
.10
.05
0
-.05
-.10
.20
.15
.10
.05
0
-.05
-.10
0
100
200
300
400
500
600
700
800

As noted earlier, a necessary condition for the validity of the correlation function analysis is that $\langle\sigma\rangle$ be energy independent over the range taken into the computation. A glance at Fig. (3.25) of Chapter III shows that the condition is not satisfied in the range E_p = 6 - 10 Mev, and it is to this that the behaviour of the 160 point $R(\epsilon)$ (Fig. 6.1) is attributed. For the 80 point and 40 point $R(\epsilon)$, the condition is much more nearly satisfied, and in fact their behaviour (for small ϵ) is quantitatively that predicted by Ericson (Er63). Inasmuch as R(o) and Γ (FWHM near ϵ = 0) for the 80 and 40 point $R(\epsilon)$ are approximately the same, it would appear that these autocorrelation function parameters are not very sensitive to the averageing range (Δ E), within the restrictions (a) $\langle\sigma\rangle$ = const. over ΔE, and (b) $\Delta E \gg \Gamma$. Fig. 6.1 also shows that the amplitude of oscillations about 0 in $R(\epsilon)$ for large ϵ is greater for the 40 point function than for the 80 point function. This is to be expected, on the grounds that fewer data items are included in the averages.

In the top half of Fig. 6.1 is shown the cross-correlation function $R(\epsilon_{ij})$ between $d\sigma/d\Omega(135^\circ, \alpha_0)$ and $d\sigma/d\Omega(135^\circ, \alpha_1)$, taken over the first 40 points of the

energy range. The general form is typical of most $R(\epsilon)^{ij}$ measured in this study. $R(o)^{ij}$ is small and negative, and the curve shape near $\epsilon = 0$ is clearly non-Lorentzian. The fluctuation about 0 for large ϵ is thought to be due, as before, to the finite number of points included in the averages.

The measured values of $R(o)^{ij}$ are meaningful only in comparison with the R(o) for groups i and j taken separately. A significant cross-correlation between groups was considered to exist if the value $|R(o)^{ij}|$ was of the same order as the smaller of the two R(o), and if the shape of the $R(\epsilon)^{ij}$ curve for small ϵ was approximately Lorentzian. Although this criterion is rather arbitrary, it is expected to provide at least a lower limit.

Both the $R(\epsilon)$ and $R(\epsilon)^{ij}$ functions have been applied to $C^{12}(O^{16},\alpha)Mg^{24}$ data by Halbert et al. (Ha63), and curves similar to those of Fig. 6.1 are obtained.

3.3(b). Autocorrelation Function Results for $d\sigma/d\Omega(90^\circ, 135^\circ)$.

$R(\epsilon)$ functions were measured for all $d\sigma/d\Omega(90^\circ, 135^\circ, \alpha_i)$ excitation functions given in Chapter III, section (3.3), and the parameters R(o), and Γ extracted from each curve. In extracting Γ, the first few $R(\epsilon)$

points were plotted and the FWHM (near $\epsilon = 0$) visually estimated from the connecting curve. The error in this estimate is thought to be $\sim 10\%$.

For reasons given in Chapter III, the measured $d\sigma/d\Omega$ energy range decreases with increasing α-group number; but all terminate at 10 Mev. For computational convenience, therefore, the $d\sigma/d\Omega$ were broken into 30 point segments, beginning at 10.00 Mev and running downward in energy. (All points in excess of integral sets of 30 were ignored). Each 30 point segment was treated as a separate excitation function, so that 4 contiguous $R(\epsilon)$ were computed for groups α_0 and α_1, 3 for α_2 and α_3, 2 for α_4, and 1 for α_5. This procedure ensured that the criterion $\langle\sigma\rangle$ = const. within ΔE was satisfied; however, it is possible that the 30 point segments were too short for the restraint $\Delta E \gg \Gamma$ to be satisfactory. Results are given in Table 6.1, where the columns (reading left-to-right) contain: alpha group number; observation angle; R(o) and Γ for each energy interval, ΔE_i; and, average values of R(o) and Γ. The energy intervals are: ΔE_1 = 7.025 - 7.750 Mev, ΔE_2 = 7.775 - 8.500 Mev, ΔE_3 = 8.525 - 9.250, and ΔE_4 = 9.275 - 10.000 Mev.

TABLE 6.1

$R(\epsilon)$ for $d\sigma/d\Omega(90^\circ, 135^\circ)$.

GROUP	OBS. ANGLE	ΔE_1 R(o) Γ	ΔE_2 R(o) Γ	ΔE_3 R(o) Γ	ΔE_4 R(o) Γ	AVERAGE $\langle R(o)\rangle\langle\Gamma\rangle$
0	90°	.216 20	.189 30	.316 25	.140 29	.215 26
	135°	.177 19	.199 24	.190 30	.205 27	.193 25
1	90°	.084 23	.062 39	.198 20	.048 33	.098 29
	135°	.068 19	.066 22	.055 19	.062 40	.062 25
2	90°		.067 40	.084 33	.030 12	.060 28
	135°		.077 20	.056 23	.129 33	.088 25
3	90°		.102 56	.096 28	.043 34	.081 39
	135°		.047 21	.067 27	.092 28	.069 25
4	90°			.089 32	.026 26	.058 29
	135°			.094 24	.055 19	.072 22
5	90°				.079 26	.079 26
	135°				.049 25	.049 25

It is seen that there is a considerable scatter in the several Γ values measured for each $d\sigma/d\Omega(\alpha_i)$. The magnitude of deviations from the mean is similar for each α group, and $\langle\Gamma\rangle$ takes a value of $\cong$ 25 kev, independent of α group. The 90° Γ are consistently somewhat higher than those measured at 135°. It is worth noting that $\langle\Gamma\rangle$ found here is close to the energy step size used in obtaining the differential cross sections.

Tabulated values of R(o) for the different ΔE_i also show considerable scatter, for all alpha groups. However, the average values $\langle R(o) \rangle$ display the following general characteristics: (a) $\langle R(o) \rangle$ for α_o is $\sim$3 times the values for all higher α-groups. This is in rough qualitative agreement with the prediction (section 2.1(b)) that $\langle R(o) \rangle \sim 1/n$, where n in this case is just the number of magnetic sub-states (2J+1) for the relevant level of spin J in Mg^{24}. The Mg^{24} ground state has J = 0, and all higher states considered here have $J \geq 2$; therefore the ratios of (1/n) (i.e. $\langle R(o) \rangle$) factors for α_o and α_1 ($i \neq 0$) are expected to be ≥ 5. It is possible that the experimental values are too low because of cross section maxima and minima missed by taking too large a step size; if this is not the case the lack of agreement would seem to be evidence for the existence of a significant D.I. component in the $Al^{27}(p,\alpha)Mg^{24}$ reaction, (see equation 6.12), and for a partial failure of the random phase approximation. An inspection of ratios of the $\langle R(o) \rangle$ for higher α_i reveals no quantitative correspondence with theoretical values of (1/n) ratios expected from spin assignments.

(b) Values of $\langle R(o) \rangle$ are greater at $\theta = 90^\circ$, than at 135° in more than half the cases. This is in disagreement with the predictions of Ericson (Er63), which suggest that

fluctuations should be greater at backward-forward angles than at angles near 90^{o}.

Two additional observations appropriate to this section are: (a) As compound nucleus excitation energy is increased, more reaction channels are opened and the compound nucleus lifetime is expected to decrease, with a corresponding increase in Γ. Within the excitation range studied in this work, there is no clear evidence for such a trend in Γ.

(b) Similarly, no marked change is observed in R(o) values as excitation energy is increased. This implies that the fluctuations are not damped by the inclusion of increasing numbers of contributing compound levels within the "coherence energy", Γ, in agreement with theory, (Bo62). It is interesting to note that the cross section data of Ogata et al. (Og60), at compound excitations higher than those of the present work, do reveal considerable fluctuation damping.

3.3(c) Cross-correlations $R^{ij}(\epsilon)$ for $d\sigma/d\Omega(90^{o}, 135^{o}, \alpha_{i})$

Cross-correlation functions $R(^{ij}_{\epsilon})$, were obtained for all possible pairs of α-groups i, j at $\theta = 90^{o}$, and 135^{o}. In $R(^{ij}_{\epsilon})$ where one or both groups are higher than

α_1, the number of 30 point excitation function segments is less than 4 for reasons given in section (3.3(b)). Results are shown in Table 6.2., where the leftmost column indicates the groups i, j, used in the calculation, and the remaining columns contain the computed values of $R^{ij}(o)$ for each ΔE_i, and the average, $\langle R^{ij}(o) \rangle$.

TABLE 6.2.

$R^{ij}(o)$ for $d\sigma/d\Omega(90^\circ, 135^\circ, \alpha_i)$.

GROUP NO. α_i, α_j	OBS. ANGLE	ΔE_1 $R^{ij}(o)$	ΔE_2 $R^{ij}(o)$	ΔE_3 $R^{ij}(o)$	ΔE_4 $R^{ij}(o)$	AVERAGE $\langle R^{ij}(o) \rangle$
0,1	90°	.011	.037	.017	.023	.022
	135°	.020	.001	.019	.056	.024
0,2	90°		-.036	.083	-.036	.004
	135°		.001	.028	-.001	.009
0,3	90°		.011	.009	.007	.009
	135°		.009	.023	.047	.027
0,4	90°			.033	.001	.017
	135°			.040	.009	.025
0,5	90°				-.007	-.007
	135°				.015	.015
1,2	90°		-.021	.003	-.120	-.046
	135°		-.011	-.002	-.003	-.006
1,3	90°		-.001	.012	-.002	-.003
	135°		.007	.025	.021	.018
1,4	90°			.001	-.007	-.003
	135°			.045	.034	.039
1,5	90°				-.007	-.007
	135°				.036	.036
2,3	90°		-.039	.004	.077	.021
	135°		-.007	-.002	.069	.019
2,4	90°			.009	.077	.043
	135°			.001	.021	.010
2,5	90°				-.054	-.054
	135°				.042	.042
3,4	90°			.026	.039	.032
	135°			.022	.028	.025
3,5	90°				.032	.032
	135°				.026	.026
4,5	90°				.048	.048
	135°				.046	.046

In general, it is seen that the $R^{ij}(o)$ values are of order 1/10 the values of corresponding R(o) in Table 6.1 if positive, and are sometimes negative. A few cases occur in which $R^{ij}(o)$ is comparable in magnitude with the corresponding R(o); however, it is thought that these are fortuitous, since they involve only isolated 30 point segments ΔE_i. The overall conclusion to be drawn from Table 6.2 is that no significant correlation exists between any pairs of alpha groups i, j, at either angle (90°, 135°).

3.3(d) R(o) for $d\sigma/d\Omega(90^\circ,135^\circ)$ Summed Over α_i by Stages.

In order to test Ericson's prediction that $R(o)\sim 1/n$, where n is the total number of magnetic-substates included in the cross section, the $d\sigma/d\Omega\,(90^\circ,135^\circ,\alpha_i)$ for each α group were consecutively summed, and the value of R(o) was computed at each stage of the sum. Results are shown in Table 6.3, where column 1 (reading from left) contains the α groups included in the separate sum stages, column 2 gives the total number of substates included, $n = \sum_i (2J_i+1)$, and the remaining columns give R(o) for each ΔE_i, and $\langle R(o)\rangle$.

TABLE 6.3

$R(o)$ for $\sum_i d\sigma/d\Omega(90^\circ, 135^\circ, \alpha_i)$

GROUP NUMBERS	NO. STATES	OBS. ANGLE	ΔE_1 R(o)	ΔE_2 R(o)	ΔE_3 R(o)	ΔE_4 R(o)	AVERAGE $\langle R(o) \rangle$
0,1	6	90°	.060	.128	.040	.058	.072
		135°	.063	.053	.063	.075	.064
0,1,2	15	90°		.067	.037	.046	.050
		135°		.032	.038	.098	.055
0,1,2, 3	20	90°		.046	.030	.042	.039
		135°		.023	.032	.076	.043
0,1,2, 3,4	27	90°			.026	.039	.032
		135°			.031	.062	.047
0,1,2, 3,4,5	36	90°				.037	.037
		135°				.058	.058

Although, it is clear that the R(o) measurements corresponding to individual ΔE_i show considerable scatter, the averages $\langle R(o) \rangle$ show a definite decrease as the summation proceeds. The measured overall decrease in $\langle R(o) \rangle$ is approximately a factor of 2; this is much less than the theoretically expected (n(final)/n(initial)) decrease of a factor of 6. The same conclusions regarding D.I. contributions, and failure of the random phase assumption can be drawn as in section (3.3(b)).

3.4. Correlation Function Analysis of 8.00-8.34 Mev Data.

The 8.00 - 8.34 Mev data of section (3.5), Chapter III, allow a partial investigation of the angular

dependence of Γ and R(o) in a representative range of excitation in Si^{28}. Since the averageing interval is relatively short (340 kev), a rather large statistical error (possibly as high as 20 - 25%) is expected; this is due both to the "finite data range" discussed by Allardyce et al. (Al63), and to the criteria of section (3.3(a)). This uncertainty necessarily limits the conclusions to be drawn from the correlation analysis.

3.4(a) Autocorrelation for $d\sigma/d\Omega(\theta, \alpha_i)$.

$R(\epsilon)$ were computed for all alpha groups, at $\theta = 15^{\circ}$-165°(in 5° steps). The parameters Γ and R(o) were extracted as described in section (3.3(b)). The distribution of measured Γ are plotted in Fig. 6.2 as $f(\theta)$. The values of Γ averaged over angle are $\langle\Gamma\rangle_{\theta}$= 27kev($\alpha_o$), 17 kev ($\alpha_1$), 25 kev ($\alpha_2$), and 15 kev ($\alpha_3$). The scatter about $\langle\Gamma\rangle_{\theta}$ is of the same order of magnitude as $\langle\Gamma\rangle_{\theta}$ and in all cases shows a relatively smooth angular dependence. It seems clear that, within the noted statistical uncertainty, the compound nucleus width Γ computed from $d\sigma/d\Omega$ excitation functions is not constant or independent of the angle of measurement. This suggests that the approximation Γ_J = const. (section (2.1(c)) is not satisfactory, so that the mathematical simplification of section (2.1(c))

Fig. 6.2 Angular dependence of the "coherence" width Γ obtained from autocorrelation calculations on the 8.00 - 8.34 Mev (E_p) $Al^{27}(p,\alpha_i)Mg^{24}$ $d\sigma/d\Omega$ (θ) excitation functions. ($i = 0 - 3$).

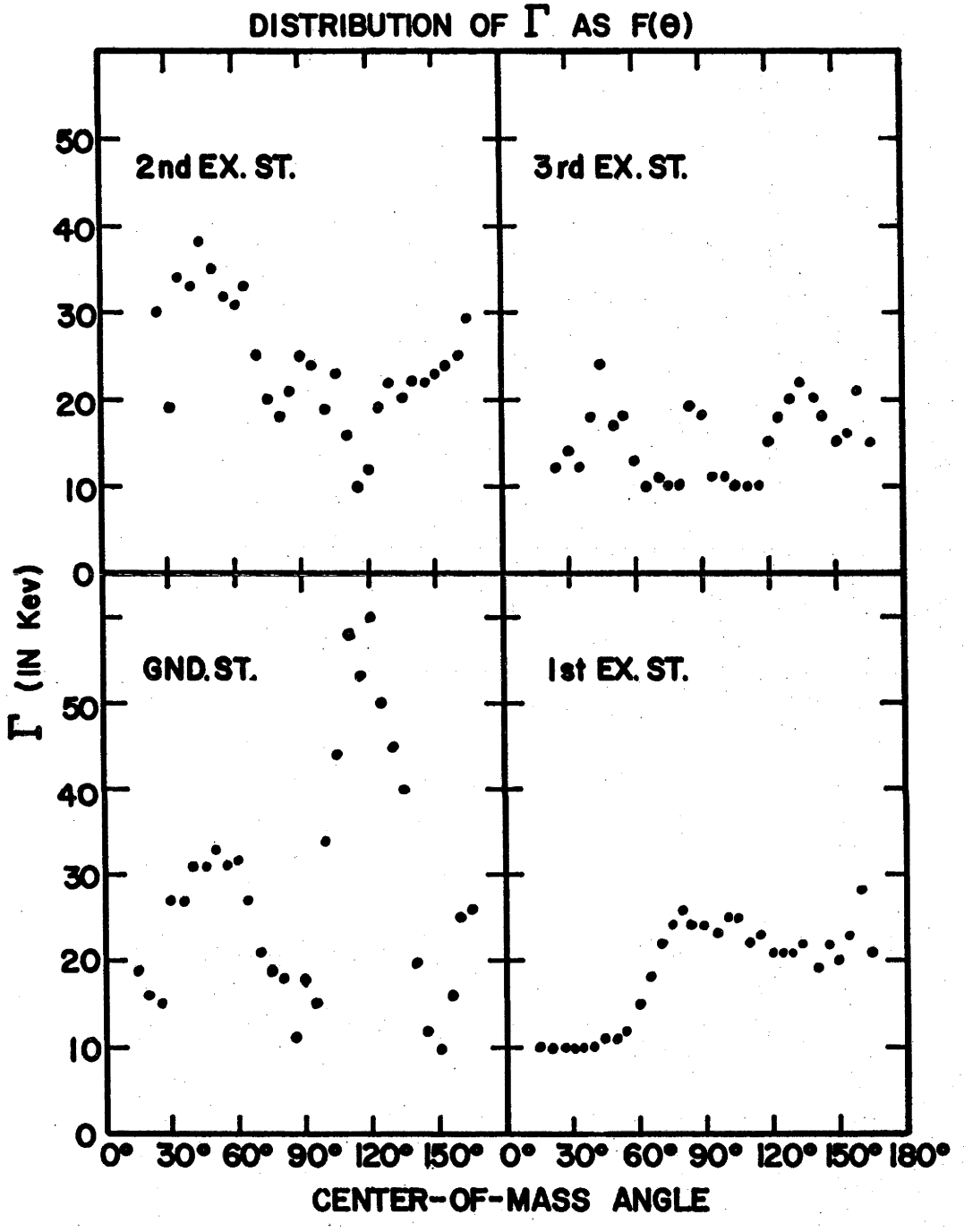
DISTRIBUTION OF Γ AS F(θ)
2nd EX. ST.
3rd EX. ST.
GND. ST.
1st EX. ST.
Γ (IN Kev)
0
10
20
30
40
50
0° 30° 60° 90° 120° 150° 0° 30° 60° 90° 120° 150° 180°
CENTER-OF-MASS ANGLE

cannot be justified. Further implications are noted in section (4).

The angular dependence of R(o) is plotted in Fig. 6.3. Relatively smooth variation with angle is observed for all α groups, and in general the R(o) are small near 90^{o} and large at backward and forward angles, as predicted by Ericson. However, the α_{o} and α_{1} R(o) distributions show a marked peak near the middle of the angular range. The significance of this anomaly is not understood.

3.4(b) Cross-correlations for $d\sigma/d\Omega(\theta, \alpha_i, \alpha_j)$

Cross-correlations $R^{ij}(\epsilon)$ were computed for all possible α_i, α_j, combinations at the sample angles (chosen arbitrarily) $\theta = 25^{o}, 45^{o}, 90^{o}, 135^{o}, 165^{o}$. Results are given in Table 6.4. Values of $R^{ij}(\epsilon)$ for $\epsilon = 0, 20, 40$ kev are shown. Column 1 (from left) contains the sampling angle, and remaining columns contain the $R^{ij}(\epsilon)$ for the indicated α group combinations.

Fig. 6.3 Angular dependence of the R.M.S. fluctuations amplitude (R(0)) measured in autocorrelation calculations on the 8.00 - 8.34 Mev (E_p) $Al^{27}(p,\alpha_i)Mg^{24}$ $d\sigma/d\Omega$ (θ) excitation functions. ($i = 0 - 3$).

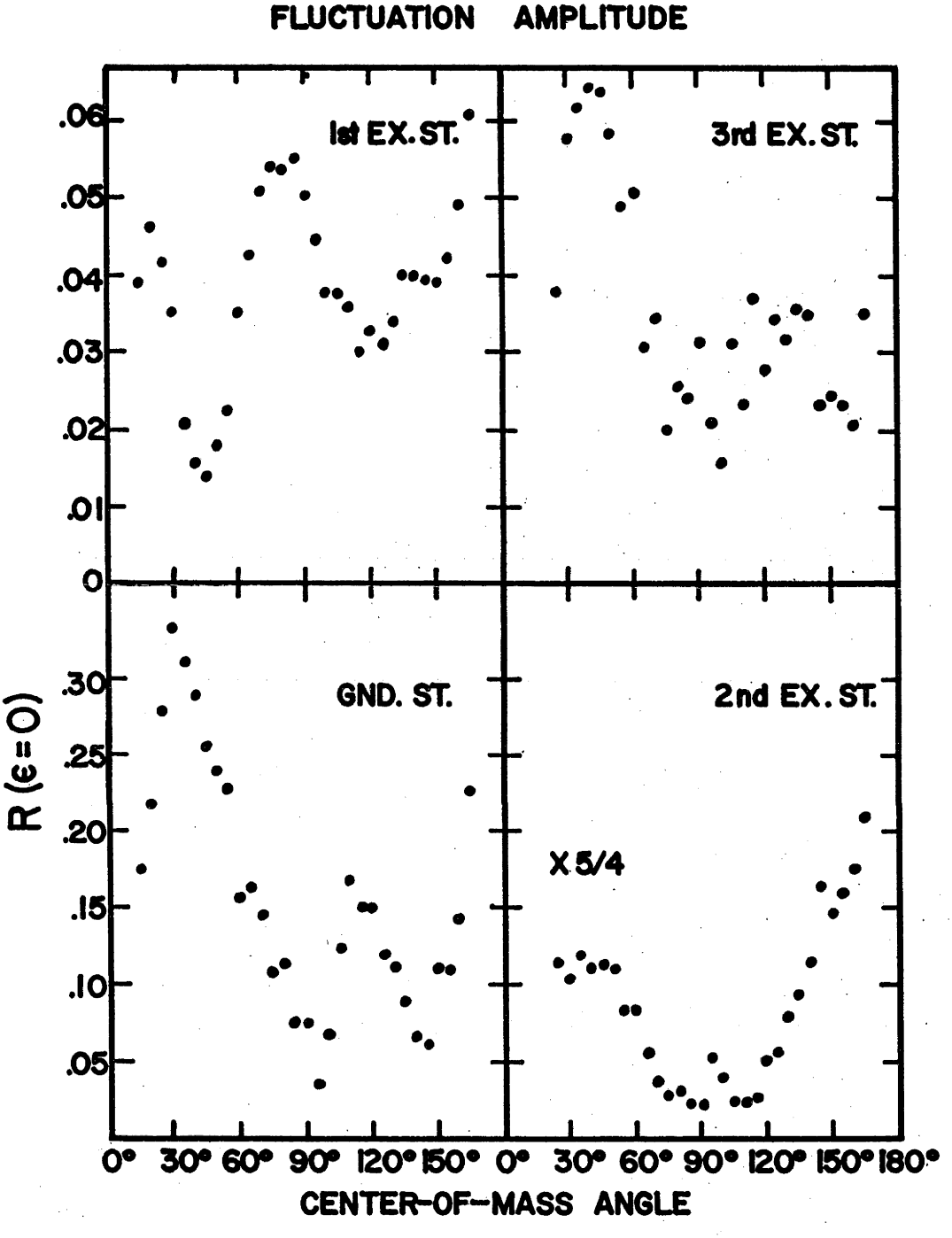
FLUCTUATION AMPLITUDE
1st EX. ST.
3rd EX. ST.
GND. ST.
2nd EX. ST.
X 5/4
R (ε=0)
.06
.05
.04
.03
.02
.01
0
.30
.25
.20
.15
.10
.05
0° 30° 60° 90° 120° 150° 0° 30° 60° 90° 120° 150° 180°
CENTER-OF-MASS ANGLE

TABLE 6.4.

$R^{ij}(\epsilon)$ for $d\sigma/d\Omega(\theta,\alpha_i,\alpha_j)$ 8.00-8.34 Mev Data.

Sample Angle	(α_o,α_1) $R^{ij}(\epsilon)$	(α_o,α_2) $R^{ij}(\epsilon)$	(α_o,α_3) $R^{ij}(\epsilon)$	(α_1,α_2) $R^{ij}(\epsilon)$	(α_1,α_3) $R^{ij}(\epsilon)$	(α_2,α_3) $R^{ij}(\epsilon)$
25°	.021	.011	-.018	.001	-.006	.008
	-.035	.009	.004	-.005	.004	.015
	-.024	.021	-.002	-.003	.003	.009
45°	.020	.029	.030	-.006	.003	.054
	.012	.037	.053	-.004	-.001	.046
	-.002	.045	.067	.002	-.002	.025
90°	-.002	.001	.003	-.009	.019	.003
	-.006	-.001	.001	-.010	.008	.004
	-.004	.007	.008	-.011	.003	-.002
135°	.020	-.013	-.010	-.008	-.009	-.029
	.016	.004	-.006	-.006	.004	-.025
	.024	.013	-.001	-.002	-.004	-.008
165°	.012	.101	.016	-.012	-.017	.010
	-.022	.089	.008	-.017	-.020	.015
	-.023	.065	.015	-.021	-.009	.016

Values of $R^{ij}(o)$ in this table must be compared with the R(o) of Fig. 6.3, for significance. It is seen that the $R^{ij}(\epsilon$ small) are non-Lorentzian in shape and are generally small. A few i, j combinations result in significant positive values for $R^{ij}(o)$, but only at one or two sampling angles; for the same i, j set, other angles give negative $R^{ij}(o)$. This behaviour is thought to imply overall lack of correlation, and it is therefore concluded

that the 8.00 - 8.34 Mev multiple $d\sigma/d\Omega(\theta)$ reveal no evidence for the existence of correlations between cross sections corresponding to different final states.

3.4(c). Integrated σ Correlation Function Analysis 8.00 - 8.34 Mev.

In order to compare the properties of the $d\sigma/d\Omega(\theta, \alpha_i)$ excitation functions with those of the integrated σ (α_i), $R(\epsilon)$ and $R_{ij}(\epsilon)$ correlations were computed for the A_L coefficient excitation functions extracted from the Legendre-Polynomial fits of section (4.8), Chapter III. The values of R(o) for the A_o (which are just the integrated σ) are: .028 (α_o), .018 (α_1), .027(α_2) and .010(α_3) respectively. A comparison of these results with those of Fig 6.3 indicates that all fall below or coincide with the lowest R(o)(θ) values for each alpha group, which is in agreement with the prediction that (section 2.1(c)) the mean fluctuation amplitude is much smaller for the integrated σ (α_i) than for the $d\sigma/d\Omega(\theta, \alpha_i)$.

The extracted Γ for the various $A_L(\alpha_i)$ are given in Table 6.5. Although the variation in values is considerable it appears that Γ is roughly independent of

Polynomial number for each α group. The $\Gamma(A_o)$ is just the "coherence width" for the integrated σ, and can be compared with the results of Fig. 6.2 for the $d\sigma/d\Omega(\theta)\langle\Gamma\rangle_\theta$ values. It is seen that the $\Gamma(A_o)$, which agree closely with the $\langle\Gamma\rangle_\theta$, are rather different for each α group. Ericson's model, on the contrary, predicts a Γ independent of α group.

TABLE 6.5

Γ(kev) for $A_L(\alpha_i)$ Excitation Functions 8.00-8.34 Mev.

COEFFICIENT	(α_o)	(α_1)	(α_2)	(α_3)
A_o	17	19	30	11
A_1	41	18	30	15
A_2	21	21	28	17
A_3	62	20	33	22
A_4	63	23	30	48

The cross correlation $R(\epsilon)$ was computed for the integrated $\sigma(\alpha_i)$, using all possible i, j combinations. Results are given in Table 6.6., which shows the $R^{ij}(\epsilon)$ values for ϵ = 0, 20 and 40 kev.

TABLE 6.6

$R^{ij}(\epsilon)$ for integrated $\sigma(\alpha_i)$ 8.00 - 8.34 Mev.

(α_0,α_1)	(α_0,α_2)	(α_0,α_3)	(α_1,α_2)	(α_1,α_3)	(α_2,α_3)
.008	-.001	-.008	-.005	.001	.004
-.001	.002	-.001	-.007	.001	.001
-.003	.005	.004	-.006	-.003	-.003

It is clear that the R^{ij}(small ϵ) are non-Lorentzian, and that any positive values for $R^{ij}(o)$ are much smaller than the R(o) for the corresponding $\sigma(\alpha_i)$ (given above). There would thus appear to be no significant correlation between integrated cross sections corresponding to different α groups.

In order to further test the theoretical relation $R(o) \sim 1/n$ (see section (3.3(d)), the integrated $\sigma(\alpha_i)$ were summed in sets of 2, 3 and 4, using all possible α group permutations for each set. The parameter R(o) was computed for each partial sum, and results are shown in Table 6.7. Numbers in brackets correspond to the α groups included in the sum. As in section (3.3(d)), a qualitative agreement with theory is obtained; i.e. the sums over 2 α groups have larger R(o) values than the sums over 3 and 4 α groups respectively. However, there is no quantitative

proportionality between R(o) and the exact number of states (magnetic substates) included in each sum.

TABLE 6.7.

R(o) for $\sigma(\alpha_i)$ Summed By Stages 8.00 - 8.34 Mev.

$\sum 2$	R(o)	$\sum 3$	R(o)	$\sum 4$	R(o)
(1,2)	.016	(1,2,3)	.008	(1,2,3,4)	.005
(1,3)	.017	(1,2,4)	.009		
(1,4)	.004	(1,3,4)	.008		
(2,3)	.008	(2,3,4)	.006		
(2,4)	.010				
(3,4)	.013				

The R(o) for $(\sigma(\alpha_0) + (\alpha_1))$ is 0.16 and R(o) for $\sum_{i=0}^{3} \sigma(\alpha_i)$ is .005. This is a factor of 2.6 decrease in R(o) values, to be compared with a theoretical expectation of 6 (section 3.3(d)). The discrepancy is somewhat less than that found in connection with the $d\sigma/d\Omega(90^\circ, 135^\circ)$ excitation functions (section3.3(d)), but is still large enough to suggest the previous conclusions.

Section 4. CONCLUSIONS.

The Statistical Fluctuation model of Ericson is only partially successful in accounting for the $Al^{27}(p,\alpha)Mg^{24}$ cross section data of Chapter III. Significant results of the analysis are the following:-

(a) All cross-correlation calculations indicate that there is no appreciable level of correlation between cross sections corresponding to different final states in Mg^{24}. This is a strong argument for the correctness of the Statistical Model approach, and directly contradicts the predictions of Izumo's Partial Equilibrium Model. Results of sections (3.3(d), 3.4(c)) indicate that the $R(o) \sim 1/n$ rule is not well satisfied; this can be explained either by the existence of strong correlations between compound nucleus cross sections leading to different final states, or by the presence of significant D.I. contributions. In view of the cross-correlation evidence, the latter appears more plausible.

(b) Section (3.4(a)) indicates that Γ extracted from $d\sigma/d\Omega(\theta)$ excitation functions may be a strong function of θ, implying that $\Gamma_J \neq$ constant, and hence that the simplifications introduced into equation (6.16, 6.17) are

not permissible. The recent Γ measurements of groups (Ha63, Al63) who have performed single angle $d\sigma/d\Omega(\theta)$ correlation calculations (using the assumption Γ_J = const.) would therefore appear to be questionable. It is noted that (see equation 6.17), under the restriction $\Gamma_J \neq$ const., the Γ values extracted from integrated cross sections represent weighted averages of the different Γ_J; such measurements may therefore constitute at least an approximation to the average (over levels of different J) compound nucleus width. The integrated cross section Γ values measured in this chapter for the $Al^{27}(p,\alpha)Mg^{24}$ reaction are $\sim$ 20 - 30 kev, which correspond to compound nucleus lifetimes of 2.1 - 3.1 x 10^{-20} sec. Since the energy step size (20 kev) used in measuring the cross sections was relatively large, some fluctuation maxima and minima may have been missed; hence the quoted lifetime is expected to be merely a lower limit.

Although the results of this chapter suggest that Statistical Fluctuation Theory can be usefully applied in the A = 20 - 30 mass region, more unambiguous tests are expected in the region of medium weight and heavy nuclei, where the "classical" Statistical Model has had greater success. The only data of this type so far reported is

that of Lee and Schiffer (Le63) on Ni^{58}, $Ni^{60}(p,p)Ni^{58},Ni^{60}$. It appears that much information on the nature of compound nuclear systems and reaction mechanisms can be obtained from studies of cross section fluctuations, but that a great deal of experimental data covering a variety of reaction types will be required before any general conclusions can be drawn.

REFERENCES

Al 60a — Almqvist, Bromley, and Kuehner, 2nd Gatlinburg Conf. on Reactions Between Complex Nuclei (1960), 282.

Al 60b — Almqvist, Bromley, and Kuehner, Phys. Rev. Letters, 4 (1960), 515.

Al 63a — Allardyce, Graham, and Hall, (1963) to be published.

Al 63b — Almqvist, Bromley, Kuehner, and Whalen, Phys. Rev., 130 (1963), 1140.

An 62 — Andersson-Lindström, Zeits für Natur, 17A (1962), 238.

An 63 — Andersson-Lindström and Roessle, Physics Letters, 5 (1963), 71.

Ba 59 — Babcock, Davis, Ruby, Sun and Wolley, Nucleonics, 17 (1959), 116.

Ba 61 — Babcock, I.R.E. Trans. Nuclear Science, NS-8, 1 (1961), 98.

Bi 63 — Birk, Goldring, and Hillman, Nuclear. Instr. and Methods, 21 (1963), 197.

Bl 52 — Blatt and Biederharn, Revs. Mod. Phys., 24 (1952), 258.

Bl 60 — Blankenship and Halbert, Nuclear Instr. and Methods, 8 (1960), 106.

Bl 62 — Blanc, Gambon, Devillers, Reme, Vedrenne, and Ambrosino, Nuovo Cimento, 23 (1962), 1140.

Bo 39 — Bohr and Wheeler, Phys. Rev., 56 (1939), 426.

Bo 62a — Bodansky, Ann. Revs. Nuc. Sci., 12 (1962), 79.

Bo 62b Bormann, Kernforschungsanlage, Jülich, Germany, JUL-20-RE, (1962).

Br 54 Briggs, Rev. Mod. Phys., 26 (1954), 1.

Br 60a Bromley, Kuehner, and Almqvist, 2nd Gatlinburg Conf. on Reactions Between Complex Nuclei (1960), 151.

Br 60b Bromley, Kuehner, and Almqvist, Phys. Rev. Letters, 4 (1960), 365.

Br 62 Bromley, I.R.E. Trans. Nuclear Science, NS-9, 3(1962), 124.

Br 63a von Brentano, Ph.D. Thesis, Heidleberg, (1963).

Br 63b Brink and Stephen, Physics Letters, 5 (1963), 77.

Co 61 Colli, Marcazzan, Merzari, Sona and Tomas, Nuovo Cimento, 20 (1961), 928.

Co 62a Colli, Facchini, Iori, Marcazzan, Milazzo and Tonolini, Physics Letters, 1 (1962), 120.

Co 62b Colli, Facchini, Iori, Marcazzan, Milazzo, Menichella and Tonolini, Energia Nuclear, 9 (1962), 439.

Co 62c Colli, Iori, Marcazzan and Milazzo, Physics Letters, 2 (1962),12.

Co 63 Colli, Iori, Marcazzan and Milazzo, Nuclear Physics, 43 (1963), 529.

Da 60a Dabbs and Walter, Proc. Conf. on Semiconductor Nuclear Particle Detectors, Asheville (1960), NASNRC-R-32.

Da 60b Davis, Phys. Rev. Letters, 4 (1960), 521.

De 61a Dearnaley and Whitehead, A.E.R.E. R-3662 (1961).

De 61b Deuchars and Lawrence, Nature, 191 (1961), 995.

De 61c Deuchars and Lawrence, Nature, 192 (1961), 1278.

De 61d Dearnaley and Ferguson, Proc. Rutherford Jubilee Conf. (1961).

De 62a Dearnaley and Ferguson, Nucleonics 20 (1962), 84.

De 62b Dearnaley, Ferguson and Morrison, I.R.E. Trans. Nuclear Science. NS-9, 3 (1962), 174.

De 62d Dearnaley and Ferguson, Physics Letters 1 (1962), 196.

De 62e Depraz, Duborgel, Grenier and Salin, Compt. Rend. 255 (1962), 2938.

Di 62 Dixon and Aitken, Physics Letters, 2 (1962), 152.

Di 63 Didier, Fort and Thouvenin, Compt. Rend., 256 (1963), 124.

En 57 Endt and Braams, Rev. Mod. Phys., 29 (1957), 683.

En 62a Endres, Bramson, and Medcalf, Hanford, HW-SA-2624, June (1962).

En 62b Endt and Van der Leun, Nuclear Physics, 34 (1962), 1.

Er 60 Ericson, Advances in Physics, 9 (1960), 425.

Er 62 Ericson, Symposium on Direct Interactions and Nuclear Reaction Mechanisms, Padua, Sept. (1962).

Er 63 Ericson, Annals of Physics (to be published), (1963).

Ev 55 Evans, The Atomic Nucleus, McGraw-Hill Book Co., Inc., N.Y., (1955), 516.

Ev 63 Evans, Kuehner, Litherland and Almqvist, Phys. Rev., 131 (1963), 818.

Fa 60 Fairstein, O.R.N.L. Report, TID-6119(1960).

Fa 62 Facchini, Marcazzan, Merzari and Tonolini, Physics Letters, 1 (1962), 6.

Fa 62a Ferguson, Montague and Whitehead, Nuclear Electronics, 1 (1962), 523.

Fe 62b Feshbach, Annals of Physics, 19 (1962), 287.

Fi 58 Fischer, Fischer, Remler and Tatcher, Phys. Rev., 110 (1958), 286(L).

Fi 63 Fitch, Nuclear Instr. and Methods, 20 (1963), 247.

Fo 56 Fowley and Brolley, Revs. Mod. Phys., 28 (1956), 103.

Ga 59 Gabbard, Davis and Bonner, Phys. Rev., 114 (1959), 201.

Ga 60 Gatti, Cottini, Giannelli and Rozzi, Nuovo Cimento, 3 (1960), 473.

Gi 53 Gillespie, Signal, Noise and Resolution in Nuclear Counter Amplifiers, McGraw-Hill Book Co., Inc., N.Y. (1955).

Gi 62 Gibson and Donovan, Ann. Revs. Nuclear Science, 12 (1962), 189.

Gl 61 Glover and Weigold, Nuclear Physics, 24 (1961), 630.

Ha 63 Halbert, Durham, Moak and Zucker, Nuclear Physics 47 (1963), 353.

Hi 60a Hinds and Middleton, Proc. Kingston Conf. on Nuclear Structure, R/C No.121. (1960).

Hi 60b Hinds and Middleton, Proc. Phys. Soc., 76 (1960), 553.

Hi 61 Hinds, Middleton and Litherland, Proc. Phys. Soc., 77 (1961), 1210(L).

Iz 61 Izumo, Prog. of Theoretical Physics, 26 (1961), 807.

Iz 62 Izumo, University of Tokyo Inst. for Nuclear Study INSJ-51, Oct. (1962).

Je 63 Jenkin, Earwaker and Titterton, Nuclear Physics, 44 (1963), 453.

Ke 59 Kern, Thompson and Ferguson, Nuclear Physics, 10 (1959), 226.

Kl 61 Klingensmith, I.R.E. Trans. Nuclear Science. NS-8, 1 (1961)112.

Ku 63a Kuehner, Almqvist and Bromley, Phys. Rev., 131 (1963), 1254.

Ku 63b Kuehner, Prentice and Almqvist, Physics Letters, 4 (1963), 332.

La 63 Lawrence and Hay, Nuclear Physics, 44(1963),518.

Le 63 Lee and Schiffer, Physics Letters, 4(1963), 104.

Li 61 Litherland, Can. J. Phys., 39 (1961), 1245.

Ma 56 Marion, Brugger and Chapman, Phys. Rev., 101 (1956), 247.

Ma 62 Marcazzan, Merzari, and Tonolini, Physics Letters, 1 (1962), 21.

Mo 59 Moray and Schmitt, Phys. Rev., 115 (1959), 1707.

Mu 62 Murphy, UCRL-6505, Feb. (1962).

Og 60 Ogata, Itoh, Matsuda, Takamatsu, Kawashima, Masaika, and Kumabe, J. Phys. Soc., Japan, 15 (1960), 1719.

Pa 53 Paul and Clarke, Can. J. Phys., 31 (1953), 267.

Po 63 Potenza, Ricamo and Rubbino, Nuclear Physics, 41 (1963), 298.

Qu 62 Quinton and Lawrence, Nuclear Physics, 37 (1962), 244.

Qu 63 Quinton and Lawrence, Physics Letters, 6 (1963), 231.

Ro 53 Rose, Phys. Rev., 91 (1953), 610.

Ro 60 Roll and Steigert, Nuclear Physics, 17 (1960), 54.

Sa 62 Sakai, Nuclear Electronics, 1 (1962), 551.

Sh 51 Shoemaker, Faulkner, Bouricius, Kaufmann and Mooring, Phys. Rev. 83 (1951), 1011.

Sm 60 Smith, Bostrom and Hudspeth, Phys. Rev., 117 (1960), 514.

Ts 63 Tsukada and Tanaka, J. Phys. Soc. Japan, 18 (1963), 610.

Va 57 Van Patter, Porter and Rothman, Phys. Rev., 106 (1957), 1016.

Vo 60 Vogt and McManus, 2nd Gatlinburg Conf. on Reactions Between Complex Nuclei.(1960), 291.

Wa 60 Wapstra, Everling, Koenig and Mattauch, USAEC Nuclear Data Tables (1960).

Wa 63 Warsch, Temmer and Bleiden, Nuclear Physics, 44 (1963), 329.

Wh 58 Whaling, Handbuch der Physik, E. Flügge, ed., Springer-Verlag, Berlin, 1958, Vol.34, p.193.

Wh 61 White, Dearnaley and Ferguson, Harwell (1961), unpublished.

Wi 60 Wildermuth and Carovillano, Nuclear Physics, 28 (1960, 636.

Ya 61 Yamashita, J. Phys. Soc. Japan, 16 (1961), 2378.